Development of nanobody-based surfaces for on-demand smart switchable biosensing

Bárbara Sofia Fialho Simões

A thesis submitted to the University of Birmingham

For the degree of DOCTOR OF PHILOSOPHY

School of Chemical Engineering

College of Engineering and Physical Sciences

The University of Birmingham

August 2021

Abstract

The biosensing field has been evolving with the advances of nanotechnology, medicine and with the need for diagnostics and health monitoring. Biosensors are facing high demands related to sensitivity, long term stability and on demand sensing. Control over detection provides the opportunity for on-demand biosensing and smart materials such as stimuli-responsive surfaces that can control a wide range of bio-interactions. However, there are few smart surfaces for on demand biosensing and these are limited to control over simple molecular structures. To address these challenges, this research used single domain antibodies, known as nanobodies (Nbs), with great potential as biorecognition elements for sensors due to their small size, specificity and robustness. Different strategies for Nbs immobilisation on gold sensors were optimised to retain their maximum functionality. The experimental data and detailed computational simulations confirmed the formation of stable, well-oriented nanobody monolayers. Furthermore, this work explored challenges related with Nbs' orientation and antigen dimensions, emphasizing crucial factors to consider when designing nanobody-based biosensors. Envisioning new smart electrically-responsive surfaces, preliminary studies showed the stability and high response of Nbs under applied potentials. Additionally, electrically-responsive oligopeptides, potential switching units for nanobody-antigen binding control, were designed and investigated. These oligopeptides are required to conceal the Nbs binding site, only exposing it to bind the antigen upon applied potential.

In conclusion, this work provides a step forward with the vision of combining stimulus-responsive surfaces with nanobodies for on-demand biosensing, contributing for the design and fabrication of stable, reliable, and robust biosensing platforms for a wide range of medical, biotechnological, environmental, and food applications.

Acknowledgements

I would first like to thank my supervisor Prof. Mendes for the guidance, support and trust. Your optimism was an inspiration throughout my years at the University of Birmingham.

I would like to give my thanks to the post docs from the group, which were incredibly supportive, including with PhD-life-crisis questions: Stefano, Eduardo, Josh G., Marcos, Craig, Nasim, Seyed and Setarah. Additionally, I would like to thank my great colleagues that shared with me this PhD adventure in the lab, office and in the atrium with loads of coffee in between: Bárbara G., Monika, Phillipa, Kam, Josh N., Yazmin, Francia, Alice, Pushpa, Dario, Laura B., Charlie and Miguel. A special thanks to Laura Buccoli, Gianluca, João, Inês, Carlos, Ana, Sanje, Carolina, and Paulo, who where part of the best moments. Thank you to Neil Fariley and Dr. David Morgan for sharing their knowledge on XPS. Thank you to Dr. Scurr and Anna for showing me the SIMs world. Thank you to Dr. Mulheran and Dr. Kubiak-Ossowska, for teaching me MDS at Glasgow. Thank you to the Guedens Group at Hasselt University for providing the nanobody NbVCAM1 and their expertise.

Thank you to my friends of always: Isabel and Artur. You are like family to me, and these years were one more proof of our amazing friendship. Also Cláudia, Kevin, Sara, Rafael, Sevde, Julia, Neetu and Konrad, thank you so much for being there for me.

Lastly, but most importantly, my family. Um agradecimento do fundo do coração aos meus pais e maninho. Vocês são a minha definição de saudade, luta e felicidade. Agradeço também aos meus avós, e em especial ao meu avô Daniel. A nossa estrela do mar no céu. Sei que estás orgulhoso e se há quem me tenha inspirado a ser o que sou hoje, foste tu avôzinho. Finally, to my husband Lorenzo who has been incredibly patient, supportive and loving. Without you, this would not have been possible. You are my strength and happiness. Thank you!

Table of contents

List of Figures

List of Tables

List of Abbreviations and Acronyms

ABT	4-azidobutane-1-thiol
AHA	Azidohomoalanine
BDMT	1,4-benzenedimethanethiol
BE	Binding Energy
BSA	Bovine serum albumin
C3βD	Cysteine-(proline-proline-diamino propionic acid)$_3$-proline-proline
C3εK	Cysteine-(proline-proline-ε-lysine)$_3$-proline-proline
C5K	Cysteine-(εLysine)$_4$-εLysine
C8K	Cysteine-(εLysine)$_7$-εLysine
CD	Circular dichroism
CDR	Complementary determinant region
CE	Counter electrode
COVID	Corona virus disease
CPS	Counts per second
CUAAC	Copper azide alkyne cyclo addition
CV	Coefficient of variability
CYS	Cysteine
DA	Dodecylamine
DNA	Deoxyribonucleic acid
EDC	1-ethyl-3-(3-dimethylaminopropyl)carbodiimide hydro chloride
EDTA	Dihydrogen sodium phosphate dihydrate
EGFP	Enhanced green fluorescent protein
EPL	Expressed protein ligation
FET	Field-effect transistors
FWHM	Full width at half maximum
GCIB	Gas cluster ion beam
GL	Gaussian/Lorentzian
GLN	Glutamine
HEPES	(4-(2-hydroxyethyl)-1-piperazineethanesulfonic acid)
HPLC	High Performance Liquid Chromatography
hVCAM1	Human vascular cell adhesion molecule 1
IPA	Isopropyl alcohol
KE	Kinetics energy
LCP	Left handed circlar polarised light
LCST	lower critical solution temperature
LEU	Leucine
LFA	Lateral flow analysis
LYS	Lysine
MDS	Molecular dynamics simulations
MPTES	Mercapto-trimethoxysilane
MUA	Mercaptoundecanoic acid

MW	Molecular weight
Nb	Nanobody
NbGFP	Nanobody green fluorescent protein
NbVCAM1	Nanobody vascular cell adhesion molecule 1
NHS	N-hydroxysuccinimide
NMR	Nuclear magnetic resonance
NVT	Number of particles, volume and temperature
OC	Open circuit
ORBISIMS	Orbi secondary ion mass spectrometer
PBS	Phosphate buffer saline
PNIPAM	Poly(N-isopropylacrylamide)
POC	Point of care
RB	Running buffer
RCP	Right handed circular polarised light
RE	Reference electrode
RGD	Arginine-glycine-aspartate
RMSD	Root mean square deviation
RMSF	Root mean square fluctuation
RT	Room temperature
RU	Response unit
SAM	Self assembled monolayer
SARS-CoV-2	Severe acute respiratory syndrome coronavirus 2)
SDS	Sodium dodecyl sulfate
SPME	Smooth particle mesh ewald
SPR	Surface plasmon resnoance
TEG11	Triethylene glycol mono-11-mercaptoundecyl ether
TFA	Trifluoroacetic acid
THPTA	Tris(3-hydroxypropyltriazolylmethyl)amine
TOF SIMS	Time of flight secondary ion mass spectrometer
TYR	Tyrosine
UV	Ultra violet
VMD	Visual molecular dynamics
WE	Working electrode
XPS	X-ray photoelectron spectroscopy

Chapter 1 Introduction

Biosensors are devices that detect the presence or concentration of a biological analyte. Control over the biological analyte detection provides the opportunity for on-demand biosensing (i.e. sensing upon requirement). Smart, stimuli-responsive surfaces are a class of materials that can control a wide range of bio-interactions, including antibody-antigen binding. However, in order for these surfaces to achieve high sensing performance there are various challenges such as long-term usability in complex media (such as media with cells or clinical samples) and sensitivity. To address these challenges, single domain antibodies, known as nanobodies have great potential as biorecognition elements for sensors due to their small size, affinity, specificity and robustness. Combining stimulus-responsive surfaces with nanobodies, the research from this thesis provides a step forward to the development of nanobody-based surfaces for on-demand biosensing. This chapter introduces a brief review on smart surfaces composed by stimuli-responsive surfaces and on nanobodies and their use on sensing platforms.

This chapter is partially based on the review (1) and article (2) co-written by the author of this thesis:

[1] Simões, B.; Gomes, B.; & Mendes, P. The increasing dynamic, functional complexity of bio-interface materials. Nat Rev Chem 2, 0120 (2018).

[2] Simões, B.; Guedens, W. J.; Keene, C.; Kubiak-Ossowska, K.; Mulheran, P.; Kotowska, A. M.; Scurr, D. J.; Alexander, M. R.; Broisat, A.; Johnson, S.; Muyldermans, S.; Devoogdt, N.; Adriaensens, P.; Mendes, P. M., Direct Immobilisation of Engineered Nanobodies on Gold Sensors. ACS Applied Materials & Interfaces 2021, 13 (15), 17353-17360

1.1 Literature Review

1.1.1. Outlook

At the core of many biosensing platforms is the detection of bio-interactions, such as antibody-antigen binding[3]. Surfaces functionalised with capture entities like antibodies or antigens, are devised for the detection of their binding targets in solution. These surfaces have been developed into numerous research, non-clinical[4] applications including research tools in structural, cell, and developmental biology[4], and clinical[5] applications such as nanobody-based cancer therapy for solid tumours[5]. However, while a vast variety of sensitive antibody detection strategies have been developed[6], there are only a limited number of reported systems with the ability to control the detection of the target[7]. Reasons for this limitation include the antibody dimensions[8] and lack of stability over long periods of time[9]. Recent developments could address these limitations by including surfaces functionalised with nanobodies as capture entities[4]. Nanobodies are smaller fragments of antibodies and preserve their affinity and specificity whilst being robust[4]. These attributes are not only promising for the development of more sensitive nanobody-based surfaces but also for the control over detection. The latter could allow a biosensing surface to remain inactive and sense upon demand. On-demand specific detection could be applied for near real-time, long-term monitoring of biological processes in cell culture systems or in diagnostic devices for disease detection and surveillance on-demand[1, 7].

Bio-interactions can be controlled by their surrounding environment, including stimuli-responsive surfaces[1, 10]. Surfaces with the ability to modulate their properties in response to diverse external stimuli have been created to control non-specific and specific interactions[1, 10]. Among other strategies, self-assembled monolayers (SAMs) have proven to be instrumental for the design and development of stimuli-responsive surfaces[1].

The following sections start by addressing SAMs, building up to further functionalisation of SAMs with macromolecules and different immobilisation strategies. The immobilisation strategies relevant for this thesis includes the use of engineered cysteines, amino-coupling, and click chemistry. Following the immobilisation methods, an introduction to nanobodies and nanobody-based surfaces is presented with different experimental and computational studies based on molecular dynamic simulations. Thereafter, applications of nanobody-based biosensors for diagnostic tools are presented, including the current state and limitations of static detection. Moving towards future applications of dynamic biosensing, relevant stimuli-responsive surfaces are described. The stimuli-responsive surfaces are organized based on the stimulus applied (chemical, temperature, light and electrical) with special focus given to electrical stimulus and biosensing applications due to the relevance to this thesis. This literature review concludes with a brief comparison between the stimuli used for biosensing applications. Lastly, the aims and objectives of this thesis are introduced, followed by a thesis outline with a brief description of each chapter.

1.1.2. **Self-assembled monolayers (SAMs)**

Naturally occurring in biological systems, self-assembly occurs through covalent or non-covalent interactions (i.e. hydrogen bonding, van der Waals, electrostatic, π-π interactions, hydrophobic interactions), that lead to the formation and organisation of stable structures (from atoms to mesoscale objects[11]) at the thermodynamic equilibrium. Self-assembly is a very effective and versatile strategy for surface functionalisation, leading scientists to pursue the bottom-up construction of functional assemblies[12]. Self-assembled monolayers (SAMs) form as a result of the spontaneous adsorption of molecules onto a substrate which results in

organized and packed monolayers. By convention, the molecular structure of SAMs is divided into three features[12, 13] (Figure 1.1): 1) the headgroup, which with strong affinity to the substrate will anchor the SAM molecule to the surface; 2) the backbone, which plays an important role in the molecular ordering and 3) the terminal group which determines the surface properties and functionality.

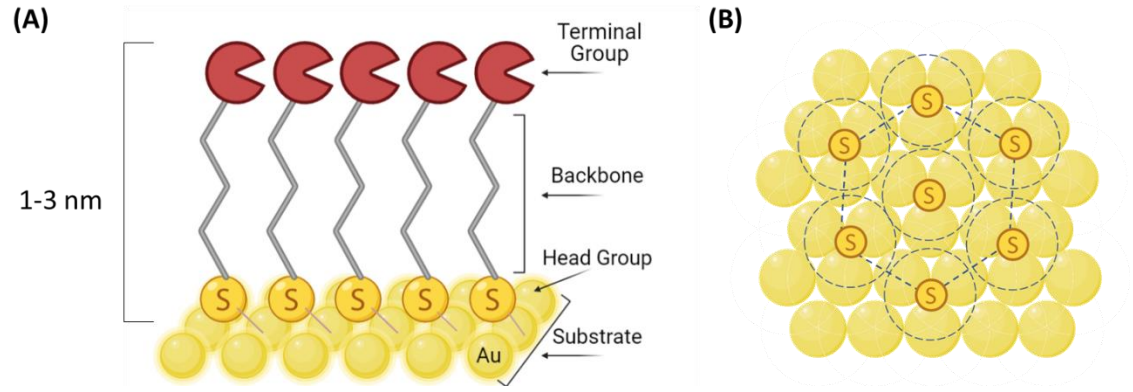

Figure 1.1 - Schematic representation of a self-assembled monolayer (SAM).(A) Side view showing SAMs with three distinguishable features: the headgroup that anchors the SAM molecule to the substrate, the spacer and the terminal group, which determines the properties and functionality of the final surface. (B) Top view of a maximum coverage of head groups on the substrate lattice (for instance, S-Au, thiolates), The dashed circles indicate the projected surface area occupied by the respective backbone chains.

Characteristics of the SAM result from an interplay role between 1) the affinity of the head group to the substrate, which influences the orientation of the adlayer, 2) the lateral non-covalent interactions between backbones (chains) that stabilise the structure and regulates the packing yield, and 3) the intramolecular interactions which determines the details of the super-lattice structure (e.g. tilt-angle, surface lattice reconstruction)[12]. SAMs can be formed in diverse substrates such as Au (gold), Cu (copper), Ag (silver). Au is one of the most used substrates

due to its various advantages, such as being inert, biocompatible and suitable to use with various analytical techniques such as plasmon resonance spectroscopy (SPR), quartz crystal microbalance (QCM) and ellipsometry[13]. These advantages and thiol-gold interaction (thiolate bond) makes SAMs of thiols on gold surfaces one of the most popular models, with extensive research on SAMs particularly composed by alkanethiols[13, 14]. Although the early literature on the thiolate (S-Au) formation starting from thiols (HS-R) or disulphides (R-S-S-R) have debated the means for the thiol (-SH) to lose its hydrogen, it is well accepted that S-Au bonding occurs in two steps: 1) fast physisorption and then 2) slow chemisorption whereas an initial "laying down" position moves towards a "standing up" position[15] (Figure 1.2).

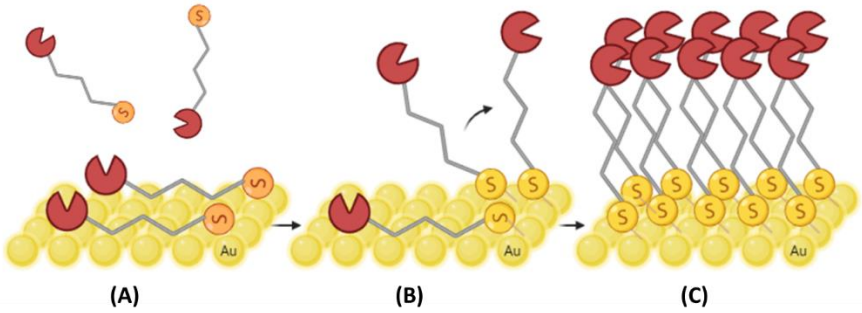

Figure 1.2 – SAM formation schematics. The S-Au bonding happens after a (A) fast physisorption, giving place to a (B) slow chemisorption in which the SAM molecules transition from a laying down position to a standing up position. (C) Packed and organized SAM.

When in the "standing up" position, the tilt angle is defined between the linear backbone chain and the normal to the surface. The tilts of alkanethiol chains vary for the various metals, being the largest angles (with an absolute value near 30°) found on gold Au(111)[13], having an impact in the expected thickness from these SAMs. Studies of alkanethiols adsorption kinetics onto Au(111) surfaces have shown that at diluted solutions (10^{-3} M) the chemisorption step can take a few minutes, with contact angles and thickness at about 80-90% of their maximum values,

whilst only after several hours the thickness and contacts angles reach their plateau[16]. The chemisorption step can be well described by diffusion-controlled Langmuir adsorption being dependent on the thiol concentration. Thereafter the SAM evolves from a disordered to an ordered state of the backbone chains. Thus, the kinetics of the chemisorption is governed by the surface-head group reaction, whilst the final step kinetics, with limited number of free Au adsorption sites, it is related to the chain disorder (e.g. gauche chain defects), chain to chain interactions (VDW, dipole-dipole, etc) and surface mobility of chains[16]. For instance, the longer alkyl chains result in faster kinetics, due probably to their increased VDW interactions[16, 17].

In general, alkanethiol SAMs with different terminal groups are easy to prepare, needing a gas or liquid phase in contact with the surface, the latter being the most common in academic laboratories[18]. Depending on the chemistry of the alkanethiol, the optimal incubation solvents, times and temperature vary, specially considering that adsorption rate can differ with the alkanethiols' chain length, concentration and other experimental settings, such as the cleanliness of the substrate[19]. Understanding and controlling how the described parameters influence the different types of SAMs allows the monolayer kinetics of formation to be manipulated fairly easily[17]. Furthermore, free thiols from the solution can replace thiols at the surface, forming a new thiolate bond. Even though the thiol-gold affinity promotes the thiol interaction over other adventitious organic impurities at the surface, this replacement influences the kinetics of SAM formation[17]. Thus it is good practice to apply thorough cleaning steps before SAM formation to achieve better reproducibility[17].

Regarding the gold-thiol model limitations, the gold substrate can undergo oxidation after some period of time depending on its storage conditions (weeks or months)[15] which results in thiol desorption. Furthermore, in order to avoid thiol desorption from gold reduction[13, 20] when the substrate is used as a working electrode, the negative potential applied should not go lower than

a certain potential, depending on the SAM and the structure of the metal[21, 22]. To overcome these stability limitations, the silanes on conductive indium tin oxide (ITO) could be an alternative self-assembly system (forming siloxane, Si-O), being thermally and chemically more stable than thiols[10]. However, the uncontrolled ITO surface roughness can lead to reproducibility issues for SAM formation[23].

Overall, gold substrate surfaces and a thorough understanding of SAM formation strategies provides a controllable and convenient platform for proof of concept experiments that can be characterised with several techniques.

1.1.3. **Surface functionalisation with macromolecules**

The immobilisation of macromolecules at the surface provides biological functionality. Some macromolecules have engineered thiol-containing residues, allowing their self-assembly on gold[24-26]. However, very often initial SAMs undergo further treatment towards the posterior immobilisation of various classes of macromolecules such as DNA, antibodies, enzymes, growth factors, peptide fragments and proteins[10, 13]. In order to immobilize macromolecules, the SAM terminal group must be a functional group, which allows the adequate surface properties for molecular adhesion (through non-specific binding) and/or will form a complex with the macromolecule chemical ligand (Figure 1.3). Depending on the size and complexity of the required functional group, the molecules can either first be pre-synthesized to form functionalised SAMs later, or SAMs are initially formed and the functional group is added later. The latter strategy has shown to require lower amounts of reagents and avoids complex synthesis processes[13]. Furthermore, upon a densely packed and stable SAM, compatibility

between the latter added functional groups (or macromolecules to immobilise) and the end groups (such as thiols) it is not required which is advantageous.[13]

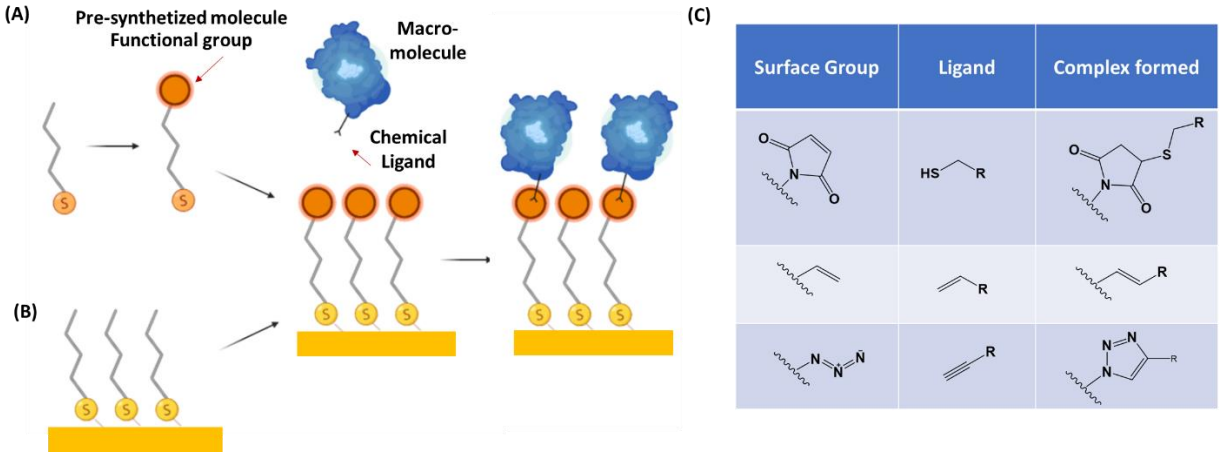

Figure 1.3 -Schematic representation on strategies for SAM functionalisation. (A) The thiol molecule is pre-synthetised with the functional group of interest before SAM formation; (B) The SAM is formed and modified after to incorporate the functional group of interest. (C) Different surface functional groups and respective chemical ligands (linkers) to macromolecules, which can also work vice-versa.

Typically multi-component SAMs are selected over the homogenous SAMs, providing various benefits. These include change in the wettability of surface, optimised space between functional groups which avoids steric hindrance within these[27] and ideally minimises non-specific interactions. To this end, ethylene glycol (EG)-terminated thiols are commonly used due to their anti-fouling capacity to resist non-specific protein adsorption.[28-33] Two different mechanisms can explain how oligo(EG)-terminated SAMs[28-31, 34] resist protein adsorption: 1) steric repulsion as a result of compression on the oligo(EG) caused by proteins approaching the surface and 2) a water barrier formed of strong hydrogen bonds between the oligo(EG) oxygen atoms and hydrogen atoms of the water molecules. Basically, the more hydrated the oligo(EG) SAM is, the more resistant to non-specific interactions. Therefore, the oligo(EG) SAM non-

fouling capacity depends on different parameters that influence the SAM hydration levels, such as packing density[32], ionic solution strength and temperature[28]. All considered, in the context of building a sensor platform the multi-component SAM must be optimised towards the end goal: high sensitivity for target detection. This implies that the immobilised macromolecules are optimally spaced and the space between does not bind non-specifically.

When immobilising macromolecules, a wide variety of methods have been applied for SAM surface modification: ranging from non-covalent to covalent and impacting randomly or specifically the posterior macromolecules orientation[35]. For instance, macromolecules have been immobilised onto SAM surfaces by either adsorption[36], molecular recognition with the immobilised chemical ligands[37] or covalent coupling to the SAM surface[38, 39]. Ideally, these methods do not cause denaturation or loss of biological activity, being biocompatible with the moieties to bind. Amongst the strategies involving covalent bonding is the amino coupling and "click chemistry". Whilst the amino coupling mainly takes advantage of the functional groups naturally existing on proteins, "click" chemistry provides directional and efficient immobilisation, but requires bioconjugation with a non-natural ligand at the protein's surface[40].

1.1.3.1. Macromolecules directly on gold: Engineered cysteine residues

The direct immobilisation of macromolecules on surfaces has proven to be challenging. Previous studies have shown that physical adsorption of proteins onto surfaces leads to activity loss, unreliable exchange events and reversibility of the adsorption process[35]. In particular, protein activity loss has been described as a consequence of random orientation upon immobilisation at the surfaces[41]. Efforts to address this issue used cysteines, natural thiol containing amino-acids, to pursue thiolate bonds between macromolecules and gold (Figure 1.4

(B)). In the case of antibodies, their native disulphide bonds were reduced to thiols, separating the Fab regions (antigen binding regions).[42-45] These studies have shown to specifically immobilize the Fab regions which obtained higher antigen responses than the randomly adsorbed full antibodies. When no native thiols are available, strategies to achieve the best performance upon direct immobilisation on gold have explored the engineering of cysteine residues opposite to the binding site of proteins[2, 24-26]. These studies have shown to successfully engineer cysteines on proteins whilst preserving the biological activity, achieving higher bio-interactions than the non-engineered proteins randomly immobilised. To conclude, although the immobilisation of macromolecules directly on gold is an attainable approach, there are challenges that need to be addressed, including the achievement of exclusively well-oriented adsorption.

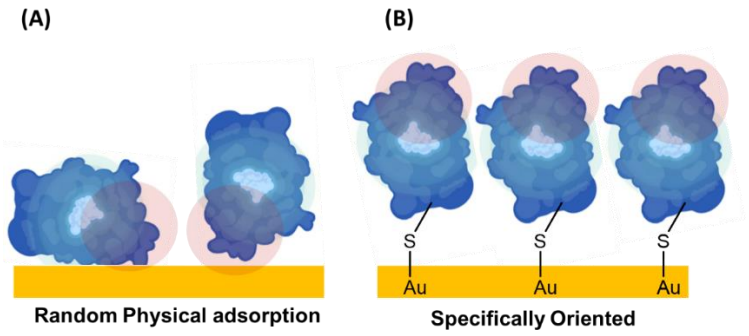

Figure 1.4 – Direct immobilisation of macromolecules on gold schematics. (a) Physical immobilisation; (B) specifically oriented immobilisation through a thiolate bond between the macromolecules' cysteines and the gold surface.

1.1.3.2. EDC-NHS amino coupling

The amino coupling methods to immobilize macromolecules is one of most frequently used technique. Although many methods for covalent coupling have been developed, the amino coupling is often the chosen method due to high yields and convenience[46] by using the proteins' native amino-acids and not requiring further modification. Amino coupling involves activation of a carboxylate group that can react with a primary amine so that an amide bond is formed. When functionalizing surfaces, the surface bound carboxylates react with the amine side chains of lysines and the N-terminus in the protein. The immobilisation process starts with the surface activation with reactive 1-ethyl-3-(3-dimethylaminopropyl)carbodiimide (EDC)-mediated N-hydroxysuccinimide (NHS). First EDC reacts with a carboxylic acid to form an active ester intermediate which is then replaced by a NHS ester (Figure 1.5). The latter is more reactive and couples with the primary amines of the followed protein solution.

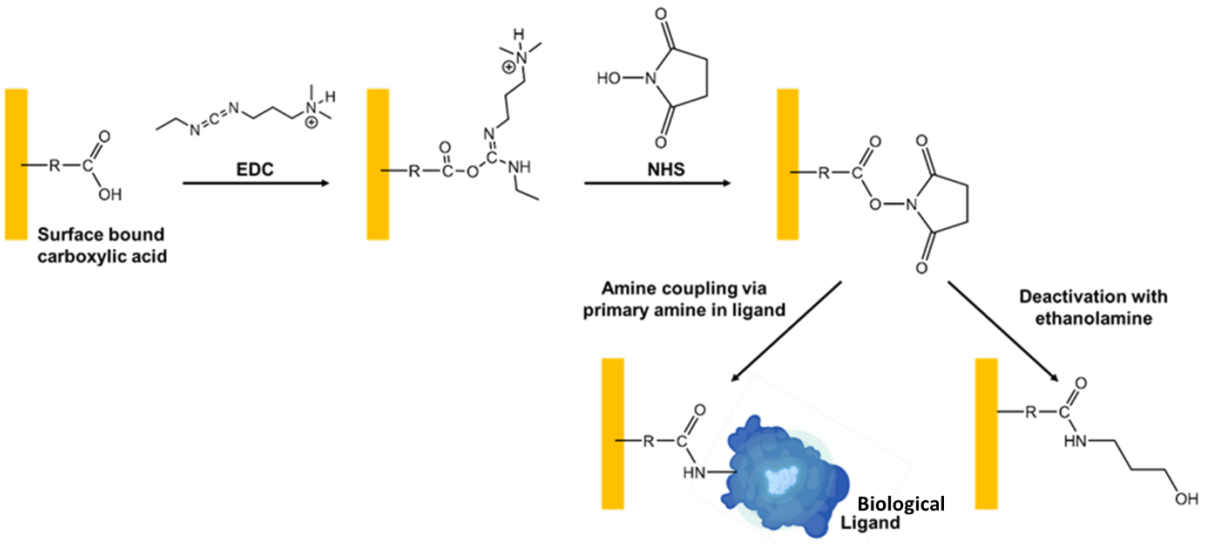

Figure 1.5 – Strategy for immobilisation at the carboxylate-terminated SAM surface through EDC/NHS amino coupling.

The reaction without NHS would be less efficient, as EDC is less reactive and its hydrolysis occurs faster. Parameters like solution ionic strength, pH, protein concentration, incubation time and reagents concentration are important to optimize the immobilisation[46, 47] (Figure 1.6). For instance, to facilitate the immobilisation through the electrostatic interactions between the protein and the negatively charged carboxylate surface prior to amine coupling, the solution pH should be below the pI (isoelectric point) of the proteins (net charge of the protein more positive)[47]. Efforts have also been made to allow the immobilisation of negatively charged proteins above their pI, by inverting the surface charge to positive by immobilising initially an asymmetric diamine comprising a reactive primary amine and a unreactive cationic tertiary amine[48]. The orientation of the proteins immobilised through amino-coupling relies on the proteins' amine groups position. Thus, it is ideal when no specific orientation is required[27] or when the amine groups are located opposite to the binding site[39, 49] but inadequate otherwise.

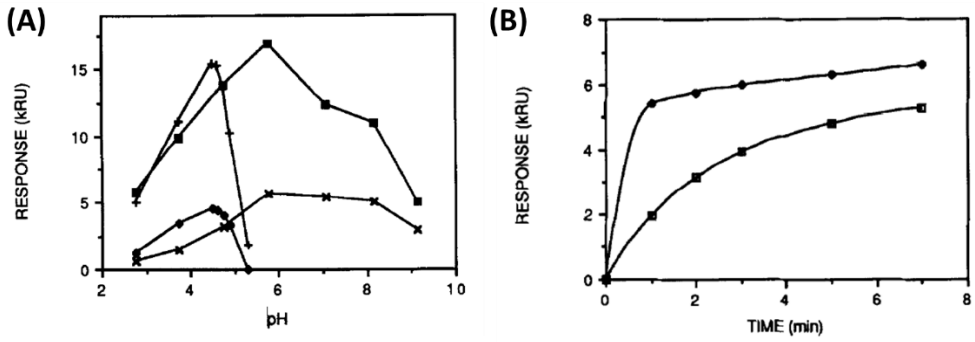

Figure 1.6 – NHS/EDC amino coupling efficiency of proteins based on pH and reaction time parameters. (A) Response of electrostatically adsorbed (+) and immobilised (♦) SpA protein and electrostatically adsorbed (■) and immobillised (×) RNase protein. (B) Response of immobilised RNase in a buffer at pH 4.7(■) and pH 7.1 (♦) as a function of reaction time. Adapted from[47]

1.1.3.3. Click-chemistry

Exclusively well-oriented functionalisation of surfaces plays a crucial role in the development of biosensors and their resulting performance. The established concept of "click chemistry"[50] provides an excellent platform for biomedical applications through effective surface modification[38, 51-56]. There are four kinds of click chemistry reactions mainly used in biochemical assays namely cycloaddition reaction, nucleophilic ring opening reaction, non-aldol carbonylation reaction and carbon-carbon multiple bonds addition reaction[50, 53, 57]. Among these, copper(I) catalysed azide-alkyne cycloaddition (CuAAC) is the most popular and has shown to be a powerful tool due to the high yields achieved, absence of by-products and moderate conditions required both in aqueous medium and under physiological conditions[57]. The CuAAC reaction occurs between an azide and an alkyne moiety forming a stable 5 membered 1,2,3-triazole ring under Cu(I) catalysis[38] (Figure 1.7). The catalyst Cu(I), usually resulting from the reduction of Cu(II) salt by the reducing agent sodium ascorbate, accelerates the reaction rate and allows it to occur at room temperature. In the absence of a catalyst, the reaction between the azides and alkynes requires high temperatures[58]. A potential disadvantage is the presence of Cu(II) ions which can be cytotoxic[59]. The water soluble chemical ligand THPTA can be used to assure the strong stabilisation of the Cu(I) oxidation state, therefore dropping the Cu-induced cytotoxicity by allowing lower copper usage[59]. An alternative to CuAAc is the cycloaddition between 1,2,4,5-tetrazines and trans-cyclooctene, a copper free reaction with rapid kinetics and low toxicity[57].

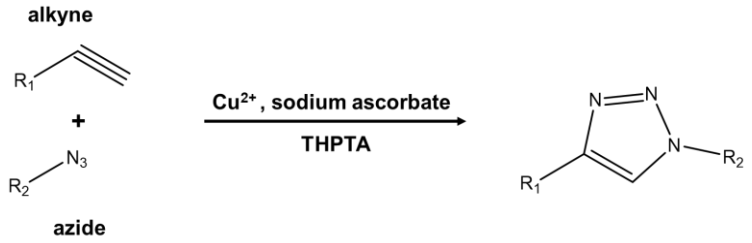

Figure 1.7 – Click chemistry: copper catalised azide-alkyne cycloaddition (CuAAc)

Two approaches have been used to obtain functionalised SAMs through click chemistry: either 1) the click reaction occurs in solution to the thiol-moeities (click in solution), being the substrate functionalised later, or 2) the SAM is firstly formed and the click reaction is carried out on the SAM (click on SAM)[55]. When involving small compounds, the click in solution might be beneficial[55], but larger biomolecules such as proteins usually require the click on SAM approach, which simultaneously avoid non-specific interactions with the substrate through direct contact[34, 38, 54, 56]. With click on SAM, the SAM functional group can be either the alkyne or the azide, being in solution respectively the azide- or alkyne-terminated moiety[13]. The CuAAc strategy for protein immobilisation on SAM surfaces provides highly oriented and functional homogenously covered surfaces[38]. It has been shown that orientation is particularly important to increase biosensor sensitivity as the bioreceptor-analyte binding events are highly dependent on the orientation of bioreceptors on the sensor surface and their availability to capture the analyte[54].

1.1.4. **Nanobodies and nanobody-based surfaces**

Single domain antibodies, generally referred to as nanobodies, are emerging as robust and versatile affinity reagents for research, diagnostics and therapeutics[60, 61]. They are an attractive

alternative to antibodies since they offer similar high affinity and high selectivity for a broad range of analytes (small organic molecules, proteins, cell epitopes) but they are smaller in size (~15 kDa, Figure 1.8). This latter characteristic allows nanobodies to have increased solubility and stability, easier production and low steric hindrance to reach targets[62-64]. The robustness of nanobodies has been shown in multiple regeneration cycles (when the nanobody surface can be reused)[65] and they have an extended shelf-life when compared with full size antibodies[66]. Moreover, their thermostability has been studied[4] but so far there are no reports on the nanobodies stability upon an applied potential.

Past literature on nanobodies has been primarily focused on free-form nanobodies and on nanobodies immobilised on nanoparticles[4]. Most of these studies highlight the nanobodies solubility and capability of reaching hidden and hard to access epitopes due to their size[66].

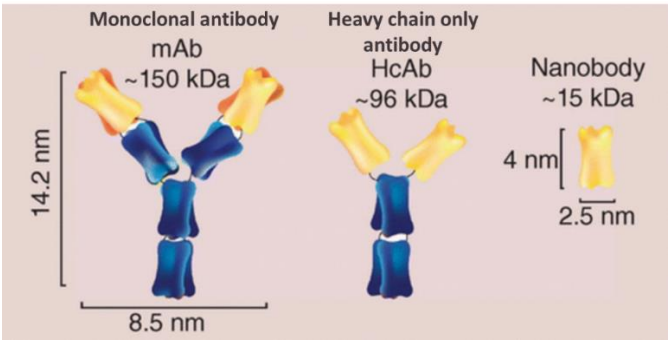

Figure 1.8 – Comparison schematics between antibodies, heavy chain antibodies and nanobodies. Adapted from[5]

1.1.4.1. Optimisation of nanobody-based surfaces

Small sized receptor molecules can create highly dense biologically active probes, thus nanobodies on surfaces could form highly functionalised platforms. Despite the advantages of

biosensor functionalised with nanobodies, few platforms have explored this approach[4]. Concerning the immobilisation of nanobodies on surfaces, orientation has been postulated as crucial to increasing the immobilisation efficiency[67] and thus the biological activity. Beekwilder et al[54], focused on comparing the immobilisation of nanobodies uniformly or randomly oriented via click chemistry on dextran cyclooctyne-terminated SPR chips[54] (Figure 1.9). To do so, the studied nanobodies had azide moeities incorporated into their sequence through the non-natural amino-acid azidohomoalanine (AHA). The AHA moeities were inserted specifically on either 1) one site at the C-terminus, opposite to the binding site (Nb1) or 2) five sites within the sequence (Nb5)[54]. The resulting nanobodies Nb1 and Nb5 either coupled to the surface with one orientation or five different orientations, respectively. The resulting SPR studies presented a 10 fold higher biosensor sensitivity when using the uniformly oriented Nb1, comparatively to Nb5 randomly oriented via click chemistry and NHS chemistry[54].

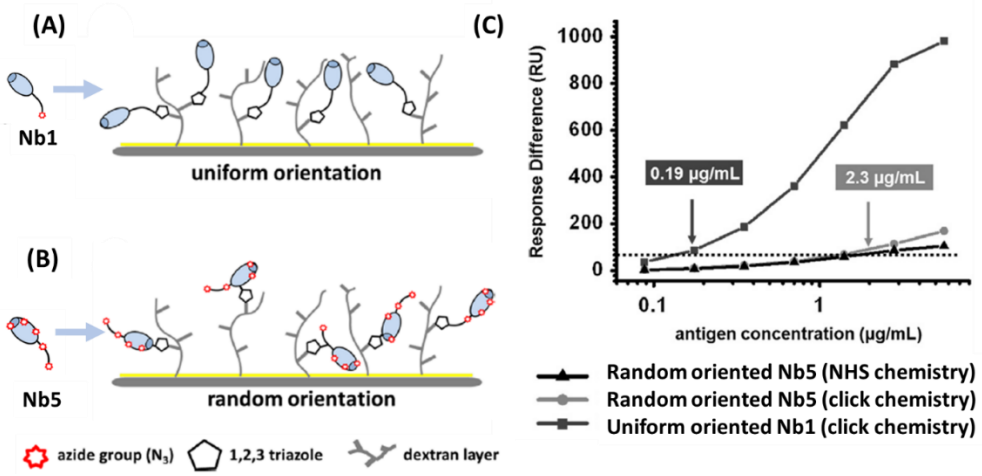

Figure 1.9 – Random and uniform orientation of immobilised nanobodies. (A-B) Schematics of the azide functionalised nanobodies covalently coupled in a (A) uniform orientation or (B) in a random orientation via one of the 5 available azides onto a cyclooctyne-tailored dextran sensor. (C) SPR results of Nb1 and Nb5 functionalised sensors, with antigen dilution series analysed on randomly oriented Nb5

click chemistry (circles) and NHS chemistry (triangles) and uniformly oriented click chemistry (squares). Adapted from[54].

In another study, besides orientation, the stability of the immobilisation method was demonstrated as an important factor for nanobody-antigen interactions through SPR[39]. Della Pia et al, immobilised green fluorescent protein nanobodies (NbGFP) through various immobilisation strategies[36,]. The nanobodies were immobilised on Ni^{2+}:nitrilotriacetic acid (NTA) (Figure 1.10(A)) and anti-polyhistidine chips (Figure 1.10(B)) *via* histidine tag, streptavidin-functionalised surfaces *via* biotin tag (Figure 1.10(C)) or directly on carboxylic-terminated surfaces via EDC/NHS amino-coupling[36,]. In all the cases the orientation of immobilised NbGFP was expected to be similar. Thereafter the nanobody-antigen (NbGFP-GFP) interaction was compared across the different nanobody immobilisation strategies. The results showed that the binding affinity was marginally affected (Figure 1.10) by the immobilisation strategies. Interestingly, the immobilisation method that showed a lower dissociation constant was the highly stable streptavidin/biotin based immobilisation, which the authors theorized to be due to potential additional stabilisation between nanobodies and the analyte[36,]. These studies[39, 54] showed that in addition to the nanobody orientation, the stability of the immobilisation method for nanobodies can play a role in the nanobody-antigen interactions.

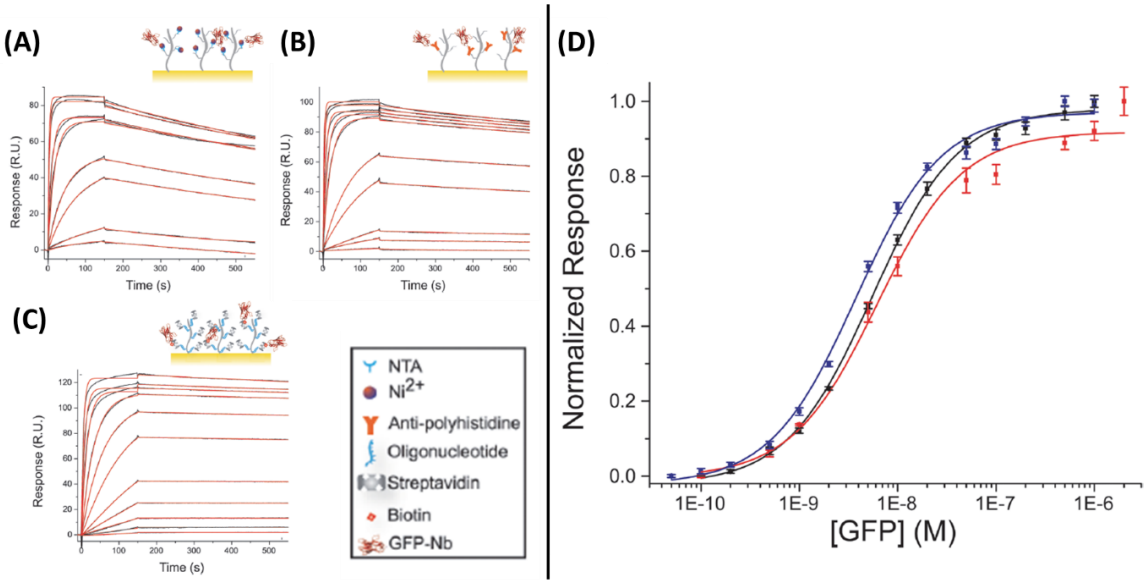

Figure 1.10 – NbGFP-GFP interaction as measured by SPR. (A-C) Binding of GFP to NbGFP immobilised on (A) Ni:NTA; (B) anti-polyhistidine antibody and (C) streptavidin terminated surfaces. (D) Endpoint response of the normalised binding curves as function of GFP concentration: red, blue and black correspond to results on Ni:NTA, anti-polyhistidine antibody and streptavidin terminated surfaces respectively, with Hill's equation fit. Adapted from[36].

Functionalising substrates directly with nanobodies can be highly desirable when the analyte detection is dependent on its proximity to the surface. The previously mentioned studies immobilised nanobodies on pre-functionalised dextran-containing surfaces[39, 54] which brings the analyte further away from the surface. Limitations for this type of functionalisation include the reduced Debye length (distance from the charged surface that can influence particles of the opposite charge) particularly under physiological conditions[68]. A reduced Debye length implies that in order to sense the target needs to be in close proximity to the surface. A larger Debye length gives a higher margin for detection above the surface. Filipiak et al, showed the advantage of functionalizing carbon nanotube transistors with nanobodies. Briefly, the basic principle of these nanotube field-effect transistors (FET) relies on the current change *via* the field effect as consequence of charged species adsorption[68]. The study has shown that FET

functionalised with NbGFP resulted in a sensitive label-free detection of GFP antigen under a buffer that recreates physiological conditions (high ionic strength which decreases the Debye length)[68]. The carbon nanotubes were also functionalised with polyethylene-glycol (PEG) and further blocked with bovine serum albumin protein (BSA) to avoid non-specific interactions (Figure 1.11(A)). Despite the short Debye length under physiological conditions (approximately 1 nm) the results showed that nanobodies could achieve lower detection limits that have only been achieved with antibodies and diluted samples (lower ionic strength and higher Debye length)[68]. Thus direct immobilisation of nanobodies to the surface can enhance analyte detection.

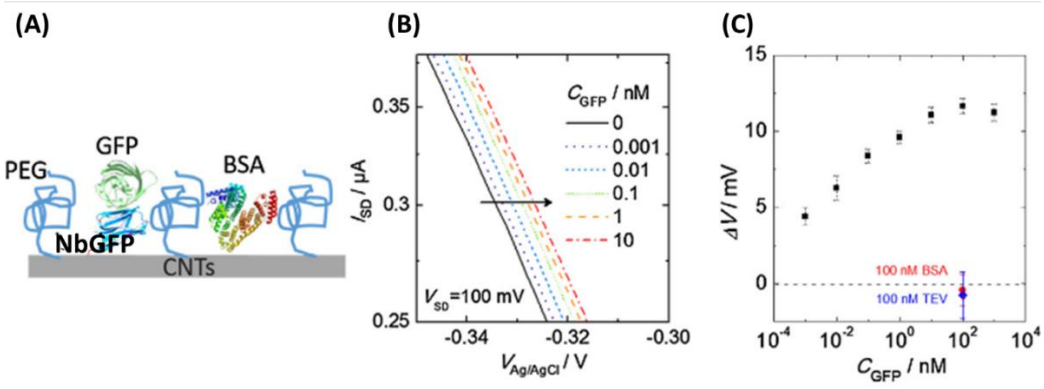

Figure 1.11 – FET-based nanobody assay for GFP detection. (A) Label-free schematics of the functionalised carbon nanotubes (CNTs) with NbGFP and PEG which was afterwards blocked with BSA to avoid non-specific interactions with the substrate. (B) Transfer curves measured in buffer for a wide range of GFP concentrations. With increasing GFP concentration a shift of the transfer curve to more positive voltages is visible (indicated by the arrow). (C) Sensor voltage shift in function of GFP concentration. The dashed line represents the blank value (no GFP) and the controls are represented for non-specific response with BSA and another protein (tobacco etch virus protease, TEV). Adapted from [68].

However, when functionalising surfaces directly with nanobodies the steric hindrance at the surface is another relevant factor to consider. On this note, the size of nanobodies can be a

disadvantage for successful bio-interactions. If the target antigen structure is large or has an hidden epitope, there is an increased likelihood of steric hindrance whilst approaching the surface where the nanobody is immobilised[67]. To overcome these difficulties, one study used oligopeptide spacers which were added to a nanobody sequence, allowing the nanobody to be oriented and distant from the substrate[67]. This study showed that nanobodies spaced with 5 amino-acid oligopeptides outperformed the nanobodies without spacer at analyte detection[67]. However, whilst the distance from the surface was optimised in this study, there was no approach to optimise the distance between nanobodies.

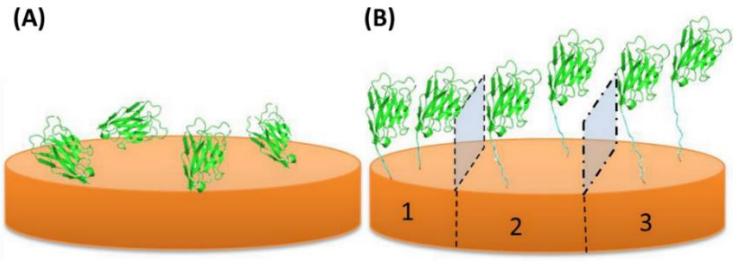

Figure 1.12 – Nanobodies immobilised at the surface and distant from the surface. Biosensors based on (A) non-oriented and (B) oriented nanobodies with engineered peptide spacer of 5, 10 and 15 amino acids (1, 2 and 3 respectively). Reproduced from [67].

In conclusion, upon the nanobodies' immobilisation, factors such as the orientation of the nanobody, the stability of the immobilisation strategies and the distance of a nanobody from the substrate can contribute to higher biological activity and surface performance with lower detection limits. The unique set of properties such as small size, high affinity and robustness, makes nanobodies ideal building blocks for a wide range of sensing devices and assays for use in biomedical and biotechnology, however optimisation of surface functionalisation parameters remains a challenge to fully unlock these advantages.

1.1.4.2. Analysis of nanobodies via molecular dynamic simulation

Alongside practical experimentation, computational modelling can create detailed predictions of interactions at the molecular level. Molecular dynamic simulations (MDS) have helped to describe the behaviour of molecules and proteins approaching and at the surface. MDS has revealed the structures of SAMs on gold[69], the mechanisms of protein adsorption[70], including specific amino-acids or domains involved in the protein adsorption[71] and it has been used to evaluate protein denaturation after adsorption[72].

Conceptually, MDS is based on the motion of atoms (not under extreme temperatures or pressures) of any molecular system computed by implementing Newton's laws of motion[73]. Thus it requires an accurate description of the interaction forces between atoms, described by well-known force fields[73]. Commonly, the root-mean-square deviation (RMSD) and root-mean-square-fluctuation (RMSF) are used to quantify the conformation variability within a protein[74]. RMSD measures the degree of similarity between two three-dimensional (3D) structures with the same number of atoms, while RMSF reflects the fluctuation of a protein's residues during its trajectory[74]. Typically MDS are performed for systems with single proteins, as complex biological systems are not trivial to simulate[75]. Even with simple structures, the time scales are a limitation of MDS as they are in the order of 10^2 ns, which are short time scales to describe important processes such as protein diffusion or rearrangement at surfaces[71, 75]. Despite this limitation, MDS can still provide means to observe protein mechanisms which is important to predict, for instance, protein approach to surfaces.

Concerning nanobodies, MDS studies have facilitated the understanding of nanobody thermostability[76], adsorption[2], nanobody-antigen interactions[77] and the prediction of ways to

improve nanobody-antigen affinity[78]. Hasannia, et al. investigated through MDS the mechanisms that play a role in stabilising nanobodies at high temperatures, up to 358 K (~85 °C)[76]. Their RMSD and RMSF results (Figure 1.13(A-C)) confirmed the stability of the nanobody over the studied temperatures, and showed the typical flexibility for loop regions such as complementary determining regions (CDR). Additionally their findings showed that π-π stacking interactions between the aromatic residues of the CDR3, the CDR3 loop stability, and the interactions between the CDR3 the and the β-sheets of the nanobody studied are important to keep its structural stability and function (Figure 1.13(D))[76].

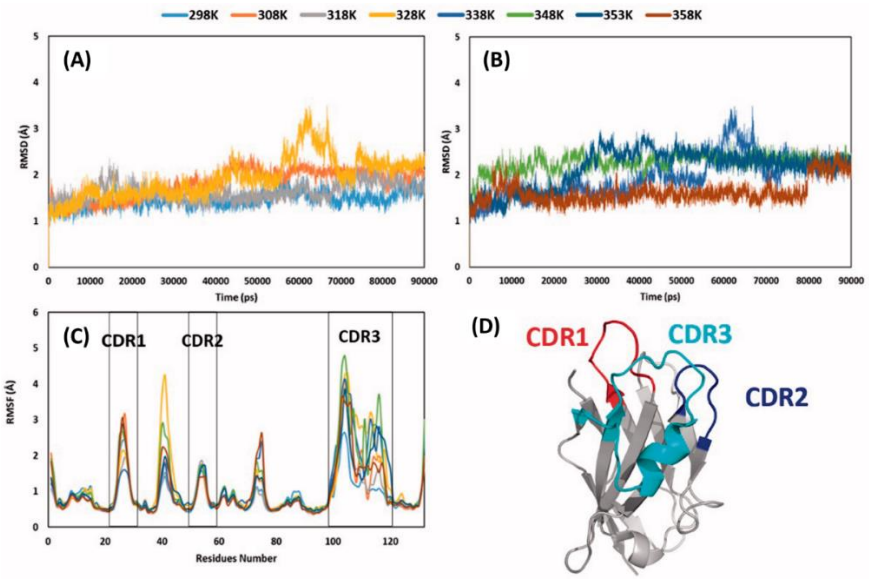

Figure 1.13 – MDS of a nanobody thermostability. (A-B) Root-mean-square deviations (MSD) at different temperatures (A) 298, 308, 318, 328 K and (B) 338, 348, 353, 358 K. (C) Root-mean-square fluctuations (RMSF) of Cα atoms with CDR regions highlighted by the boxes. (D) Nanobody 3D structure, with CDR1, CDR2 and CDR3 shown in red, blue and cyan respectively. Trajectory times were 90 ns. Adapted from[76].

Overall, MDS allows the investigation and prediction of mechanisms at the molecular level by exploring conditions that are not accessible in a laboratory setting. MDS are simpler when the studied proteins are small. The short sequence of nanobodies makes them relatively easy to simulate with MDS. However, to date there are not many reported MDS studies on nanobodies.

1.1.5. **Nanobody-based biosensors as diagnostic tools**

The studies mentioned earlier highlighted nanobody-based surfaces which are proof-of-concept for biosensing applications. To date a wide range of Nb-based biosensors have been explored for health monitoring and early diagnosis of disease and are herein introduced. Nb-based biosensors have been developed for cancer [79, 80], toxins[81], parasites[82] and virus[83, 84] screening in humans, and in animals[85, 86]. The potential of using nanobodies in biosensors for diagnostics has been demonstrated in different assay formats including through sandwich assays[65, 79-81, 86-91] whereas the nanobodies were used as capture and/or detection entities. Assay formats have been shown in lateral flow assays (LFA)[84, 86] for point-of-care diagnostics (POC) and in electrochemical immunoassays[83].

1.1.5.1. Point of care (POC) nanobody-based biosensors

POC testing must allow for diagnostic testing outside of laboratory conditions. Antibody-based POC lateral flow tests can be compromised by variations in temperature and humidity as these directly affect the stability of antibodies. Nanobodies were previously presented as an alternative due to their stability[92].

Pinto Torres et al, developed a LFA for point of care diagnostics based on a nanobody sandwich assay[86] (Figure 1.14 (A)) to detect disease affecting cattle livestock[86]. Once the sample is loaded, it flows through the conjugate pad mixing with its components (that includes the detecting nanobody with gold nanoparticles (Nb2-AuNPs) and the control conjugate (Figure 1.14 (B)). After the conjugate pad, the mixture moves to the test line (with the capturing nanobody (Nb1)) and finally to the control line (where the control conjugate is captured) (Figure 1.14 (B)). On their assay the capture nanobody (Nb1) was either physically adsorbed directly on the pad, or biotinylated (becoming Nb1-biotin) and then adsorbed on a pad pre-treated with streptavidin. The second approach allowed a decrease in the limit-of-detection (LoD), which was suggested to be due better Nb1 adherence to the surface and orientation[86]. Therefore the optimisation of nanobody immobilisation methods, that can impact the orientation, is an important design factor for biosensor development.

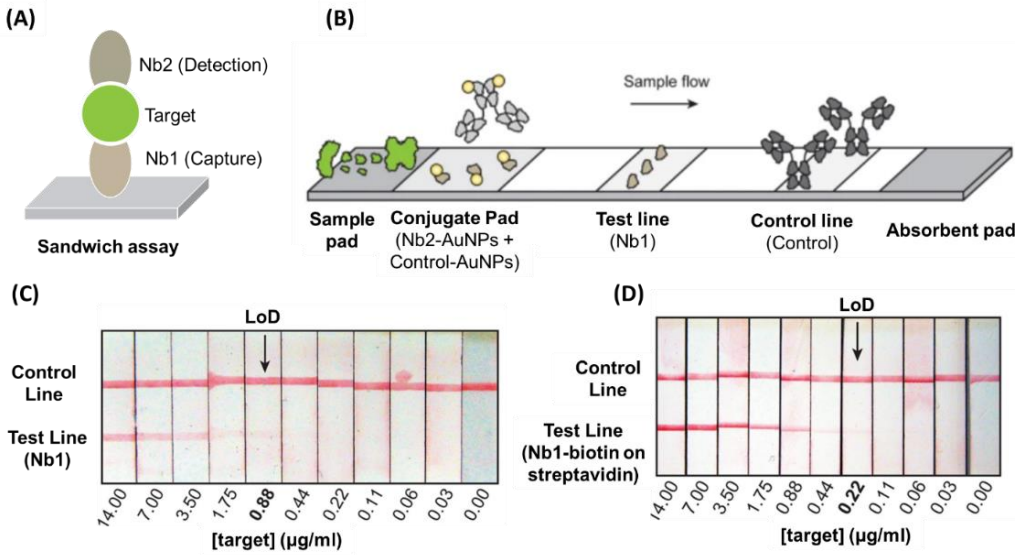

Figure 1.14 – Lateral flow test based on nanobodies sandwich assay. (A) Sandwich assay schematics: the immobilised capture nanobody (Nb1) catches the target which binds to the detection nanobody (Nb2). (B) Lateral flow assay (LFA) schematics based on nanobodies sandwich assay using detection nanobodies conjugated with nanoparticles. (C-D) Finally, LFA read-outs for a dilution series of target using (C) direct coating of Nb1 on the test line and (D) streptavidin-based coating of biotinylated Nb1 on the test line. Black arrows highlight the limit of detection. Adapted from[86].

In the same study, the resulting LFA test was used on samples of infected cattle showing an specificity of 92%[86]. However, the lowest LoD achieved was 0.22 μg/mL (Figure 1.14(D)), a range that can diagnose the herd but not the individual cattle[86]. Therefore higher sensitivity is required which could potentially be achieved with other approaches, such as electrochemical nanobody-based biosensors.

1.1.5.2. Electrochemical nanobody-based biosensors

Electrochemical nanobody-based biosensors have been developed for use when the targeted antigen is in low concentrations, requiring high sensitivities in the picomolar range[92].

Guo et al, presented a bioelectric sensor platform that fulfils current POC challenges previously stated such as the trade off between sensitivity and time to result[83]. With these challenges being highlighted by the current COVID (corona virus disease)-19 pandemic crisis, this platform validated performance with unprocessed clinical samples from COVID-19 patients with a time to result of under 15 min[83]. Their platform was based on a gold electrode transistor functionalised with 1,6-hexanedithiol (HDT) which was then linked to a SpyTag peptide. The SpyTag peptide bonds strongly to the SpyCatcher[93] (a protein) which was fused to a nanobody through a flexible linker (Figure 1.15(B)). This arrangement allowed a robust and controlled nanobody orientation on the surface[83]. The used nanobodies targeted the SARS-CoV-2 (severe acute respiratory syndrome coronavirus 2) spike proteins[83] (Figure 1.15(A)).

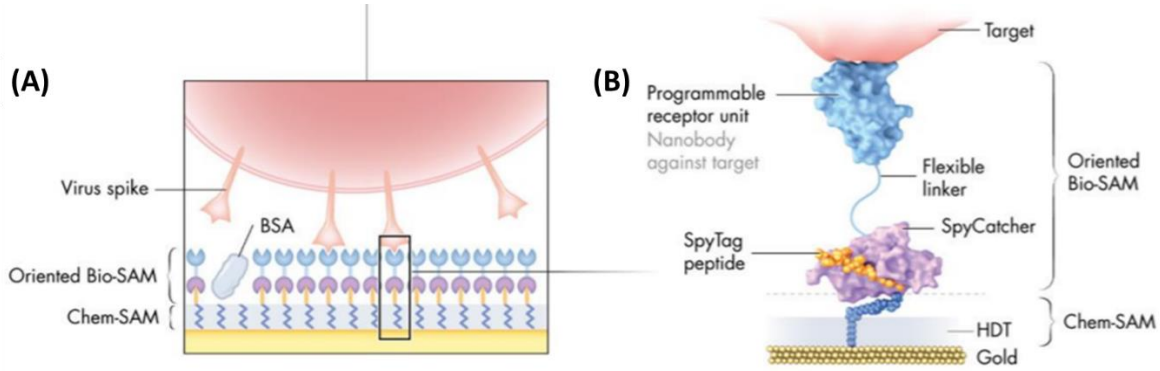

Figure 1.15 – Nanobody functionalised organic electrochemical transistor sensor. (A) Functionalisation layers: chemical and biological monolayers (Chem-SAM and Bio-SAM) are self-assembled to the electrode surface. (B) Molecular architecture: A synthetic SpyTag peptide is chemically coupled to the 1,6-hexanedithiol (HDT) monolayer to form a Chem-SAM on gold. The nanobody-SpyCatcher fusion protein couples after a covalent SpyCatcher-SpyTag bond, forming the Bio-SAM. Lastly, BSA is physiosorbed during the final step of functionalisation to prevent non-specific binding. Adapted from[83].

The preliminary clinical results demonstrated sensitivity comparable to reverse transcription polymerase chain reaction methods (RT-PCR)[83]. The choice of nanobodies over usual antibodies (or antibody fragments) further improved the density and robustness of the biorecognition layer[83]. Overall, this study demonstrated that electrochemical nanobody-based biosensors, with controlled nanobody orientation, can achieve high specificity and fast results for clinical diagnosis.

Other examples of electrochemical biosensors with nanobodies reported in literature included impedance sensors[94], amperometric immunoassay sensors[80, 90] and field-effect transistor (FET) based sensors[68].

1.1.6. **Nanobody-based surfaces and biosensors overview**

The previous sections demonstrated that nanobodies are a promising alternative to antibodies, and have been successfully used to functionalise surfaces for biosensing applications. Studies have highlighted design factors such as orientation[54], immobilisation method[39] and distance from the surface[67] to be relevant for efficient nanobody-antigen interactions. Immobilisation methods previously reported include nanobodies randomly oriented *via* physical adsorption[86] and covalent bonding[65, 79, 80] or oriented *via* a linker, such as biotin[65, 87, 89, 91] or histidine tag[65, 88, 90]. These approaches allow for highly active surfaces with additional stability and sensitivity inherent to nanobodies.

To enable the future generation of biosensing devices new strategies for detection and monitoring of biomolecules are essential. To date, most biosensors rely on a static detection approach, which means that, contact with a sample is irreversible, therefore these platforms will be for one time use and not suitable for long-term monitoring. The reusability of such platforms requires regeneration cycles that usually use harsh conditions (such as acids or high salt concentrations)[95] to disrupt, for instance, the antibody-antigen interactions. These harsh conditions limit static biosensors to external (non-invasive) applications. Furthermore regeneration cycles decrease sensing efficiency. To address these challenges, dynamic detection offers potential solutions for long-term and real-time biosensing which can interact with more complex bio-interfaces[1] such as inside the human body or within bioreactors. Rather than static, a dynamic sensing through stimuli-responsive detection could allow on-demand sensing. This topic is covered in the following section, after a brief introduction to dynamic-responsive interfaces.

1.1.7. **Dynamic-responsive interfaces and on-demand biosensing**

Control of specific capture of biomolecules on surfaces provides the opportunity for on-demand biosensing[1]. In order to achieve on-demand biosensing it is necessary for a biosensor that remains inactive over time (i.e. not capturing any biomolecules) and changes to its active state (i.e capturing and detecting specific biomolecules) upon requirement. Stimuli-responsive surfaces emerge as potential on-demand biosensing platforms as they have the ability to remain inactive, changing to an active state following an applied stimulus.

The natural ability of living organisms to respond to a multitude of stimuli has inspired the development of synthetic materials with tailored stimuli-responsive properties. Stimuli-responsive mechanisms have been incorporated into bio-interfaces to dynamically control their properties and functionalities (Figure 1.16). A wide range of stimuli have been used, including electrical potentials and fields[96], magnetic fields[97], mechanical forces[98], light[99, 100], temperature[101, 102], pH[103] and the presence of molecules such as enzymes[104].

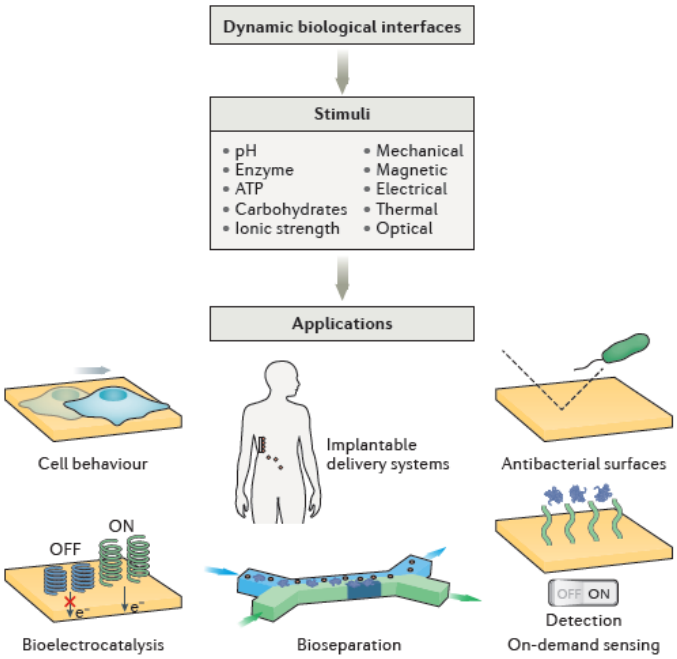

Figure 1.16 – Types of stimuli explored to develop dynamic bio-interfaces and their applications. Dynamic bio-interfaces can be responsive to different stimuli providing opportunities to develop implantable delivery systems for medical applications, antibacterial surfaces to control biofouling, bioseparation to aid in the isolation or detection of proteins and many other applications. Reproduced from [1].

Among other systems, self-assembled monolayers (SAMs)[96] are proving to be instrumental for the rational design of stimuli-responsive surfaces. Consequently, advances have been made in active and switchable bio-interfaces owing to their relevance in many biotechnological and biomedical applications[10] including biosensing[101].

The following sections will address different stimulus-responsive surfaces that were developed for different applications, with an emphasis on biosensing applications. Stimulus-responsive surfaces are summarized based on the applied stimulus, including chemical, temperature, light and electrical. More extended research is shown for examples with electrical stimulus due to the relevance to this thesis.

1.1.7.1. Chemical-responsive surfaces

Chemical-responsive surfaces allow for the development of novel biochemical sensors that respond to the surrounding chemical environment. Stimulus for chemically-responsive surfaces include ionic strength, pH, adenosine triphosphate (ATP) and other chemicals. One example includes a microfluidic system that has been built to allow capture and release of thrombin with a pH-responsive polymer. The bendable polymer used was poly(acrylamide-co-acrylic acid) (P(AAm-co-AAc)) shaped into microscopic fins (microfins) and functionalised with a pH sensitive thrombin-specific aptamer[103] (Figure 1.17). In this system, depending on the pH, the P(AAm-co-AAc) hydrogel is present either in its deprotonated form, which is capable of absorbing water and swelling, or in its protonated form, which expels water and results in hydrogel contraction. Based on volume changes, at pH 7.2, the microfins protrude into the top fluidic layer, exposing the aptamer which captures the thrombin proteins. In acidic conditions (pH 3.2), the hydrogel contracts into the bottom fluidic layer and the aptamer simultaneously undergoes denaturation, resulting in release of the captured thrombin molecules into the bottom fluidic layer[103]. Such microfluidic system demonstrated effective bioseparation between the two fluidic layers following a chemical response.

The advantages of chemical stimuli, such as pH, include easy addressability and direct affect on the binding affinity at the interface[103]. However, a limitation inherent to chemically-driven surfaces include the lack of spatial control[1]. Localised stimulation is not achievable as it extends throughout the involving media, which simultaneously can be challenging to control.

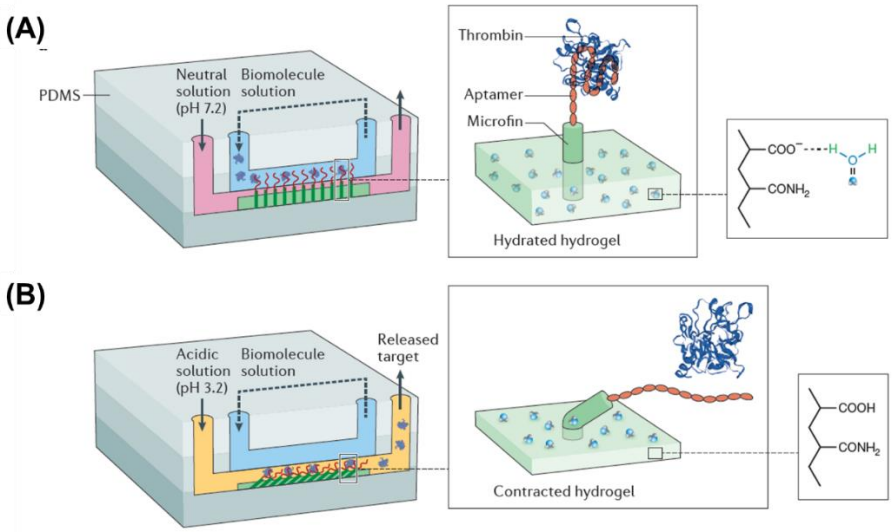

Figure 1.17 – Representative schematics of a pH-responsive surface. (A) A microfluidic chamber containing a hydrogel with poly(acrylamide-co-acrylic acid) microfins that are decorated with a thrombin-binding aptamer. At neutral pH the hydrogen swells allowing the capture of thrombin. (B) Upon contraction of the hydrogel and denaturation of the aptamer at acidic pH, the thrombin is released. Adapted from [103].

1.1.7.2. Mechanically-responsive surfaces

The conversion of physical forces such as shear stress, vibration and stretching into a biochemical response is known as mechanotransduction. Inspired by mechanotransduction, mechanically-responsive surfaces have been used to prevent biofilm attachment[98], control drug delivery[105] and activate biocatalysis[106].

As an example, Mertz et al, developed a platform based on multilayer polyelectrolyte films that can control enzymatic activity upon mechanical stimulus[106]. The architecture consisted of a stretchable capping barrier composed by poly(diallyldimethylammonium) and poly(sodium 4-styrenesulphonate) that separated the solution from an enzymatic reservoir deposited on silicone sheets. Upon stretching, the capping barrier exposed the enzymes and also stretched

their binding sites, allowing access to the substrates and switching ON the biocatalysis. The biocatalytic activity was switched on and off reversibly by mechanical stretching[106].

Taking the previous example of biocatalysis activation, such a concept could potentially allow for on-demand detection of substrates. However, it would be limited to the use of mechanotransducer proteins, of which conformational changes promote biological activity. Furthermore, localised mechanical stimulation could present an additional design challenge. In regards to sensing, platforms that are mechanically triggered are thought to detect the stimulus rather than use it as a means to control detection and thus applications are limited.

1.1.7.3. Thermo-responsive surfaces

Another convenient stimulus is temperature which can be used to regulate the biological properties of surfaces. Smart thermo-responsive surfaces have been used for bio-applications, including to control bioelectrocatalysis[107] and biosensing[101, 108]. Often these smart surfaces are designed to control thermo-responsive polymers[10], taking advantage of the polymers' induced rapid and reversible phase transition between conformational swell and shrinkage.

Past literature has demonstrated how to benefit from the reversible behaviour of thermo-responsive polymers, such as poly(N-isopropylacrylamide) (PNIPAM)[101, 102]. These polymers in aqueous solution have a temperature responsive phase transition, being the transition temperature known as lower critical solution temperature (LCST). Bellow the LCST, PNIPAM due to hydration, remains an expanded coil-like structure. Above the LCST, PNIPAM dehydrates and turns into a globular structure. One example demonstrated how an anti-cardiac troponin T (cTnT) antibody immobilised on a gold surface was strategically conjugated with PNIPAM to mediate ON and OFF antibody binding[101]. In this case, above the LCST the

globular PNIPAM conformation allowed the binding of troponin (CTnT) antibody, increasing the electrochemical signal as faradaic impedance at the sensing surface. Reducing the temperature to bellow the LCST, the extended coil PNIPAM formation pushes the antibody away, disrupting the interaction and allowing 2regeneration of the immune sensor.[101]

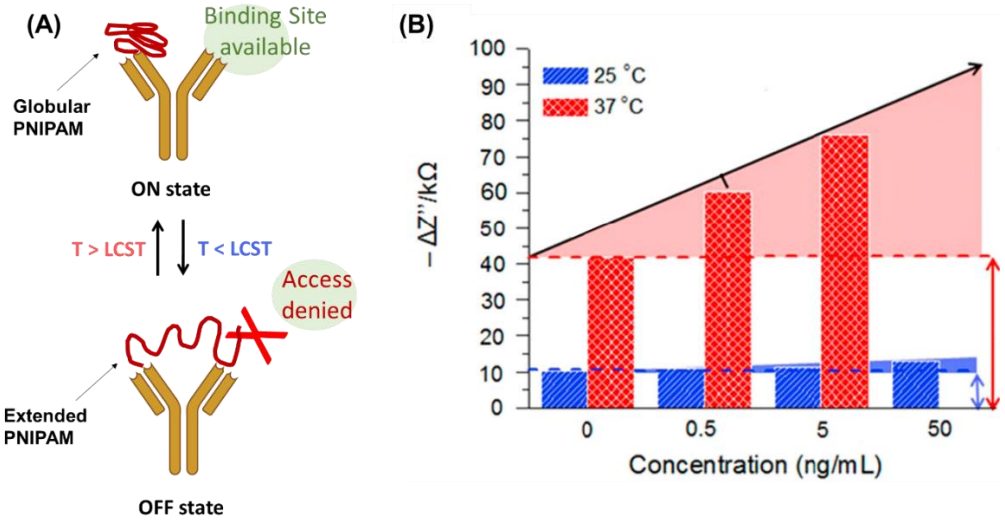

Figure 1.18 –Antibody-antigen interaction in a thermo-responsive bioelectrode.Schematic representation of the thermo-responsive system: on the top, the PNIPAM-conjugated antibody with temperature above the LCST (e.g. 37°C) turns the bioelectrode to an "ON state". The PNIPAM is under a globular conformation (red), allowing antigen binding through the available binding site. At the bottom, the temperature bellow the LCST (e.g. 25°C) allows an extended PNIPAM conformation. This turns the system to an "OFF state" as the binding site is blocked and antigen access is denied. (B) Impedance results for different antigen concentrations. The blue bars represent the response obtained at 25°C (<LCST), and the red bars the response at 37°C (>LCST). Adapted from [101].

Temperature stimulus can be remotely actuated, tuning biomolecular interactions without altering the interface composition[102]. However, spatial control is not possible[1], limiting the conditions where the monitoring system can be applied. Furthermore, thermo compatibility must be aligned with the biological system, as temperature directly impacts the kinetics for

performance. Additionally, it also requires efficient insulation to avoid external environment impact. Overall, thermoresponsive surfaces have the potential to control biosensing interactions, however their applications are limited.

1.1.7.4. Light-responsive surfaces

Light is an appealing source of energy to regulate biomaterial behaviour. Its intensity and wavelength are easily tuned remotely and this allows for accurate spatial-temporal control. Photo responsive surfaces rely on molecular groups that undergo photochemical reactions, leading to changes in the surface biological properties. These can include surface patterning, with photocleavable groups (irreversible), or photochemical conformational changes (reversible) that intermediate biological interactions[1]. Past research has demonstrated these two distinct surface responses to light actuation[99, 100] that are a proof-of-concept for potential biosensing applications.

The irreversible photocleavage of o-nitrobenzyl derivative moieties[95] and the reversible photo-triggered isomerisation of azobenzene moieties[96] are photoreactions commonly used to achieve photoswitchable bio-interfaces. In the case of the nitrobenzyl group, it acts as a photoremovable group as it undergoes a specific bond cleavage upon UV light exposure. Surface patterning has been possible by using the nitrobenzyl group as a general linker between the surface and bioactive molecules. Upon exposure to UV light, the nitrobenzyl photocleaved, releasing the previously linked bioactive molecules (Figure 1.19(A))[99]. In the case of azobenzene, it has been used to cover or uncover a coupled RGD peptide within a mixed SAM (Figure 1.19(B)). In order to reversible switch cell adhesion between visible and UV light, azobenzene fused to

RGD shown to promote cell attachment when at trans configuration (visible light, RGD accessible) and cell detachment when at cis configuration (UV light, hidden RGD)[100].

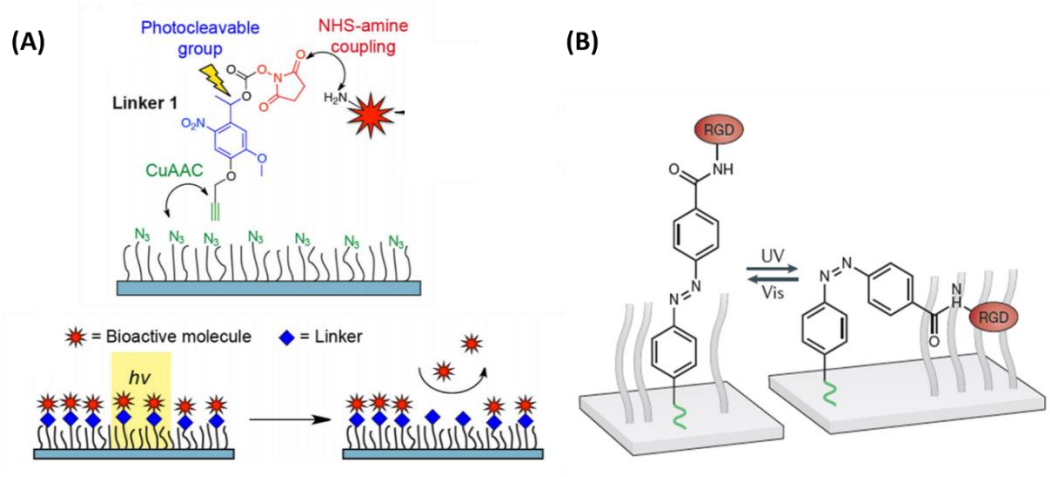

Figure 1.19 – Representative examples of light-responsive surfaces. (A) The release of previously immobilised bioactive molecules, that were linked through a nitrobenzyl moiety to the surface, can locally occur after UV light exposure. Adapted from [99]. (B) The availability of the RGD moiety is controlled by the azobenzene cis-trans conformal response to the exposure of either UV or visible light. Adapted from [100].

The presented examples focus on dynamic surfaces for surface patterning and cell attachment, however the mechanisms for both could be used to control on demand biosensing. The reversible *cis-trans* conformation approach has been successfully used for biosensing applications to detect proteins[109, 110]. As an example, Horsley and co-workers used a photoswitchable azobenzene-peptide-based biosensor to detect, through electrochemical impedance, the α-1-syntrophin protein (Figure 1.20). The biosensor consisted of a truncated form of a native protein that is known to bind with α-1-syntrophin, with an azobenzene component. Functionalised on a gold surface, the azobenzene allowed the reversible transition between the *trans* isomer which deformed the peptide, and the *cis* isomer which provided to the

peptide a well defined secondary structure (Figure 1.20 (A)). Under the *cis* conformation the biosensor was OFF with a deformed peptide, and under *trans* conformation the biosensor was ON and able to detect the target protein that binds the peptide secondary structure (Figure 1.20 (B)).

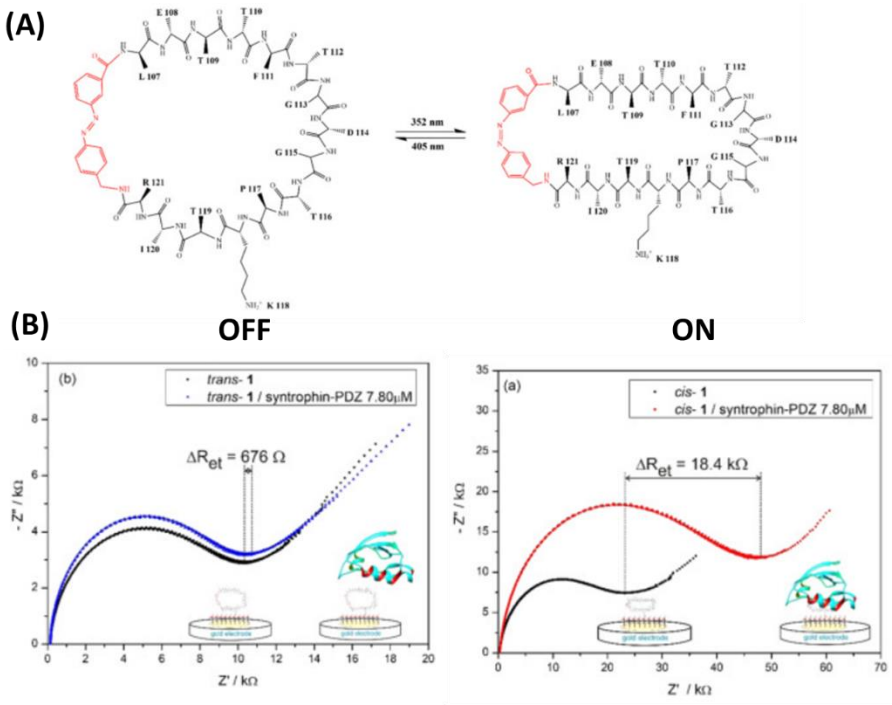

Figure 1.20 – Photoswitchable ON/OFF biosensor for the detection of proteins. (A) schematic representation of the photoswitchable peptide. Peptide in trans (left) and cis (right) conformation with the azobenzene (in red). (B) Nyquist plots for surface-bound cis and trans of the peptide (black) and in the presence of α-1-syntrophin. At trans conformation the peptide does not bind and there is minimal charge transfer resistance (blue.). At cis, the protein binds and it is detected with a jump in charge transfer resistance (red). Adapted from[109].

These studies demonstrate that light-responsive surfaces can be used for biosensing applications.

1.1.7.5. Electrically-responsive surfaces

Smart electrically-switchable surfaces operate under similar trigger-induced modifications as photoswitchable surfaces, where the hydroquinone– quinone redox couple[111], charged molecular backbones[20] or end groups[112] and molecular imprinted polymers[113] feature as the switching units. These surfaces have been developed to respond, for instance, to conformational changes under application of electrical potentials, exhibiting different and reversible surface properties. Switching from a hydrophilic to a hydrophobic surface through the response to an applied field has been possible using carboxylic acid-terminated[114-117] or amine-terminated alkyl molecules[117], developing surfaces that control protein assembly[116], and with anti-bacterial properties[115]. Past literature has shown that the long alkyl molecules, such as 16-mercapto hexadecanoic acid[114, 116, 117] or N-(aminomethyl)-16-mercapto hexadecanamide[117], could undergo conformational changes upon an applied potential field to the substrate. The attraction of the end group, either carboxylate anions or the ammonium cations, move towards the positive or negative surfaces respectively. To accommodate this, a low packing density was crucial, achieved by spacing the long alkyls chains with a smaller spacer such as mercaptoethanol[115]. This allowed for conformal changes between 1) the straight chains with the charged end groups exposed to the bulk solution (hydrophilic surface), and 2) the bent chains with the alkyl chains exposed at the surface (hydrophobic surface) (Figure 1.21).

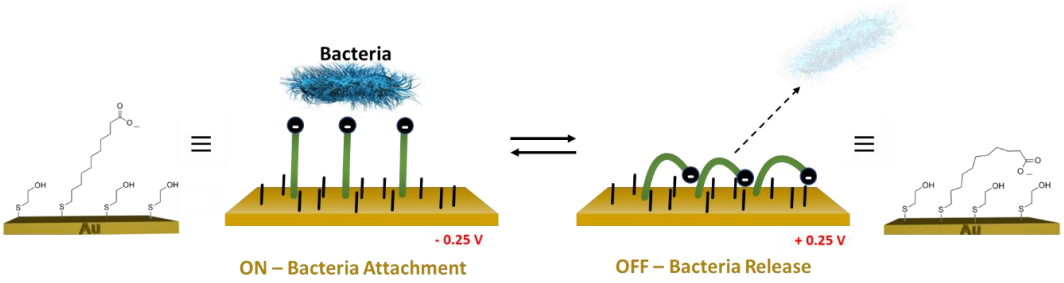

Figure 1.21 - An electrically switchable surface for the control of non-specific interactions with bacteria. Under a negative potential, the exposed negative carboxylate anions interact with the positively charged regions of the bacteria allowing bacterial adhesion. Then under positive potential the surface changes from positively charged to non-charged and hydrophobic, preventing bacteria from attaching.

Further to controlling non-specific interactions, electrically switchable surfaces have also been developed to control specific biomolecular interactions. The construction of these surfaces have used different actuation methods towards the control of the specific interactions: by either 1) hiding or exposing the binding moiety (Figure 1.22(A and B)) or 2) changing the binding moiety conformation (Figure 1.22(C)). Taking the actuation example of Figure 1.22(A), an electro-switchable surface was able to control the activity between biotin (ligand) and neutravidin (protein). This was achieved through a SAM mixed with a biotin-terminated charged molecular backbone[20]. The mixed SAM was composed of 1) oligopeptides tethered to the gold surface by a cysteine (C), followed by 4 positively charged lysine (K) with a terminal biotin (C4K-biotin) and 2) an ethylene glycol-terminated thiol (*i.e.* (3-mercaptopropyl) tri(ethylene glycol)) that spaced out the C4K-biotin peptides, simultaneously preventing non-specific binding.

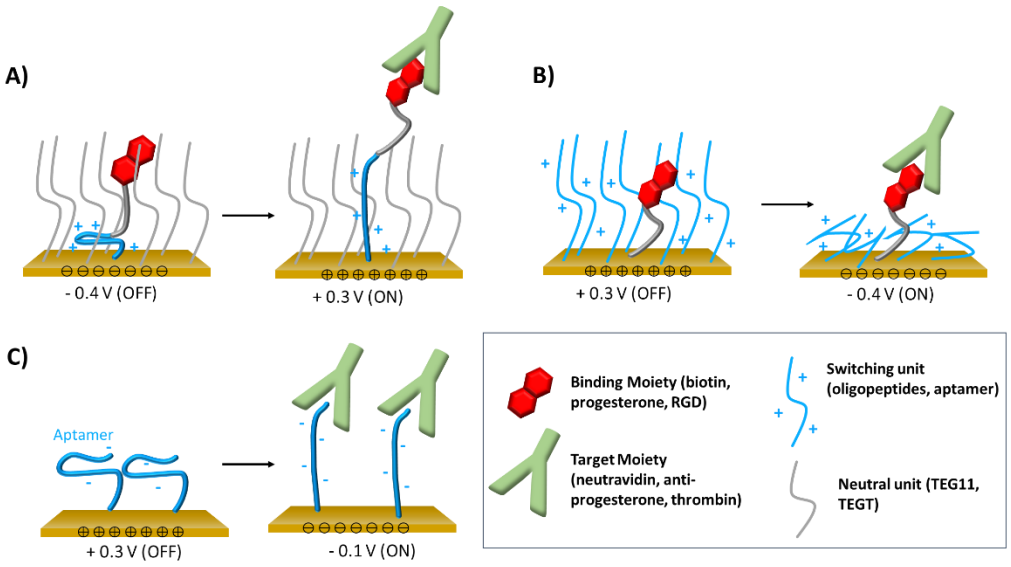

Figure 1.22 – Electrically switchable surfaces of specific interactions. Different switching units result in different actuation methods. Hiding or exposing the binding moiety: (A) the switching unit contains the binding moiety - while retracted, embeds the binding moiety within the surrounding SAM, concealing it from interaction; when extended, exposes it to bind [7, 20, 118]; (B) the binding unit stays fixed while the surrounding is responsive to the electrical field, either extended and covering it from binding, or attracted to the substrate, concealed and exposing the binding moiety to the target[112]. Lastly, the binding moiety itself is responsive to the electrical field: (C) the aptamer is either concealed, with a conformation that does not allow binding, or extended to the right conformation to interact with its target[119, 120].

The biomolecular interactions were controlled by the oligopeptides' conformational changes between 1) fully extended at positive potential (+0.3 V), exposing the biotin (biological ON state) and 2) collapsed under negative potential (–0.4 V), hiding the biotin within the surrounding SAM (biological OFF state). While the positive potential resulted in free biotin and thus high neutravidin binding, the negative potential resulted in a sterically shielded biotin with minimal binding. Following this switching mechanism, platforms using the binding units Arginine-Glycine-Aspartate (RGD)[118] and the low molecular weight antigen anti-progesterone[7], were able to control cell adhesion[118] and antibody binding[7], respectively.

Figure 1.22(B) shows a different method of actuation. In this case the binding moiety stays fixed while the surrounding molecules are the switching units. In order to control RGD accessibility to cells[112], SAMs were formed on silicon containing 1) an ethylene glycol chain with charged end groups, either a sulfonate (anionic) or an ammonium (cationic) moiety and 2) a RGD peptide. When applying a potential of the same polarity as the switching units, they repealed from the surface; extending and concealing the RGD from the cells. On the contrary, when applying a potential of the opposite polarity, the switching units were attracted to the surface exposing the RGD peptide to promote cell adhesion[112].

Regarding Figure 1.22(C), the switching unit is the binding unit itself. For example, DNA single strands (or aptamers), directly linked at the gold surface through thiol linkers have been shown to switch conformation under applied potential[119], and effectively promote or inhibit hybridisation, as well as allow specific interactions with thrombin, catching it, or releasing it by stopping the interaction[120].

Overall, the choice of electrical stimulus requires conductive materials that can be remotely actuated to allow accurate spatial control. Various designs for smart electrically switchable surfaces provide platforms potentially capable of on demand biosensing. Currently, the versatility of design principles and strategies for high switching efficiencies of specific interactions have been mainly shown for low molecular weight proteins.

1.1.7.6. Comparison of dynamic responsive stimuli for on-demand biosensing and conclusions

The previous sections showed that different stimuli responsive surfaces driven by pH[103], temperature,[101, 102] light[99], and electrical stimulus[7, 20] that can control the capture of different

biomolecules have been developed. Each stimulus has certain strengths and limitations. Certain stimulus are more effective depending on the environment and the targeted bio-interaction of the dynamic system. In addition, the capability to apply a specific stimulus (addressability), actuation mode and spatial control are characteristics associated with all different stimuli that can also be determinant in the appropriate stimulus selection (Table 1.1).

Table 1.1 – Bio-interfaces switching stimuli characteristics

	ADDRESSABILITY	ACTUATION	SPATIAL CONTROL	SWITCHABLE ENTITIES EXAMPLES
CHEMICAL	Easy	Contact	No	P(AAm-c-AAc)[103]
TEMPERATURE	Easy	Remote	No	PNIPAM[101, 102]
MECHANICAL FORCES	Advanced	Remote	No	PMDS[98]
LIGHT	Intermediate	Remote	Yes	o-Nitrobenzyl derivatives[99], azobenzene[100, 109]
MAGNETIC FIELD	Advanced	Remote	Yes	Magnetic particles[97]
ELECTRICAL POTENTIAL AND FIELD	Advanced	Remote	Yes (high level, nanoscale)	Hydroquinone-quinone redox couple[111], charged molecular entities[20, 112]

Localized stimulation is generally not possible with chemical, thermal or mechanical stimuli (Table 1.1) because activating sensor platforms based on these stimuli would mean to directly impact the embedding media. In cases where all the media changes, responsive-surfaces could be designed that take advantage of those certain specific events (such as pH or temperature change, for instance, in a bioreactor). However, in order to reactivate these biosensing surfaces, it would require self-regenerating surfaces and a switch back to the initial environmental conditions. Otherwise, these platforms would be of one time use only. Thus, chemical, thermal or mechanical might not be the ideal choice for on demand biosensing.

Considering platforms for long term monitoring and on demand biosensing, ideally these have not only high spatial control, but are also independent of the media conditions where they are embedded. Guaranteeing that these platforms are independent of the surrounding conditions provides opportunity for activation only upon user requirement. For precise spatial control, optical, electrical and magnetic stimuli are more suitable. While light can directly activate regions, electrical stimulus requires an electrically conductive substrate and allows for multiple, individually addressable, nanoregions on the surface[121]. Additionally, biocompatibility must be considered if choosing between light or electrical stimulus (such as secondary effects to light or electrical charge). In conclusion, electrical and optical stimulus are of a better choice for on demand biosensing. However, while light would require an additional read-out platform, an obvious advantage of choosing the electrical stimulus includes the use of the conductive substrate to both activate the surface and acquire the response signal. This ability makes electrical stimuli more convenient.

Long-term switching capability and stability, and sensitivity are crucial and challenging aspects of high-performance sensing that have not been investigated extensively to date[1]. Only when achieving these different capabilities, the practical applicability of real-time monitoring of complex biological processes will be possible. This is important for the future of biosensing in cell culture systems, biomarker detection for disease surveillance and diagnosis or integration in medical devices or biomaterials for *in vivo* implantation.

1.2 Motivation and Aim of studies

Considering the growing interest in high performance biosensing, there is a need to develop robust, highly selective smart surfaces for long term monitoring. The convenient characteristics associated with nanobodies (small size, selectivity and robustness) motivated the early development of nanobody-based surfaces aiming to open the path towards smart switchable nanobody surfaces for on-demand biosensing. Thus this thesis aims to apply advances in nanobody technology to develop high performance surfaces for on demand biosensing. In order to achieve this aim, the following objectives and sub-goals were determined:

1. Design and develop a nanobody-SAM surface on a gold substrate:
    1.1. Surface characterisation of the nanobody-SAM;
    1.2. Biological molecule response assessment and optimisation for nanobody-antigen binding;
    1.3. Molecular dynamic simulations to study and confirm nanobody adsorption on gold.
2. Investigation of the antigen dimensions impact on functionalised surfaces with oriented nanobodies;
    2.1. Immobilisation of nanobodies that bind to antigens of distinct dimensions;
    2.2. Surface characterisation and optimisation for nanobody immobilisation;
    2.3. Biological molecule response assessment and optimisation for nanobody-antigen binding.
3. Design and development of potential electrical-responsive surfaces that can control the nanobody-antigen interactions;
    3.1. Investigation on the impact of using electrical potential as a stimulus to nanobodies;
    3.2. Characterisation and optimisation of surface thickness with different charged moieties;
    3.3. Identification of potential switching moieties to use with nanobodies.

1.3 Thesis outline

Chapter 1 presents a literature review on the relevant fundamentals of this research, including self-assembled monolayers (SAMs), methods for immobilisation of macromolecules, nanobodies and stimuli-responsive surfaces.

Chapter 2 briefly describes the principles behind the experimental techniques most used throughout this research, mainly for surface characterisation.

Chapter 3 is a research chapter that explores direct immobilisation of engineered nanobodies on gold surfaces. It begins with a short introduction on nanobodies that have been physically adsorbed on gold and summarizes detection methods employed that use these surfaces. The novel strategy presented in this chapter has been published and provides another option for the design of nanobody-based biosensors.

Chapter 4 is a research chapter that focus on exclusively well-oriented nanobodies and the impact of their antigens with different dimensions. It begins with the short introduction of the alternative strategies used to immobilise nanobodies on gold. The investigation of this chapter provided valuable insight for nanobody-antigen selection when aiming for nanobody-based switchable surfaces.

Chapter 5 is a research chapter that presents a brief introduction on the development of charged moieties and their different ways of actuation on electro-switchable surfaces. This chapter investigates different charged oligopeptides and identifies potential switching moieties that could be mixed with nanobodies for bio-interactions control upon applied potential.

Chapter 6 describes the experimental procedures, including chemicals, materials and instrumentation related to the research presented in chapters 3-5.

Chapter 7 includes this research's conclusions and final remarks, including the author's views on the direction of the field with suggestions of future investigations.

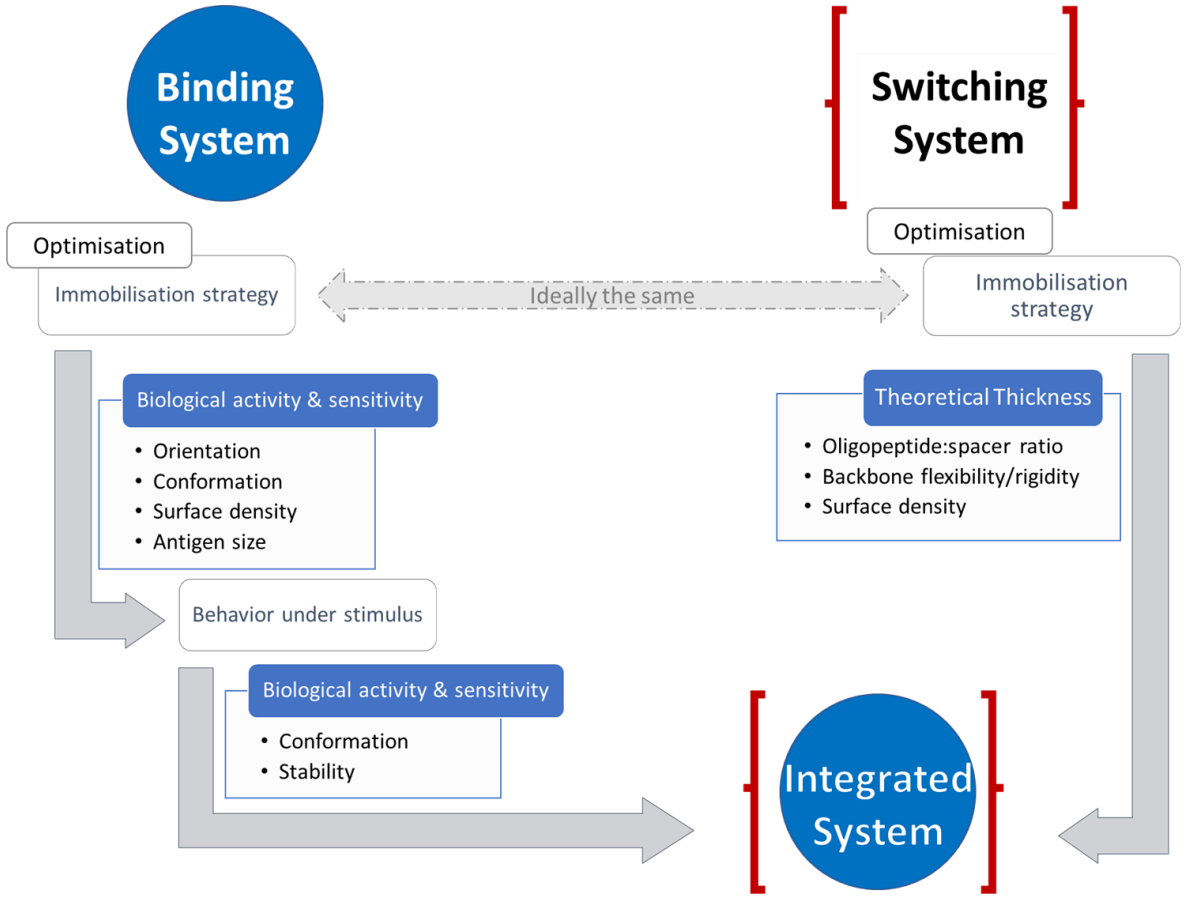

Figure 1.23 – Thesis schematic overview .

Chapter 2 Principles behind the techniques

This chapter briefly describes the principles behind the techniques used throughout this dissertation. Alongside surface preparation and SAMs formation, techniques for surface characterisation and to further study interactions at the surface were used. These included contact angle (CA); spectroscopy-based techniques such as ellipsometry, X-ray photoelectron spectroscopy (XPS), surface plasmon resonance (SPR) and circular dichroism spectroscopy (CD); and spectrometry-based techniques such as mass spectrometry, time-of-flight secondary ion mass spectrometry (ToF-SIMs) and time-of-flight secondary ion mass spectrometer with hybrid OrbiTrapTM (3D OrbiSIMs). More than one technique was used to characterise a surface and to validate findings. Additional techniques were used to confirm product synthesis.

2.1 Introduction

The design and development of biosensor platforms strongly depends on the ability to characterize surfaces at the molecular level. The main goal of this thesis was to develop nanobody-based surfaces that could be used as platforms for the next generation of on demand biosensing. In order to develop nanobody-based surfaces, the majority of the experimental work along this research involved three steps: 1) functionalisation of surfaces with self-assembled monolayers (SAMs) including nanobodies (self-assembled or added after to the initial SAM); 2) characterisation of the resulting surfaces and 3) detection of molecular interactions with the surfaces. Therefore, after functionalisation of gold substrates the surface was characterised with ellipsometry and contact angle. These accessible techniques allowed for quick analysis of the surface thickness, wettability and roughness. The results of these techniques were a starting

point and worked as a quality indicator, to assess whether to proceed with the SAM or optimise the initial functionalisation step. The next step consisted in obtaining additional information about the surface chemistry, including the elemental composition and chemical state of the elements at the surface, through X-ray photoelectron spectroscopy (XPS). In order to obtain further evidence of the surface chemistry including the thiolate bond between a self-assembled nanobody and the gold surface, the TOF-SIMs and 3D OrbiSIMs techniques were also applied. Additionally, circular dichroism (CD) was performed to confirm the structural conformation of nanobodies at the surface. Finally, the following step consisted in further confirming and measuring the nanobody capacity to bind its antigen, through the surface plasmon resonance (SPR).

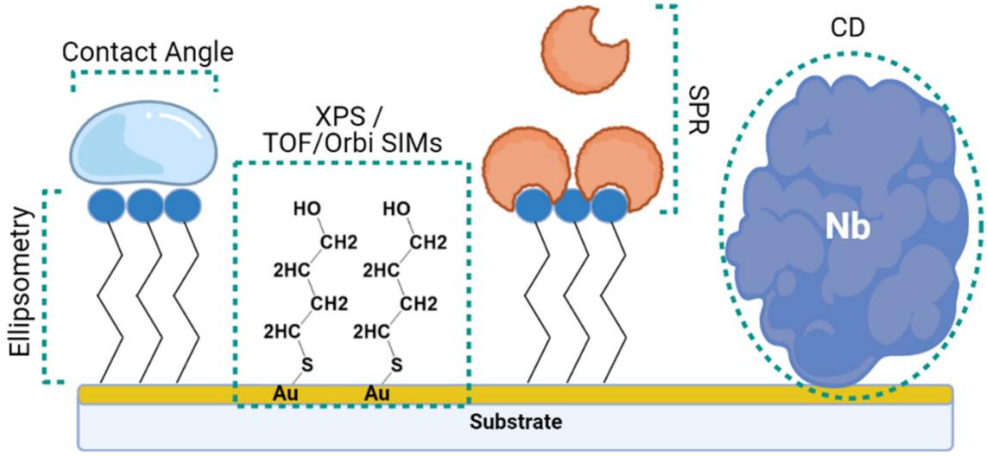

Figure 2.1 – Schematic overview of the surface characterisation methods.

2.2 **Contact angle goniometry**

To investigate the wettability of a solid, a liquid drop can be placed on the plane solid surface being analysed and the resulting contact angle can be measured. This system consists of three

interfaces: solid-vapour (SV), solid-liquid (SL) and liquid vapour (LV) interface[122]. At the three-interfaces contact point there are three forces or interfacial tensions (γ) acting between solid, liquid and vapour[122]. The contact angle (Θ) is defined by the angle formed between the tangent to the liquid surface and the solid surface at the three interfaces[122] (Figure 2.2(A)). Young's equation define the contact angle at the equilibrium as a function of the interfacial tensions (Equation 2.1).

$$cos\ (\theta) = \frac{\gamma_{SV} - \gamma_{SL}}{\gamma_{LV}} \qquad \text{Equation 2.1}$$

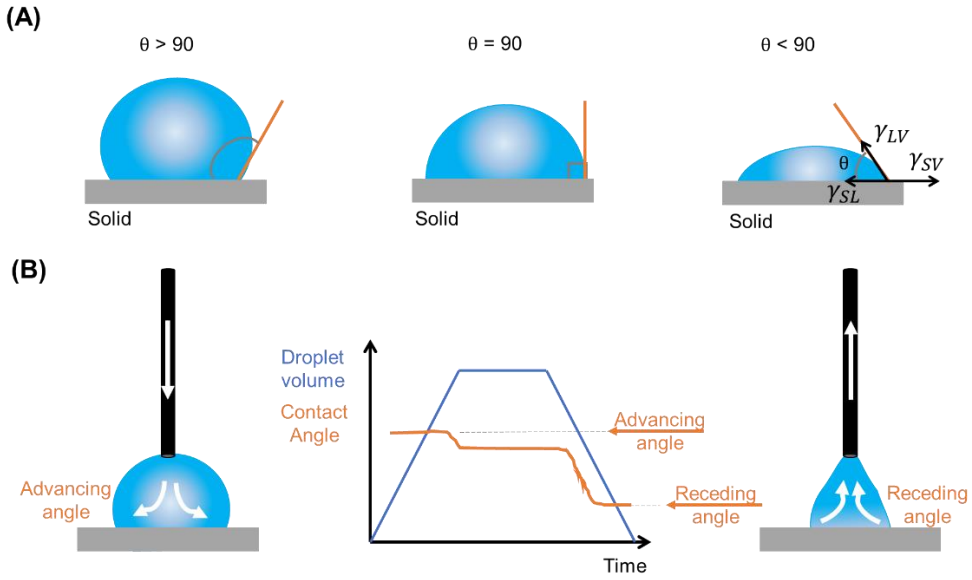

Figure 2.2 - Schematic representation of contact angle measurements. (A) The diagram shows the contact point of the three phases (solid-vapour (SV), solid-liquid (SL) and liquid-vapour (LV). (B) It shows the advancing or receding angle obtained by dispensing a droplet on the surface or collecting it, respectively. The dynamic contact angles correspond to the angle plateau obtained when the droplet volume rises or decreases.

Contact angle measurements can be static or dynamic, providing further insight into surface chemistry. The static contact angles (i.e. sessile drop) are measured when the droplet is sitting on the surface and the three-phase boundary is not moving. Static contact angles are used to

define the surface free energy (i.e surface tension of the solid) and provide wettability values for smooth and homogenous surfaces. High contact angles demonstrate hydrophobicity (low surface energy), while low angles show hydrophilic surfaces (high surface energy)[122] (Figure 2.2A). While it is widely accepted that hydrophilicity is defined by the cut-off angle of 90° (surface is hydrophobic at angles >90° and hydrophilic at <90°), it has been suggested to use these definitions only when defined by the dynamic receding angle[123]. Dynamic contact angles are measured when the three-phase boundary is moving, and they can be divided in either advancing or receding contact angles, corresponding to when the droplet front advances or recedes, respectively (Figure 2.2(B)). Contact angle hysteresis is the difference between these two values (Equation 2.2). The contact angle hysteresis is the consequence of chemical and topographical heterogeneity of the surface, providing further insights about the surface such as roughness[124].

$$Contact\ angle\ hysteresis = \theta_{advancing} - \theta_{receding} \qquad \text{Equation 2.2}$$

Chemically heterogeneous (two-component) surface can follow Cassie's law[125] (Equation 2.3). For example, a mixed SAM composed by compounds 1 and 2, with the respective contact angle (θ_{12}), can have an estimated molecular fraction of each component (x_1 and x_2 respectively) after knowing the contact angle of the respective pure SAMs composed by either compound 1 or 2 (θ_1 and θ_2)[125].

$$cos\,\theta_{12} = x_1 cos\theta_1 + x_2 cos\theta_2 \qquad \text{Equation 2.3}$$

$$x_1 + x_2 = 1 \qquad \text{Equation 2.4}$$

In this thesis, contact angle measurements were performed on SAM surfaces to confirm SAM formation by monitoring the contact angle change between different functionalisation steps and thus investigate the SAM hydrophilicity.

2.3 Spectroscopic Ellipsometry

Spectroscopic ellipsometry is a non-destructive optical technique that analyses the reflected polarized light from the surface of interest[126] and allows the thickness characterisation of a surface. Light is an electromagnetic wave and its polarisation is defined by the electric field component (E)[126]. Two waves can sum up their electric fields, resulting in a light beam polarized according to their phases and amplitudes[126]. Two waves in phase will result in a linear polarized light (Figure 2.3(A)); two waves with the same amplitude and in 90º out of phase will result in a circular polarized light[127] (Figure 2.3(B)); while two waves with different amplitudes and/or arbitrary phases will result in elliptical polarized light[127] (Figure 2.3(C)). The term "ellipsometry" refers to elliptical polarized light.

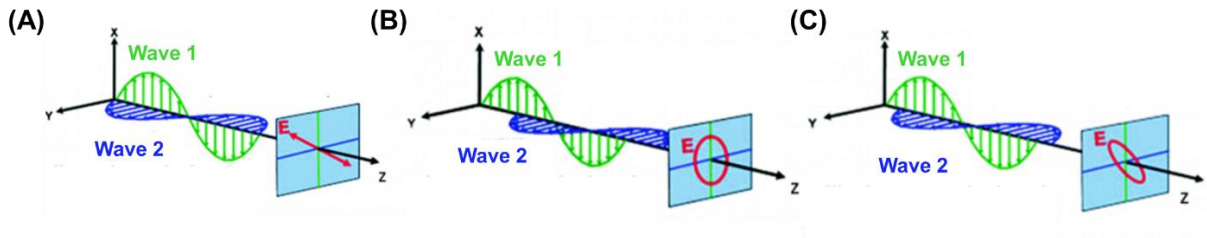

Figure 2.3 – Resulting electrical field (E, noted in red) from the sum of light waves (green and blue) (A) in phase (B) with the same amplitude and 90º out of phase, and (C) with different amplitudes and/or arbitrary phases.

Ellipsometer machines can vary in their polarizer and analyser systems, providing different results of polarized incident light (linear or elliptical) and obtaining relative intensities[128]. Figure 2.4 shows schematically the main components of an ellipsometer: a light source, a polarizer (to convert unpolarized light to linearly polarized light), a compensator (optional, to convert linearly to elliptically polarized light), an analyser (to determine the state of polarisation of the resultant light beam) and a detector (to measure the light intensity).

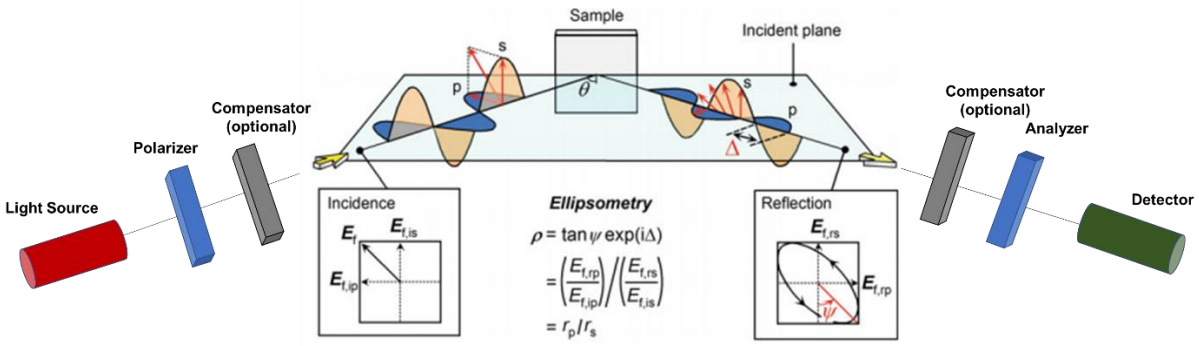

Figure 2.4 – Basic principles and components of an ellipsometer. The light source and polarizer provide polarized light defined by s- and p-polarized light waves represented as "s" and "p", with an incident angle indicated by θ. The p-polarisation oscillatory direction is parallel to the incident plane of samples. Passing the analyser and detector, ellipsometry measures the amplitude ratio ψ and the phase difference Δ between the reflection p- and s-polarisations (rp and rs respectively). The E_f shows the electric field vector and the resulting vectors for the p- and s-polarisations are indicated by red arrows. Adapted from [126].

Briefly, the ellipsometer's light source focus on the sample of interest at a given angle of incidence, defining the incident plane (Figure 2.4). The electric field on this plane is known as p-polarized light, while the electric field perpendicular to this plane is known as s-polarized light[126]. The enabling principle of ellipsometry is that the sample induces changes in the state of polarisation which are then reflected to the analyser, i.e. p- and s-polarized light reflect

differently. Ellipsometry measures the complex reflectivity ratio of p- and s-polarized light and reports the results in terms of psi (Ψ, the relative amplitude change) and delta (Δ, the relative phase change) ellipsometric parameters[126]. The parameters measured through this technique allow the calculation of some properties of the sample, such as thickness of thin films (ranging from nanometer to micrometer scale) and their optical constants like the refractive index. Therefore, this indirect method requires modelling for calculation and analysis that correctly describe the interaction of light with the respective materials. However, modelling must be considered with care as an incorrect optical model will use the correct measured values of Ψ and Δ, but calculate incorrect results for thickness and/or refractive index[127].

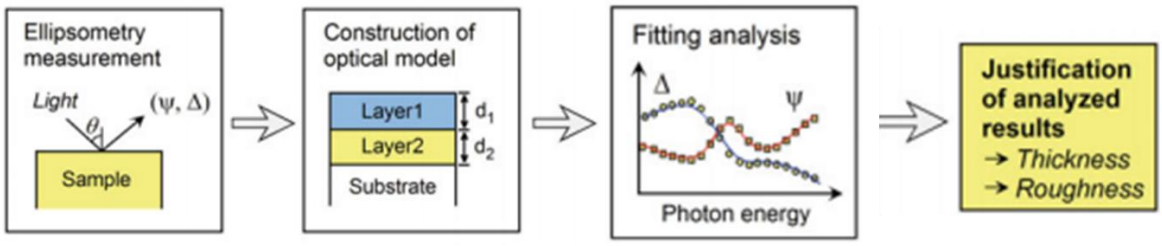

Figure 2.5 – Ellipsometric data analysis flowchart. Adapted from [126].

In what concerns the work presented in this thesis, ellipsometry was used to calculate the thickness of organic films composed by SAMs and nanobody structures on gold. These are expected to be very thin, with thicknesses up to 5-10 nm, and considered transparent (with the extinction coefficient k = 0, like protein layers[128]). Being transparent, the light will penetrate to the underlying gold layer. Reflection and refraction of light when it moves between films with different refractive indexes are described by the Fresnel equations.

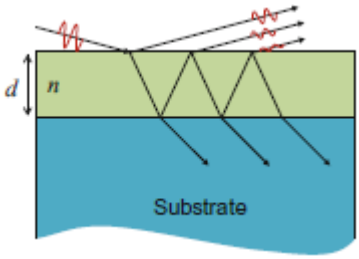

Figure 2.6 – The light reflects and travels through a transparent film. Adapted from [126].

For the optical model analysis, it is important to know the substrate optical properties which depend on several factors such as grain size, roughness, crystallinity, etc. Rather than using literature standard optical constants, it is preferable and more accurate to measure optical constants using a substrate reference, such as the gold substrate before deposition[127]. This is particularly important if roughness is to be ignored, considering the growth of a thin film as parallel plane interfaces[127]. Upon film thickness increase, a phase delay is observed as the separation between the light reflected from the surface and the light that travels through the film also increases[126]. Films with different optical properties will also cause phase shifts and/or amplitude attenuation[126]. In the case of thin films, the spectroscopic ellipsometry is very sensitive in terms of phase change, but less sensitive in terms of film refractive index[129]. Thus, a value for the refractive index can be assumed rather than calculated. The Cauchy model is often not only used to characterize SAMs but also protein layers on surfaces, and some models also consider the presence of voids in their layers[129]. In this thesis, ellipsometry was used to measure the thicknesses of different SAMs, and therefore confirming their formation.

2.4 X-ray photoelectron spectrometry (XPS)

X-ray Photoelectron Spectroscopy (XPS), also known as Electron Spectroscopy for Chemical Analysis (ESCA), it is widely used as an analytical technique to monitor the surface chemistry of solid materials. In XPS, the sample is irradiated by soft X-rays (energies lower than ~6 keV) and the emitted photoelectrons from the surface are detected[130]. The energy of a photoelectron is given by Equation 2.5, whereas BE is the binding energy of the electron in the atom, *hν* is the energy of the X-ray source, KE is the kinetic energy of the emitted electron that is measured, and Φ_{spec} the spectrometer work function (constant)[130].

$$BE = h\nu - KE - \Phi_{spec} \qquad \text{Equation 2.5}$$

Since there are different electrons and BEs in an atom, each element produces a unique identifying set of peaks in the photoelectron spectrum[130]. By knowing the KE of the emitted photoelectrons, elemental composition of the sample can be obtained[130] (excluding the elements He and H)[131]. The typical XPS instrument includes an ultra-high vacuum system, X-ray source, electron gun, electron energy analyser and data acquisition system (Figure 2.7). The X-ray source, commonly aluminium or magnesium Kα, can be used in a chromatic or monochromatic mode, the latter providing overall improved resolution[132]. Under ultra-high vacuum conditions, depending on the atom environment of the sample, different emitted photoelectrons will carry different KE, making it possible to distinguish different chemical/oxidation states of an element[132].

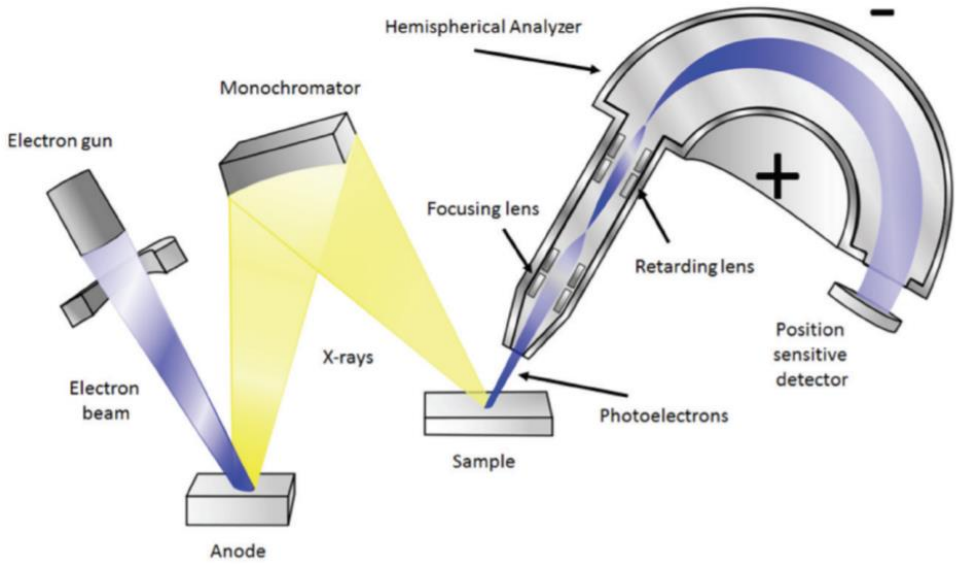

Figure 2.7 – Schematic XPS instrumentation setup.Adapted from [132].

While X-rays can penetrate around a micron into a material, the XPS is sensitive to the top layer of the surface (up to 10 nm depth)[132]. This is due the produced photoelectrons having a short mean free path (2-5 nm) before loss of energy via inelastic collisions (collisions that involve loss of energy) and being unable to escape the sample [130, 132]. Thus, only photoelectrons emitted from the top surface are likely to reach the detector, resulting in specific peaks of the spectrum. Inelastic electron scattering also occurs, resulting in the spectra signal background (Figure 2.8). The number of electrons recorded for a defined energy is proportional to the number of atoms at the surface [130].

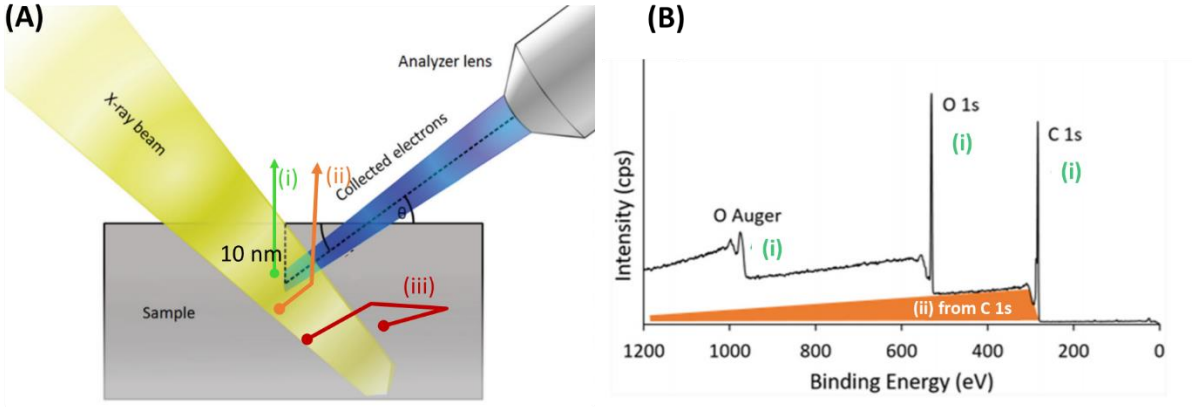

Figure 2.8 – Schematics on the photoelectron emission. (A) X-rays on the sample produce (i, green) electrons emitted without interaction which produce the XPS photoelectron and Auger peaks; (ii, orange) electrons that suffered inelastic collision which contribute to the background; and (iii, red) electrons that undergo multiple collisions and do not escape the sample. (B) Example of a XPS spectrum with (i) photoelectron and Auger peaks labelled. The orange area underneath the carbon C 1s peak shows the contribution to the background from electrons that suffered inelastic collisions (ii). Adapted from [130].

Typically data acquisition includes a survey spectrum to determine the overall elements present in the sample followed by a high resolution spectra of the elements of interest to determine peak shapes or/and intensity and chemical shifts. Scan parameters including pass energy (filters electrons at the analyser), step size and dwell time need to be set appropriately to collect quality data[130]. Additionally, when analysing electrically insulating samples (materials that have no or very little electrical conduction) it is essential to use a charge compensation system. Usually a connection to ground allows the electrons lost due to photoemission to be replaced, therefore avoiding positive charge accumulation. Charge accumulation results in unwanted peak shifts and distortions in peak shapes[130].

For data analysis, the identification of peaks requires the energy scale to be calibrated by adjustment based on the position of a reference peak. Once calibrated, it is possible to make

accurate BE measurements to identify chemical states for specific elements[133]. Peak modelling and background removal allows quantitative surface composition. Transitions from different electronic states from the same element (for example, O 1s and O 2s for oxygen) are detected at different energies[133]. For quantification purposes, only one transition per element is required[133] and usually is the transition that gives the most intense peaks, without the presence of other elements interfering peaks. All photoelectron peak areas are normalised by relative sensitivity factors (RSF) and an instrument transmission function. For XPS the detection limit is generally quoted as ~0.1–1 atomic % but will depend on the sensitivity factor of the trace element and the sample matrix[132, 134]. Comparison between samples is made through relative atomic percentages as peak areas are dependent on experimental conditions.

CasaXPS software[133] facilitates data processing and quantification, but it requires manual introduction of the right background and constraints such as full width at half maximum (FWHM). Caution is needed when considering peak attribution as the addition of peaks might improve the overall fitting, but could have no physical meaning. Overlapping transitions are one of the main challenges when analysing XPS data[133] and must be carefully analysed or reported.

On the experimental side, the contamination of samples upon storage/transport will have an effect on the XPS results. Carbon and oxygen are the most abundant contaminants of air-exposed surfaces and therefore adventitious contamination is expected to be present in all the samples[130, 135]. Volatile contaminants or residues from previous measurements at the vacuum chamber can also be source of contamination[130]. Furthermore, irradiation and vacuum can cause sample degradation[130] Certain elements can be more susceptive to degradation upon long exposures times[136] and therefore exposure times should be optimised.

In this thesis, XPS was used to determine and quantify the elemental composition of various SAMs.

2.5 Time-of-flight secondary ion mass spectrometer (ToF-SIMs) and with hybrid 3D OrbiTrap (3D OrbiSIMs)

The surface analysis technique time-of-flight secondary ion mass spectrometer (ToF-SIMS) provides in situ label-free analysis of chemical composition and distribution, ranging from a depth of few nanometers to several hundred micrometers[137]. The ToF-SIMs instrument uses several incident ion sources (such as pulsed primary ion beam, Bi_n^+, Cs^+, Ar^+, etc.) to impact on a sample surface and induce a fragmentation cascade[138]. The resulting fragments are composed by desorption of neutrals, secondary ions (+/-) and electrons from the superficial sample monolayers (Figure 2.9). The secondary ions are accelerated into a "flight tube" and their mass is determined by measuring the exact time at which they reach the detector (i.e. time-of-flight)[139].

ToF-SIMS mass analysis is based on the fact that after all ions are accelerated to the same kinetic energy (by the ion source), each resulting ion will acquire a characteristic velocity dependent on its mass to charge (m/z) ratio[139]. Small ions arrive earlier at the detector than heavy ions[139]. A single secondary ion mass spectrum can describe the composition of a point at the surface. Additionally, if the incident beam is rastered across several points within a given surface area it is possible to build a chemical image map from the resulting ions[138]. Using clustered incident ions such as Cs^+, Ar_n^+ C_{60}^+ in a dual beam approach, it is possible to sputter through the top layers of the inorganic or organic surfaces while monitoring the incidence profile of elemental or molecular species.

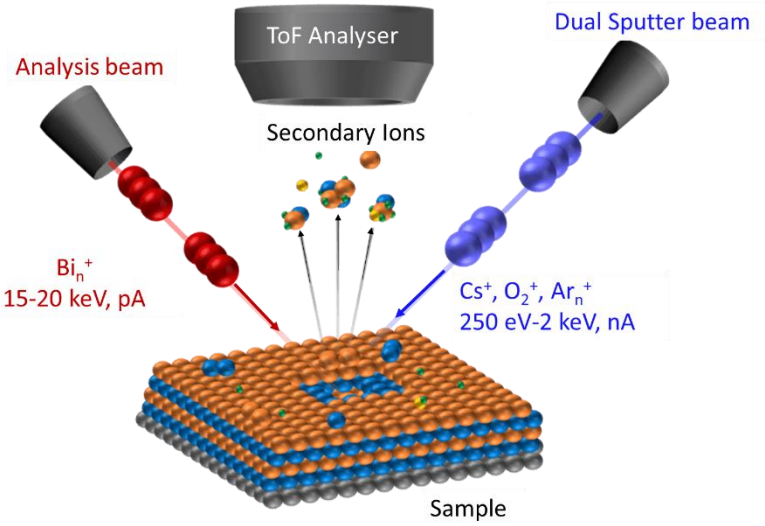

Figure 2.9 – Schematics of ToF-SIMs actuation method. Ion beam sources impact the surface resulting in fragmentation that includes neutral, secondary ions (+/-) and electrons.

Limitations of ToF-SIMS includes the analysis of proteins. With ToF-SIMs, proteins are heavily fragmented by the energetic primary ions beams, resulting in single amino acid residue secondary ions[140], which are unable to provide protein primary structural information. Additionally, in ToF-SIMs the analysis of macromolecules is limited by the mass-resolving power of the ToF analyser, which is dependent on statistical analysis of known protein samples to confirm identity, conformation and orientation[140]. Efforts to address this include a large cluster primary ion source and gas cluster ion beams, which enables detection of larger peptides and small proteins up to 12 kDa[140].

In order to overcome these limitations, the 3D OrbiSIMS instrument combines a gas cluster ion beam (GCIB) and an OrbitrapTM analyser to aid analysis of biological samples (Figure 2.10). The Orbitrap analyser gives high mass accuracy and high mass resolution. The argon GCIB creates mass spectra richer in intact biomolecules with significantly less fragmentation[141]. For

the purposes of this thesis, ToF-SIMs and OrbiSIMs techniques were applied aiming to verify the formation of a thiolate bond between nanobodies and the gold surface

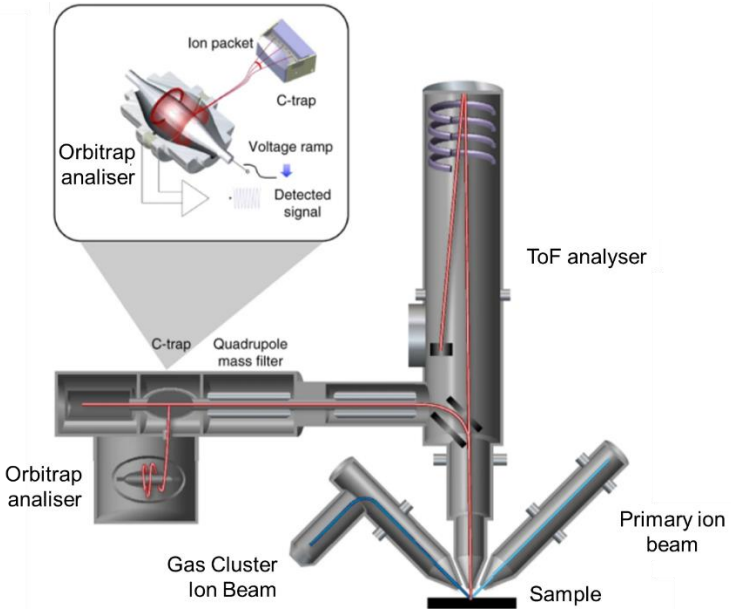

Figure 2.10 – ToF SIMs hybrid with 3D OrbiTrap analyser (3D OrbiSIMs) instrument schematics. Adapted from[141].

2.6 **Circular Dichroism (CD)**

Circular dichroism (CD) is an optical technique that measures the interaction of circularly polarised light with molecules[21]. It is also used to investigate the conformation of proteins[21]. In the context of this thesis work, CD was applied to verify the integrity of nanobodies through their conformation upon immobilisation at the surface, and under a range of applied temperatures. Thus, the summary herein presented focus on the explanation of CD with proteins. Circularly polarised (CP) light propagates in left- (LCP) and right-handed (RCP) directions. A material is said to exhibit circular dichroism if its absorption of RCP light is different from the absorption of LCP light[142]. LCP and RCP light interact equally with non-chiral chromophores (molecular group responsible for the compound's colour) but differently

when the chromophore is chiral (i.e. optically active)[142]. When measuring with CD, both LCP and RCP light are directed to the protein of interest[142, 143] (Figure 2.11).

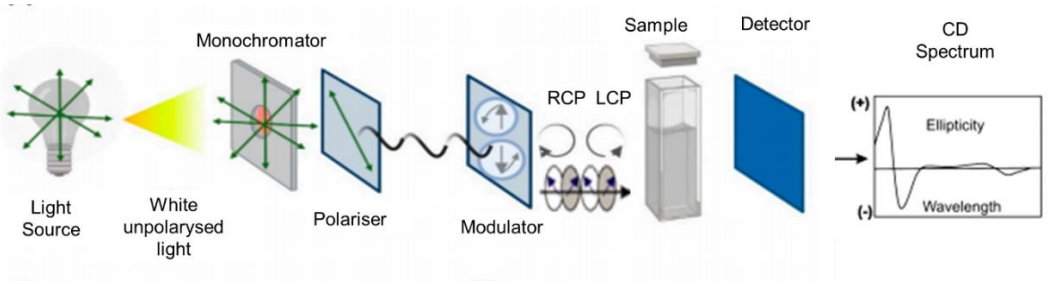

Figure 2.11 – Schematics of the typical circular dichroism set up. Adapted from[144].

After passage through the sample, if the LCP and RCP components are not absorbed (or absorbed to the same extent), the combination of the components would regenerate the light polarised in the original plane. However, upon the greater adsorption of one of the components, the resultant radiation is elliptically polarised. The CD results are expressed in either the difference in absorbance (A) of the two component ($\Delta A = A_{left} - A_{right}$) or as the ellipticity in degrees (θ)[143] (Figure 2.12(A)).

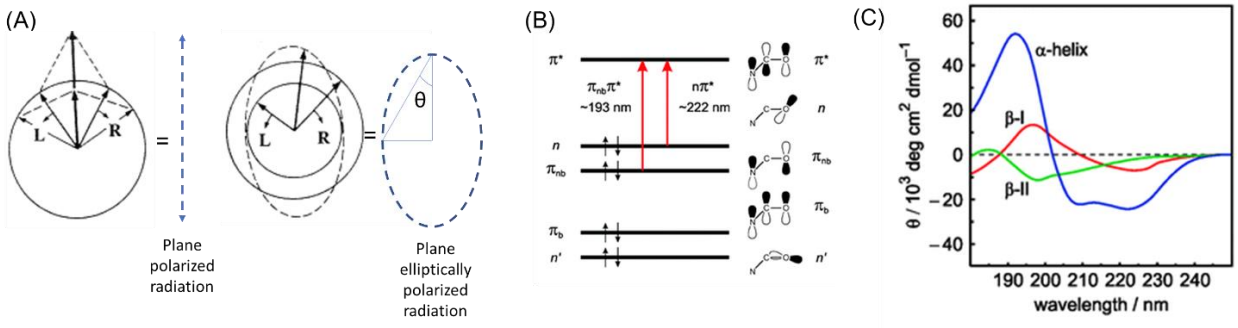

Figure 2.12 – Circular dichroism principles applied to proteins. (A) Resulting linearly or elliptically plane polarised radiation from achiral or optically active molecules respectively. (B) Electronic transitions of the amide group in the far-UV region. Molecular orbitals shown: bonding, nonbonding and antibonding π orbitals (πb, π_{nb} and π) and two lone pairs on the oxygen atom (n and n'). (C) Characteristic CD curves of secondary structure elements. Adapted from[143, 145]*

In proteins, the chromophores of interest include the peptide bond (absorption bellow 240 nm), aromatic amino acid side chains (absorption between 260 to 320 nm) and disulphide bonds (weak broad absorption bands centered around 260 nm)[22]. A typical CD spectra showing the various secondary structural features such as α-helices and β-sheets or β-turns results at the absorption regions below 240 nm in the far ultraviolet (UV) (Figure 2.12(C). This region arises from transitions that occur within the peptide backbone, mostly abundant in the amide group [23]. For example, in an α-helix structure, from the exciton splitting of electronic transitions from the amide non-bonding π orbital (π_{nb}) to the anti-bonding π orbital (π*), an intense positive band at 190 nm and a negative band at 208 nm is formed. Located at about 220 nm, a negative band arises from the electronic transition from an oxygen lone pair orbital, n, to the π* orbital (Figure 2.12(B). Other spectroscopic signatures will result from other motifs. CD can measure changes to proteins structures that are induced by variations in the surrounding environment for example with temperature, solvation or constituent concentration. Overall, CD is an important tool which was used to confirm the nanobodies secondary structure in solution and when immobilised on the gold substrates.

2.7 **Surface Plasmon Resonance (SPR)**

Surface Plasmon Resonance (SPR) spectroscopy is an optical technique that allows in real-time, label-free detection of biomolecular interactions[146]. In the SPR instrument, a light source points polarized light to an electrically conductive surface (usually gold) at the interface between two media[146] (Figure 2.13). At a precise angle of incidence, when the light incident photons hit the metal surface, they transfer energy exciting the metal band electrons capable of resonating. This generates electron charged density waves called plasmons that propagate parallel to the

surface[146]. Typically the incident light beam goes through a prism with high refractive index promoting the total internal reflection (TIR), and creates an evanescent wave that penetrates through the metal film. The detection occurs by measuring the changes in reflected light, obtained on a detector[146]. The refractive index close to the metal film is the determinant, thus if the local effective refractive index changes, it results in the SPR angle shift that is captured in a sensorgram. The change in SPR signal is directly proportional do the mass captured at the sensor[146].

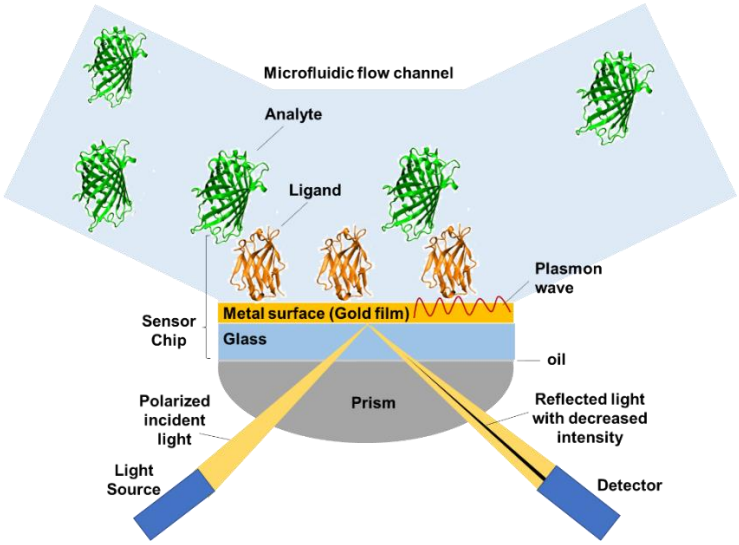

Figure 2.13 – SPR set-up schematics.

A SPR sensor chip consists of a glass slide covered with a thin layer of metal functionalised with the ligands of interest, which will interact with the analyte present at the injection solution[146] (Figure 2.13). A drop of oil with the same refractive index as the glass substrate coated with gold is used to promote the contact between the prism surface and the chip (Figure 2.13). The integrated microfluidic system allows the use of low volumes of reagents. Whilst running an experiment, the chip is in contact with a flowing solution (i.e. running buffer) at a constant controlled temperature (as it can affect the refractive index[147]) achieving a baseline.

Upon the injection of analyte, molecular interactions are monitored as the properties of the reflected light change when the analyte binds (association) or dissociates from the ligand (Figure 2.14(A)). The evanescent wave created by the plasmons has a range of around 300 nm from the boundary between the metal and the sample solution[147] (Figure 2.14(B)).

In the case of this thesis work, SPR was used to mainly measure biomolecular interactions between nanobodies functionalised at the surface and their antigens in solution. The biomolecular interactions were expected on films at a depth of up to 5-10 nm.

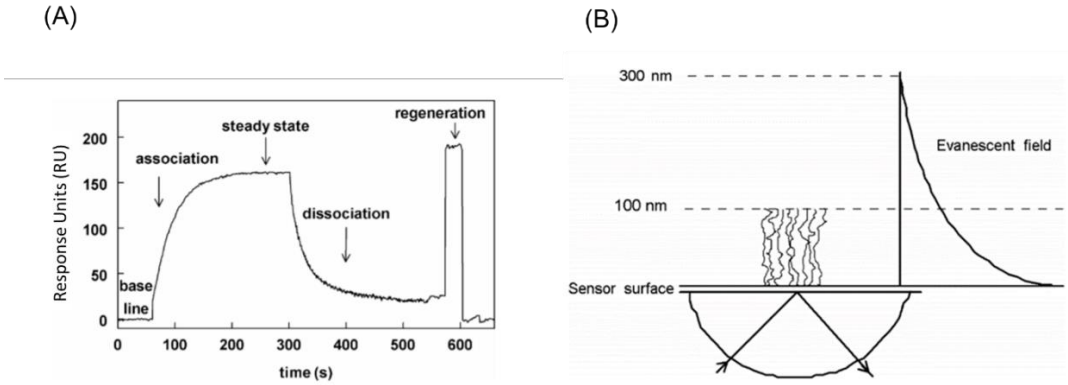

Figure 2.14 – SPR typical sensorgram and sensitivity range. (A) The SPR response changes during analyte-ligand association, returning to the baseline after dissociation and chip regeneration. (B) The SPR effect is sensed only in the evanescent field coupled to surface plasmon resonance waves. The strength of this field decays exponentially with the distance from the surface. Adapted from [147].

2.7.1. **Electrochemical Surface Plasmon Resonance (E-SPR)**

In order to simultaneously provide insight of the surface's optical and electrochemical properties, SPR can be integrated with a 3-electrode electrochemistry flow cell, connected to a potentiostat[146] (Figure 2.15). In the context of this thesis, this set-up was used to apply electrical potentials on the surface.

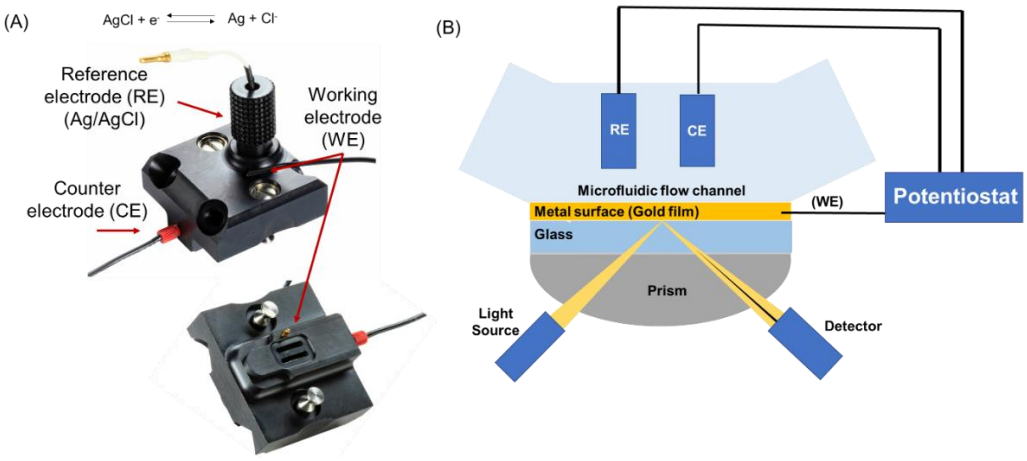

Figure 2.15 – Schematic electrochemistry SPR (E-SPR) integrated system. (A) 3-electrode electrochemical flow cell that composes the electrical circuit between the counter (CE) and working electrodes (WE). (B) E-SPR set-up.

In the integrated E-SPR system, the current travels between the gold chip surface (working electrode, WE) and the counter electrode (CE) which is a platinum wire in contact with the solution in the flowcell[148] (Figure 2.15). The potentiostat measures and controls the applied potential between the WE and the CE. After the user input, a current is applied to the counter electrode and the potential at the working electrode is adjusted following a feedback mechanism with respect to the reference electrode (Ag/AgCl)[148]. The reversible redox reaction at Ag/AgCl electrode occurs providing a stable and reproducible potential. It is important to note that the 3-eletrode flow cell is composed of two fluidic channels. However, only one channel has the CE and the reference electrode (RE) in solution, being in contact to the second channel through a loop. Thus, only the first channel can accurately apply the set potential, as the current towards the second channel suffers a high resistance.

Overall, E-SPR allows potential-controlled molecular biointeractions at the surface whilst allowing real-time measurements. In this thesis, E-SPR allowed to verify the biological activity

between the functionalised nanobodies at the gold surface (under applied potential) with their respective antigens in solution.

Chapter 3 Direct immobilisation of engineered nanobodies on gold sensors

Nanobodies have great potential as biorecognition elements for sensors due to their small size, affinity, specificity and robustness. However, facile and efficient methods of nanobody immobilisation are sought that retain their maximum functionality. Herein, the direct immobilisation of nanobodies NbVCAM1 on gold sensors by exploiting a modified cysteine strategically positioned at the C-terminal end of the nanobody is described. The experimental data based on secondary ion mass spectrometry, circular dichroism and surface plasmon resonance, taken together with detailed computational work (molecular dynamics simulations), provide evidence of the formation of stable and well-oriented nanobody monolayers. Furthermore, the nanobody structure and activity is preserved, wherein the nanobody is immobilised at high density (approximately 1 nanobody per 13 nm^2). The strategy for spontaneous nanobody self-assembly (Figure 3.1) is simple and effective and possesses exceptional potential to be used in numerous sensing platforms, ranging from clinical diagnosis to environmental monitoring.

This chapter is partially based on the article (2) co-written by the author of this thesis:

[2] Simões, B.; Guedens, W. J.; Keene, C.; Kubiak-Ossowska, K.; Mulheran, P.; Kotowska, A. M.; Scurr, D. J.; Alexander, M. R.; Broisat, A.; Johnson, S.; Muyldermans, S.; Devoogdt, N.; Adriaensens, P.; Mendes, P. M., Direct Immobilisation of Engineered Nanobodies on Gold Sensors. ACS Applied Materials & Interfaces 2021, 13 (15), 17353-17360

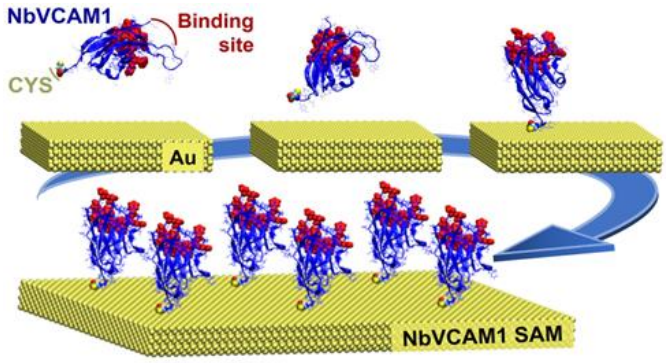

Figure 3.1 – Schematics of NbVCAM1 nanobodies self-assembly on gold surfaces.

All the experimental work of this chapter was conducted by Bárbara Simões including the preparation work for the various techniques, unless otherwise stated. ToF-SIMs and 3D OrbiSIMS was conducted in collaboration with David Scurr and Anna Kotowska. The Circular Dichroism was done in collaboration with Steve Johnson. All the computational work was performed by Bárbara Simões. All the data analysis was performed by Bárbara Simões, with collaboration of David Scurr, Anna Kotowska, Steve Johnson, Karina Kotowska for the respective experimental work.

3.1 Introduction

A unique set of properties, such as small size, stability, high affinity and high selectivity, make nanobodies ideal building blocks for a wide range of sensing devices and assays for use in medical, biotechnology, environmental, food and even military settings.

Despite great advances in nanobody technology, limited approaches have been reported for the immobilisation of nanobodies on sensing platforms.[88, 149, 150] Physical adsorption has been investigated for nanobody immobilisation on gold nanoparticles, which are used as immunoassay detection labels.[150] While stable nanobody-gold nanoparticle conjugates can be generated,[151] this requires careful consideration of the influence of the nanobody isoelectric point, and pH and ionic strength of the working solution. Instead of relying on direct immobilisation on a sensor surface, Adriaensens and co-workers[149] established a two-step protocol in which the sensor surface was initially functionalised with an azide-terminated monolayer and then exposed to an engineered nanobody carrying a C-terminal alkyne function. Taking advantage of the copper (I)-catalyzed cycloaddition reaction ("click" chemistry), the formation of a stable and well-oriented nanobody monolayer was achieved. In a recent example, nanobodies have been tagged with histidines, which served to couple the nanobody to cobalt-nitrilotriacetic acid metal-chelate beads.[88]

In spite of these and other efforts in the literature,[39, 152, 153] efficient, alternative immobilisation methods are still needed to meet the requirements of a wide range of sensing applications. In this context, gold surfaces are widely employed as interfaces in various biochemical and chemical sensors due to their high electrical conductivity, unique optical properties, biocompatibility and chemical stability.[154, 155] The mechanisms of these sensors are based on various detection methods, including electrochemical (*impedance spectroscopy*[156] *and cyclic*

voltammetry[157]), piezoelectric (*surface acoustic wave (SAW)*[158] and quartz crystal microbalance (QCM)[159]) and optical (e.g. surface plasmon resonance (SPR),[160] localized surface plasmon resonance (LSPR)[161], and surface enhanced Raman spectroscopy (SERS)[162]). The prevailing involvement of gold surfaces in a diversity of sensing technologies highlights the necessity for strategies that not only promote fast and robust immobilisation but also high efficiency target binding.

With this proviso in mind, in this work the ability of an engineered nanobody comprising a modified cysteine to readily generate stable, well-oriented and packed nanobody monolayers on gold surfaces was investigated. The expressed protein ligation (EPL) technique was used to incorporate an alkyne-modified cysteine at the C-terminal of the model nanobody NbVCAM1, which targets the human vascular cell adhesion molecule-1 (hVCAM1).[40] The hVCAM1 plays an important role in disease progression by attracting inflammatory cells to the developed injury[163]. In the engineered NbVCAM1, the modified cysteine group, which binds to gold via the thiol group, is located at the opposite end of the binding pocket (Figure 3.2). While the native nanobody contains two other cysteines and four methionines, these moieties are not expected to interact with the gold surface. The two native cysteine residues are located in the interior core of the nanobody, forming the typical disulfide bridge responsible for structural stability[64], which makes the moieties unlikely to interact with gold. Additionally, previous studies have shown that methionines poorly interact with gold[164-166].

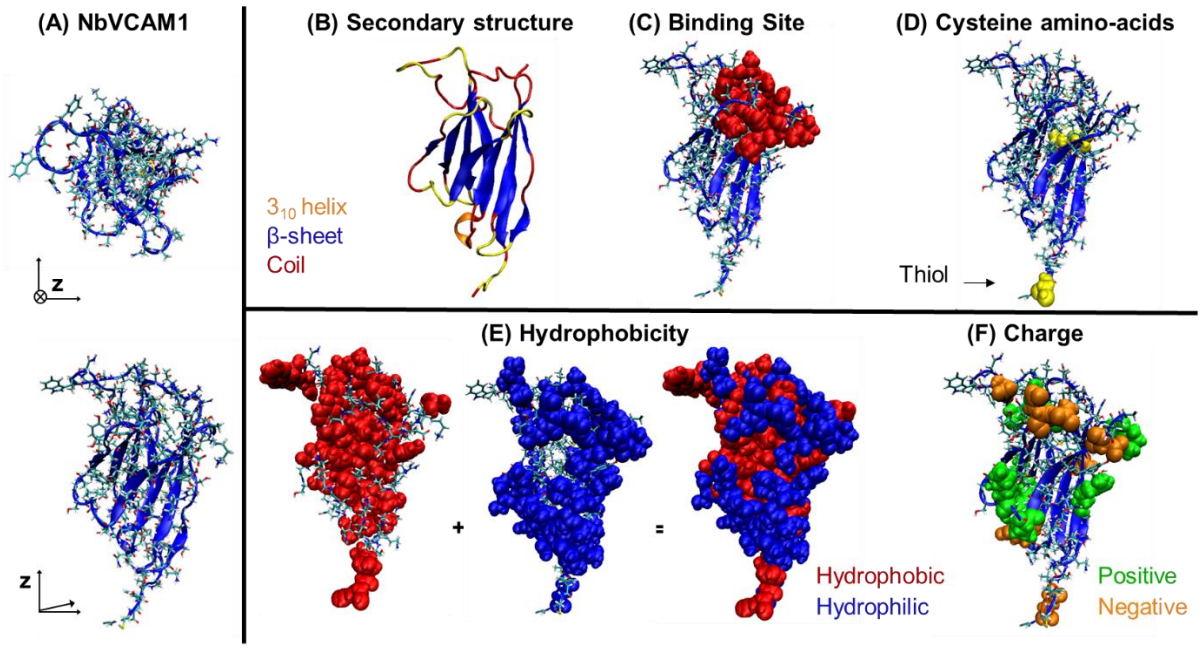

Figure 3.2 – NbVCAM1 nanobody (14.5 kDa) Visual Molecular Dynamics (VMD) images , shown by new cartoon merged with bonds representations: (A) The NbVCAM1 top and side views, with dimensions 3.1 nm x 4.0 nm x 5.3 nm; (B) The secondary structure with colours: 3_{10} helix (orange), β-sheet (blue), turn (yellow) and coil (red); (C) The amino acids forming the antigen binding site (van der Waals representation (VDW), red) located at the N-terminus side of the domain; (D) The cysteines (VDW, yellow) that form a disulfide bridge at the core, and the one located at the C-terminus; (E) Hydrophobic (VDW, red) and hydrophilic (VDW, blue) amino-acids; (F) Negative (VDW, orange) and positive (VDW, green) amino-acids. The NbVCAM1 has a net charge of +2e at pH 7.0

In order to have a detailed insight on the interface chemistry and structural stability, orientation and activity of the immobilised nanobodies, a suite of complementary surface analysis techniques was employed, including contact angle, ellipsometry, time-of-flight secondary ion mass spectrometry (ToF-SIMS), three dimensional Orbitrap secondary ion mass spectroscopy (3D OrbiSIMS), circular dichroism (CD) and SPR. The molecular interactions occurring at the gold-nanobody interface and the stable conformation of the immobilised nanobodies are further validated using molecular dynamic (MD) simulations.

3.2 Results and Discussion

3.2.1. Formation and characterisation of NbVCAM1 SAMs

NbVCAM1 monolayers were formed by immersing freshly cleaned gold substrates in a solution of 1 μM NbVCAM1 in phosphate buffer saline (PBS) for 24 h, which provides the time for the formation of a gold-thiolate bond between the gold surface and the NbVCAM1 nanobody[19]. Contact angle data shows the formation of a hydrophilic surface, with the NbVCAM1 monolayers exhibiting advancing and receding contact angles of 62.6 ± 2.3° and 26.0 ± 6.5°, respectively. These values are comparable to those obtained for protein monolayers,[167] with the large contact hysteresis (36.6 °) indicating the presence of a heterogeneous surface due likely to the exposure at the interface of hydrophobic and hydrophilic amino acids from the nanobody and/or nanobody packing arrangement. The ellipsometric thickness observed for the NbVCAM1 monolayer was 1.99 ± 0.09 nm, which is less than the theoretical molecular length of the nanobody from the C-terminally added cysteine-alkyne linker to the N-terminal, i.e. 5.3 nm (Figure 3.2). This discrepancy, between molecular length and self-assembly monolayer (SAM) thickness, can be explained by the presence of air voids between the nanobodies and within the nanobodies themselves[168, 169].

Following these initial results which provided evidence of NbVCAM1 monolayer formation, 3D OrbiSIMS and ToF-SIMS were used to investigate whether or not the gold-thiolate bond was formed upon adsorption. 3D OrbiSIMS and ToF-SIMS *survey spectra* (Figure 6.2 in Chapter 6) along with high-resolution spectra (Figure 3.3 and Figure 3.4) were collected for NbVCAM1 SAM and control bare gold. The mass resolving power of the 3D OrbiSIMS allows the assignment of secondary ion peaks associated with the proposed Au-S bond (shown in Figure 3.3), which could not be confidently distinguished in the Negative polarity 3D OrbiSIMS

spectra of the NbVCAM1 monolayer on gold are illustrated in Figure 3.3, together with clean gold as a control. Secondary ions associated with the AuS^- ion and related fragments ($AuSH^-$, AuS_2^-, AuS_2H^-, $AuS_2H_2^-$) can be observed clearly for the NbVCAM1 monolayer, but are absent in the clean gold control. Additionally, the NbVCAM1 monolayer attenuated the intensity of Au^- ion fragments, which were less accessible to be ionized due to the presence of NbVCAM1 (Figure 3.3(F)). In addition to providing further evidence supporting the formation of the NbVCAM1 monolayer on gold, these results also confirm the formation of a thiolate bond between the NbVCAM1 and the gold surface, wherein adventitious sulphur is excluded as a possible source of AuS^- ions.

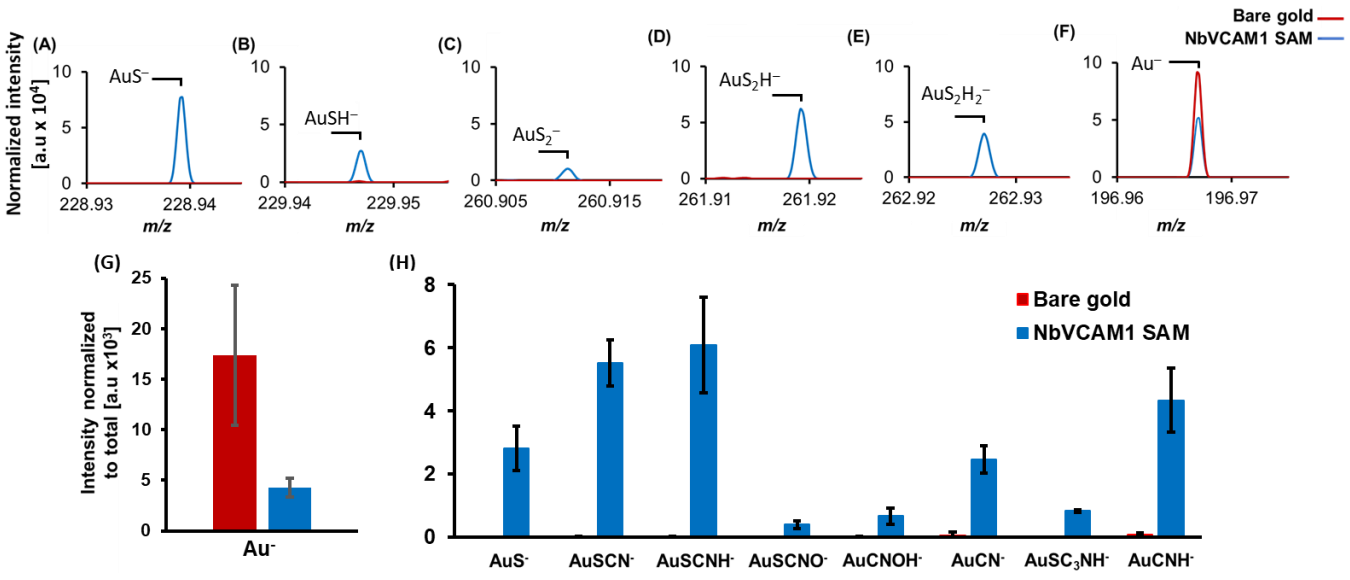

Figure 3.3 – NbVCAM1 SAMs 3D OrbiSIMs results. Overlay of 3D OrbiSIMS spectra (20 keV Ar_{3000}^+ as primary ion beam) for the peak intensities of AuS^- and related ions (A-E) and the substrate ion Au^- (F) on the control bare gold (red) and NbVCAM1 SAM (blue). Intensity was normalized to total ion counts. 'a.u' refers to arbitrary units. Comparison of (G) gold and (H) gold-sulphur and gold-nitrogen containing species ion peak intensities in the gold reference samples (red) and NbVCAM1 SAM samples (blue). Average and standard deviation for four 3D OrbiSIMS measurements. Intensity was normalized to total ion counts.

Along with fragments associated with the Au-thiolate bond, the presence of ions containing Au and nitrogen are also observed (Figure 3.4(A)). They are present at a much higher intensity than on clean gold surfaces, indicating the interactions between the amino acid residues in the NbVCAM1 and the gold surface. These interactions can arise from nitrogen atoms located in positions close to the cysteine-alkyne linker since there is the possibility of the nanobody making more than one point of contact with the gold surface. However, the possibility that some nanobodies might be randomly oriented on the surface cannot be excluded. The 3D OrbiSIMS results are further supported by ToF-SIMS analysis (TOF IV instrument with 25 keV Bi_3^+ primary ion beam), wherein a peak for the ion fragment $AuSC_6H_8ON^-$ can be distinguished from the clean gold control surface (Figure 3.4(B)). This distinctive fragment belongs to the alkyne-modified cysteine, thus supporting the formation of a thiolate bond between the thiol group in the modified NbVCAM1's cysteine and the gold surface.

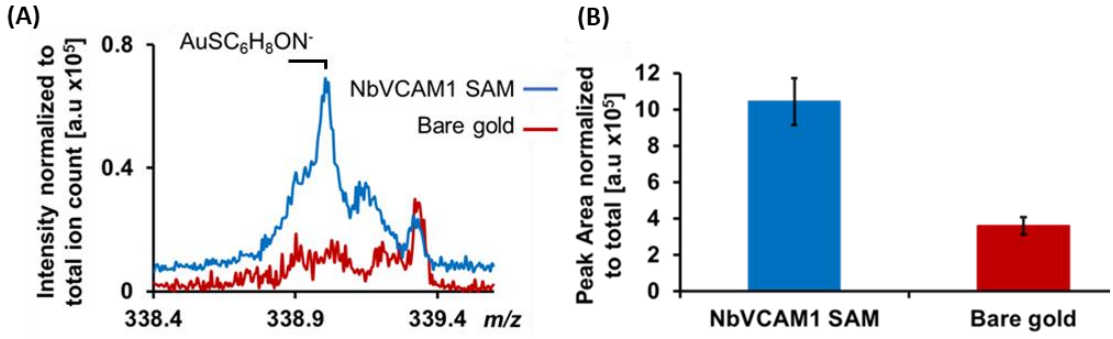

Figure 3.4 – NbVCAM1 SAMs ToF-SIMS results. (A) ToF-SIMS (IONTOF GmbH) spectra and (B) respective normalized peak intensity areas showing the presence of the $AuSC_6H_8ON^-$ ion fragment on the NbVCAM1 SAM but its absence on the clean gold control surface. Average and standard deviation for three measurements over two samples. 'a.u' refers to arbitrary units.

ToF-SIMS can also directly map the distribution of the different nanobody fragments on the gold surface to provide insights into the chemical interactions between the nanobody and gold surface. Distribution maps have been plotted for amino acids fragments (Figure 3.5(A-B)). While the lateral resolution of the technique is not sufficient to resolve individual nanobodies, the uniform ion distribution across the surface does indicate that the NbVCAM1 nanobodies are uniformly distributed on the gold surface (Figure 3.5(B)). The amino acid fragments (proline, tryptophan and tyrosine) were assigned according to Lhoest et al.[170] These amino acid fragments are not present on clean bare gold surfaces, as illustrated in Figure 3.5 (A) and (C).

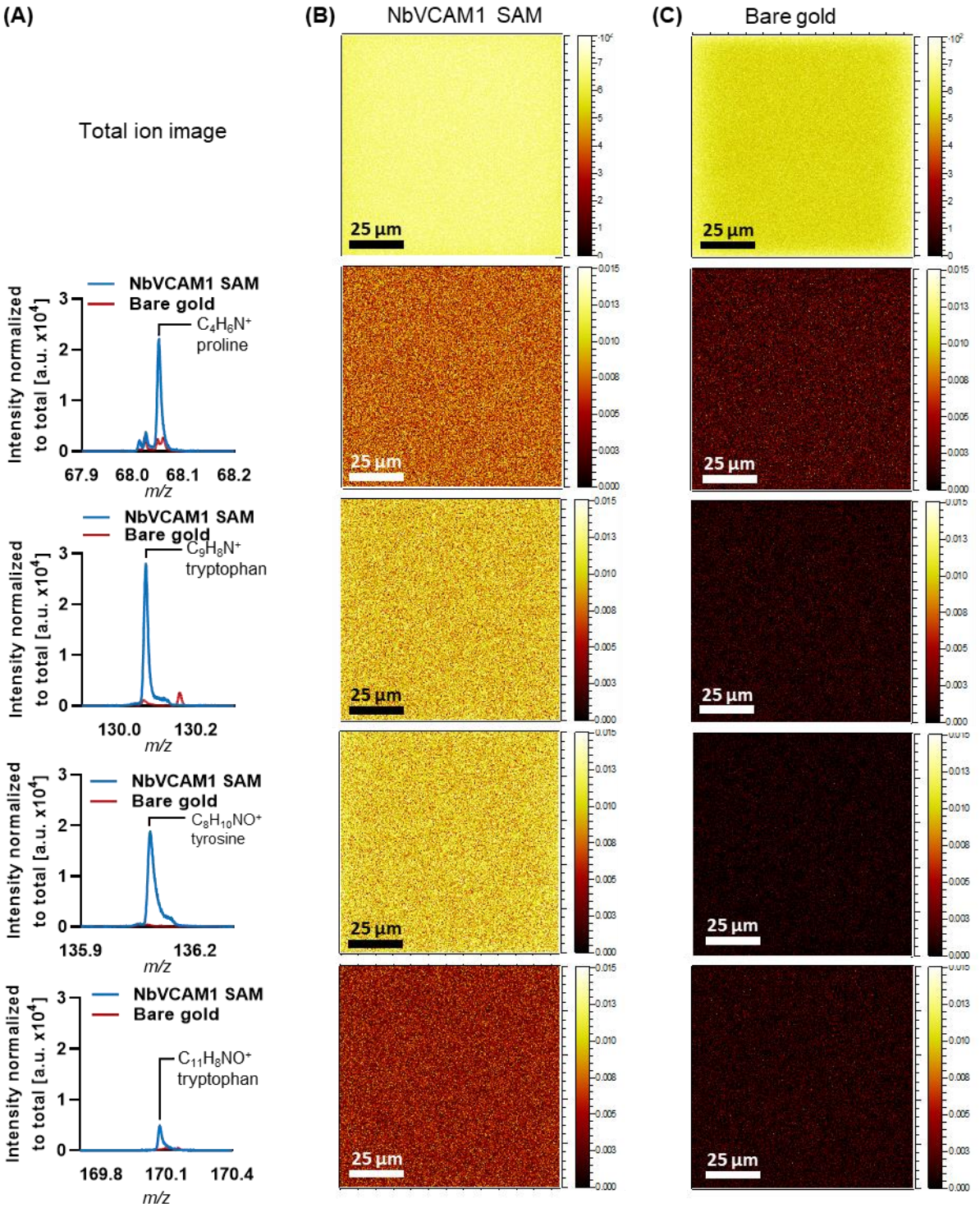

Figure 3.5 - NbVCAM1 SAMs ToF-SIMS results for amino-acid fragments.(A) Spectra overlay of amino acid fragments (proline, tryptophan and tyrosine) assigned in positive polarity spectra of NbVCAM1 (blue) and gold reference (red), intensity was normalized to total ion counts. 'a.u' refers to arbitrary units. (B) respective ToF-SIMS images of gold chips incubated with NbVCAM1 SAM. (C) Amino acid fragments are not detected in ToF-SIMS images of bare gold reference. All ion images have been normalized to total ion counts.

Additional information from TOF SIMs/3D OrbiSIMs about the nanobodies orientation or conformation at the surface would have required higher amounts of sample (being NbVCAM1-SAM a monolayer, its high fragmentation resulted in small weight fragments, which are harder to unambiguously be assigned). Additionally, it would also be required that the nanobody be functionalised on a different surface (e.g. silicon) to guarantee a statistical difference between oriented and non-oriented nanobodies.

3.2.2. **Conformational structure and biological activity of NbVCAM1 SAMs**

Following the analysis determining the nature of the gold-nanobody interaction, attention was turned towards understanding the structure of the surface-immobilised NbVCAM1 using circular dichroism (CD). Nanobody monolayers were formed on copper-ion-functionalised quartz slides[171] onto which NbVCAM1 can chemisorb, in a similar manner as on gold, through the modified cysteine. Quartz was used rather than gold substrates to avoid a low signal to noise ratio due to the high absorption of gold in the UV region. The CD spectrum of the surface-tethered NbVCAM1, shown in Figure 3.6(A), is similar to that of the nanobody in solution (insert in Figure 3.6(A)), both illustrating that the NbVCAM1 is composed largely of β-sheets (typified by a negative band at 217 nm and a positive band at 195 nm). The observed peak shift and reduced intensity between the CD spectrum of the control solution (inset) and the surface-tethered NbVCAM1 could be explained by the difference in concentrations (higher concentration for the control NbVCAM1 solution (1 mg/ml) compared with the NbVCAM1 SAM which resulted of incubation with 0.1 mg/ml followed by rinsing of unbound NbVCAM1). These findings are in agreement with literature,[63, 172, 173] that had shown that the Nb domain is composed of folded β-sheets with three loops in the regions homologous to the

CDRs of the IgG VH domains. These results suggest that the nanobody conformation is not altered when they are organised in a two-dimensional monolayer. Further evidence of the conformational stability of NbVCAM1 was obtained by increasing the temperature of the NbVCAM1 functionalised quartz substrate from 20 ºC to 70 ºC (Figure 3.6(B)). The CD spectra taken at different temperatures show similar features, with the β-sheet peak remaining unchanged.

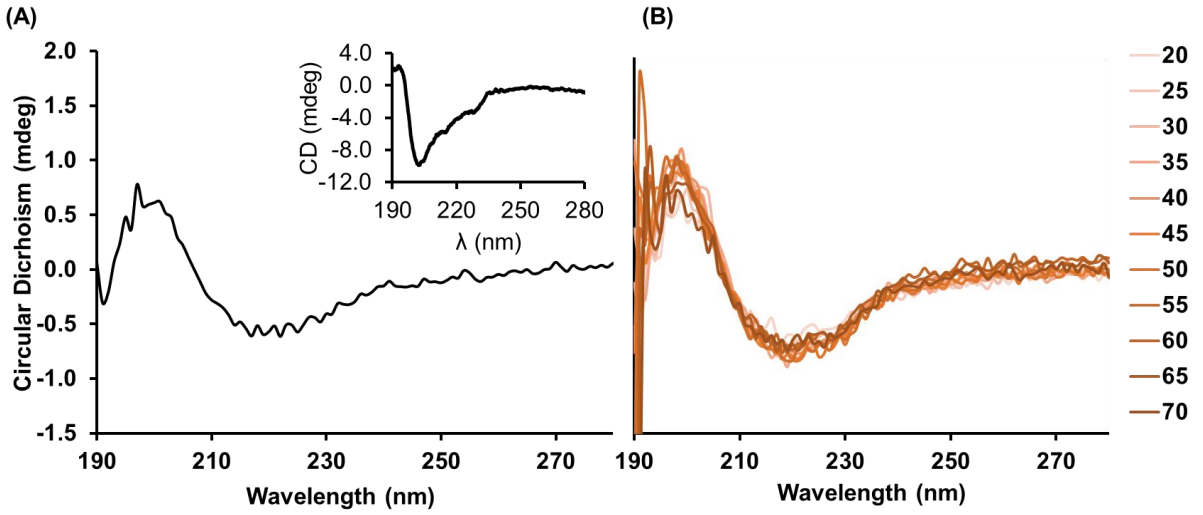

Figure 3.6 - Circular Dichroism (CD) spectra of NbVCAM1 on a surface immobilised on a Cu^{2+} terminated SAM on a quartz slide. (A) The average spectra of three measurements at room temperature; insert: NbVCAM1 in solution as a control; (B) Spectra overlay at temperatures ranging from 20ºC to 70ºC by an increment of 5ºC.

Having established that the nanobody retains its structure while forming a homogeneous, covalently bound monolayer on the gold surface, thereafter the antigen (hVCAM1) binding capacity using surface plasmon resonance (SPR) was assessed. Figure 3.7 portrays the formation of a NbVCAM1 monolayer in real-time, followed by hVCAM1 antigen binding. From a stable baseline of PBS flowing over the clean gold chip, an injection of NbVCAM1

shows a response of ~ 2000 response units (RU), which reduces to 1800 RU as the solution is washed away with PBS. Following the initial removal of non-specifically bound NbVCAM1, prolonged rinsing (i.e. ~ 2 h) had no effect on the integrity of the NbVCAM1 monolayer, indicating the presence of a stable monolayer (Figure 3.7(A)). Since 1000 RU is equivalent to a change in surface concentration of approximately 1 ng/mm^2,[20] the amount of immobilised nanobody (i.e. nanobody loading capacity on the gold surface) achieved was 1.8 ng/mm^2, corresponding to approximately 1 NbVCAM1 nanobody (14.5 kDa) per 13 nm^2. Based on the size of NbVCAM1 (i.e. 3.1 x 4.0 x 5.3 nm), the results imply the formation of a high packed nanobody monolayer on the gold surface that enables the specific capture of the antigen. Injection of the hVCAM1 antigen produced a change in the SPR response of ~ 600 RU (Figure 3.7(B)), with the rinsing having a minimal effect on the final response. The hVCAM1 antigen (74.1 kDa) with dimensions of 12.9 x 7.4 x 7.6 nm is eleven times larger in volume than the NbVCAM1, thus the hVCAM1 antigen was shown to be immobilised at high density on the NbVCAM1 monolayer, with an experimental density of 1 hVCAM1 per 205 nm^2. These findings confirm the high capability for the NbVCAM1 monolayer to bind its antigen (K_D=1.61 ± 0.14 nM[149]), wherein a high degree of well-oriented nanobodies must be in place otherwise antigen binding would have been considerably affected. These results contrast with those obtained when an unmodified NbVCAM1 containing no cysteine at the C-terminal is immobilised on a gold surface (Figure 3.7(C)). Exposure of the gold surface to the unmodified NbVCAM1 led to a much lower SPR response of ~ 180 RU, a 10 fold decrease in immobilisation compared with the modified NbVCAM1 cysteine-containing at the C-terminal. These results further support the role of the added cysteine in enabling a gold-thiolate bond and formation of a high packed nanobody monolayer on the gold surface. Antigen binding is also reduced to half of the one observed in the NbVCAM1 monolayer. Due to the low coverage of

the unmodified NbVCAM1 on the gold surface, the binding properties are difficult to interpret since hVCAM1 antigen can be specifically bound to some of the nanobodies but also non-specifically adsorbed on the gold surface.

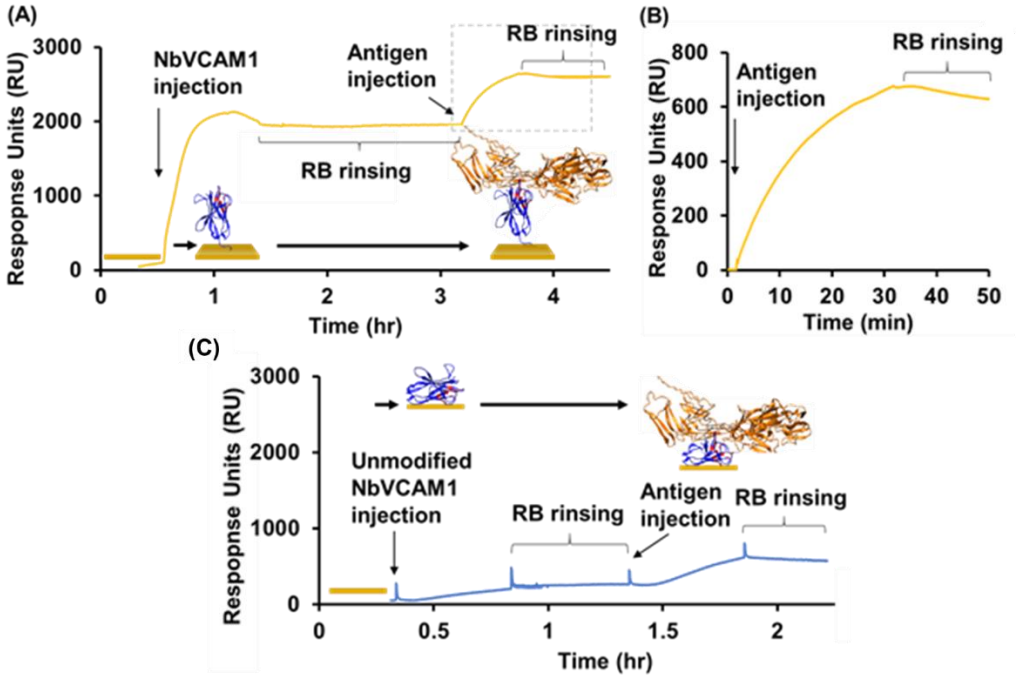

Figure 3.7 - SPR results for NbVCAM1 adsorption followed by antigen injection. (A) Overview of NbVCAM1 adsorption (1 μM) followed by blank injection with running buffer (RB) and posterior antigen hVCAM1 injection (0.27 μM). (B) hVCAM1 injection response. (C) Unmodified NbVCAM1 adsorption (1 μM) followed by blank injection with RB and posterior antigen hVCAM1 injection (0.27 μM).

3.2.3. **Further optimisation of the NbVCAM1 SAMs**

After successfully confirming the biological response from NbVCAM1 SAM with the injections of hVCAM1 (~ 600 RU), the next step focused on increasing the response further. There was a possibility that the biological response had not yet achieved the maximum signal due to steric hindrance. This limitation could potentially occur due to a too highly packed

NbVCAM1 SAM. Therefore, different ratios of NbVCAM1 and a spacer molecule at the surface were investigated. SAMs of NbVCAM1 and 3-Chloro-1-propanethiol (spacer) at the molecular ratios of 500:1, 100:1 and 1:10 were formed and characterised with SPR for the biological response (Figure 3.8). The SPR results showed no signal improvement, but instead a decay. Such reduction in signal could be explained by the likely reduced amount of NbVCAM1 at the surface. This reduction had a negative impact as it resulted in the reduction of captured antigens. This result suggests that following this immobilisation method, the limit of response has been achieved without a spacer.

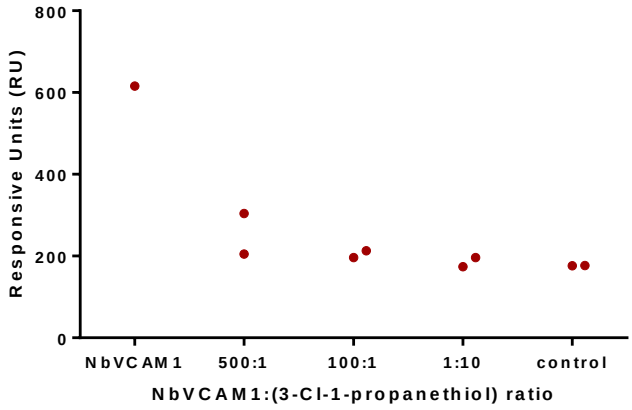

Figure 3.8 – SPR response for hVCAM1 (0.27 μM) injection on SAMs of NbVCAM1:3Cl-1-propanethiol. By incubating the gold chips with solution ratios of Nb: 3Cl-1-propanethiol at 500:1, 100:1 and 1:10 the NbVCAM1 was spaced out at the surface. As controls, the NbVCAM1 SAM and the 3Cl-propanethiol SAM were also tested. Duplicates were measured.

3.2.4. **Molecular dynamic simulations of the adsorption of NbVCAM1 on gold**

To complement the experimental findings, a straightforward model to simulate NbVCAM1 adsorption onto a gold surface was developed. These simulations yield insight into several aspects of the nanobody adsorption, including i) the protein's structural behavior before, during and after adsorption, ii) the interactions between the protein and gold during and after

adsorption, and iii) the footprint of the adsorbed protein, which is relevant to the monolayer density that it might subsequently form. The model was built with the NbVCAM1 in water/0.15M NaCl with a starting position at a distance of 20 Å from the gold surface. As an approach to randomize the results, the nanobody was placed at different starting orientations in a sequence of separate trajectories: with the C- to N-terminal axis approximately perpendicular to the surface (C-terminal either facing the gold surface or the bulk solution), or with the axis parallel to the surface.

It was found that the physical adsorption process can yield various adsorbed nanobody orientations, as might be expected for adsorption to a gold surface.[174] Amongst these, it was observed the desired orientation with the modified cysteine adsorbed to the surface and the N-terminal exposed to solution (Figure 3.9(A)). The simulations do not directly simulate the formation of the thiolate bond, but do show that these are likely to form due to the close approach of the sulphur to the gold surface. Indeed, the literature widely reports that thiolate formation starts with physisorption followed by chemisorption,[14] which stabilises the adsorbed orientation.[175] In contrast, adsorbed nanobody with undesired orientations (e.g. Figure 3.9(B)) are likely to be less stable, allowing the re-orientation of the nanobody over time to create the more stable thiolate-bonded structure.

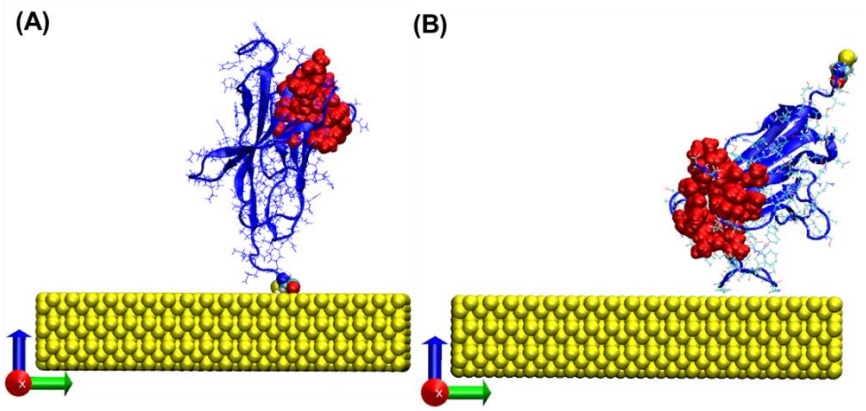

Figure 3.9 - Representative VMD images from MD simulations of the physical adsorption of NbVCAM1 on gold , resulting in (A) well-oriented and (B) non-oriented nanobodies. The NbVCAM1 representation highlights the modified cysteine at the C-terminal (white- hydrogen; cyan – carbon; red – oxygen; blue - nitrogen and yellow – sulphur) and the amino-acids that belong to the antigen binding site located at the N-terminus side in the folded domain (all atoms red) with the gold slab (yellow).

The root-mean-square deviation (RMSD) and root-mean-square-fluctuation (RMSF) are tools of analysis to quantify the conformation variability within a protein.[74] RMSD measures the degree of similarity between two three-dimensional (3D) structures with the same number of atoms. In this case, the NbVCAM1 was compared at each step of the trajectory (step = 0.04 ns) with its initial structure (at t = 0). For RMSF, the RMSD is calculated for each nanobody's residue, reflecting its fluctuations across the total trajectory. Figure 3.10 shows the RMSD and RMSF results for the trajectories taken before and after adsorption compared with the control trajectory obtained for NbVCAM1 in solution (with no model gold surface). At the time of adsorption (Figure 3.10(B), identified with arrows), there is no evident spike in the RMSD data, and indeed, for the whole duration of the simulations there is no indication of significant structural changes from the control.

Similarly, a brief analysis of the RMSF data (Figure 3.10(C)) yields the same conclusion, as the residues at the adsorption site do not vary significantly from the NbVCAM1 control. This

means that the successfully adsorbed NbVCAM1 on the gold surface did not have major differences in its conformation when compared with the NbVCAM1 conformation whilst in solution. These findings support the experimental results showing that the nanobody structure and activity is preserved upon monolayer formation.

Thereafter, a deeper analysis of each individual residue allows us to infer which ones approach the surface and contribute to the NbVCAM1 adsorption (Figure 3.10(C)). As expected, higher RMSF values were seen in the amino-acids that belong to the nanobody's loops (especially the CDR3 loop starting at amino-acid 99 to 111[4, 176]) and at the N- and C-terminals. The exception is when one of these regions is underneath the nanobody and interacting with the gold surface, slightly reducing the flexibility and lowering the RMSF values compared to the control. On the other hand, some non-loop amino-acids showed slightly higher RMSF than the control, which meant that they contributed to the approach to the surface resulting in increased movement. These amino-acids were SER30, 101, 104 and 126 (serine), ASN29, 106, 108, 112, 114 (asparagine), PHE53, 105 (phenylalanine) and TYR103, 115, 126 and 129 (tyrosine). LYS (lysine)[177] and amine interaction with gold[178] has been previously reported and likewise, with intermittent contact, LYS43, 44 and 76 contributed to the NbVCAM1 immobilisation at the surface.

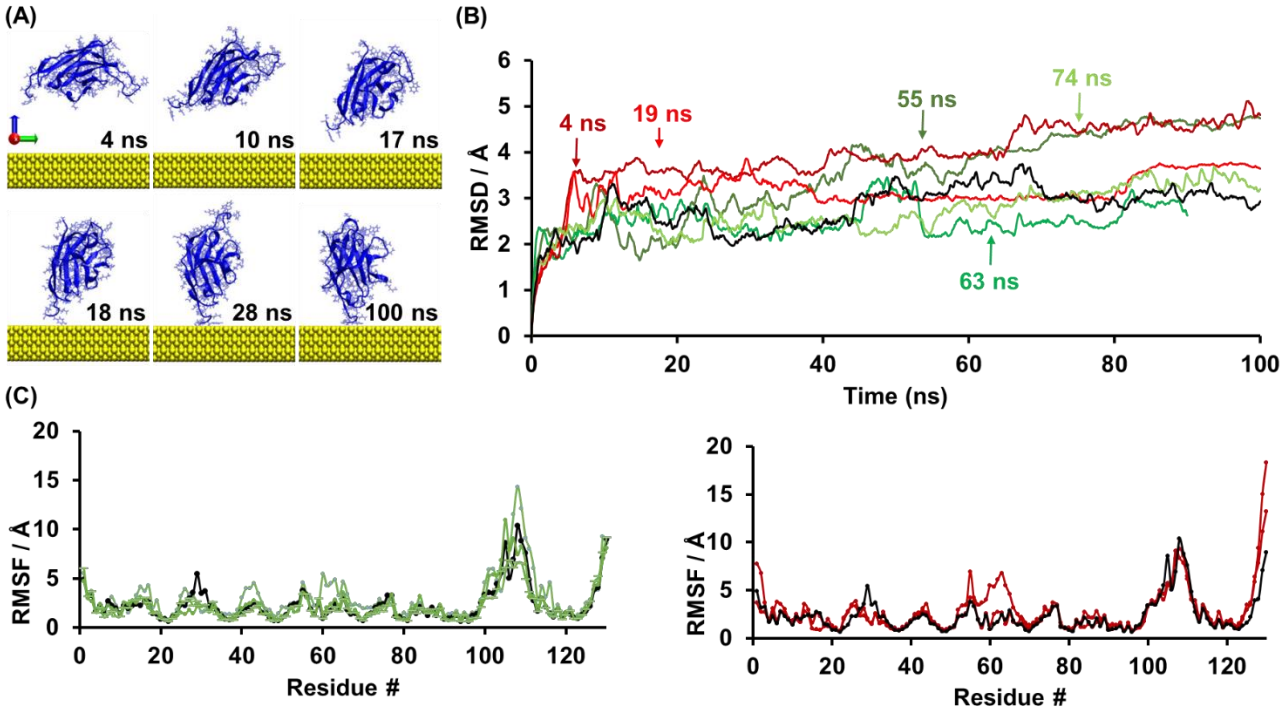

Figure 3.10 -MDS results for NbVCAM1 adsorption on gold. (A) MD results at various simulation time-points for NbVCAM1 adsorption onto the model gold surface. (B) The root-mean square (RMS) deviation for the NbVCAM1 α-carbons during the adsorption process on gold over several different trajectories of 100 ns duration. The steady trend indicates that the NbVCAM1 structure was kept before, during and after adsorption. Arrows indicate the time of adsorption in each trajectory. (C) RMS fluctuation for the same trajectories for each NbVCAM1 residue (0 to 130 residues from N to C-terminal). Residues with higher RMSF values belong to loop areas, revealing higher mobility. (B-C) In black, the control represents the trajectory of NbVCAM1 in solution while green and red colours represent NbVCAM1 that adsorbed non-oriented or oriented, respectively, onto the gold surface.

Finally, in order to understand how the adsorbed NbVCAM1 orientation might change over time, and how it might be affected by the creation of the thiolate bond, a second model was developed with NbVCAM1 tethered by a thiolate bond to the gold surface (Figure 3.11(A-B)). This model allowed us to observe the flexing of the nanobody above the surface. The simulations reveal nitrogen-gold interactions from the amino-acids (CYS130, LEU127, TYR 129r and GLN13) near to the thiolate bond site, which are involved in creating a rather tilted

orientation. It was observed that these features are also present in the simulations where the thiolate bond was not created, with additional nitrogen interactions (LYS44, 45, GLN87, ASN 84, 85, 87, 108)(Figure 3.11(C-D)). These observations further confirm earlier findings from the SIMS analysis, wherein nanobody immobilisation on the gold surface can be attributed to the simultaneous formation of a gold-thiolate bond and nitrogen-gold interactions.

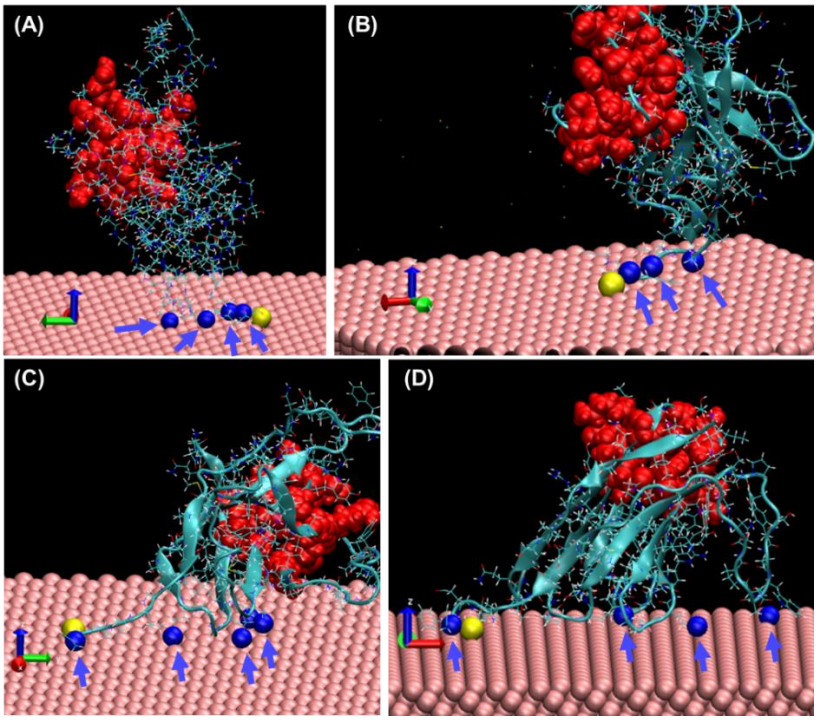

Figure 3.11 - Representative VMD images of NbVCAM1 immobilised by a thiolate bond (A-B) and physically adsorbed by the modified cysteine (C-D). Highlighted are the NbVCAM1's nitrogen-gold interactions, the sulphur at the modified cysteine (yellow) and the binding site (red). Arrows point to the closest nitrogens (blue) to the gold surface.

3.3 Conclusions and Future Work

The nanobodies' relatively small size (~15 kDa) and their prominent stability meet the highly desired characteristics when designing and developing a vast range of biosensors and diagnostic tools. In order to take advantage of these characteristics, it was hypothesized that adding a modified cysteine would promote the direct surface functionalisation on gold. This chapter's findings demonstrated, through ToF-SIMS and 3D OrbiSIMS, the formation of a thiolate bond between the NbVCAM1 nanobody and the gold surface. The secondary ion imaging results also provided compelling evidence of the formation of a homogenous, stable and well-packed nanobody monolayer.

The SPR studies confirmed the biological activity of NbVCAM1 at the surface. Furthermore, the experimental and theoretical findings of this work support the presence of a high degree of well-oriented nanobodies on the gold surface, leading to a high capacity for antigen binding. Thus, these results indicate that NbVCAM1 nanobodies are promising to investigate as building blocks for nanobody-based surfaces. Yet, when aiming for on-demand biosensing, ideally the nanobody-antigen response should be even higher. Higher responses provide capacity to include switching units at the surface which are required to provide control over sensing. When attempting to increase the signal (as a consequence of reducing possible steric hindrance) by spacing out the NbVCAM1, the antigen response suffered a decay (Figure 3.8). Such decrease was likely due to the reduction of nanobodies at the surface.

Further optimisation of this work could include the antigen injection on surfaces that have been incubated for longer times with the NbVCAM1 solution. In addition, the antigen concentration could be increased and the temperature during injection as well, in order to boost the kinetics. In terms of the diluent, different pHs, salts and addition of surfactant could perhaps have an

influence on how the nanobodies immobilize at the surface and further avoid non-specific interaction with gold. On this note, this work can not disregard the possibility for the immobilisation of non-oriented nanobodies at the surface. Indeed, the results from 3D OrbiSIMS (Figure 3.3 (H)) and MDS simulations (Figure 3.9) have demonstrated alternative orientations, based on the interactions of nitrogen species and other than cysteine amino-acids with gold, respectively. Based on these findings, future steps that aim to proceed with NbVCAM1 for dynamic surfaces should include an immobilisation strategy that excludes non-oriented nanobodies. Considering the alkyne placed at the N-terminal of the NbVCAM1, click chemistry could be a potential immobilisation method. Otherwise, the NbVCAM1 could be re-engineered to allow other controllable and specific immobilisation methods.

The relatively large size of antigen hVCAM1 (74.1 kDa) is another potential limiting factor for the signal achieved. To address this, future studies could compare nanobodies with smaller antigens to investigate the antigen's size impact on the signal. In the case of NbVCAM1, an immobilisation strategy that would allow for more distance from the surface and consequent freedom to move and adjust, could potentially allow to capture more antigens.

The strategy for nanobody immobilisation is simple and effective and will be able to be adapted to other highly relevant nanobody-antigen systems. Considering all these attributes, this work opens up new avenues for the design and scalable fabrication of stable, reliable and robust biosensing platforms for a wide range of medical, biotechnological, environmental and food applications.

Chapter 4 Studies on nanobody functionalised surfaces to maximise antigen binding

The previous findings of this research showed that the nanobody NbVCAM1 immobilised directly on the a surface through a thiolate bond resulted in a specific antigen binding response. Although these results were successful, direct immobilisation at the surface potentially included physically adsorbed randomly oriented nanobodies. Thus, likely not all the binding sites will be available to bind, limiting the full potential of antigen interaction (Figure 4.1(A)). To address this potential limitation, this chapter presents an alternative immobilisation method for NbVCAM1: the copper Cu(I) catalysed azide-alkyne cycloaddition applied between an initial azide-terminated SAM and the alkyne-terminated NbVCAM1 (NbVCAM1-LEY-C-alkyne). This approach ensures the surface is only functionalised with NbVCAM1 through their alkyne, keeping their binding site fully available (Figure 4.1(B)).

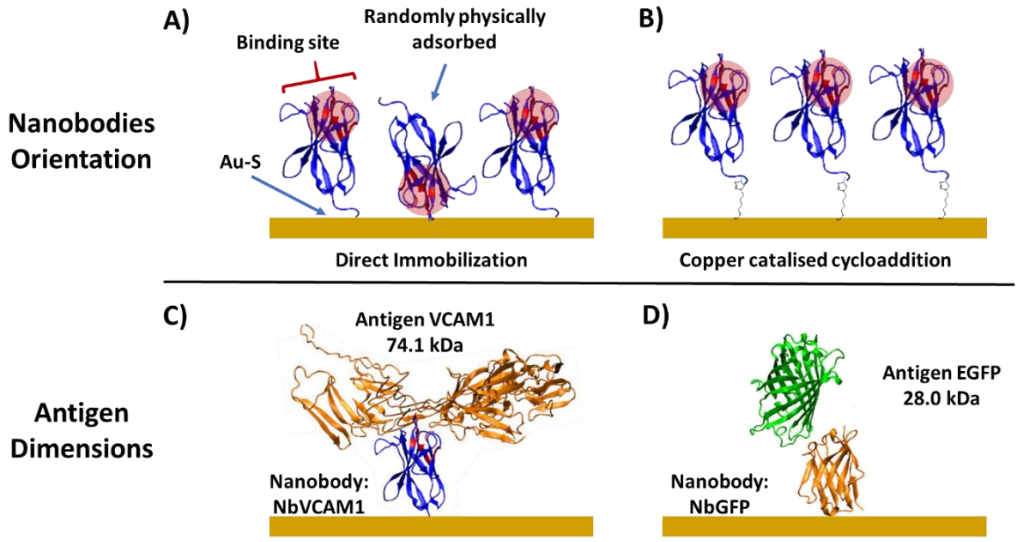

Figure 4.1 – Schematics of important factors to consider when designing nanobody-based biosensing platforms. Nanobodies orientation: (A) direct immobilisation which could result in randomly oriented nanobodies; and (B) oriented copper Cu(I) catalysed azide-alkyne cycloaddition. Antigen dimensions: (C) hVCAM1antigen with 74.1 kDa was compared with (D) EGFP antigen with 28.0 kDa.

Furthermore, this chapter demonstrates that in addition to the nanobody's orientation, the antigen dimensions is a crucial factor to consider when designing nanobody-based biosensing platforms. To assess the antigen dimensions' impact on the biosensor sensitivity, an alternative nanobody (NbGFP) with a smaller antigen (EGFP) was studied (Figure 4.1 (D)) and compared with the NbVCAM1-VCAM1 pair ((Figure 4.1 (C)).

Finally, studies involving an applied potential on NbGFP-EGFP open the opportunity to use this nanobody-antigen pair for electroswitchable nanobody-based biosensing platforms.

In this Chapter, Bárbara Simões conducted all the experimental work with exception of XPS experimental work that was conducted by David Morgan. All data was analysed by Bárbara Simões.

4.1 Introduction

High selectivity and sensitivity are crucial parameters to obtain a successful biosensor platform, and particularly important when envisioning a smart nanobody-based biosensor with switching properties. Techniques that use physisorption and covalent couplings through protein's amino acids functional groups are simple and cheap immobilisation methods, however these methods do not eliminate the chance for random orientation. The results from Chapter 3 showed the increased response from the gold surface functionalised with oriented cysteine modified NbVCAM1 through a thiolate bond when compared with unmodified NbVCAM1 that was physiosorbed and randomly oriented. Despite the nanobody binding improvement, there remains the possibility for the cysteine modified nanobody to functionalize on gold in a random orientation. Considering the need for a highly responsive surface before implementing additional properties, herein suggested to be higher than 1000 RU on the SPR, further optimisation to the NbVCAM1 immobilisation was performed.

Extensive literature has shown that optimised protein orientation improves binding efficiency[179]. More specifically, nanobodies as capture molecules in biosensing applications have been oriented to be used through sandwich assays[65, 79, 80, 87-90], with nanobodies biotinylated[65, 87, 89] and histidine tagged [65, 88, 90] and other engineered ligands in their structure[40, 54, 180]. Trilling and co-workers[54] incorporated into a nanobody azide moeities through a non natural amino acid (azidohomoalanine), either in one strategic position, or in five different positions. While the nanobodies containing one azide were "clicked" at the surface in an oriented manner, the nanobodies with five azide moeities, showing five different "clicking" options, immobilised purposely in a random manner. Using the same immobilisation method, the oriented nanobodies strongly improved the SPR sensor sensitivity compared to the ones randomly immobilised[54].

In order to guarantee the gold surface functionalised exclusively with oriented nanobodies, and taking advantage of NbVCAM1 engineered C-terminal alkyne[40] (opposite to the binding site), this chapter applies "click chemistry" as shown by Adriaensens and co-workers[149] to an azide-terminated SAM surface. Copper(I)-catalyzed Huisgen 1,3-dipolar azide - alkyne cycloaddition (CuAAC) is a "click" biocompatible reaction that specifically occurs between an azide and an alkyne moiety to form a stable 5-membered 1,2,3-triazole ring under Cu(I) catalysis and mild reaction conditions (Figure 4.2).

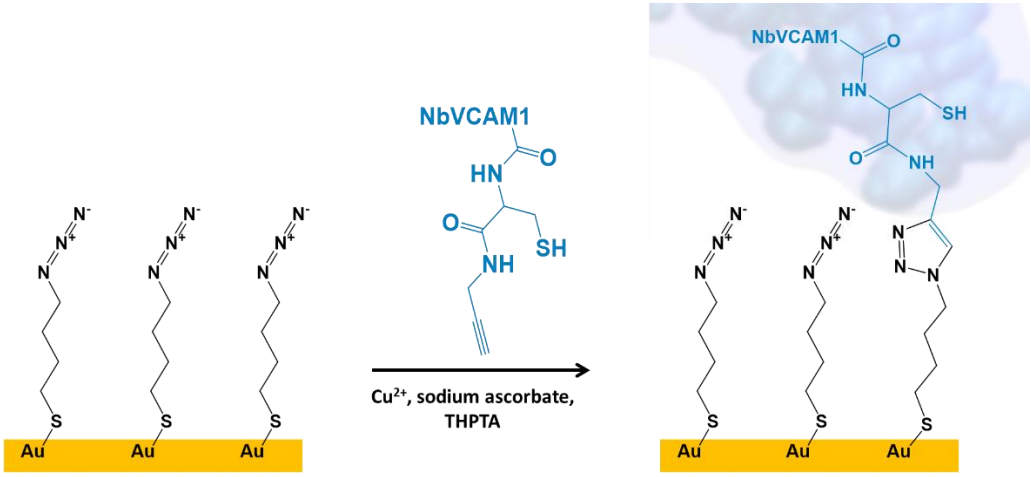

Figure 4.2 - Click chemistry: copper catalised azide-alkyne cycloaddition (CuAAc) between the azide-terminated SAM and the alkyne-terminated NbVCAM1.

Following this strategy, a protein can be coupled keeping its biological activity and with an uniform orientation to a solid substrate, resulting in highly functional and homogeneously covered surfaces. A straightforward method to determine the success of CuAAC "click chemistry" used biotin moeities "clicked" at the surface[181]. The biotinylated surface was then incubated with streptavidin bioconjugated with a dye, allowing verification of successful binding using confocal microscopy. Inspired by this example, the initial studies from this

chapter used an alkyne terminated biotin, “clicked” at the surface and then verified through injection of neutravidin on the SPR. Thereafter, the “click reaction” was applied between an azide-terminated SAM and the NbVCAM1, in order to increase the NbVCAM1-VCAM1 interaction and hence this platform sensitivity. The surfaces clicked with NbVCAM1 were characterised by ellipsometry, contact angle, x-ray photoelectron spectrometry (XPS), and surface plasmon resonance (SPR).

In addition to the nanobody orientation at the surface, the antigen dimension is also an important factor to consider when designing nanobody-based biosensor platforms. Previous studies used oligopeptide spacers to attach the nanobodies to the surface, allowing these to be simultaneously oriented and distant from the surface[67], overcoming steric hindrance that the antigen would otherwise encounter. For this research, the initial studies used the NbVCAM1-VCAM1 pair where hVCAM1 is 74.1 kDa. In order to test a smaller antigen, an alternative promising nanobody-antigen pair was used. The enhanced green fluorescent protein (EGFP) is an antigen of 28.0 kDa, and binds to the green fluorescent protein nanobody (NbGFP), a nanobody with a barrel-shaped structure (2.5 nm x 4.5 nm) and molecular weight of 13.9 kDa[182]. The NbGFP-EGFP complex has been well studied regarding their interaction[183].

Additionally, because NbGFP can be used as a universal adapter, allowing the capture of easily available GFP chimeric proteins, the NbGFP-EGFP complex was used as a model in previous SPR studies[39]. In these studies, Della Pia and co-workers[39] immobilised NbGFP through different immobilisation methods, including the covalent amino-coupling immobilisation using 1-ethyl-3-(3-dimethylaminopropyl)carbodiimide hydrochloride (EDC) and N-hydroxysuccinimide (NHS) on a surface with carboxymethylated dextran. The fact that the lysine residues of NbGFP are located at the antipode of its binding site contributes to a likely oriented immobilisation which resulted in efficient and high antigen binding[39]. Given the

favorable properties, herein the NbGFP was immobilised through the EDC/NHS amino coupling on a carboxylic-terminated SAM. Upon high antigen response (>1000 RU) on the immobilised NbGFP, this chapter further demonstrates, through SPR, NbGFP-EGFP as a potential pair to be used on switchable nanobody-based biosensor platforms.

4.2 Results and Discussion

4.2.1. Copper catalysed azide-alkyne cycloaddition (CuAAC) click chemistry

4.2.1.1. Initial azide-terminated SAM characterisation

Freshly cleaned gold chips were incubated with 4-azidobutane-1-thiol (ABT), allowing an azide-terminated SAM to form that was characterised by ellipsometry, contact angle, XPS and TOF-SIMs. The experimental thickness was measured by ellipsometry for ABT SAM and resulted in 0.47 ± 0.21 nm, smaller than the theoretical thickness for the fully stretched molecule (0.86 nm, *ChemDraw software*). The smaller experimental value for the thickness of the ABT SAM indicates a rather tilted monolayer. Additional characterisation through contact angle measurements resulted in the advancing and receding contact angle of 83.1 ± 0.90° and 69.5 ± 0.30°, the advancing angle was in agreement with the literature[184, 185]. Regarding the hysteresis of 13.6°, it could suggest an uneven packed SAM, where besides the azide groups, also the underlying alkyl groups could interact with the water at the interface. In order to further characterise the elemental composition and chemical states at the ABT SAM surfaces, these were investigated with the surface analysis technique X-ray photoelectron spectroscopy (XPS). Figure 4.3 shows a representative XPS high resolution spectra of the Au 4f, S 2p, N 1s, C 1s, and O 1s regions for the bare gold (control) and azide-terminated ABT SAM. The analysed spectra results regarding relative atomic and relative components percentages are described in Table 4.1.

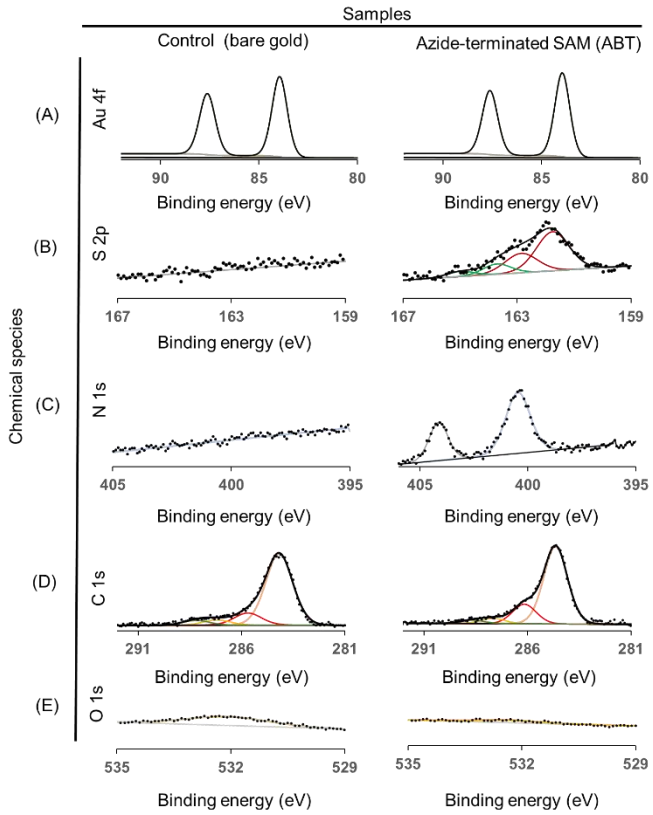

Figure 4.3 – ABT SAMs XPS results. Representative XPS high resolution spectra of the (A) Au 4f, (B) S 2p, (C) N 1s, (D) C 1s, and (E) O 1s regions for the bare gold (control) and azide-terminated ABT SAM samples. Duplicates were measured twice in different chip positions.

Table 4.1 - Relative atomic percentages and relative components percentages calculated by XPS for ABT SAM. Theoretical values were obtained considering the ABT atomic formula ($C_4H_8N_3S$-Au). Duplicates were measured twice in different chip positions.

ABT SAM surfaces

	Relative Atomic %		**Components**	**Relative Components %**	
	Experimental	**Theoretical**		**Experimental**	**Theoretical**
S	12.3 ± 1.4	12.5	**S-Au**	85.2 ± 3.9	~100.0
			S-H	14.8 ± 3.9	~0.0
N	25.7 ± 5.7	37.5	**N^+**	30.2 ± 2.1	33.3
			N, N^-	69.8 ± 2.1	66.7
C	59.1 ± 5.8	50.0	**C-C**	70.4 ± 2.1	50.0
			C-S, C-N, C-O	22.3 ± 1.7	50.0
			C=O	5.5 ± 0.7	0.0
			OC=O	residual	0.0
O	2.8 ± 1.3	0.0	**O-C**	residual	~0.0
			O=C	~100	~0.0

As expected, the bare gold controls did not show traces of either sulphur or nitrogen (as seen in Figure 4.3(B) and (C)), indicating that their presence at the ABT SAM surface was due to the formed SAM. Regarding the sulphur element, the spectra for the ABT SAM showed the presence of sulphur in two states (Figure 4.3(B)), with values according to the literature[166, 186, 187]: bound sulphur (thiolate, BE= ~162 eV) and unbound sulphur (BE= ~163-164 eV). Ideally, the ABT surfaces would not show any unbound sulphur, which indicates that the washing steps before XPS analysis could be improved.

In what concerns the nitrogen element XPS measurements Figure 4.3(C)), the different chemical states on the ABT surfaces represented by two peaks are confirmation of azide presence. While the positive environment (N^+) is visualised in one peak at higher binding energy, the peaks for the negative and neutral (N^-/N) environments overlap[188]. Theoretically, each azide moiety contains a positive, neutral and negative environment of nitrogen, meaning that their relative percentages should be 33.3% for N^+ and 66.7% for N/N^-. Table 4.1 shows that

the ABT SAM had an experimental component percentage for N^+ of 30.2 ± 2.1 % and for N/N^- of 69.8 ± 2.1 %, corresponding to the referred theoretical percentages.

With respect to carbon and oxygen XPS measurements, such elements are common to obtain as contaminants[189] when samples are exposed to atmosphere prior to analysis. This explains their presence at the bare gold controls and the presence of the carbonyl group (C=O, ~ 288.5 eV, Table 4.1, 5.5% of component C=O) and the residual oxygen (2.8%, which corresponds entirely to the carbonyl group) on the ABT SAM surfaces. Despite this, it was possible to observe on the ABT SAM an increase from 12.4% on the bare gold to 22.3% in carbon environments associated to C-OH, C-S and C-N with superposed binding energies (BEs)[186] (C-OH, C-S, C-N, ~ 286 eV), which are expected on the ABT SAM surface. All considered, the XPS data confirmed the successful formation of ABT SAM.

To further confirm the ABT SAM formation the samples were analysed by TOF-SIMS/3D OrbiSIMs techniques. Figure 4.4 shows the distinct presence of thiolate related ions (AuS^-, $AuSH^-$, $AuSCN^-$ and $AuSCNH^-$) on the ABT surface, confirming that the initial ABT SAM was formed. Furthermore, the results indicate some carbon and nitrogen contamination at the gold surface present on both samples (Figure 4.4), which is in agreement with the XPS results regarding the adventitious carbon, but not the adventitious nitrogen (Figure 4.3 (C) and (D)). Nonetheless, adventitious nitrogen should not have any implications at the SAM formation and should not compete with the thiol formation[17].

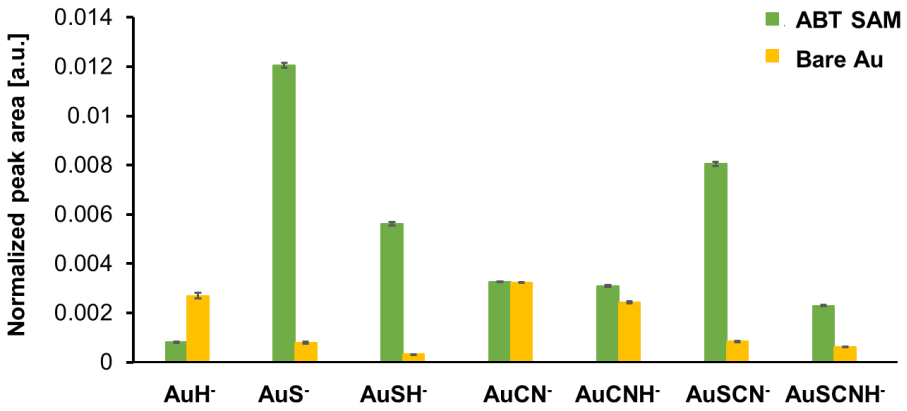

Figure 4.4 – ABT SAMs TOF-SIMs results. Peak areas comparison of gold related fragments (arbitrary units (a.u.)) between the ABT SAM surface (green) and the bare gold control (yellow). Each bar represents an average of 8 measurements, made on duplicated samples.

Following the confirmation of successfully formed ABT surfaces and their respective characterisation, the next experimental steps included applying copper-catalysed azide-alkyne cycloaddition (CuAAC) click chemistry of NbVCAM1-LEY-Cys-alkyne on the azide terminated surfaces.

4.2.1.2. NbVCAM1-LEY-Cys-alkyne on the azide-terminated SAM

Freshly formed ABT SAMs were submitted to copper-catalysed azide-alkyne cycloaddition (CuAAC) mediated click chemistry (for 45 min)[38], which allowed the click between the initial azide-terminated surface and the alkynated nanobody NbVCAM1, forming the NbVCAM1 clicked monolayer (Figure 4.5). To confirm successful click chemistry, these chips and respective controls were characterised by ellipsometry, contact angle and XPS.

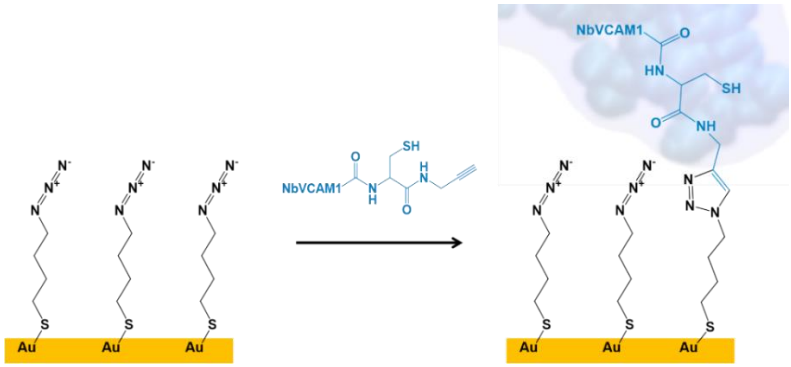

Figure 4.5 – Schematic representation of the CuAAC click between ABT SAM and NbVCAM1. The copper-catalysed azide-alkyne cycloaddition (CuAAC) click reaction allows the formation of a triazole between the azide terminated surface (ABT SAM) and the alkyne-terminated NbVCAM1 (NbVCAM1-LEY-Cis-alkyne).

The NbVCAM1 monolayer after click chemistry resulted in advancing and receding angles of 72.5 ± 1.1 º and 39.1 ± 9.1 º respectively. Both presented decreased angles from the initial azide-terminated surface (Table 4.2), suggesting the presence of NbVCAM1 at the surface.

Table 4.2 – Ellipsometric and contact angle results obtained on ABT surfaces before and after copper catalised azide-alkyne cycloaddition CuAAC click chemistry of the nanobody NbVCAM1. Experimental thickness was measured via ellipsometry, and theoretical thickness was calculated using ChemDraw software. For contact angle (CA), both advancing (Adv.) and receding (Rec.) angles were measured.

		Before click, ABT SAM	**After click, NbVCAM1 SAM**
Thickness (nm)	Theoretical	0.86	~ 6
	Experimental	0.47 ± 0.21	2.22 ± 0.81
CA (º)	Adv.	83.2 ± 0.90	72.5 ± 1.1
	Rec.	69.5 ± 0.30	39.1 ± 9.1

Furthermore, when comparing with the previously studied NbVCAM1 SAM (Chapter 3, section 3.2.1) obtained by direct immobilisation on gold, the results show similar large

hysteresis (directly on gold of 36.6 º and in this case of 33.4 º), common to protein monolayers[167]. These results are in agreement as the nanobody is intended to have identical (controlled) orientation after both immobilisation methods due to the alkyne moiety being located at the cysteine at the C-terminus[149], responsible for the thiolate bond at the surface. Therefore, it would be expected to have similar ratio between hydrophobic and hydrophilic amino-acids exposed at the N-terminal, contributing to an heterogenous surface. Additionally, it is possible to observe an overall higher advancing and receding angle after click chemistry (results for direct immobilisation for advancing and receding angles of 62.6 ± 2.3 º and 26.0 ± 6.5 º, respectively as in Chapter 3), which could indicate the exposition of unreacted azide-moeities, that could contribute to higher angles and would suggest a less packed monolayer compared to the one obtained at direct immobilisation on gold.

Concerning the experimental thickness (Table 4.2), despite the NbVCAM1 layer after click chemistry showing an increased thickness when compared with the initial ABT SAM, it also showed a big discrepancy with the theoretical values. Similarly with the findings of the previous Chapter 3, this could be explained by the presence of air voids between the nanobodies and within the nanobodies themselves[168, 169].

Overall, the ellipsometry and contact angle results, together with the previous findings (Chapter 3), suggest a successful click chemistry between the azide-terminated surface and the alkynated NbVCAM1.

In order to further characterise the elemental composition and chemical states at the surfaces before and after click chemistry, ABT and NbVCAM1 monolayer surfaces were investigated with XPS.

Figure 4.6 shows the representative obtained XPS high resolution spectra of the Au 4f, S 2p, N 1s, C 1s, and O 1s regions for the bare gold (control), ABT SAM (azide-terminated control) and NbVCAM1 clicked on ABT samples. Note that the ABT SAM XPS results were previously shown and discussed in Section 4.2.1.1, and herein repeatedly mentioned for clarity whilst the analysis. The analysed spectra results regarding experimental and theoretical relative atomic and relative components percentages for the NbVCAM1 clicked on ABT are described in Table 4.3. The theoretical values shown on Table 4.3 were based on the footprint areas of ABT (0.214 nm^2, thiol footprint[190]) and NbVCAM1 (12.4 nm^2) which allowed to calculate the theoretical ratio after click chemistry of 1 NbVCAM1 to 58 ABT molecules.

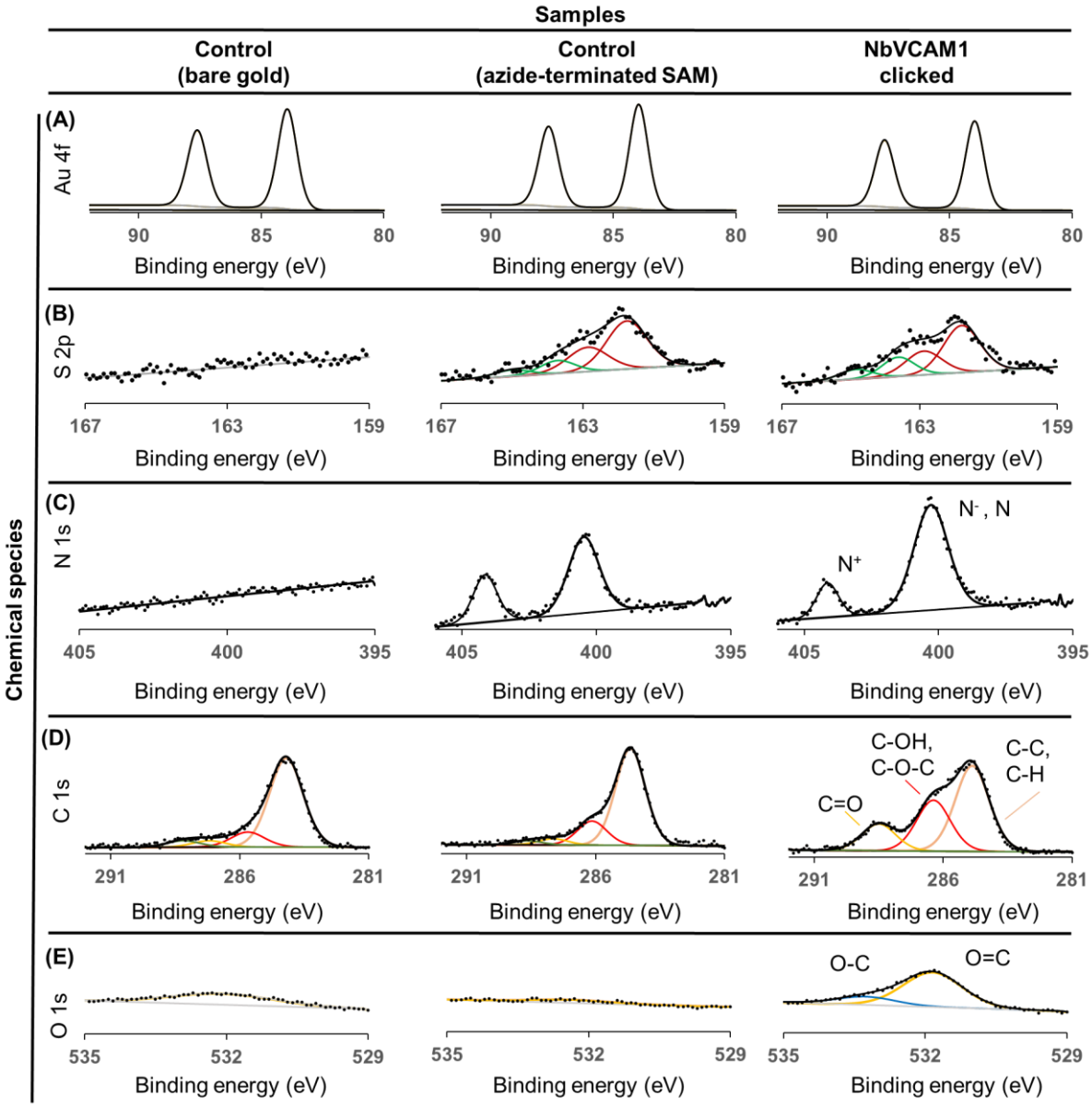

Figure 4.6 – ABT SAMs XPS results. Representative XPS high resolution spectra of the (A) Au 4f, (B) S 2p, (C) N 1s, (D) C 1s, and (E) O 1s regions for the bare gold, azide-terminated ABT SAM (controls) and NbVCAM1 clicked on ABT samples.

Table 4.3 - Relative atomic percentages and relative components percentages calculated by XPS for NbVCAM1 after click chemistry. Theoretical values were obtained considering the atomic formulas of the SAM molecules, and assuming a theoretical ratio of 1:58 Nb:ABT (obtained from footprints) obtained after click chemistry. Duplicates were measure twice in different chip positions.

Clicked NbVCAM1 surfaces					
	Relative Atomic %			**Relative Components %**	
	Experimental	**Theoretical 1 Nb: 58 ABT**		**Experimental**	**Theoretical 1 Nb: 58 ABT**
S	6.6 ± 0.1	4.4	**S-Au**	81.6 ± 3.8	89.2
			S-H, S-S, S-C	18.4 ± 3.8	10.8
N	20.4 ± 0.5	23.6	**N^+**	17.2 ± 1	19.5
			N, N^-	82.8 ± 1	80.5
C	60.4 ± 0.1	58.5	**C-C**	53.0 ± 0.6	44.9
			C-S, C-N, C-O	30.6 ± 0.4	37.0
			C=O	16.4 ± 0.2	17.0
			OC=O	residual	1.0
O	12.7 ± 0.5	13.4	**O-C**	17.0 ± 1.7	21.2
			O=C	83.0 ± 1.7	78.8

Regarding the sulphur element, the spectra for the NbVCAM1 monolayer showed the presence of sulphur in two states (Figure 4.6(B) for NbVCAM1), with values according to the literature[166, 186, 187]: bounded sulphur (thiolate, BE= ~162 eV) and unbounded sulphur (BE= ~163-164 eV). On the NbVCAM1 monolayer some unbound sulphurs are expected, originating from the nanobody methionine amino-acids. Additionally, some sulphur peak attenuation was observed when comparing both ABT and clicked NbVCAM1 spectra Figure 4.6(B)) (attenuation also observed on the gold spectra, Figure 4.6(A)). Such an effect has been previously reported and varies with the thickness of the samples analysed[191], making substrate elements less reliable to use in element ratios.

In what concerns the nitrogen element XPS measurements (Figure 4.6(C)), as previously mentioned, the azide moiety can be identified through its positive, negative and neutral environment. Upon click chemistry, the azide moiety forms an 5-membered 1,2,3-triazole ring, loosing its positive environment. Despite this, the complete disappearance of the positive nitrogen environment was not expected due to the NbVCAM1 size and the NbVCAM's own contribution with positive nitrogens (with origin from a final neutral pH). Considering the theoretical ratio after click chemistry of 1 NbVCAM1 to 58 ABT molecules, and knowing the balance between the N^+ disappearance due to the click chemistry, and the nitrogen gain (both positive and neutral environments) from the new clicked nanobody (which has likely positive lysines and arginines at pH 7.4[192]) it was possible to calculate theoretically the relative percentage of 19.2% for the N^+ and 80.8% for N/ N^-. The spectra from

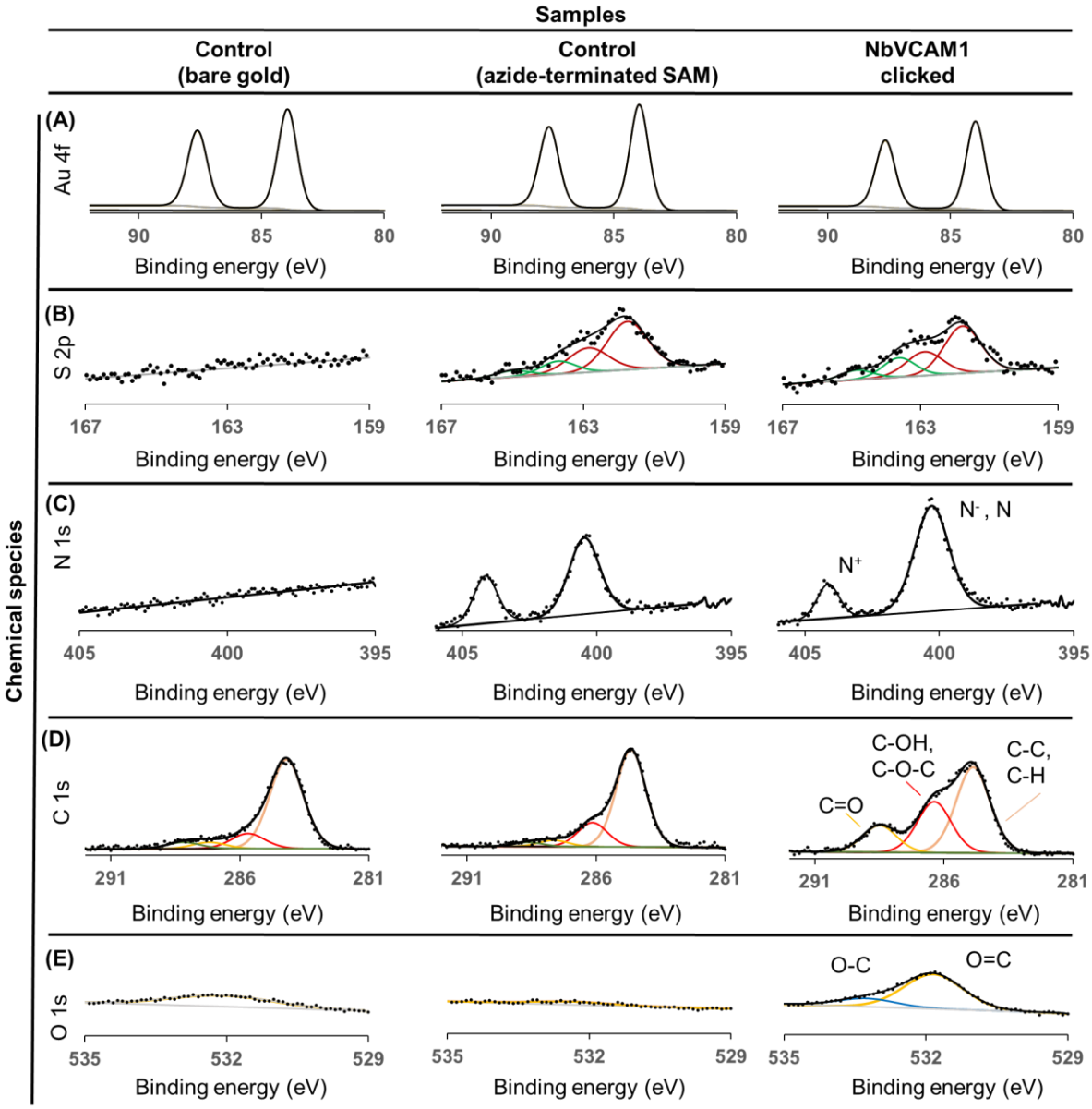

Figure 4.6(C) clearly shows the peak differences before and after click chemistry for the nitrogen environments. The experimental results were approximately 17.2 % and 82.8 % for N^+ and N/N^- respectively (Table 4.3, clicked NbVCAM1) suggesting that NbVCAM1 was successfully clicked at the surface.

In respect to carbon and oxygen XPS measurements, even though expected as contaminants at the surface[189], it was possible to observe an overall increase in carbon environments, especially

associated to the carbonyl group (C=O, ~ 288.5 eV, in Table 4.3, component C=O from 5.5% on ABT SAM to 16% on NbVCAM1 SAM), and the C-OH, C-S and C-N environments with superposed binding energies (BEs)[186] (C-OH, C-S, C-N, ~ 286 eV and C-C, 284.8 eV). Similarly, regarding oxygen presence, it was possible to observe an increase in both environments (O-C and O=C) with respective BEs of 533.1 eV and 531.3 eV[193].

A deeper but simplistic analysis could use the molecular formulas for ABT ($C_4H_9N_3S$) and for the NbVCAM1 ($C_{632}H_{941}N_{175}O_{198}S_7$) which allow to write the Equation 4.1 and Equation 4.2, whereas N_{Nb}, N_{ABT} represent the peak area of nitrogen while S_{Nb} and S_{ABT} represent the area of sulphur, for the NbVCAM1 and ABT respectively. The XPS output regarding the total areas for the elements nitrogen and sulphur, are the sum of the areas of the respective elements from the NbVCAM1 and the ABT moiety (Equation 4.3 and Equation 4.4).

$$N_{Nb} = \frac{175}{7} S_{Nb} \qquad \text{Equation 4.1}$$

$$N_{ABT} = 3S_{ABT} \qquad \text{Equation 4.2}$$

$$N_{total} = N_{Nb} + N_{ABT} \qquad \text{Equation 4.3}$$

$$S_{total} = S_{Nb} + S_{ABT} \qquad \text{Equation 4.4}$$

The resultant Equation 4.5 solves in order to the sulphur area for NbVCAM1 (see Section 6.4.3.1). Additionally, knowing that the NbVCAM1 has 7 sulphurs, while ABT has 1, it is

possible to write Equation 4.6, which gives the experimental ratio between the compounds of the SAM at the surface.

$$S_{Nb} = \frac{N_{total} - 3S_{total}}{22} \qquad \text{Equation 4.5}$$

$$Ratio\ between\ Nanobody\ and\ ABT = \frac{S_{Nb}}{7\ S_{ABT}} \qquad \text{Equation 4.6}$$

Table 4.4 shows the experimental ratios between nanobody and ABT. The results indicate that for each nanobody clicked there were ~ 1903 ABT moieties (or 1 NbVCAM1 per ~ 406 nm^2), with a considerable high coefficient of variability (CV = 37%). This CV is high due to the amplification of error from the calculation of the sulphur relative to the NbVCAM1 (S_{Nb} in Equation 4.5). In addition to the amplification of error, it is important to mention the uncertainty associated with these simplified equations and the quantitative resolution of the XPS measurements (taken at the takeoff angle of 70°) which depends on the thickness of the clicked NbVCAM1. The attenuation of deeper photoelectrons increases exponentially with the increasing protein layer thickness[191]. For instance, previously published work on a monolayer of 4 nm on gold could only detect bound sulfur with a takeoff angle of 0°, whilst increasing substantially the detection of nitrogen (closer to the upper surface) with higher takeoff angles[194]. Thus, the results shown in Table 4.4 must be considered as solely for indication, and potentially inaccurate.

Nevertheless, with possibly a more disperse NbVCAM1 clicked on the ABT SAM compared with the NbVCAM1 directly immobilised on gold (Chapter 3, Section 3.2.2) with a density of 1 NbVCAM1 per 13 nm^2, these results indicate that the click chemistry for 45 min has been successful. Additionally, with potential to be further optimised, for instance with an increase in the reaction time (motivated by supplementary data on preliminary CuAAc studies with biotin-PEG on azide SAMs, Section 4.4.1).

Table 4.4 – Theoretical and experimental ratio between the NbVCAM1 nanobodies and the ABT molecules at the surface. The theoretical ratio was based on the footprint areas of both ABT and NbVCAM1 nanobodies. The experimental ratio obtained based on XPS data for sulphur and nitrogen species.

$$\textbf{Ratio between Nanobody and ABT} = \frac{S_{Nb}}{7\,S_{ABT}}$$

Theoretical	1/58
Experimental	1/ (1903 ± 709)

Overall, the results of contact angle, ellipsometry and XPS were reassuring regarding the successful formation of the initial ABT SAM and thereafter the NbVCAM1 monolayer *via* click chemistry. Confirmation of the clicked NbVCAM1 monolayers could now be tested with SPR studies and further optimised. These studies were performed to increase further the optimal ratio of nanobody at the surface towards maximum antigen binding. The antigen hVCAM1 was injected on the NbVCAM1-terminated surfaces that were controlled via incubation time and the initial SAM surface (studies motivated by Supplementary data, Section 4.4.1, Figure 4.15 that showed a positive impact by performing click on mixed initial azide monolayers, characterised in Table 4.8).

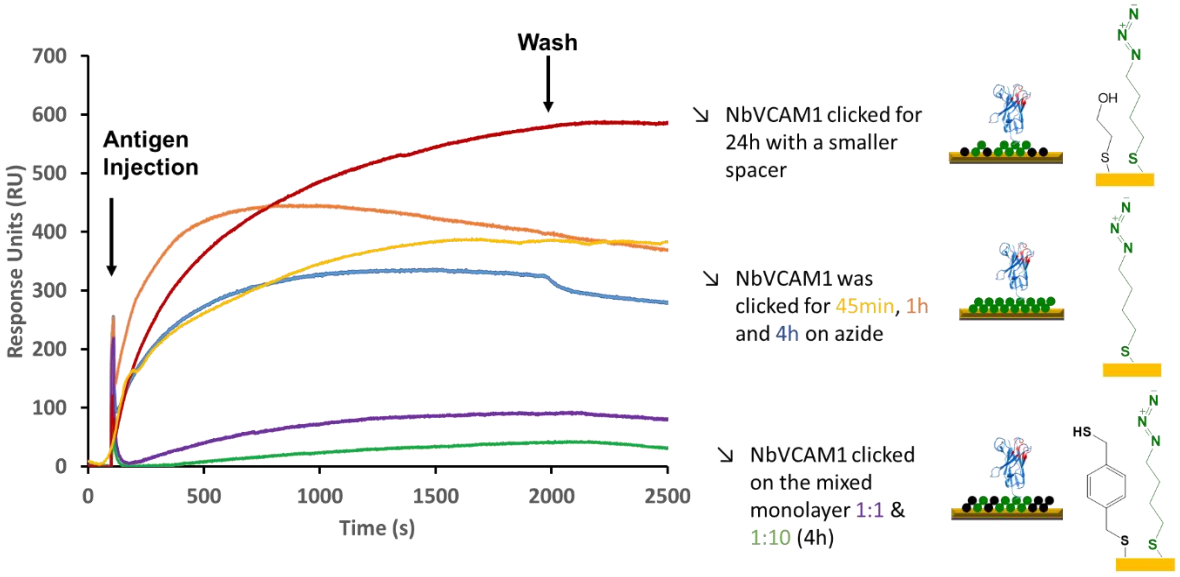

Figure 4.7 - SPR sensorgram for hVCAM1 antigen immobilisation on NbVCAM1 monolayers. The NbVCAM1 monolayer was obtained through different conditions upon CuAAc click chemistry: with different initial surfaces of either ABT or ABT mixed with BDMT or 2ME, and different incubation times.

On the ABT surfaces, the results showed that after 4 h of click chemistry (Figure 4.7, blue line), the antigen binding was not higher than after 45 min, or 1 h, (Figure 4.7, yellow and orange lines) and actually decreased by ~100 RU. These results suggest that incubation time did not improve antigen binding and that the click chemistry has reached a plateau under those conditions likely due to steric hindrance between the ABT moeities. On the mixed ABT:BMDT SAMs, the results revealed low antigen binding (Figure 4.7, purple and green lines). This was unlike studies done with the alkyne-PEG4-biotin molecules clicked on ABT:BMDT SAMs which showed improvement from neutravidin binding (Supplementary Data, Section 4.2.1, Figure 4.15). These results demonstrated that the azide moiety was not covered by BDMT and could be exposed to react upon CuAAc click chemistry with the alkyne-PEG4-biotin. However, the alkyne-PEG4-biotin molecules are low molecular weight and linear structures, differing from a bulky nanobody (14.5 kDa). When mixed with the BDMT molecule, the NbVCAM1

was potentially unable to reach the ABT moiety, leading to unsuccessful click chemistry and consequent low antigen binding.

To confirm that the NbVCAM1-antigen binding could still be improved by spacing the azide moeities, the smaller spacer 2-mercaptoethanol moiety (2ME) was chosen, aiming to guarantee that the spaced azide moieties could react upon CuAAC click chemistry (Figure 4.7, red line). On this note, the incubation time was also increased to 24h to increase the chances of NbVCAM1 reacting with the available azide moieties. The 2ME spacer improved the antigen binding at the surface, to about 600 RU (Figure 4.7, red line) which was higher than the ~ 400 RU obtained from the NbVCAM1 clicked on the ABT SAM (Figure 4.7, orange and yellow lines). These results indicate that the spacer was successful in exposing the azide moieties to the NbVCAM1, and that a less packed NbVCAM1 could bind more antigen.

Figure 4.8 (A) shows that despite the increased antigen hVCAM1 immobilisation obtained on the latest CuAAC click conditions, the obtained antigen binding results from the oriented clicked NbVCAM1 immobilisation showed similar response when comparing with the strategy of the direct immobilisation on gold, both about 600 RU, which means that 4.88×10^9 hVCAM1antigens per mm^2 were immobilised. Both immobilisations of NbVCAM1 reached a maximum value for antigen binding of ~600 RU (approximately half of the theoretical value for packed antigen immobilisation). On both methods, different nanobody densities at the surface did not improve the overall antigen binding. These results indicate a possible limitation from the antigen itself considering its large dimensions (74.1 kDa and estimated 99.1 nm^2 footprint area, see Figure 4.8) and potential consequent steric hindrance.

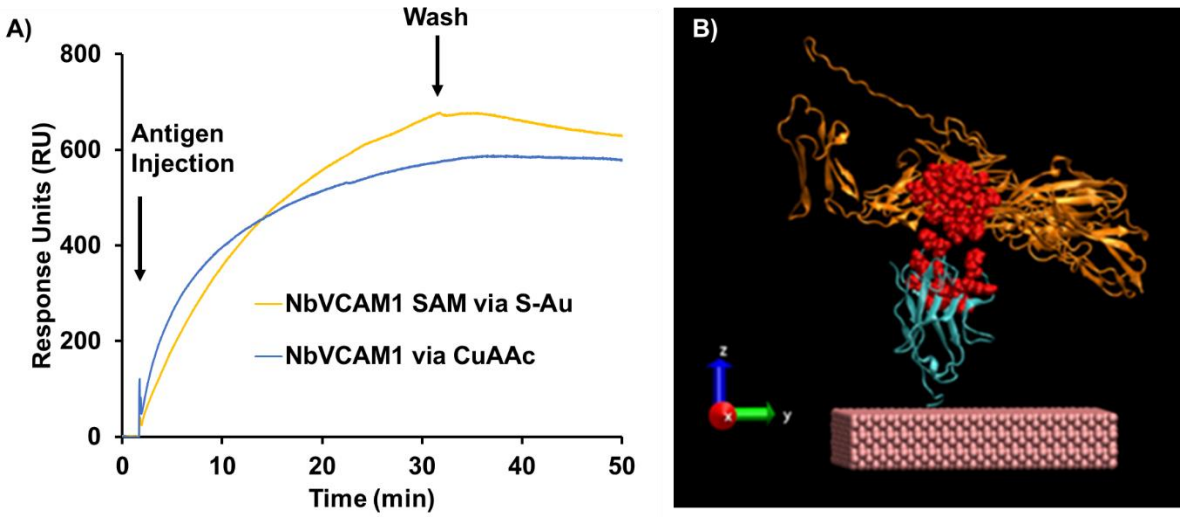

Figure 4.8 –Direct SAM vs CuAAc click chemistry immobilisation on gold of NbVCAM1 nanobodies. A) SPR sensorgram for antigen hVCAM1 binding on NbVCAM1 immobilised either via direct incubation on gold (yellow) or via CuAAC click chemistry (blue). B) Visual molecular dynamics (VMD) side-view representation of the potential binding between NbVCAM1 (blue) and hVCAM1 (orange), with their respective binding site highlighted in red.

Summarising, herein CuAAc click chemistry was successfully applied on the NbVCAM1-LEY-Cys-alkyne, which resulted in a binding response of ~ 600 RU, identical to the response obtained with its direct immobilisation on gold (demonstrated on the previous Chapter 3). In order to maximize further the nanobody-antigen binding efficiency other immobilisation methods could be applied.

4.2.2. **Amino coupling immobilisation through EDC/NHS**

The amino coupling method 1-ethyl-3-(3-dimethylaminopropyl)carbodiimidehydrochloride/N-hydroxysuccinimide (EDC/NHS), allows the external primary amino groups of the protein of interest to react to the NHS-ester active groups of an initial carboxylic acid-terminated monolayer. As an alternative method to the ones previously presented in this thesis for

nanobody-functionalised surfaces, this approach generates randomly orientated immobilisation dependent on the location of the amino-groups at the nanobody's surface. Previous studies have shown promising results for the nanobody NbGFP-EGFP antigen binding, after NbGFP immobilisation on a gold surface covered with a carboxymethylated dextran layer through EDC/NHS[39]. Based on these, it was hypothesized that the EDC/NHS coupling of the same nanobody on a carboxylic-acid terminated SAM would result on the nanobody-antigen binding maximisation needed towards switching nanobody-based biosensing platforms.

4.2.2.1. Initial carboxylic-acid terminated SAM characterisation

The initial carboxylic-acid terminated SAM protocol was optimised following two different methods for comparison. While in method (1) fresh gold clean chips were incubated with mercapto-undecanoic acid (MUA) in ethanol, in method (2) the chips were incubated with MUA in a mixture of ethanol and trifluoroacetic acid (TFA) 3% (v/v) as an improved method (Experimental Procedure, Section 6.3.2.4). Differently to method (1), the improved method (2) allowed for the disruption of interplane hydrogen bonds, as demonstrated in previous studies[195], which would likely reduce the EDC/NHS reaction. The chips functionalised with MUA SAMs were measured for their thickness and contact angle (Table 4.5).

Table 4.5 – Ellipsometric and contact angle results for MUA SAMs obtained with different methods. The data is presented as the average and standard deviation of two measurements in different locations of each chip, being each method done in triplicates.

MUA SAM		**Method (1)**	**Improved method (2)**
Thickness (nm)	Theoretical	1.56	
	Experimental	0.99 ± 0.15	1.15 ± 0.16
CA (º)	Adv.	49.9 ± 7.7	21.6 ± 2.7
	Rec.	15.0 ± 5.3	7.2 ± 1.2

Ellipsometric data (Table 4.5) showed for the improved method (2) a thickness of 1.15 ± 0.16 nm for the MUA SAM, 14 % higher than the thickness obtained from method (1) and lower than the theoretical value (1.56 nm for the straight molecule, ChemDraw software), but in agreement with the literature[196]. The contact angle data revealed for the improved method (2) a hydrophilic surface with advancing and receding angles of 21.6 ± 2.7 º and 7.2 ± 1.2 º respectively, which indicates a fairly organized monolayer at the surface (hysteresis of 14.4 º). These results showed a better organized MUA SAM, in comparison with the method (1) that had a considerably higher hysteresis (34.9 º). The fact that method (1) reports high contact angles, but low thickness, of 0.99 ± 0.15 nm, does not seem entirely explained by the formed double layers described in previous studies[195], which reported thickness up to 3 nm. Unless partial double layers could have been formed simultaneously at a low coverage. It was hypothesized that a rather disperse initial SAM layer was formed (Figure 4.9 (2)). This could be a consequence of hydrogen bond interactions within the carboxylic groups of the thiolate molecules, which are limiting the initial SAM formation in a packed manner. This could justify the lower thickness and higher contact angles due to bent aliphatic chains.

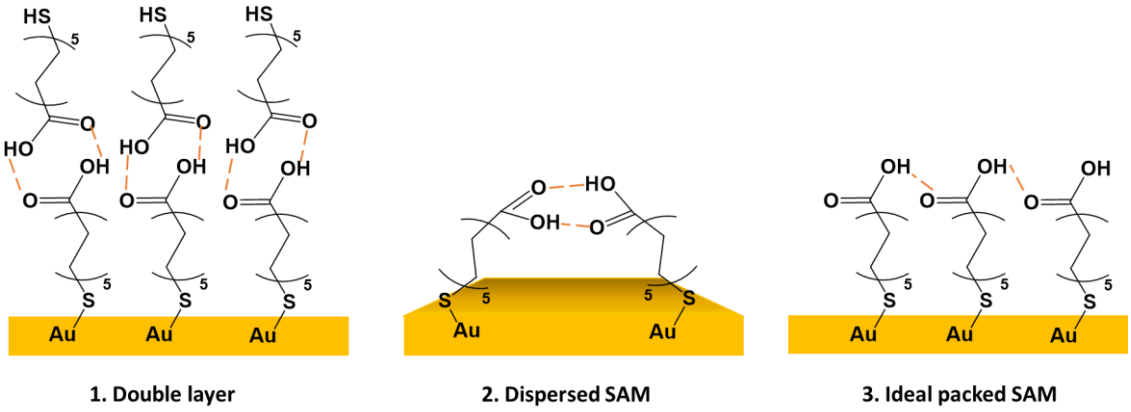

Figure 4.9 – Different outcomes for different methods towards MUA SAM formation. 1) Double layer formation as consequence of interplanar hydrogen interactions[195]; 2) Disperse initial monolayer, consequence of hydrogen interactions between thiolate molecules; 3) Ideally packed MUA SAM..

4.2.2.2. NbGFP immobilisation

NbGFP-EGFP antigen binding after NbGFP immobilisation via NHS/EDC has been successful in the past[39] and motivated investigation into the same method and nanobody to immobilize on a carboxylic-acid terminated SAM.

Freshly formed MUA SAMs through the improved method (2) previously described (see Section 4.2.2.1) were used to immobilize the green fluorescent protein nanobody (NbGFP, 13.9 kDa) onto the surface via NHS/EDC.

The previously reported EDC/NHS applied to NbGFP was only investigated between the pH range 4-6[39]. Preliminary studies with lysozyme (similar in size and isoelectric point to NbGFP, Supplementary data, Section 4.4.1) have shown preferential electrostatic attraction to the surface at higher pHs. These studies motivated the testing of higher pH conditions (7 and 8) in addition to the optimal reported pH (5.4)[39].

SPR allowed real-time monitoring of the full nanobody immobilisation at different pH conditions: pH 5.4, 7 and 8, and thereafter the antigen enhanced green fluorescent protein (EGFP, 28 kDa) binding. Table 4.6 shows the SPR response obtained for the NbGFP immobilisation at each different pH condition, and the respective response obtained by the antigen that bound to the resulting surface.

Table 4.6 – NHS/EDC coupling of NbGFP and respective antigen EGFP (100 nM) binding: optimisation conditions. Conditions tested included EDC/NHS coupling pH at 5.4, 7.4 and 8.0. Even though higher pH coupling conditions led to a higher NbGFP immobilisation, they did not result in higher posterior antigen binding.

coupling pH	NbGFP (50 μg/mL) response (RU)	EGFP (100 nM) response (RU)
8.0	3332	591
7.4	3300	250
5.4	2203	1151

It was possible to observe that indeed at pH 7.4 and 8.0 there was a higher immobilisation of NbGFP, as both responses were approximately 50% higher than the response obtained with pH 5.4 (Table 4.6). Interestingly, even though pH 7.4 and pH 8 only differ by 32 RU at the NbGFP immobilisation, pH 8 led to more than double the response from the antigen bound to the surface (Table 4.6, EGFP response), possibly due to more favourable nanobody orientation at the surface. The lowest immobilisation of nanobody happened at pH 5.4, potentially due to less -NH_2 available and less electrostatic interactions. Despite the lowest nanobody immobilised at pH 5.4 (approximately 1 NbGFP per 10 nm^2, based on 1000 RU being equivalent to a change in surface concentration of approximately 1 ng/mm^2 [20]), it resulted in 1.9 fold and 4.6 fold the antigen bound to the NbGFP that was immobilised at pH 8 and 7.4 respectively (Table 4.6 EGFP response). The results suggest that at higher pHs the high nanobody immobilisation lead

to steric hindrance at the surface, not allowing the antigen EGFP to bind. The result obtained at pH 5.4 described in Table 4.6 can be seen in Figure 4.10 (A), (orange line), which represents the workflow followed with all the tested pH conditions.

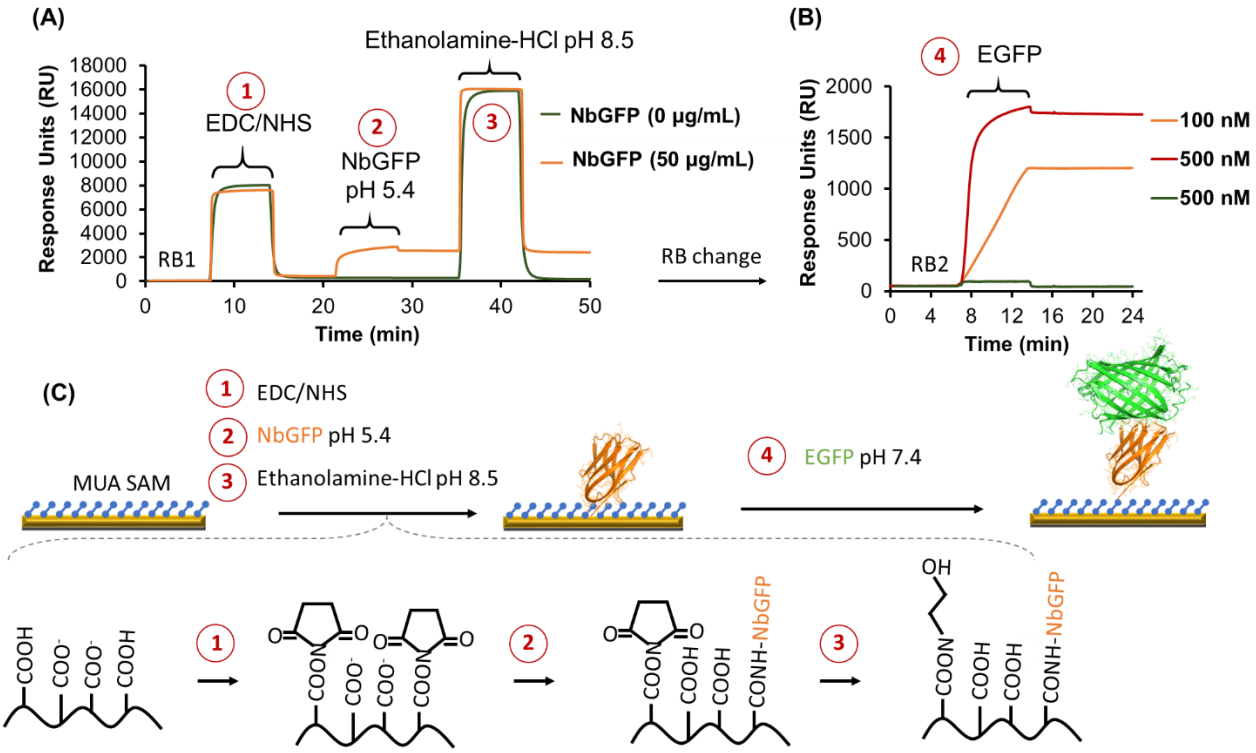

Figure 4.10 – SPR sensorgram results and schematics for NbGFP immobilisation via EDC/NHS followed by antigen injection. (A) Overview of NbGFP (13.9 kDa) immobilisation at pH 5.4, starting the program with a stabilised trace with running buffer (RB1, pH 5.4) over a chip functionalised with MUA; then injection of 0.4 EDC/0.1 NHS (1:1) followed by RB1; and NbGFP injection (in orange at 50 µg/mL, and in green at 0 µg/mL as a control) followed by RB1; then ethanolamine-HCl 1M pH 8.5 injection followed by RB1 until stabilised, which was then changed to RB2 (HEPES, pH 7.4). (B) The continuation traces from the initial stabilisation with RB2 which follows EGFP antigen injections response (500 nM and 100 nM, orange and red respectively, on the NbGFP functionalised surface and 500 nM on a control surface (EDC/NHS with ethanolamine), green). (C) Representative schematics of the NHS/EDC amino coupling of NbGFP (orange) at the MUA (blue) surface followed by EGFP (green) injection.

Similarly to the previous studies with lysozyme (see Experimental Procedures, Section 6.4.6.5), initially a stable baseline was achieved with the first running buffer (RB1, either sodium acetate, pH 5.4 (Figure 4.10(A)) or sodium phosphate, pH 7.4 or 8.0, all buffers $[Na^+]$=10 mM). Then, an injection of water mixture of EDC/NHS allowed the surface activation, following thereafter the incubation with NbGFP 50 µg/mL which was dissolved in the respective running buffer (in the case of the control sample, this step included buffer without NbGFP). After deactivation of any remaining unreacted NHS esters with ethanolamine 1M pH 8.5, the new baseline with the immobilised NbGFP was allowed to stabilise, before changing the running buffer to HEPES 10 mM, NaCl 0.15 M, 0.05% Tween 20, pH 7.4, the second running buffer (RB2). With the new stable baseline (Figure 4.10 (B)), the antigen EGFP (100 nM or 500 nM) was injected on the surface, binding the immobilised NbGFP. It was possible to observe that with an injection of antigen at 100 nM, the response trend did not reach a saturation point, suggesting that a higher concentration could lead to a higher response. Saturation was seen with the 500 nM injection achieving 1672 RU, which means that 1 EGFP antigens per approximately 28 nm^2 were captured (based on 1000 RU being equivalent to a change in surface concentration of approximately 1 ng/mm^2 [20], results shown in Table 4.7, EGFP response). The response obtained of 1672 RU at saturation provided the amplitude required from the nanobody-antigen interaction before increasing complexity towards the design of a switchable nanobody-based platform. With a response higher than 1000 RU, NbGFP can be considered a good candidate for further sensor design.

Table 4.7 - Results for NbGFP immobilisation via NHS/EDC at pH 5.4 and posterior antigen binding response. At pH 5.4 after NbGFP immobilisation, two concentrations of antigen were injected: 100 nM and 500 nM, resulting in an increase of response, indicating that with 100 nM the surface was yet not saturated. Regarding the control, the lack of NbGFP injection resulted in residual antigen response.

NbGFP injection (μg/mL)	NbGFP response (RU)	EGFP injection (nM)	EGFP response (RU)
0	Residual	100	Residual
50	2203	100	1151
50	2363	500	1672

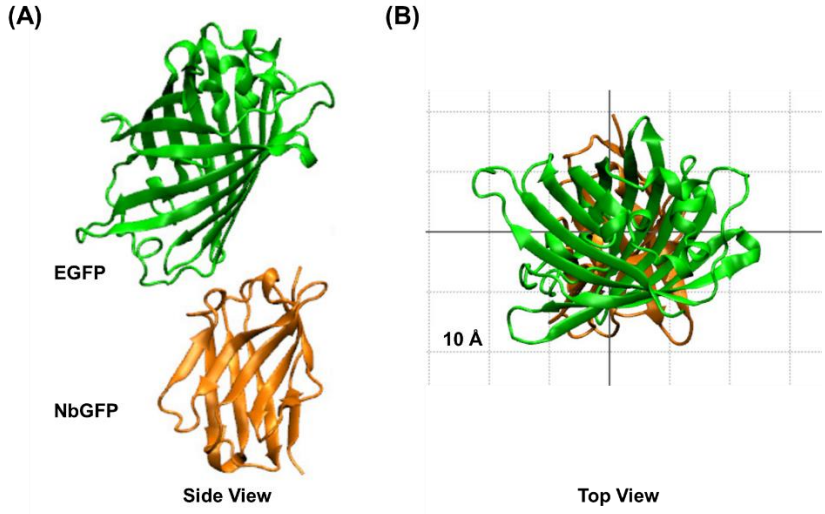

Figure 4.11 – Visual molecular dynamics (VMD) of NbGFP-EGFP interaction. (A) side view and (B) top view of NbGFP (in orange)-EGFP (in green) interaction. Protein data base (PDB) files obtained from the NCBI data base, which then were treated on VMD. Grid scale: 1 nm

Considering the response of NbGFP immobilisation and the antigen (and knowing that 1000 RU = 1 ng/mm^2), the data shows that 35% of the immobilised nanobodies bound to the antigen. Knowing the NbGFP-EGFP dimensions[39] and interaction[183], as seen in Figure 4.11 (B) which indicates from the top view a footprint area of roughly 20 nm^2, it was possible to estimate that

72% of the surface was occupied by the antigen, showing a highly efficient antigen immobilisation.

Overall, the response obtained with the NbGFP-EGFP system of above 1500 RU meets the required initial response from antigen binding suggested in this thesis (>1000 RU). Once meeting the criteria, the following studies with the NbGFP as potential candidate for electrically switching nanobody-based biosensing platforms should include the investigation on nanobody stability upon applied potential at the surface.

4.2.3. **Stability of NbGFP-EGFP on gold surfaces under applied potential**

Conductive surfaces functionalised with nanobodies that can efficiently immobilize the targeted antigen represent platforms with great potential to be used in electrically-activated on demand biosensing. The previous section showed the optimal conditions to target EGFP, achieving a high range of response on the SPR. Such results were encouraging to investigate how well the NbGFP-EGFP system would respond to applied potential at the surface. The optimal EDC/NHS conditions previously reported (pH 5.4) were performed under open circuit (OC) on a standard SPR cell. To undertake electrochemical studies, an SPR electrochemical cell (E-cell|) must be used with a higher volume capacity to accommodate the counter electrode (see Experimental Procedures, section 6.4.6.6). Therefore, the previous conditions were first transferred to the E-cell, to compare under OC and verify the identical range of response to the standard cell (Figure 4.12 (A), blue and black lines). Thereafter, the experiment at the E-cell was repeated, this time applying positive potential of + 0.3V during the antigen binding step. It was possible to verify that the positive potential did not affect the NbGFP-EGFP binding (Figure 4.12 (B, green line), suggesting that NbGFP keeps its biological function under a positive potential environment. By

keeping its biological function, one can conclude that its structure was robust enough to not denature at positive potentials and maintained its binding site intact and available.

Furthermore, initial control tests were performed to surfaces of positively charged molecules such as C5K, that are composed by 5 lysines (Figure 4.12 (B), represented by a chemDraw structure). The response during the injection of antigen on these C5K under + 0.3 V was about 200 RU, a result of the flowing bulky solution, which then recovered to the initial baseline once the injection ended (Figure 4.12 (B), orange line). The lack of response increase from the EGFP injection indicates the absence of non-specific interactions with the C5K surface under positive applied potential. These results open the opportunity for this system to be used in the future, towards on-demand biosensing. In future studies, oligopeptides similar to C5K, immobilised together with NbGFP, could be used to cover the nanobody, upon positive potential, avoiding NbGF-EGFP binding and other non-specific interactions. For on-demand EGFP sensing, a negative potential could retract these C5K-like structures, uncovering the NbGFP's binding site and allowing the NbGFP-EGFP binding.

Thereafter, the same experiment was performed this time under negative potential (-0.4V) to understand if NbGFP could also retain its biological function at those conditions (Figure 4.12 (C), red line). The binding response appeared to be comparable to the one obtained under positive potential, also indicating the robust capacity of NbGFP binding to EGFP under negative potential.

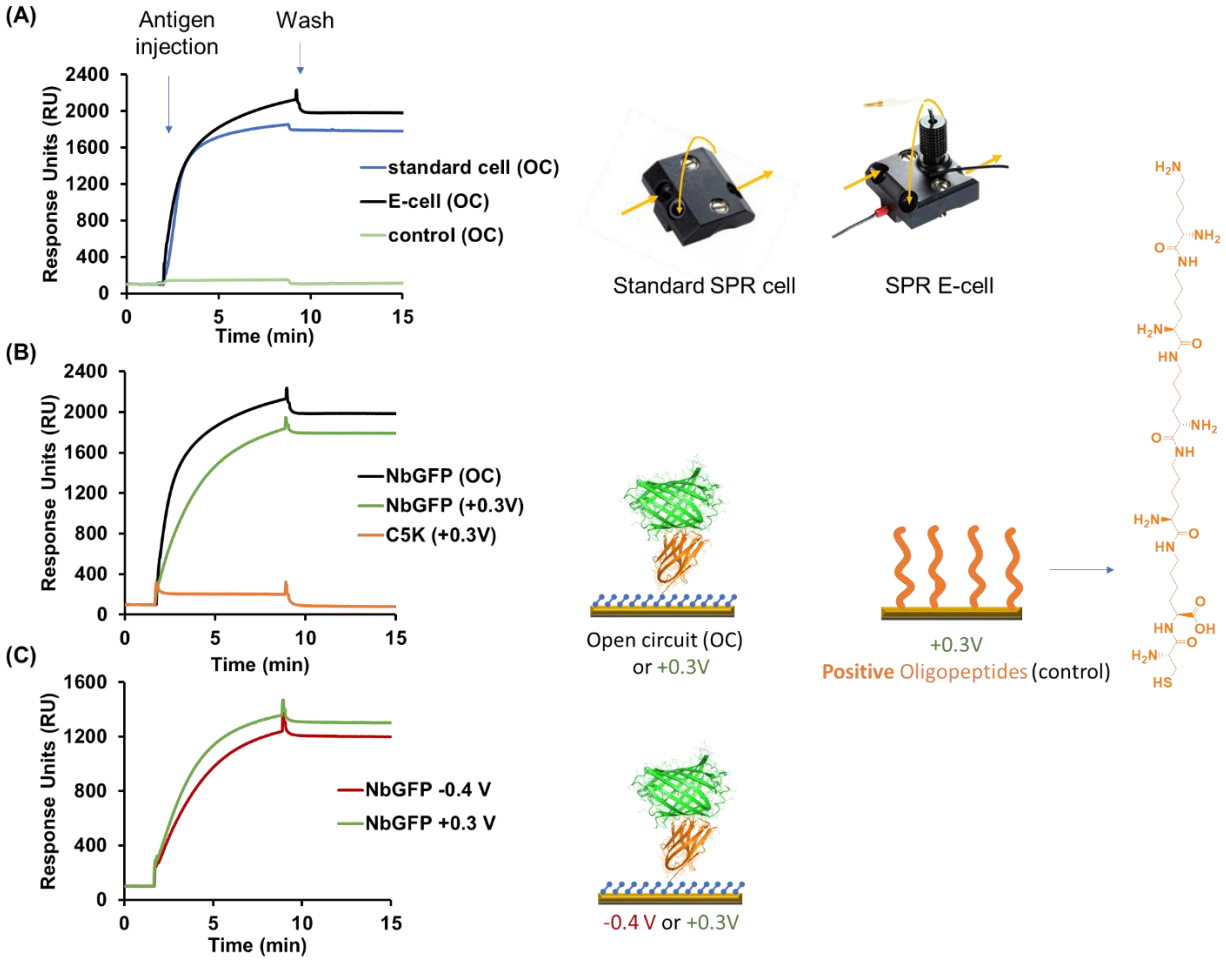

Figure 4.12 – SPR sensorgram of EGFP injection on NbVCAM1- or C5K-terminated surfaces either under open circuit (OC) or applied potential. (A) Initial studies confirmed the similar range of response obtained from the EGFP injection on the NbGFP-terminated surfaces (or on the control ethanol-terminated surface, E-cell, green) using a regular SPR cell (blue) or electrochemical cell (E-cell, black). (B) Thereafter, the EGFP injection on NbGFP- or C5K-terminated surfaces was performed under positive potential (green and orange lines respectively). (C) The EGFP injection on NbGFP-terminated surfaces under positive +0.3V (green) or negative -0.4V (red) potential.

On the latest results shown in Figure 4.12 (C), the absolute response was 27% lower than the obtained previously on Figure 4.12 (A) and (B). As these experiments were performed on different days, such variability could have been associated with solution preparation variability (observed at the NHS/EDC step, with overall lower response – results not shown), impacting

the final immobilisation and thus the antigen response. Nevertheless, the responses were comparable within the same batch of samples, still providing a valuable insight regarding the NbGFP robustness. Future work should consider this variability observed at the NHS/EDC step, before nanobody immobilisation.

Overall, the NbGFP-EGFP system remains promising for nanobody-based sensing devices. Future steps should include the functionalisation of surfaces with NbGFP mixed with electro switchable moieties in order to investigate the ability to control the NbGFP-EGFP biointeractions.

4.3 Conclusions and Future Work

This chapter started by further optimising the NbVCAM1-LEY-cys-alkyne immobilisation, this time through CuAAc click chemistry, which potentially could improve the sensitivity of the NbVCAM1-hVCAM1 pair, by reducing nanobodies immobilising randomly. The optimised clicked NbVCAM1-LEY-cys-alkyne resulted in the successful oriented NbVCAM1-terminated surfaces, that upon hVCAM1antigen injection resulted in a final response of ~ 600 RU (Section 4.2.1.2). This response was identical to the results obtained through direct immobilisation of NbVCAM1 on gold (in *Chapter 3*). These results indicate that both immobilisation methods led to identical nanobody functionalised surfaces and consequently identical antigen responses. While on one hand these results are encouraging to use the simplest immobilisation method, through a strategic cysteine directly on gold, they also suggest that the nanobodies orientation limits the platform sensitivity only to a certain extent. Thus indicating the antigen dimensions as the next potential critical parameter that limits the biosensor sensitivity.

The next step was to demonstrate that for optimised surfaces with well-oriented nanobodies the sensitivity of nanobody-based biosensing depends on the antigen dimensions. To confirm this, the alternative NbGFP-EGFP pair was tested, aiming to indirectly compare hVCAM1 (74.1 kDa) with EGFP (28 kDa). The amino coupling via NHS/EDC was used to immobilise the NbGFP nanobody on carboxylic-terminated surfaces. This immobilisation likely resulted, to a certain extent, in well-oriented nanobodies, due to the nanobody lysine groups being located opposite to its binding site. The NbGFP-terminated surfaces upon EGFP antigen injection resulted in a final response of ~ 1600 RU (Section 4.2.2.2), that was 2.7 fold the response obtained with the hVCAM1 antigen. Such results mean that in the same functionalised area, 1 hVCAM1 antigens per 205 nm^2 were captured, while 1 EGFP per 28 nm^2 were captured. These results showed that the capture ability between nanobodies dimensionally similar (such as

NbVCAM1 and NbGFP), optimally immobilised to their best performance, will depend on the antigen dimensions. Despite the effect of their antigen size, from a practical point of view both nanobody-antigen systems could be used to build capable biosensors which could also be further optimised at different temperatures and with different diluents, aiming to improve sensitivity if required.

Overall, after ensuring a successful immobilisation, nanobody density and the antigen dimensions also play a role in limiting the response obtained through steric hindrance at the surface (seen in both systems, NbVCAM1-VCAM1 with the antigen dimensions (*section 4.2.1.2*) and NbGFP-EGFP with the high nanobody density at the surface, *Section 4.2.2.2*). Thus, this chapter's work confirm three crucial matters needed to be considered to successfully conduct optimisation work on nanobody-based biosensing platforms: 1) nanobody orientation upon immobilisation; 2) nanobody density at the surface; and 3) antigen dimensions.

Furthermore, high nanobody-antigen interaction is key before increasing complexity and considering the design of switchable nanobody-based surfaces towards on demand biosensing. Establishing 1000 RU as the minimum SPR response required for the nanobody-antigen interaction, a system like NbGFP-EGFP could be considered in further designs. Additionally, the NbGFP-EGFP pair performs as a model and indicates promising results related to nanobody-antigen of similar dimensions, which would reduce considerably a screening process when designing switchable nanobody-like biosensing platforms.

Finally, initial proof-of-concept studies were conducted for a new surface molecular design with electrically responsive properties towards nanobody-antigen recognition on sensor chips. Under applied positive potential, NbGFP showed to be biologically functional, and its antigen did not show non-specific interaction with the electro-responsive C5K oligopeptides (results

from Section 4.2.3). Such a discovery makes the combination of NbGFP and C5K suitable to form an eletrically responsive nanobody-based platform. Future work should include further stability control studies and binding studies on a surface functionalised with NbGFP and C5K oligopeptides.

4.4 Supplementary Data

4.4.1. Preliminary studies of CuAAC click chemistry of biotin-PEG4-alkyne on azide-terminated SAM

Preliminary studies were designed to confidently apply azide-alkyne cycloaddition (CuAAC) mediated click chemistry between an azide-terminated surface and an alkyne-PEG4-biotin molecule (Figure 4.13). The initial steps were focused on the initial azide-terminated SAM formation and respective surface characterisation.

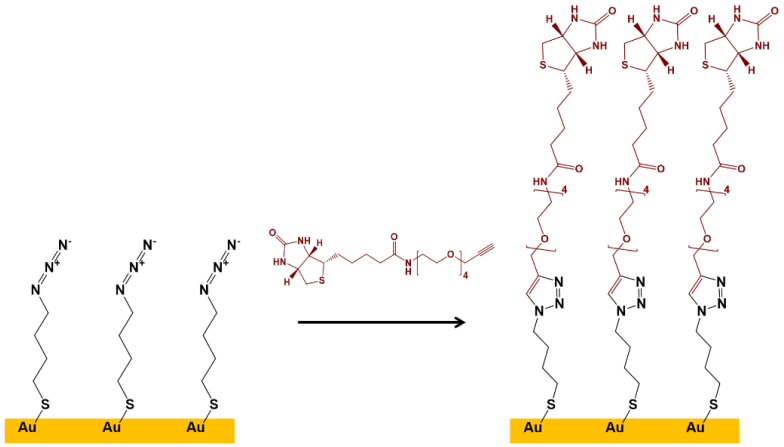

Figure 4.13 - Schematic representation of the copper catalysed azide-alkyne cycloaddition CuAAC click chemistry. Click chemistry occurred between azide-terminated surface and an alkynated biotin molecule, forming a biotin-terminate surface.

Azide-alkyne cycloaddition (CuAAC) mediated "click chemistry" was performed on ABT SAMs, in order to conjugate the azide terminated surface with an alkyne-PEG4-biotin molecule (Figure 4.13). The established biotin-neutravidin system[197-199] was used to confirm the success of the reaction via surface plasmon resonance (SPR) and further optimize the formed biotin-terminated surface.

Different incubation times for click chemistry were investigated as well as incubation conditions, where the gold chips were incubated either on the shaking plate with a determined volume (2 mL) or under the SPR flow system, whereas the incubation solution flows at a determined flow rate (8 µL/min) (see Experimental Procedure Section 6.3.3.1). A biotin-PEG4-alkyne was clicked on the azide-terminated SAM surfaces for 45 min, 1, 4, 8, 14 and 24 hours. Optimal conditions were chosen based on the subsequent neutravidin binding to the clicked biotin at the surface. Figure 4.14 summarizes the final response obtained for neutravidin injection under the different conditions.

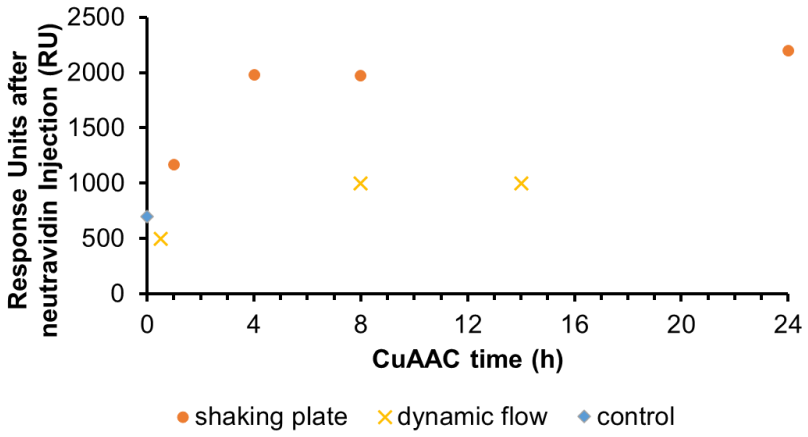

Figure 4.14 – SPR final responses after neutravidin injection on biotin-terminated surfaces CuAAc clicked at different conditions. Responses were measured after neutravidin injection (20 µg/ml, 1x PBS), and conditions tested included incubation time, and either on the shaking plate (circle, orange marker) or on the SPR under dynamic flow (8 µL/min) (cross, yellow marker). As a control, neutravidin was injected directly on the ABT surface – without any clicked biotin molecule. Each data point represents one experiment.

While the incubation under a shaking plate immerses an entire chip using a fixed solution volume, the incubation under flow uses a fresh solution overtime under a smaller chip area. In

both cases, the solution concentration was the same, however, after 4 h under 8 μL/min the total volume used surpasses the volume used under the shaking plate (2 mL). This means that after 4 h under flow, more biotin-PEG4-alkyne molecules will flow at the surface. Interestingly, the incubation under the shaking plate showed to be more efficient at all the incubation times (Figure 4.14), with higher responses when neutravidin was injected, than the incubation under the SPR at 8 μL/min. This could perhaps be explained by a slower binding kinetics from the biotin molecules that clicked at the surface under SPR flow, allowing the biotin molecules that clicked to adopt a more lying orientation on the surface and thus creating hidrance for further binding.

With the incubation under the shaking plate, more biotin molecules could bind simultanously, and therefore more biotin molecules are available from the starting point. With regard to the neutravidin injected directly on the ABT SAM (Figure 4.14, control), it showed a relatively high response (over 500 RU) indicating high non-specific interaction with the azide-terminated surface. In order to quantify how many biotin moeities have been clicked at the surface, the ideal control would have been clicking alkyne-PEG4 molecules with the same conditions, which would in theory reduce the non-specific interactions[28-33]. As a preliminary study aiming to find the most efficient way of performing the CuAAc click chemistry, Figure 4.14 shows that the plateau for the shaking plate achieved approximately the double of the plateau response obtained with the flow, giving preference to incubations under the shaking plate. Furthermore, the data shows a plateau response after 4 h incubation, making this incubation time optimal for CuAAc click chemistry performed between azide-terminated surfaces and biotin-PEG4-alkyne molecules.

The fact that a plateau was achieved at ~2000 RU after 4 h (Figure 4.14, orange) could have two reasons: either 1) the neutravidin binding was fully achieved, not allowing further binding

due to steric hindrance caused by the neutravidin itself; or 2) the biotin underneath is packed at a density that does not allow further neutravidin binding due to steric hindrance caused between the biotin molecules. Previous literature has shown higher responses from neutravidin[199], pointing to the second option being the most likely. To investigate this further and pottentially improve the biotin-neutravidin binding efficieny, a mixed SAM of 4-azidobutane-1-thiol (ABT) and 1,4- benzenedimethane thiol (BDMT) was formed by incubation at a solution ratio of 1:1. The BDMT was selected as a spacer molecule based on the theoretical smaller length than the azide (0.81 and 0.86 nm respectively), and because it would provide a binary SAM (thiol- and azide-terminated). The binary SAM could open the opportunity for future biorthogonal chemistry (click chemistry and thiolene chemistry, for instance). The respective SAMs and controls were characterised by the advancing and receding contact angles and by ellipsometry as shown in Table 4.8 to confirm the different initial azide-terminated density, which will have impact in the posterior biotin density and consequently the neutravidin binding.

Table 4.8 - Ellipsometry and contact angle results for azide-terminated (4-azidobutane-1-thiol, ABT), thiol-terminated (BDMT) and mixed monolayers ABT:BDMT 1:1. Ellipsometry measurements included theoretical and experimental thickness and contact angle measurements included advancing (Adv.) and receding (Rec.).

		ABT SAM	**BDMT SAM**	**1:1 ABT:BDMT SAM**
Thickness (nm)	Theoretical	0.86	0.81	$0.81 < x < 0.86$
	Experimental	0.47 ± 0.21	0.82 ± 0.06	0.75 ± 0.17
CA (º)	Adv.	83.2 ± 0.90	83.4 ± 0.40	85.0 ± 0.70
	Rec.	69.5 ± 0.30	50.1 ± 0.80	57.2 ± 0.80

When observing the thickness results for the ABT, BDMT and mixed ABT:BDMT SAMs in Table 4.8 it is possible to observe that BDMT SAM experimental thickness was similar to the

theoretical thickness, suggesting a well packed SAM. For the mixed SAM the experimental thickness stands as a middle point between the ABT and BDMT experimental thickness, suggesting the mix of these molecules at the surface. Regarding the contact angle measurements, the advancing contact angle does not differ between an azide-terminated or a thiol terminated surface, which is in agreement with literature[185, 200]. The contact angle hysteresis are of 13.7°, 33.3° and 27.8° for ABT, DBMT and 1:1 ABT:BDMT surfaces respectively. While the high hysteresis for the ABT:DBMT indicates a mixed monolayer, the high hysteresis for BDMT SAM was unexpected for a densely packed layer. High hysteresis points to a rather disorganized monolayer which in the case of ABT:BDMT results from mixed components, and in the case of BDMT potentially results from a mix between patches of SAM formed from thiols and formed from disulphides. High hysteresis associated with SAMs formed from disulphides have been associated to more defective SAMs and reported in literature[201] . Following the ellipsometry and contact angles analysis, the SPR studies allowed to further confirm that the ABT:BDMT surface had both components at the surface by directly impacting the click of the alkyne-terminated biotin and hence the posterior biotin-neutravidin binding efficieny

Figure 4.15 shows the SPR results for neutravidin injection on the biotin terminated surfaces that resulted from click chemistry on ABT and ABT:BDMT 1:1 surfaces with alkyne-terminate biotin moiety. Despite the higher experimental thickness of BDMT when compared with the ABT SAM, the click chemistry on the mixed SAM surface (1:1 ABT:BDMT) showed more efficient neutravidin binding, as monitored by SPR (Figure 4.15, yellow line), contributing with 25% more neutravidin at the surface. The similar response from the control surfaces (ABT and ABT:BDMT 1:1) confirm that the difference in neutravidin response between the biotin-terminated surfaces was due to the difference in biotin at the surface. These results suggest that

besides a higher experimental thickness, BDMT does not inhibit the CuAAc click chemistry from happening. Furthermore, the less packed biotin at the surface, as result of having a mixed initial monolayer with less azide content, potentially allowed less steric hindrance, contributing to a higher response from neutravidin.

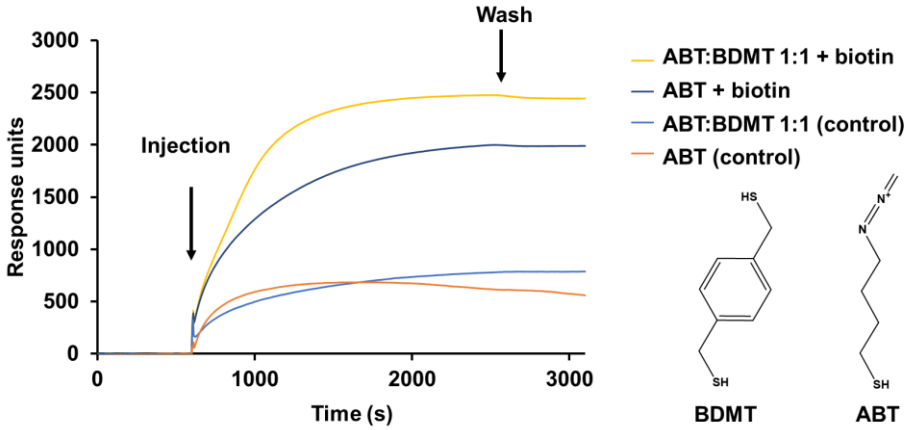

Figure 4.15 - SPR sensorgram for neutravidin (20µg/ml, 1x PBS) immobilisation on biotin-terminated surfaces incubated for 4h on azide-terminated surface and mixed surface of 4-azidobutane-1-thiol (ABT) and 1,4-benzenedimethanethiol (BDMT) 1:1. An injection of neutravidin was also performed on the pure and mixed azide-terminated surfaces that have not been exposed to click chemistry (controls).

Future studies that require the quantification of clicked biotin moieties should include additional controls where alkyne-PEG4 moeities are clicked at both surfaces (ABT and ABT:BDMT 1:1 SAMs).

These preliminary studies informed on the optimisation work on CuAAC click chemistry in terms of how incubation time and initial azide-terminated SAMs can impact the immobilisation and response. After the CuAAc studies with NbVCAM1, it was possible to conclude that although these preliminary studies with linear systems (biotin molecules) confirmed successful application of click chemistry, bulkier, nanobody-like, structures have different click efficiency

at the surface interface. This demonstrated the relevance of selecting structures with similar molecular weight and dimensions for preliminary studies.

4.4.2. **Preliminary studies of amino-coupling (EDC/NHS) with lysozyme**

The lysozyme protein, a protein with 14.3 kDa and an isoelectric point (pI) of 11.3, not too different from the nanobody of interest NbGFP (13.9 kDa and pI= 9.4), was used to preliminary test and investigate a higher range of pH conditions that were reported previously for NbGFP EDC/NHS immobilisation[39]. The success of EDC/NHS immobilisation is pH-dependent[47]: at first, the EDC/NHS coupling happens in water to a fraction of the carboxyl groups at the surface, resulting in NHS esters at the surface. Then, the NHS esters from the activated surface react with the unprotonated amines ($-NH_2$) of the protein that approached the surface. The more unprotonated amines are available at the protein's surface, the more likely it will react with the NHS esters at the substrate. Additionally, the electrostatic interaction between the protein to immobilise and the fraction of unprotonated COO^- at the substrate also play a role (depending on the protein carrier buffer pH and the surface pKa[202]): the more electrostatically attracted to the surface, the more likely the $-NH_2$ of the protein will react[47, 203, 48]. Therefore the pH of the carrier buffer usually goes up to the protein's pI, keeping the protein with a positive net charge whilst potentially having a fraction of COO^- available. This means that the most efficient EDC/NHS conditions varies with the type of surface and protein to immobilise. The previously reported EDC/NHS applied to NbGFP was only investigated between the pH range 4-6[39]. Herein, the electrostatic interactions between the MUA surface and the lysozyme protein were studied at pHs of 5.4, 6, 7 and 8, via SPR analysis (Figure 4.16).

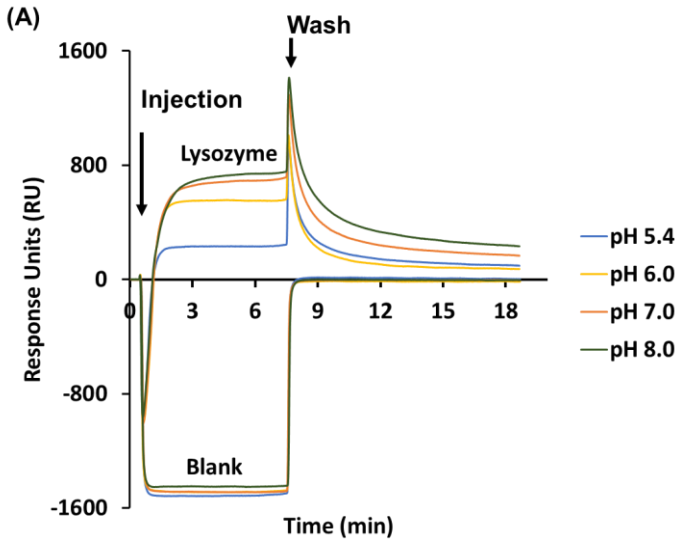

(B)

Lysozyme
MW: 14.3 kDa
PI: 11.3

pH	Total RU*
5.4	1744
6.0	2039
7.0	2178
8.0	2189

*Total RU = RU(sample pH X) – RU(blank pH X)

Figure 4.16 - Electrostatic interactions study on MUA SAMs using lysozyme injections at different pHs. (A) SPR sensorgram of lysozyme injections (50 µg/mL) and respective blanks on MUA SAMs at the pH 5.4 (blue), pH 6 (yellow), pH 7 (orange), pH 8 (dark green). (B) Table representative of the electrostatic behaviour (at equilibrium before wash), with the total response obtained from the subtraction of the blanks response to the sample response, as the running buffer was 1x PBS.

Figure 4.16 shows SPR lysozyme electrostatic interactions on MUA SAMs. This began with a stable baseline followed by an increase in response during the lysozyme injections. Since the main interactions that retain the lysozyme at the surface were electrostatic, when the lysozyme injection ended, the response lowered as the lysozyme washed off the surface. The total response, representative of the electrostatic interaction, was calculated from the subtraction of the blanks response to the sample injection response. In this case, the conditions that resulted in higher total response and protein attraction were pH 7 and 8, indicating promising conditions to test with EDC/NHS immobilisation. These studies provided an estimate of how proteins with high isoelectric pH (such as lysozyme and NbGFP by extrapolation) are attracted to MUA surface depending on pH.

Figure 4.17 shows the SPR results for the lysozyme immobilised through NHS/EDC on the MUA surface at pH 8. Following an injection of water as the first blank and then the second blank injection of the buffer at pH 8, it was possible to observe an increase in response due to the EDC/NHS injection around 38 minutes. This response did not recover to the baseline, indicating that NHS-esters were formed at the surface. Thereafter, the lysozyme response that resulted from its immobilisation was seen after the lysozyme injection, when the running buffer clears unbound protein (Figure 4.17, between 60 and 67 minutes) resulting in ~1714 RU. Afterwards, ethanolamine at pH 8.5 was injected to deactivate possible remaining unreacted NHS-esters, which did not change the final response. Still in Figure 4.17 a certain delay was observed to achieve a response, visible especially after blank injections and after the ethanolamine injection. This was due to the fact that the experiment was performed on an electrochemical SPR cell (E-cell) which has a bigger volume capacity and requires a longer time to fully stabilise (even though burst injections were introduced to accelerate this process, see Experimental Procedures, Section 6.4.6.4). Future experiments were performed on a regular SPR cell. Furthermore, the higher electrostatic interactions obtained at range of neutral to basic pH were encouraging towards the investigation of NbGFP EDC/NHS immobilisation at those conditions, which could result in better EDC/NHS performance[47, 48, 203].

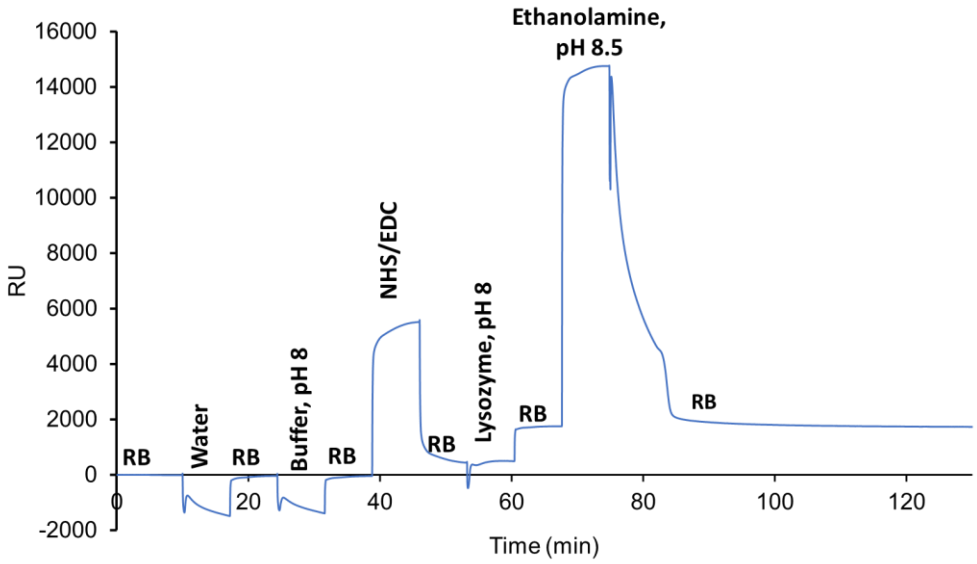

Figure 4.17 - Preliminary NHS/EDC studies via SPR. Lysozyme on a buffer pH 8 was immobilised via NHS/EDC on the MUA surface. After a baseline with the running buffer (RB) (1xPBS) water, buffer pH 8, and NHS/EDC injections were performed. Thereafter, the lysozyme (50 µg/ml) was injected followed by 1M ethanolamine at pH 8.5, finalising with an increase in response of 1714 RU.

Chapter 5 Design and development of surfaces functionalised with charged switching moieties

More interesting than having the perfect biosensing platform composed of nanobodies, is the ability to control when to sense the targeted antigens. After the studies from the previous chapters on optimisation of nanobody platforms and maximisation of antigen response, the next challenge was to design and investigate the final building blocks for switchable biological surfaces: the moeities that allow control over the binding between nanobody-like structures and their respective antigen. Ideally, these moieties have a small footprint so when anchored at the surface together with the nanobodies, there are minimal loss of nanobodies' density, and consequently antigen response. In this chapter, surfaces functionalised with electrically-responsive charged oligopeptides were designed and characterised. Challenges such as finding the ratio between oligopeptides and the spacer molecule were addressed to theoretically allow 1) elongation to conceal nanobody-like structures, and 2) flexibility to retract at the surface under stimulus and uncover the binding site (Figure 5.1).

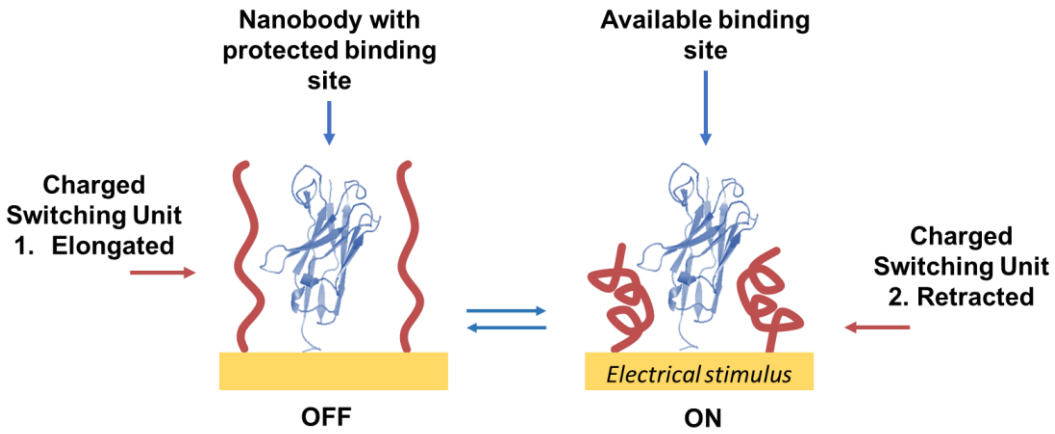

Figure 5.1 – Schematics for a nanobody-based on demand biosensing platform. When the biological state is OFF, the nanobody (blue) is surrounded by the charged switching units (red) that protect the binding site from interaction with the target antigen. By applying an electrical stimulus with the opposite charge of the switching units, these conceal at the surface allowing the antigen to bind the nanobody, turning the platform's biological state ON.

In this Chapter, Bárbara Simões conducted all the experimental work with exception of XPS experimental work that was conducted by David Morgan. All data was analysed by Bárbara Simões.

5.1 Introduction

Smart electrically-switchable surfaces have been developed to respond with conformational changes to applied electrical potentials, exhibiting different and reversible surface properties. Briefly, three different actuation methods to control specific interactions have been introduced in this thesis, in which the switching units either (A) contain the binding moiety[7, 20, 118], (B) surround the binding moieties[112] or (C) are simultaneously the binding moiety (i.e aptamers)[119, 120]. Aside from aptamers, in all the cases the binding moeities were simple structures of low molecular weight that were manipulated by charged oligopeptides. To date, similar switching units have not been adapted to control the binding of larger structures, such as nanobodies. This research envisions the use of charged oligopeptides surrounding nanobodies in order to control the binding to their targets.

Previous studies have provided valuable insight on conformational mechanisms and structural requirements for the regulation of biomolecular interactions using switching units that contain the binding moiety. Mendes et al, used switchable mixed SAMs composed by C4K-biotin moeities (cysteine– 4-mer lysine –biotin) and 3-(mercaptopropyl) tri(ethylene glycol) (TEGT) moeities (acting as spacer) on gold[20, 198]. It was shown that these SAMs had the ability to change the biotin's availability to bind neutravidin at the surface[20, 198]. The C4K-biotin exhibit protonated amino side chains at neutral pH allowing the basis for the switching "ON" and "OFF" of the biological activity on the surface by an electrical potential[20]. While the positive potential resulted in free biotin and thus high neutravidin binding, the negative potential resulted in a sterically shielded biotin with minimal binding. The best ratio between the charged oligopeptides, the spacer molecule and the length of the oligopeptides was investigated in order to achieve higher switching efficiencies[199]. These studies showed that with longer oligopeptides with less spacer molecules at the surface achieved higher switching efficiencies. Such spacing

requirement has been hypothesized to be due to the long and flexible nature of the polypeptide backbone[199].

Other switchable surfaces have been developed for different applications, including cell release and attachment[112]. Following a different actuation method, Gooding et al, used charged switching units surround the binding moiety (Arginine-Glycine-Aspartate, RGD) to control cell attachment[112]. The investigation demonstrated the use of negatively and positively charged molecules to allow switching and it was further proof for conformational rearrangement upon applied potential. Another method that relies on cleavage rather than conformational change was developed by Mrksich et al utilizing electroactive O-sily hydroquinone motif to attach RGD to a gold substrate[204]. With applied potential the oxidation of silyl hydroquinone to benzoquinone was triggered, resulting in the release of RGD peptide and consequent detachment of cells[204]. While this method was switchable for cell detachment, it does not allow for reversibility.

Herein, charged oligopeptides were designed for potential electrical switching surfaces. These charged oligopeptides were devised as potential building blocks to allow the control of specific interactions between higher molecular weight, nanobody-like structures (~15 kDa, ~ 5nm) and their respective targets. Specifically, the nanobody NbVCAM1 from Chapter 3 was considered regarding immobilisation directly on gold and its thickness. For the oligopeptides, cysteine and lysine are amino acids that are protonated under neutral pH responding through electrostatic interactions to an applied electric field[199], and oligopeptides composed by these were used in the past to perform electrical switchable surfaces[33, 96, 118, 197-199]. Inspired by the previous work of Mendes et al, with C4K-biotin molecules and TEGT[20, 198], in this research C5K and C8K oligopeptides were used alongside triethylene glycol mono-11-mercaptoundecyl ether (TEG11) to provide spacing and structural support to higher thicknesses. Alternative oligopeptide

structures containing proline (P) (C-PPεK- PPεK - PPεK-PP, or C3εK for simplicity) and diamino propionic acid (Dap) (C-PPβDap-PPβDap-PPβDap-PP, or C3βD for simplicity) which provide a more rigid backbone[205] were also designed and studied.

Furthermore, the nanobody NbGFP studied in Chapter 4 was also considered. NbGFP was immobilised on the surface through EDC/NHS amino coupling. Ideally, switching moeities for nanobody-antigen platforms obtained via EDC/NHS would be immobilised simultaneously through the same method and conditions. When designing charged oligopeptides to be anchored at the surface through EDC/NHS chemistry, positively charged oligopeptides are unsuitable due to their amine groups, as they likely would react at the surface with multiple groups, losing their ability to cover the immobilised nanobody (Figure 5.2). This limits the switching unit to have one primary amine group at its extremity (N terminal), making the immobilisation pH a more determinant factor. Herein, oligopeptides with seven glutamic acids and beta-alanine at the N-terminal (7EA) were designed and studied with EDC/NHS coupling.

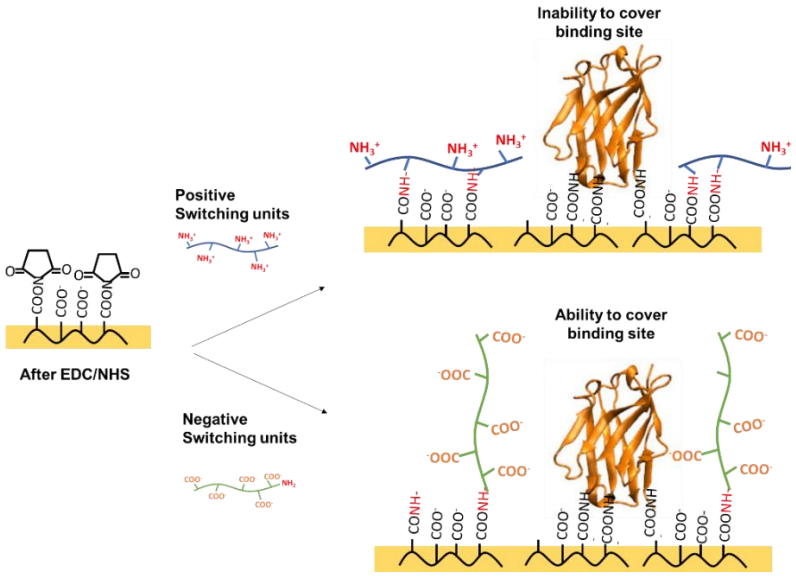

Figure 5.2 – Representative schematics for oligopeptides (switching units) and nanobodies immobilised through EDC/NHS amino-coupling. The use of positively charged oligopeptides becomes unsuitable to this application as its coupling at the surface would likely result with the laying down of the oligopeptides, losing their ability to 1) cover the binding site of the nanobody and 2) respond to an

electrical stimulus. On the other hand, the negatively charged oligopeptides, with one N-terminal amine, are promising switching units to mix with nanobodies through this immobilisation method.

5.2 Results and Discussion

5.2.1. Switching moieties: charged oligopeptides self-assembled monolayers (SAMs)

Herein, stimuli responsive moieties aiming to provide control over nanobody-like structures (~5nm) are investigated. Positively charged oligopeptides composed of cysteine (C) at the C-terminal and followed by either five lysine (C5K), eight lysine (C8K), proline (P) and lysines (C3εK) or proline and diamino propionic acid (Dap) (C3βD) have been formed purely or mixed with thriethylene glycol mono-11-mercaptoundecyl ether (TEG11). The formed SAMs were analysed by ellipsometry, contact angle and X-ray photoelectron spectrometry (XPS). Firstly, initial studies were obtained on formed TEG11 SAMs, as ethylene-glycol terminated molecules have as been previously used as a support molecules[7, 33, 96] being resistant to protein non-specific adsorption[32]. To test TEG11 SAMs, different incubation solvents were used: ethanol (EtOH), water and 1xPBS. Table 5.1. shows the results obtained for ellipsometry and contact angle measurements.

Table 5.1 – TEG11 SAMs ellipsometry and contact angle results. TEG11 SAMs were formed in different solvents: 1x PBS, water or ethanol (EtOH).

		TEG11			**Au surface**
		(1x PBS)	(water)	(EtOH)	
Thickness (nm)	Theo.	2.6 nm (ChemDraw)			-
	Exp.	1.73 ± 0.34	1.76 ± 0.03	1.15 ± 0.05	-
CA (º)	Adv.	38.4 ± 0.64	37.68 ± 1.01	38.80 ± 2.06	76.23 ± 2.28
	Rec.	22.24 ± 2.38	29.90 ± 0.36	31.34 ± 1.65	-

Table 5.1 shows that TEG11 formed in any of the conditions had smaller thickness than the theoretical estimated by the *ChemDraw* software. Such difference is expected as the estimated value consists on a fully straight molecule, perpendicular to the surface whilst the experimental SAM might present an angle. Additionally, the surfaces were analysed under dried state which potentially contributes to a smaller thickness, when compared with the SAM in solution.

Table 5.1 shows higher thicknesses for TEG11 SAMs formed in water or 1xPBS, than in ethanol which is in agreement with literature[206]. This is due the amphiphilic nature of TEG11 (Figure 5.3) which arranges the SAMs in an organized, packed manner, contributing to higher thicknesses in aqueous solutions. The experimental thickness for TEG11 in ethanol ($1.2 \pm 0.1\ nm$) is as reported in the literature ($0.9 \pm 0.15\ nm$)[207]. Finally, literature also reports similar thickness (1.7 ± 1.1 nm) for TEG11 in an aqueous solution (containing 2% Ethanol)[208], which agrees with the experimental value obtained (1.8 ± 0.1 nm).

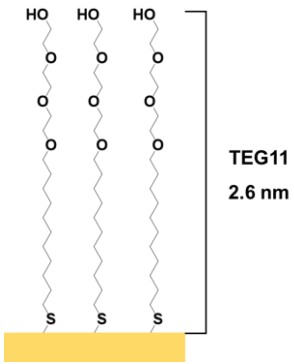

Figure 5.3 – TEG11 SAMs schematics.

The use of 1xPBS as a solvent contributed to a higher standard deviation (1.7 ± 0.3 nm), however, the thickness did not change significantly (t-test, p = 0.7) compared to the one obtained in water. The contact angle results (Table 5.1) showed similar advancing angles across

the conditions with averages ranging from 37.8° to 38.8°. Regarding the receding angles, TEG11 SAMs obtained in either water or ethanol showed similar results (29.9° – 31.3°, respectively) while TEG11 SAMs obtained in 1xPBS had a smaller receding angle (22.2 ± 2.4°) contributing to a larger hysteresis. It means a less organised monolayer and agrees with the higher standard deviation obtained at the thickness results.

Overall, 1xPBS solvent allowed a packed TEG11 SAM, and 1xPBS is a convenient solvent to use when mixing with oligopeptides and nanobody-like structures, which need salt solutions to keep their structures stable. Therefore, TEG11 SAMs obtained with 1xPBS were used for future studies. Then, XPS was used to analyze the surface composition of TEG11 SAMs, aiming to further confirm the SAM formation and be used as a control SAM for the mixed SAMs studies, as can be seen in Figure 5.4 and Table 5.2.

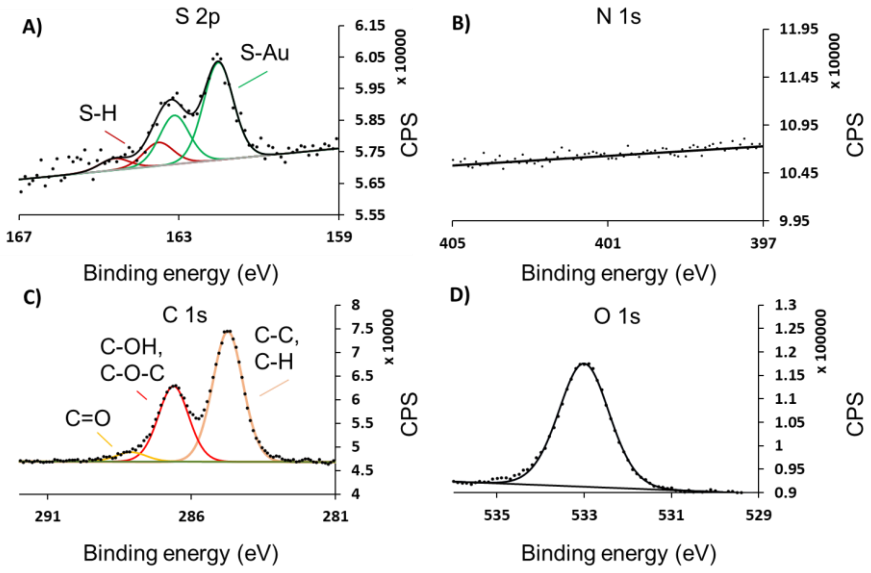

Figure 5.4 –TEG11 SAMs XPS results. Representative XPS high resolution spectra of the (A) S 2p, (B) N 1s, (C) C 1s, and (D) O 1s regions. CPS: counts per second.

Table 5.2 - Relative atomic percentages and relative components percentages calculated by XPS for TEG11 SAM. Theoretical (T) values were obtained considering the atomic formulas of the SAM molecules. Duplicates were measured twice in different chip positions. Averages and errors as standard deviation are reported. T = theoretical; E = experimental.

SAM		Relative Atomic %								
TEG11		**S**		**N**		**C**			**O**	
	T	4.5		0.0		77.3			18.2	
	E	3.8 ± 0.6		-		80.4 ± 1.9			15.8 ±1.3	
		Relative Components %								
		S-Au	**S-H**	**NH_3^+**	**N**	**C-C**	**C=O**	**CS,CN,CO**	**O-C**	**O=C**
	T	100.0	0.0	0.0	0.0	58.8	0.0	41.2	100.0	0.0
	E	79.7±1.6	20.3 ±1.6	-	-	62.6±2.9	4.1±0.4	33.4±2.6	98.4±2.3	~ 0

The high resolution spectra for S 2p (Figure 5.4 (A)) revealed the presence of both thiolate and thiol species (162.0 eV and 163-164 eV respectively), with a relative percentage of 20% of unreacted thiols (Table 5.2, S-H). This suggests that likely the washing process after SAM formation could be improved in order to remove the remaining free thiols. Furthermore, the absence of nitrogen (400-401 eV) as a contaminant (Figure 5.4 (B)) makes this surface a good control when analysing mixed SAMs composed by TEG11 and oligopeptides, which will incorporate this element to the surface composition. Regarding the carbon and oxygen elements (Figure 5.4 (C) and (D)), the presence of other elements than the expected (as C=O and therefore O=C) that contributed to the relative atomic percentages of 3% more carbon and 2% less oxygen than expected, it is likely due to the typical contamination from exposure of these samples to the atmosphere. Overall, the surface composition of TEG11 SAM in 1xPBS analysed by XPS further confirmed successful SAM formation, as can be also seen through the XPS element ratios (Table 5.3). With the aim of using use TEG11 molecules to support, organize and control the surface density of charged oligopeptides, this SAM was used as a reference for the analysis of the pure oligopeptide SAMs.

Table 5.3 - XPS element ratios for TEG11 SAMs. Theoretical (T) values were obtained considering the atomic formulas of the SAM molecules. T = theoretical; E = experimental.

SAMs		XPS Element Ratios			
		Au/S	N/S	C/S	O/S
TEG11	T	-	0	17	4
	E	18 ± 0.8	0	21 ± 4.2	4 ± 0.3

Next, SAMs composed purely by positively charged oligopeptides with a C-terminal cysteine and followed by five lysines (C5K) or mixed with TEG11 at the solution ratios of C5K:TEG11 40:1; 1:10; 1:40 and 1:100 were analysed by ellipsometry and contact angle. Results are shown in Figure 5.5.

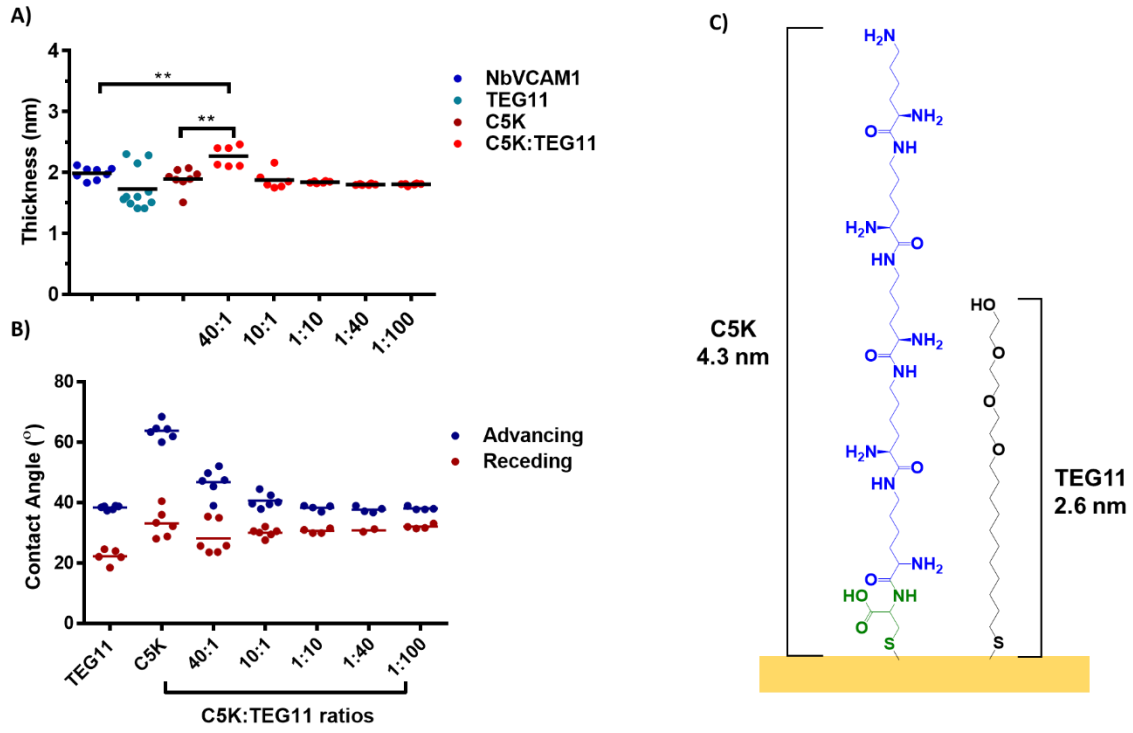

*Figure 5.5 - C5K and mixed C5K:TEG11 SAMs ellipsometry and contact angle results. Results for (A) thickness and (B) advancing and receding contact angles, show that likely the SAM surface composition remains similar when incubated with C5K:TEG11 at solution ratios of 10:1, 1:10, 1:40 and 1:100, having non significant differences within the ellipsometry and contact angle results (t test, $p > 0.05$). Significant differences noted as ** (t test, $p < 0.05$). (C) C5K:TEG11 SAM schematics with the ChemDraw theoretical thicknesses.*

Initial studies included C5K and C5K:TEG11 1:10, 1:40 and 1:100 SAMs, solution ratios chosen based on the previous experience of Mendes' group with C4K and C6K oligopeptides mixed with tri(ethylene-glycol)-terminated thiol (TEGT)[199], which had shown best switching efficiency at the ratio C4K:TEGT 1:40.[199] The pure C5K SAM, with an experimental thickness of 1.9 ± 0.2 nm (Figure 5.5 (A)), revealed 44% of the theoretical thickness (ChemDraw, in Figure 5.5 (C)), being similar to the thickness of the TEG11 SAM, of 1.7 ± 0.3 nm (no significant difference, t test, p = 0.2, in Figure 5.5 (A)). A thickness of 1.9 ± 0.2 nm would likely be insufficient to protect the binding site of nanobody-like structures, such as NbVCAM1 (with experimental thickness of 2.0 ± 0.1 nm). Such lower than expected thicknesses obtained with the pure C5K SAM could be explained by 1) a likely disperse SAM, consequence of the charged oligopeptides repealing each other during adsorption, and 2) flexible backbone, which leads the C5K to fold at the surface, instead of keeping an extended conformation. Following Cassie's law (Equation 5.1), the mole fraction of each component in the mixed SAM of C5K:TEG11 (x_1 and x_2) can be calculated from the advancing contact angle values of each pure SAM (Θ_1 and Θ_2) and of the mixed SAM (Θ_{12}).

$$cos(\Theta_{12}) = x_1 cos(\Theta_1) + x_2 cos(\Theta_2) \qquad \textit{Equation 5.1}$$

The different advancing contact angle results (Figure 5.5 (B)) obtained for the pure TEG11 and C5K SAMs, with 38.4 ± 0.6° and 63.8 ± 2.8° respectively, could allow a rough calculation of the surface composition of mixed SAMs using Equation 5.1 (see Table 5.4). The non-significant differences within the contact angles and thicknesses obtained at initial ratios (C5K:TEG11 1:10, 1:40 and 1:100) compared with the TEG11 results, suggested that the solutions with

superior ratio of TEG11 would result in surfaces with mainly TEG11, not allowing C5K to anchor at the surface. To test this theory the ratios were inverted to C5K:TEG11 10:1 and 40:1.

Table 5.4 – Results obtained from Cassie's law for the C5K:TEG11 mixed SAMs surface ratios incubated at the different solution ratios.

	C5K:TEG11
Solution ratios	**SAM on the surface (from Cassie's law)**
1:100	Fully TEG11
1:40	Fully TEG11
1:10	Fully TEG11
10:1	1:12
40:1	1:2

Only at the ratio of C5K:TEG11 40:1 the thickness increased to 2.3 ± 0.2 nm, significantly surpassing the nanobody thickness (t test, $p = 0.002$) (Figure 5.5 (A)), and it was 20% higher than the pure C5K SAM. Furthermore, the advancing contact angle at this ratio indicated a surface containing one C5K for each two TEG11 molecules, being still mainly composed of TEG11 (Table 5.4). As the thickness obtained for C5K:TEG11 40:1 could theoretically cover nanobody-like structures and allow control over biological activity, this ratio was selected, together with the pure C5K SAM as a control, to be analysed for its surface composition with XPS. The XPS results are shown in Figure 5.6 with representative high resolution spectra, and described in Table 5.5 for relative atomic and component percentages and in Table 5.6 for element ratios.

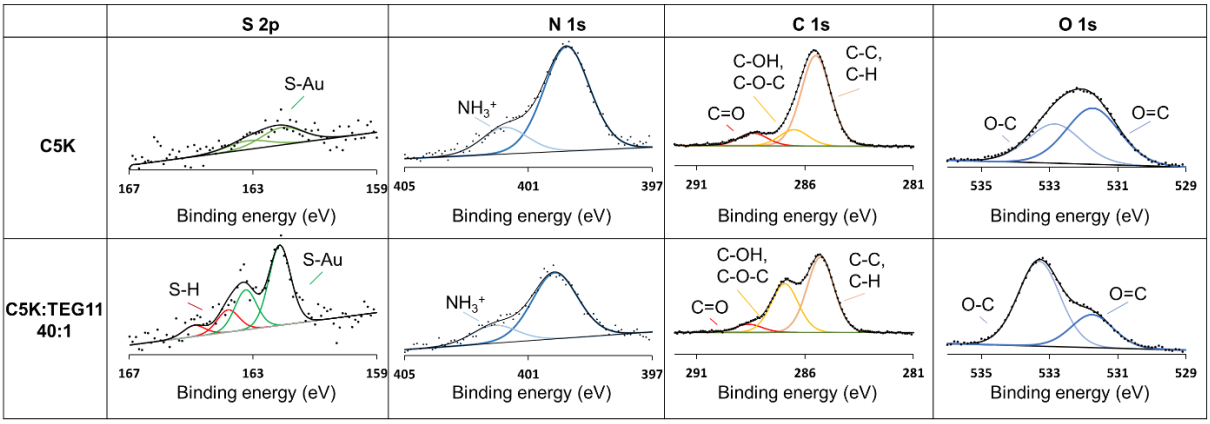

Figure 5.6 – C5K and C5K:TEG11 40:1 SAMs XPS results. Representative XPS high resolution spectra of the S 2p, N 1s, C 1s, and O 1s regions.

Table 5.5 - Relative atomic percentages and relative components percentages calculated by XPS for C5K and C5K:TEG11 40:1 SAMs. Theoretical (T) values were obtained considering the atomic formulas of the SAM molecules. Duplicates were measured twice in different chip positions. Averages and errors as standard deviation are reported. T = theoretical; E = experimental.

SAMs **Relative Atomic % and Relative Components %**

C5K		**S**		**N**		**C**			**O**	
	T	1.9		21.2		63.5			13.5	
	E	1.0±0.1		9.5±2.7		72.1±5.3			17.4±2.7	
		S-Au	**S-H**	**NH_3^+**	**N**	**C-C**	**C=O**	**CS,CN,CO**	**O-C**	**O=C**
	T	100.0	0.0	54.5	45.5	45.5	18.2	36.4	14.3	85.7
	E	100.0	-	21.5±1.1	78.5±1.1	79.9±9.4	7.9±5.1	12.2±4.5	29.2±9.4	70.8±9.4
C5K:TEG11 (40:1)		**S**		**N**		**C**			**O**	
	T	2.0		20.9		63.6			13.5	
	E	2.2±0.2		6.5 ± 0.7		74.5±1.7			16.7±0.9	
		S-Au	**S-H**	**NH_3^+**	**N**	**C-C**	**C=O**	**CS,CN,CO**	**O-C**	**O=C**
	T	100.0	0.0	54.5	45.5	45.6	18.0	36.4	15.5	84.5
	E	80.8±2.8	19.2±2.8	21.6±1.6	78.5±1.6	57.1±1	7.4±1.8	35.5±2.8	71.3±0.8	28.7±0.8

Table 5.6 – XPS element ratios for C5K and C5K:TEG11 40:1 SAMs. Theoretical (T) values were obtained considering the atomic formulas of the SAM molecules and their solution ratios. T = theoretical; E = experimental.

SAMs		XPS Element Ratios				
		Au/S	**Au/N**	**N/S**	**C/S**	**O/S**
C5K	T	-	-	11	33	7
	E	55 ± 6.5	5 ± 0.3	11 ± 1.6	84 ± 21.2	21 ± 0.6
C5K:TEG11 (40:1)	T	-	-	11	33	7
	E	22 ± 1.1	8 ± 0.1	3 ± 0.2	34 ± 4.8	8 ± 0.5

The high resolution spectra for S 2p in Figure 5.6 shows only the thiolate species present for the pure C5K SAM, demonstrating that the washing process used is efficient, removing any free thiols that did not anchor at the surface. On the other hand, the mixed C5K:TEG 40:1 SAM revealed 20% of unreacted thiols at the surface (Table 5.5), a number similar to that observed with pure TEG11 SAM (Table 5.2). This suggests that possibly non-anchored TEG11 contribute to these remaining free thiols. Furthermore, the C5K:TEG11 40:1 SAM has also shown more thiolate at the surface (Figure 5.6 (S 2p)), which is due to the TEG11 contribution to the SAM formation, also seen with the decrease in the ratio Au/S in Table 5.6 between C5K and the C5K:TEG11 40:1. In what concerns the N 1s spectra from Figure 5.6, it is possible to observe two species: the neutral nitrogen environment at 400 eV ($-NH_2$), and the positive environment ($-NH_3^+$), at a higher binding energy ~ 402 eV, which originates from the protonated amines belonging to the lysine groups. Although the relative nitrogen percentages were lower than expected (seen in Table 5.5, and possibly explained by the contributions of adventitious carbon and oxygen), the experimental ratio N/S is as expected (Table 5.6) for the pure C5K SAM. The lower than expected N/S ratio for C5K:TEG11 40:1 is an indication that the surface might have more TEG11 moeities than C5K. The theoretical percentage of nitrogen species assumes all the amine groups are protonated (+5e), while the experimental suggests that two amine groups are protonated (+2e) which could possibly be explained by the fact that the

samples were no longer under solution, but dried and under vacuum for analysis. The presence of N 1s at the mixed C5K:TEG11 40:1 confirms the presence of C5K at the surface, as TEG11 does not contribute with this element (as seen in Table 5.2). Additionally, the molecular formula for each oligopeptide (generically, $C_\alpha H_\beta Au N_\gamma O_\delta S$) allows to obtain the ratio in Equation 5.2. In Equation 5.3, S_{total} corresponds to the XPS experimental area obtained for the total sulphur, and S_{TEG11} and $S_{oligopeptide}$ to the TEG11 and oligopeptide sulphur areas respectively. With these equations it was possible to achieve the ratios between oligopeptides and TEG11, with Equation 5.4.

$$S_{oligopeptide} = \frac{N_{oligopeptide}}{\gamma} \qquad \textit{Equation 5.2}$$

$$S_{total} = S_{TEG11} + S_{oligopeptide} \qquad \textit{Equation 5.3}$$

$$Ratio\ between\ Oligopeptide\ and\ TEG11 = \frac{S_{oligopeptide}}{S_{TEG11}} \qquad \textit{Equation 5.4}$$

Following these equations it was possible to calculate the experimental ratio of C5K:TEG11 40: 1 to be 1:(3 ± 0.2), which means that 120 fold more TEG11 moieties were anchored to the surface than predicted by the solution ratio. Previous literature has shown that solution ratios do not represent the final surface ratios[20, 209]. These results are in agreement with previous findings attained through ellipsometry and contact angle, suggesting a much faster kinetics from TEG11 than C5K to bind at the surface.

Next, after understanding with C5K that it forms loosely packed SAMs, but when mixed with TEG11, the packing and thickness can be improved, it was hypothesized that longer C8K potentially could provide with thicker SAMs. Thicker SAMs could likely be necessary to efficiently control nanobody-antigen interaction. The SAM composed purely by the positively charged oligopeptides C8K or mixed with TEG11 at the solution ratios of C8K:TEG11 40:1; 1:10; 1:40 and 1:100 were analysed by ellipsometry and contact angle (see Figure 5.7).

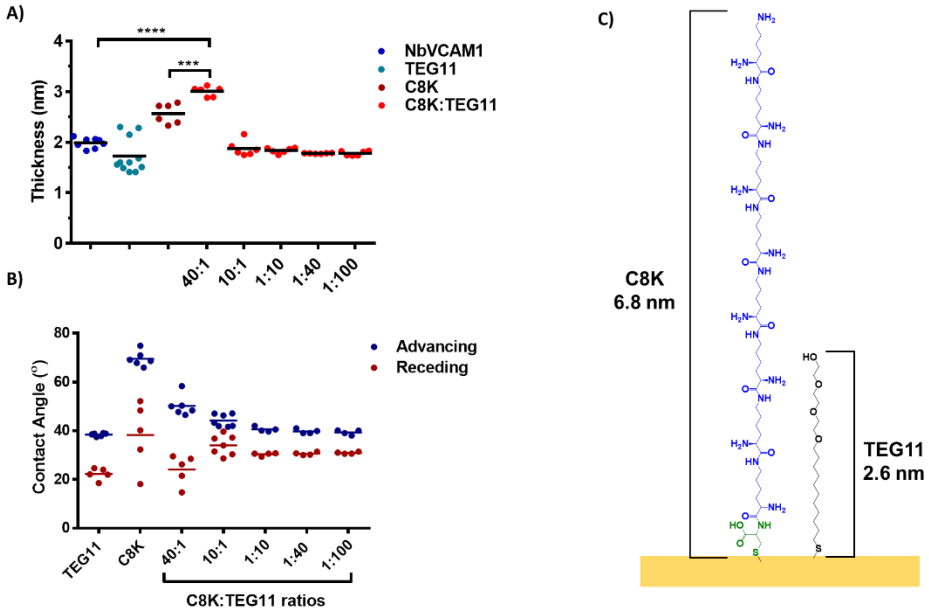

*Figure 5.7 – C8K and mixed C8K:TEG11 SAMs ellipsometry and contact angle results. Results for (A) thickness and (B) advancing and receding contact angles, show that likely the SAM surface composition remains similar when incubated with C8K:TEG11 at solution ratios of 1:10, 1:40 and 1:100. Significant differences noted as *** (t test, $p < 0.01$) and **** (test, $p < 0.0001$). (C) C8K:TEG11 SAM schematics with the ChemDraw theoretical thicknesses.*

Unlike the C5K SAM, the pure C8K oligopeptides SAM with 2.6 ± 0.2 nm, was 30% higher than the nanobody structure, and therefore could be a good candidate to be used with nanobody-like structures to control the antigen binding activity (Figure 5.7(A)). Similarly to the previous

C5K:TEG11 results, the C8K:TEG11 mixed SAMs also showed no significant differences for ellipsometry and contact angle at the ratios of 1:10, 1:40 and 1:100 (t test, $p > 0.05$), suggesting that the surfaces are mainly composed of TEG11.

At inverted ratios, the surface composition starts to change, especially at the ratio of C8K:TEG11 40:1, with 3.0 ± 0.1 nm, showed an increase in thickness of 17% relatively to the pure C8K SAM (significantly different, t test, $p < 0.0001$). C8K is similar to C5K, with three more lysine groups and the results suggest that the TEG11 molecule at the same solution ratio (40:1) was similarly efficient at providing support to both structures (20% increase from the pure C5K SAM). In addition, the receding and advancing contact angle, at the inverted C8K:TEG11 ratios, are closer to the ones obtained with the pure C8K SAM (Figure 5.7(B)). The contact angle trend towards C8K:TEG11 inverted ratios agrees with the ellipsometry data, which together confirm that only with the ratio increase of C8K in solution, it reflects an increase in C8K on the surface – results dissimilar to the ones obtained between C4K and C6K with a shorter tri(ethylene glycol)-terminated thiol TEG3[199].

The surface ratios calculated through the Cassie's law demonstrate that TEG11 is dominantly at the surface, even under incubation with mainly C8K (Table 5.7). Taking the conditions with higher thickness (which likely will cover the nanobody binding site), and higher estimated C8K surface ratio, the C8K:TEG11 40:1 ratio was selected, together with the pure C8K SAM as a control, to be analysed for its surface composition with XPS. The XPS results are shown in Figure 5.8 with representative high resolution spectra, and described in Table 5.8 for relative atomic and component percentages and in Table 5.9 for element ratios.

Table 5.7 - Results obtained from Cassie's law for the C8K:TEG11 mixed SAMs surface ratios incubated at the different solution ratios.

C8K:TEG11	
Solution ratios	**SAM on the surface (from Cassie's law)**
1:100	1:44
1:40	1:29
1:10	1:17
10:1	1:6
40:1	1:2

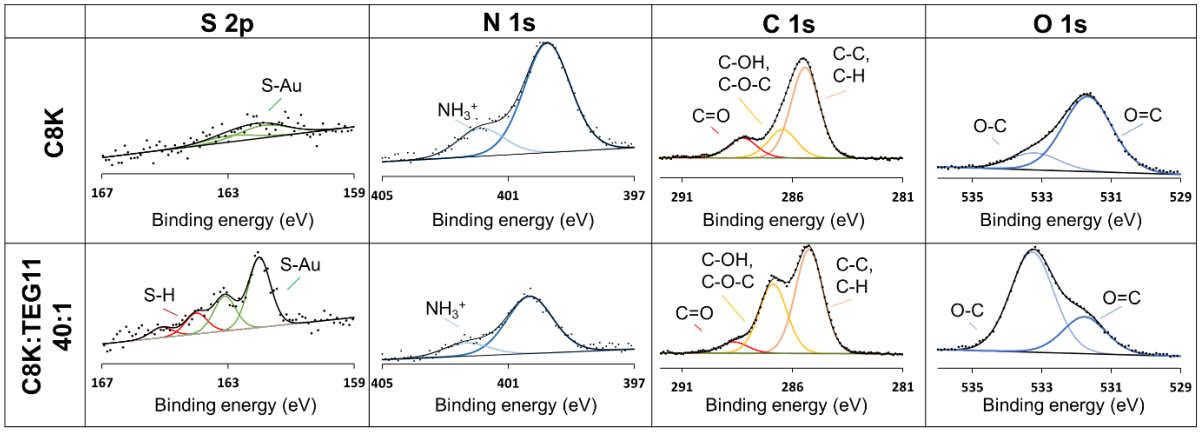

Figure 5.8 - C8K and C8K:TEG11 40:1 SAMs XPS results. Representative XPS high resolution spectra of the S 2p, N 1s, C 1s, and O 1s regions. Each spectra of each element has the same vertical scale respectively (not represented).

Table 5.8 - Relative atomic percentages and relative components percentages calculated by XPS for C8K and C8K:TEG11 40:1 SAMs. Theoretical (T) values were obtained considering the atomic formulas of the SAM molecules. Duplicates were measured twice in different chip positions. Averages and errors as standard deviation are reported. T = theoretical; E = experimental.

SAMs		Relative Atomic % and Relative Components %								
C8K		S		N		C			O	
	T	1.3		21.5		64.6			12.7	
	E	1.0 ± 0.2		15.9 ± 0.8		66.7 ± 0.9			16.5 ± 0.2	
		S-Au	S-H	NH_3^+	N	C-C	C=O	CS,CN,CO	O-C	O=C
	T	100.0	0.0	52.9	47.1	47.1	17.6	35.3	10.0	90.0
	E	100	-	18.9 ± 0.9	81.8±0.9	63.8±1.0	15.4±0.7	20.8±0.6	15.5±1.8	84.5±1.8
C8K:TEG11 (40:1)		S		N		C			O	
	T	1.3		21.4		64.6			12.7	
	E	2.4 ± 0.2		6.0 ± 0.6		73.8 ± 0.9			17.8 ± 0.4	
		S-Au	S-H	NH_3^+	N	C-C	C=O	CS,CN,CO	O-C	O=C
	T	100.0	0.0	52.9	47.1	47.2	17.5	35.3	10.9	89.1
	E	77.0±4.0	23.0 ±4.0	20.3±1.3	79.9±1.3	56.3±0.3	5.9±0.3	37.8±0.6	74.2±2.2	25.8±2.2

Table 5.9 - XPS element ratios for C8K and C8K:TEG11 40:1 SAMs. Theoretical (T) values were obtained considering the atomic formulas of the SAM molecules and their solution ratios. T = theoretical; E = experimental.

SAMs		XPS Element Ratios				
		Au/S	Au/N	N/S	C/S	O/S
C8K	T	-	-	17	51	10
	E	75 ± 13.0	4 ± 0.1	17 ± 2.5	71 ± 9.8	18 ± 2.3
C8K:TEG11 (40:1)	T	-	-	17	50	10
	E	20 ± 1.0	8 ± 1.0	3 ± 0.2	31 ±1.1	8 ± 0.4

Similar to the results seen with C5K, in the C8K SAM the high resolution spectra for S 2p in Figure 5.8 showed only the thiolate species was present in the pure C8K SAM, while C8K:TEG11 40:1 SAM revealed 23% of free thiols at the surface (Table 5.8). This was similar to the TEG11 SAM (Table 5.2), indicating its contribution with 1) thiolate species and 2) free thiols. Regarding the N 1s spectra (Figure 5.8 (N 1s)), both nitrogen neutral (400 eV) and positive (402 eV) environments were present. The relative nitrogen components percentage in

this case suggests that three amino groups are protonated (+3e) instead of the theoretical eight (+8e), which as previously mentioned, could be due to the samples being under vacuum. The presence of N 1s at the mixed C8K:TEG11 40:1 confirms the presence of C8K at the surface, as TEG11 does not contribute with this element (as seen in Table 5.2). Relative to the XPS element ratios (Table 5.9), similar observations as with the previous C5K and C5K:TEG11 SAMs (Table 5.6) are seen. Table 5.9 shows the Au/S ratio decrease from the pure C8K SAM to the C8K:TEG11 SAM, indicating a more packed layer. Additionally, Table 5.9 also indicates that at C8K:TEG11 40:1 the surface potentially has more TEG11 moeities than C8K, as the N/S ratio is lower than expected.

Finally, through the previously described equations (Equation 5.2 to Equation 5.4), the C8K:TEG11 40:1 experimental ratio was of 1:6 ± 0.6, meaning that 240 fold more TEG11 moieties anchored to the surface than predicted by the solution ratio. Having more TEG11 moieties at the surface explains the discrepancy between the theoretical and experimental values presented in Table 5.9 for C8K:TEG11 40:1 and the low N/S ratio in Table 5.9.

These XPS results are in agreement with the previous findings through ellipsometry and contact angle for C8K and C8K:TEG11, being overall similar to those obtained with the C5K:TEG11 SAMs. However, the XPS data does not agree with the contact angle results through Cassie's equation. With Cassie's equation, the results showed identical surface ratios for C5K and C8K mixed with TEG11 (1:2) after being incubated in the same conditions (ratios C5K:TEG11 or C8K:TEG11 40:1), while the XPS results showed higher ratio to C5K (1:3 ± 0.2) compared with C8K (1:6 ± 0.6). Not only the XPS data revealed lower surface ratios for both C5K and C8K in the mixed SAMs, but also suggests that when C5K and C8K compete with TEG11 to bind to the surface, C5K has a faster kinetics compared to C8K. Similar to what has been seen in alkanethiols, it makes sense that longer the structure, slower the kinetics when competing

with TEG11 for the surface[210]. Perhaps the longer C8K structure contributes to higher contact angle increase due to how it might fold on top of TEG11 (Figure 5.9(B)), but it does not necessarily mean a higher number of C8K molecules at the surface (as the XPS demonstrated).

A summary of C5K:TEG11 and C8KTEG11 SAMs experimental ratio according to XPS and thickness according to ellipsometry can be seen in Figure 5.9 and Table 5.10. Briefly, results showed similar XPS ratios for both mixed SAMs and fairly similar relative thickness increase after addition of TEG11. It is possible to conclude that TEG11 has given support to the SAM structure, when comparing the thickness for the pure SAMs and mixed SAMs. Furthermore, the support from TEG11 was only seen after a certain amount of C5K or C8K molecules at the surface (Figure 5.9(A)). Such effect makes sense as, separated by less TEG11 molecules at the surface, the closer the oligopeptides will be, keeping a higher thickness (Figure 5.9(B)). Additionally, the low thickness at the pure SAMs highlights the flexibility of these oligopeptides – likely folded without TEG11 support - and brings up the next logical question: how densely packed these SAMs need to be to 1) provide the right thickness to avoid nanobody-antigen interactions and 2) allow oligopeptides retraction at the surface, allowing nanobody-antigen interactions.

Table 5.10 – Summary table with the oligopeptide:TEG11 40:1 XPS experimental ratio results and the respective ellipsometric thickness increase relatively to each respective pure SAM. The percentages are averages comparison.

SAMs	XPS ratio	Ellipsometric thickness increase relative to the pure SAM
C5K:TEG11 40:1	1: (3 ± 0.2)	20 %
C8K:TEG11 40:1	1: (6 ± 0.6)	17 %

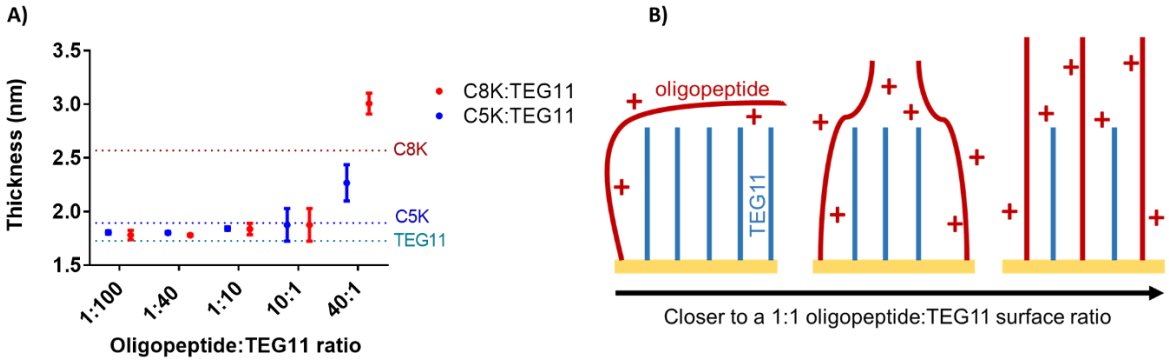

Figure 5.9 – TEG11 support effect on thickness SAMs. (A) Thickness trend for both C5K:TEG11 and C8K:TEG11. The overall SAM thickness increases with less TEG11 molecules in the incubation solution ratio. (B) Representative schematics for TEG11 support effect with charged oligopeptides.

When using these oligopeptides with nanobody-like structures, it will be crucial to conceal them when applying their opposite charge at the surface. The right TEG11 support needed has to allow a balance between 1) the right thickness to stop nanobody-antigen interaction and 2) the right flexibility to allow the oligopeptides to retract at the surface, providing nanobody-antigen interaction. To find the right balance, the next step with these oligopeptides would be including the nanobody at the surface.

Providing that low densities of TEG11 would be required to allow the oligopeptides retraction at the surface, that means that less flexible oligopeptides are needed – which with low densities of TEG11 can reach the efficient thickness to conceal a nanobody binding site. Thus, the following SAMs studied were composed by theoretically more rigid oligopeptides containing proline groups: with a cysteine (C) at the C-terminal and followed by either, proline (P) and lysine (K) (C-PPεK-PPεK- PPεK-PP, C3εK for simplicity) or proline and diamino propionic acid (Dap) (C-PPβDap-PPβDap-PPβDap-PP, C3βD for simplicity). The SAMs composed purely of C3εK or C3βD and each mixed with TEG11 were analysed by ellipsometry and contact angle, results shown in Figure 5.10. At this stage, using the knowledge from the

previous studies with C5K and C8K, the solution ratio of oligopeptide:TEG11 40:1 was directly analysed.

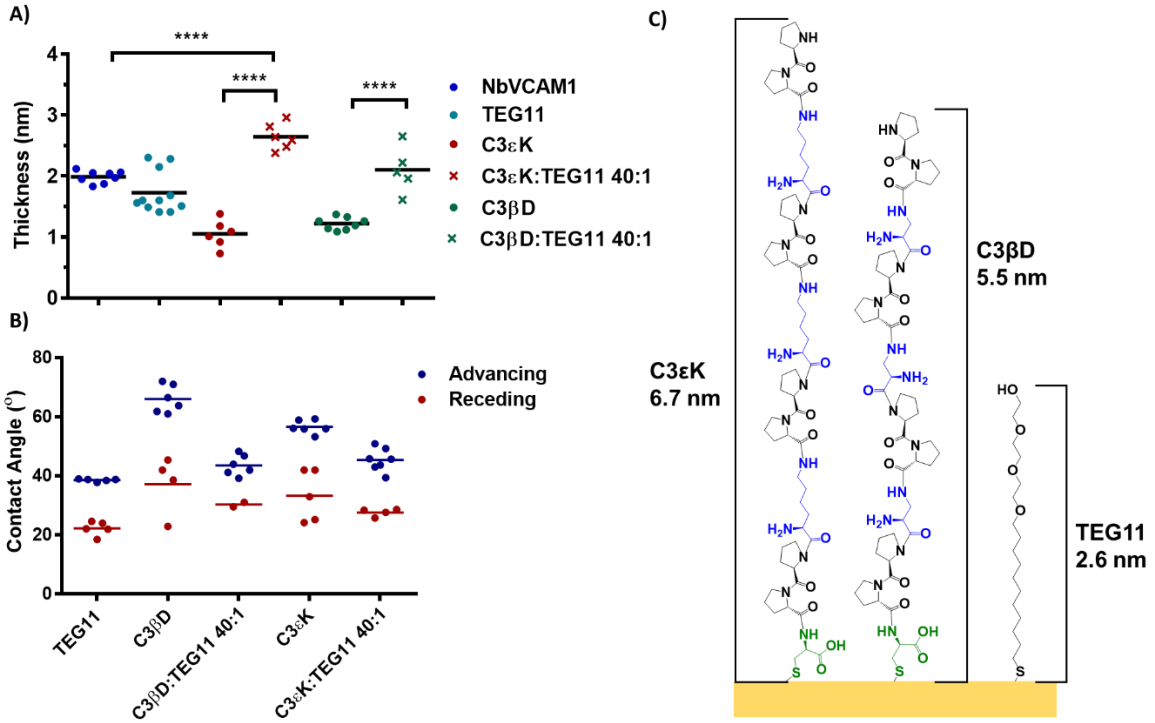

*Figure 5.10 – C3εK, C3βD, mixed C3εK:TEG11 and C3βD:TEG11 SAMs ellipsometry and contact angle results. Results for (A) thickness and (B) advancing and receding contact angles, show that TEG11 has given support to the mixed SAMs when incubated at oligopeptide:TEG11 40:1 ratio, with significantly different thickness when compared with the respective pure SAMs thickness. Significant differences noted as **** (t test, p < 0.0001). (C) C3εK, C3βD and TEG11 schematics with the ChemDraw theoretical thicknesses.*

It is possible to observe from the thickness results (Figure 5.10(A)) that there were significant differences between the mixed SAMs thickness and their respective pure SAMs (t test, $p < 0.0001$). Only after introducing TEG11 on the SAMs, these oligopeptides presented a height equivalent (C3βD with 2.1 ± 0.3 nm) or superior (C3εK with 2.6 ± 0.2 nm) to the nanobody

reference (2.0 ± 0.1 nm). From these results, C3εK:TEG11 is the SAM that most likely could efficiently avoid nanobody-antigen interactions. Looking at the contact angle results (Figure 5.10(B)) it is possible to observe how scattered the data is for the pure SAMs, with high angle hysteresis, indicating that probably these SAMs are unorganized at the surface. Following Cassie's law, an estimative of 1:2 and 1:3 oligopeptide:TEG11 surface ratios were obtained for C3εK and C3βD respectively (Table 5.11) further confirming that the solution ratio of oligopeptide:TEG11 40:1 succeeded in having both components at the surface.

Table 5.11 - Results obtained from Cassie's law for the C3εK and C3βD surface ratios in the mixed C3εK:TEG11 and C3βD:TEG11 SAMs.

Solution Ratios	Surface ratios (from Cassie's law)
C3εK:TEG11 40:1	1:2
C3βD:TEG11 40:1	1:3

In order to confirm the surface ratio for the C3εK:TEG11 and the C3βD:TEG11 SAMs, these were analysed with XPS, together with their pure SAMs as controls. The XPS results can be seen in Figure 5.11 and Figure 5.12 for the high resolution spectra of C3εK:TEG11 and C3βD:TEG11 SAMs respectively. XPS results for the relative atomic and component percentages are described in Table 5.12, and for the element ratios in Table 5.13.

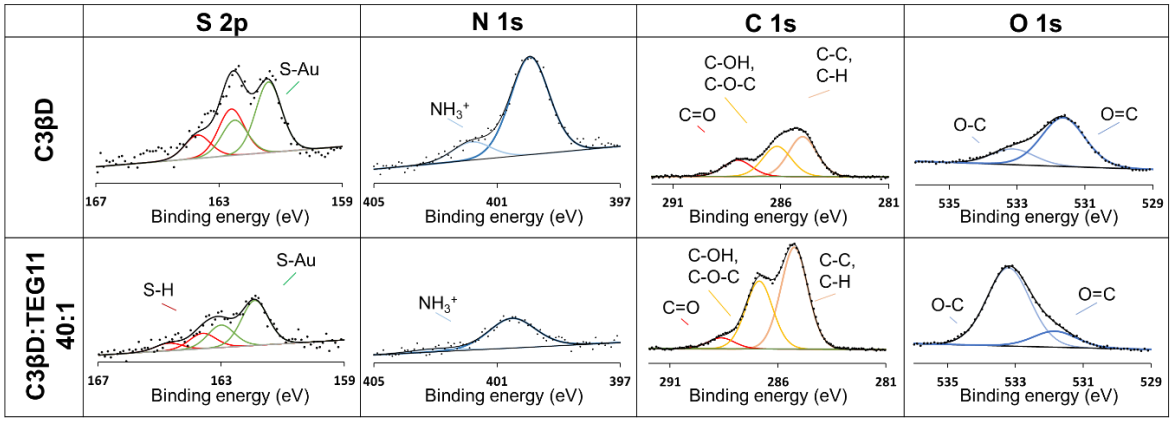

Figure 5.11 - C3βD and C3βD:TEG11 40:1 SAMs XPS results. Representative XPS high resolution spectra of the S 2p, N 1s, C 1s, and O 1s regions. Each spectra of each element has the same vertical scale respectively (not represented).

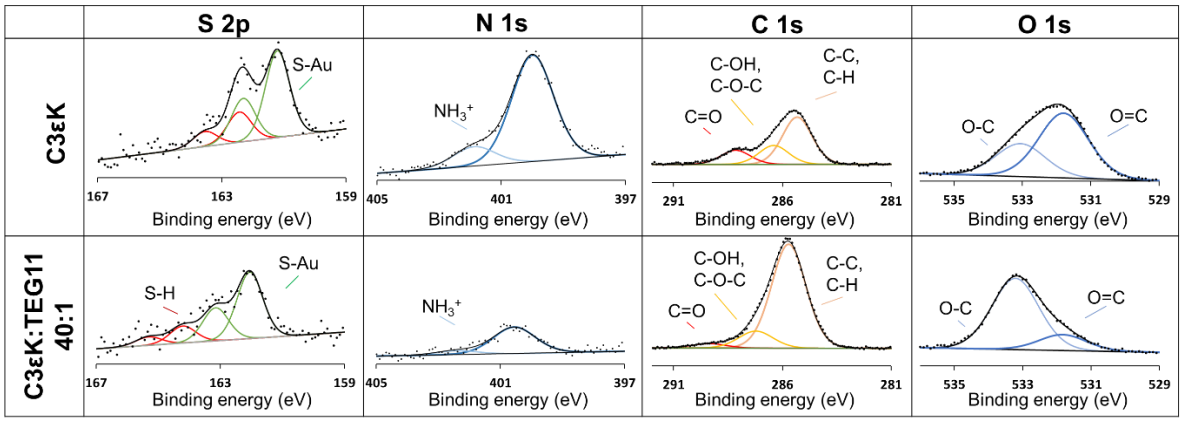

Figure 5.12 - C3εK and mixed C3εK:TEG11 40:1 SAMs XPS results. Representative XPS high resolution spectra of the S 2p, N 1s, C 1s, and O 1s regions. Each spectra of each element has the same vertical scale respectively (not represented).

The S 2p high resolution spectra for both pure SAMs of C3βD and C3εK from Figure 5.11 (S 2p) and Figure 5.12 (S 2p) respectively, show that the two sulphur environments (thiol (red) and thiolate (green)) are present at the surface. This differs from the C5K and C8K pure SAMs (Figure 5.6 and Figure 5.8) indicating that with the rigid oligopeptides (C3βD and C3εK), the washing process was not as efficient as with the flexible oligopeptides (C5K and C8K).

Additionally, looking at the sulphur atomic relative percentages obtained (Table 5.12 for S), it is possible to observe a higher experimental percentage than the theoretical in all the samples, whilst the nitrogen relative percentage is smaller than expected. Following that, Table 5.13 shows a considerable discrepancy between the theoretical and experimental ratios N/S, C/S and O/S on both pure and mixed SAMs. Despite the presence of N 1s which indicates the presence of the oligopeptides, the experimental ratios indicate a disproportional higher amount of sulphur relatively to the other elements, which could indicate either sulphur contamination or that these oligopeptides are potentially not stable for long periods (>24h, see Experimental Procedures, Section 6.3.2.6) at dry state, potentially breaking down into smaller peptides prior to analysis. Amino acids[211], including proline[212] degradation has been studied before by XPS. Further investigation should be done to confirm degradation with these oligopeptides.

When comparing the pure with the mixed SAMs (C3βD:TEG11 40:1 and C3εK:TEG11 40:1), the spectra shows overall a lower intensity for sulphur and a lower amount of free thiols, as described in Table 5.12. The sulphur components relative ratios (S-Au to S-H) ranged from overall 60%-40% at the pure SAMs, to 80%-20% at the mixed SAMs (Table 5.12). Despite the high percentages of free thiols, the introduction of TEG11 to the SAMs that potentially contributed to higher degree of organisation and packing (as previously seen with ellipsometry and contact angle results), reducing the free thiols percentage to the previously obtained with TEG11 (~20%).

Table 5.12 - Relative atomic percentages and relative components percentages calculated by XPS for C3εK, C3βD, mixed C3εK:TEG11 40:1 and C3βD:TEG11 40:1 SAMs. Theoretical (T) values were obtained considering the atomic formulas of the SAM molecules. Duplicates were measured twice in different chip positions. Averages and errors as standard deviation are reported. T = theoretical; E = experimental.

SAMs		Relative Atomic % and Relative Components %								
C3βK		S		N		C			O	
	T	1.2		18.5		64.2			16.0	
	E	8.0 ± 1.1		11.9 ± 1.4		64.3 ± 3.6			15.7 ± 1.3	
		S-Au	S-H	NH_3^+	N	C-C	C=O	CS,CN,CO	O-C	O=C
	T	100.0	0.0	20.0	80.0	30.8	23.1	46.2	7.7	92.3
	E	61.4±1.6	38.6 ±1.6	15.2±1.7	84.8±1.7	54.2±13.3	14.0±3.3	31.8±15.2	31.2±4.5	68.8±4.5
C3βK:TEG11		S		N		C			O	
	T	1.3		18.4		64.3			16.1	
	E	3.1 ± 0.5		3.3 ± 0.7		75.6 ± 2.3			18.0 ± 1.6	
		S-Au	S-H	NH_3^+	N	C-C	C=O	CS,CN,CO	O-C	O=C
	T	100.0	0.0	20.0	80.0	31.0	22.9	46.1	8.4	91.6
	E	75.9±1.8	24.1 ±1.8	10.4±2.4	89.6±2.4	56.7±2.2	5.0±0.4	38.3±1.8	85.8±2.1	14.2±2.1
C3εK		S		N		C			O	
	T	1.1		16.7		67.8			14.4	
	E	3.6 ± 0.3		12.4 ± 0.7		66.4 ± 4.4			17.6 ± 4.4	
		S-Au	S-H	NH_3^+	N	C-C	C=O	CS,CN,CO	O-C	O=C
	T	100.0	0.0	20.0	80.0	41.0	19.7	39.3	7.7	92.3
	E	67.8±19.2	32.2 ±19.2	18.4±8.9	81.6±8.9	54.2±13.3	14.0±3.3	31.8±15.2	43.7±29.9	56.3±29.9
C3εK:TEG11		S		N		C			O	
	T	1.1		16.6		67.8			14.5	
	E	2.2 ± 0.3		2.2 ± 0.9		81.0 ± 2.2			14.6± 1.3	
		S-Au	S-H	NH_3^+	N	C-C	C=O	CS,CN,CO	O-C	O=C
	T	100.0	0.0	20.0	80.0	41.1	19.5	39.4	8.4	91.6
	E	80.3±3.2	19.7 ±3.2	14.3±2.8	85.7±2.8	71.7±10.4	3.8±0.7	24.5±9.8	85.7±2.6	14.3±2.6

For the N 1s element, the predicted ratio for the positive and neutral environment of 20% – 80% respectively, considered three protonated amine groups in both rigid oligopeptides (+3e). The experimental ratio for both pure C3βD and C3εK SAMs was approximately 15% positive – 85% neutral environments (Table 5.12 for NH_3^+ and N), which could indicate that only two amine groups were protonated (+2e). The introduction of TEG11 decreased the atomic nitrogen

percentage (Figure 5.11 (N 1s) and Figure 5.12 (N 1s)) as expected, as TEG11 does not contribute with nitrogen. For carbon (C 1s) and oxygen (O 1s) elements, as observed in Figure 5.11 and Figure 5.12 (and previously seen with C5K and C8K), besides the predicted adventitious presence, TEG11 contributes particularly with C-C and O-C environments.

Table 5.13 - XPS element ratios for for C3εK, C3βD, mixed C3εK:TEG11 40:1 and C3βD:TEG11 40:1 SAMs. Theoretical (T) values were obtained considering the atomic formulas of the SAM molecules and their solution ratios. T = theoretical; E = experimental.

SAMs		XPS Element Ratios					
		Au/S	Au/N	N/S	C/S	O/S	C/N
C3βK	**T**	-	-	15	52	13	3
	E	13 ± 1.1	8 ± 0.5	2 ± 0.1	10 ± 2.2	2 ± 0.2)	6 ± 1.4
C3βK:TEG11 (40:1)	**T**	-	-	17	50	10	3
	E	18 ± 1.5	16 ± 1.8	1 ± 0.2	26 ±3.4	6 ± 0.6	24 ± 4.5
C3εK	**T**	-	-	15	61	13	4
	E	21 ± 0.6	6 ± 0.2	3 ± 0.1	18 ±1.5	4 ± 1.5	5 ± 0.2
C3εK:TEG11 (40:1)	**T**	-	-	15	60	13	4
	E	18 ± 1.7	21 ± 0.5	1 ± 0.3	39 ±5.6	7± 0.6	47 ± 17.1

In spite of the suspicion of sulphur contamination or oligopeptides degradation, the experimental surface ratio through the Equation 5.2 to Equation 5.4 previously described, for C3βD:TEG11 40:1 was of 1:(13 ± 2.5), and for C3εK:TEG11 40:1 was of 1:(17 ± 5.4) This means that on average there would be 560 and 760 fold more TEG11 moieties anchored to the surface than in the solution ratio, respectively. These calculated ratios will be less accurate in case of oligopeptides degradation, especially if the nitrogen elements are affected. Nevertheless, it is possible to conclude that these rigid oligopeptides had higher XPS variability, seen in the standard deviations reported in both Table 5.13 and Table 5.12.

To compare all oligopeptide SAMs (C5K, C8K, C3εK and C3βD) a summary of the differences in thickness, contact angle and XPS is presented in Figure 5.13 and Table 5.14.

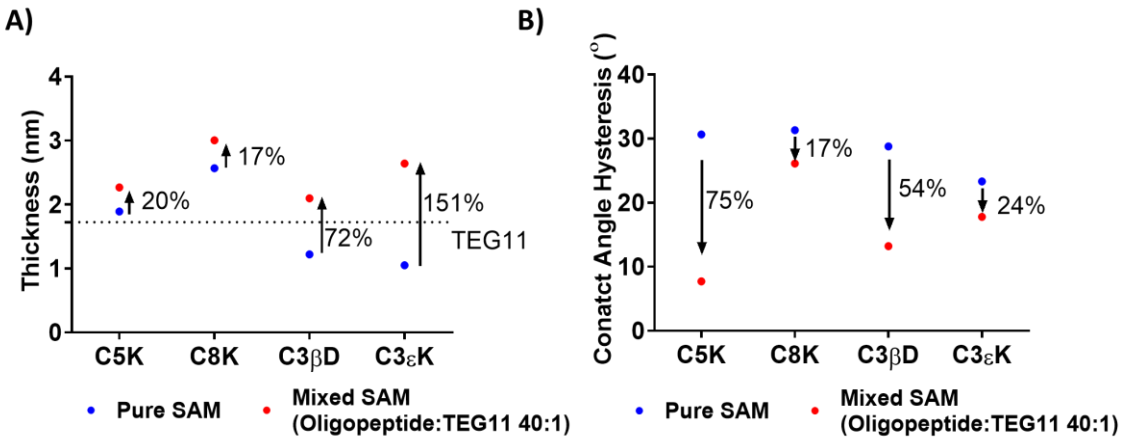

Figure 5.13 – Differences between the oligopeptides pure SAMs (blue) and mixed oligopeptide:TEG11 SAMs (red) in (A) thickness and (B) contact angle hysteresis. In (A) the dashed line represents the TEG11 average thickness. In both graphs (A and B) the averages are represented and the increase or decrease percentages were calculated relatively to the averages.

Observing Figure 5.13(A) (blue points), unlike C5K and C8K, in both the rigid oligopeptides (C3εK and C3βD), the pure SAMs had a lower thickness than TEG11 SAM which is counterintuitive and suggests disperse pure SAMs. Moreover, the results show that TEG11 provided higher thickness increase to the rigid oligopeptides relatively to their pure SAMs (Figure 5.13(A), red points for C3βD with 72% increase and C3εK with 151% increase). It is also possible to observe that TEG11 contributed to higher surface organisation (with higher decrease in angle hysteresis) when mixed with shorter oligopeptides (Figure 5.13(B) red points for C5K and C3βD with 75% and 54% lower hysteresis respectively).

In conclusion, the above results suggest that TEG11 provides 1) better support at increasing SAM thickness when mixed with rigid oligopeptides and 2) overall higher SAM organisation when mixed with any of the oligopeptides, but especially with the shorter oligopeptides.

The following Table 5.14 summarizes the ellipsometry, contact angle and XPS results obtained for the oligopeptides pure and mixed SAMs studied, also showing the results for TEG11 and

the nanobody NbVCAM1. The Cassie's ratios were seen as preliminary values being less reliable than the XPS ratios, due to the contact angles difference between the pure TEG11 SAMs and the pure oligopeptides SAMs.

Table 5.14 – Summary table of the pure C5K, C8K, C3βD and C3εK SAMs and mixed oligopeptide:TEG11 40:1 SAMs results for thickness, contact angle hysteresis and XPS oligopeptide:TEG11 ratios.

SAMs	Ellipsometry (nm)	Contact Angle Hysteresis (º)	Preliminary Cassie's Ratios	XPS ratios ($S_{peptide}/S_{TEG11}$)
NbVCAM1	2.0 ± 0.1	36.6	-	-
TEG11	1.7 ± 0.3	16.1	-	-
C5K	1.9 ± 0.2	30.7	-	-
C5K:TEG11 40:1	2.3 ± 0.2	7.7	1: 2	1: (3±0.2)
C8K	2.6 ± 0.2	31.3	-	-
C8K:TEG11 40:1	3.0 ± 0.1	26.1	1: 2	1: (6±0.6)
C3εK	1.1 ± 0.2	28.8	-	-
C3εK:TEG11 40:1	2.6 ± 0.2	13.2	1: 2	1: (17±5.4)
C3βD	1.2 ± 0.1	23.3	-	-
C3βD:TEG11 40:1	2.1 ± 0.4	17.8	1: 3	1: (13±2.5)

In conclusion, the solution ratio of oligopeptide:TEG11 at 40:1 seems promising to use when mixing any of the studied oligopeptides with nanobodies. Even when these oligopeptide:TEG11 mixed SAMs present similar thickness to the nanobody, oligopeptides could potentially still provide control over nanobody-antigen interaction. Therefore, based on their diverse lengths and properties, the studied oligopeptides provide optionality when considering a nanobody-antigen system.

5.2.1.1. Preliminary switching studies with the system NbVCAM1:C5K:TEG11

From all the oligopeptides tested previously, C5K was chosen for further testing because its thickness should provide coverage just above the nanobody's binding site and simultaneously should efficiently fold to the surface upon opposite potential. Initial open circuit studies were performed at the SPR with the nanobody-antigen system studied in Chapter 3 (NbVCAM-hVCAM1). The antigen hVCAM1 was injected on the SAM formed by the combining ratio NbVCAM1:C5K:TEG11 500:40:1 and on the respective controls composed by only C5K:TEG11 40:1, results shown in Figure 5.14.

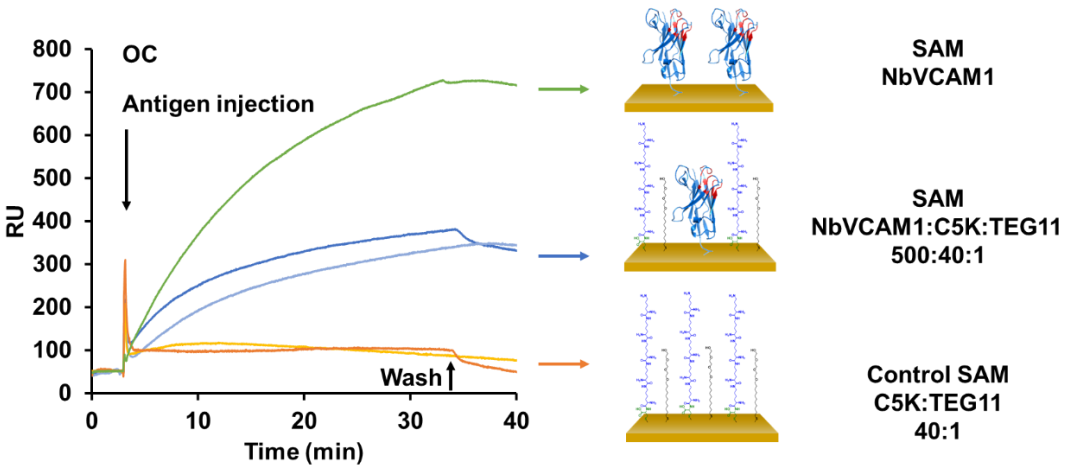

Figure 5.14 - SPR sensorgram for hVCAM1 injections under open circuit (OC) on NbVCAM1, NbVCAM1:C5K:TEG11 and control SAMs.

As expected, the mixture of C5K and TEG11 with NbVCAM1 at the surface resulted in the decrease of response upon the antigen injection (Figure 5.14, green line ~700 RU to blue lines ~300 RU). Such decrease could be due two reasons: 1) less NbVCAM1 at the surface and 2) potential partial coverage from the C5K moieties. Nevertheless, some binding was still

observed (Figure 5.14, blue) which could indicate that either 1) more C5K moieties are needed to cover the binding site or 2) longer oligopeptides. To understand if C5K could maximize further coverage, the next step was to apply positive potential (+0.3V) at the surface, which should allow the positively charged C5K to stretch perpendicular to the surface. C5K:TEG11 40:1 SAM at positive potential, after injection of the respective antigen resulted in an increase in response (to ~ 1200 RU, Figure 5.15(A)). The unexpected increase indicates non-specific interaction between the SAM and the antigen hVCAM1 (with estimated negatively charged network at pH 7), making the C5K:TEG11 SAM unsuitable to use with NbVCAM1 under applied potential. On other note, the same SAM control surface was used with a second antigen, EGFP (Figure 5.15(B)), which showed the absence of non-specific interactions, as the response goes back to the baseline after the antigen injection finished and the running buffer starts (increase in response during injection is due to the refractive index associated with the bulk solution). This further confirms that use of charged oligopeptides are dependent on the nanobody-antigen system in use, requiring initial screening and appropriate controls.

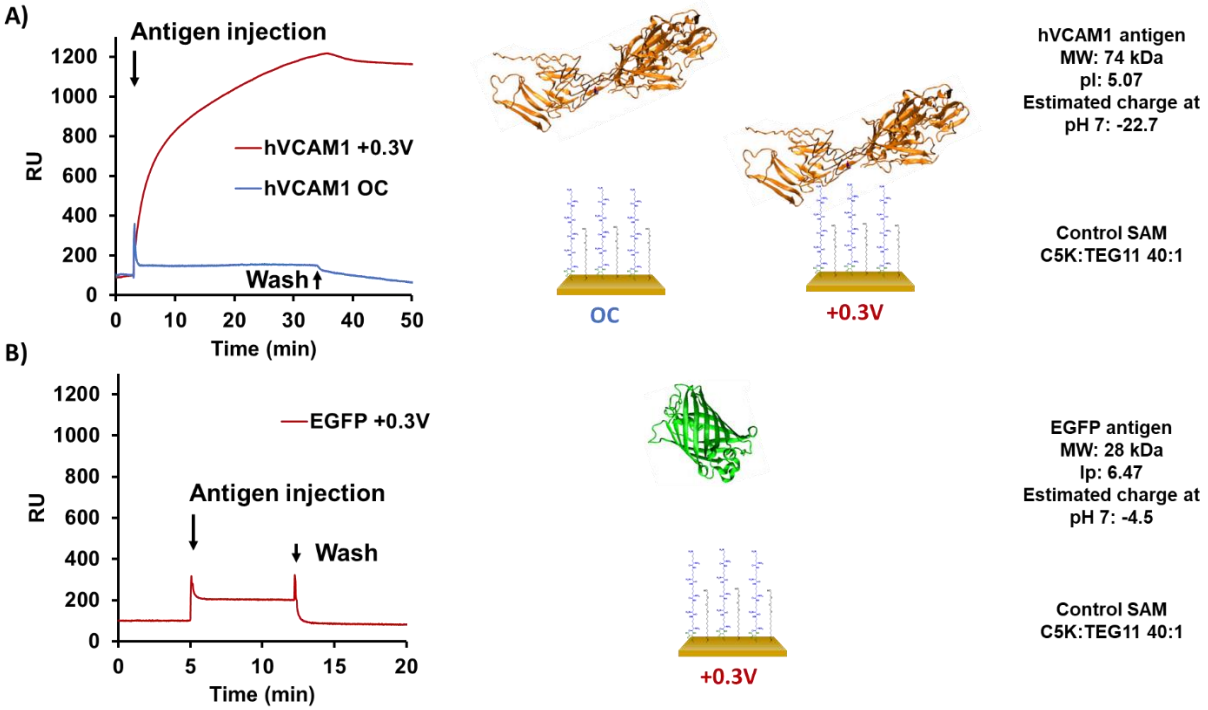

Figure 5.15 – Antigen injection studies on C5K:TEG11 40:1 SAM controls under OC and +0.3V. SPR sensorgram and schematic representation . of (A) hVCAM1 antigen injection on C5K:TEG11 40:1 SAM under either open circuit (OC, blue) or under positive potential (+0.3V, red). The latter shows non-specific interactions; (B) EGFP antigen injection on C5K:TEG11 40:1 SAM under positive potential (+0.3V, red) shows no interactions. Different time scales are presented due to different assay optimal conditions. hVCAM: pI: 5.07; estimated charge at pH 7 = -22.7 (protcalc); MW: 74 kDa. EGFP: pI: 6.47; estimated charge at pH = -4.5 (protcalc); MW: 28 kDa.

To understand if the non-specific interactions obtained at the C5K:TEG11 40:1 were exclusively related with the C5K moiety, another control was tested on the pure TEG11 SAM surface (Figure 5.16). Upon antigen injection, the TEG11 SAM had higher response from non-specific interactions with the antigen, than the mixed C5K:TEG11 40:1 SAM. These results indicate that TEG11 lower antifouling effect is partially responsible for non-specific interaction intensified by the surface opposite charge to the antigen. Thus TEG11 should be replaced by other support molecule (at least with this nanobody-antigen system). To further conclude on

the non-specific interactions exclusively related to the C5K, other control with the pure C5K SAM at positive potential should be tested.

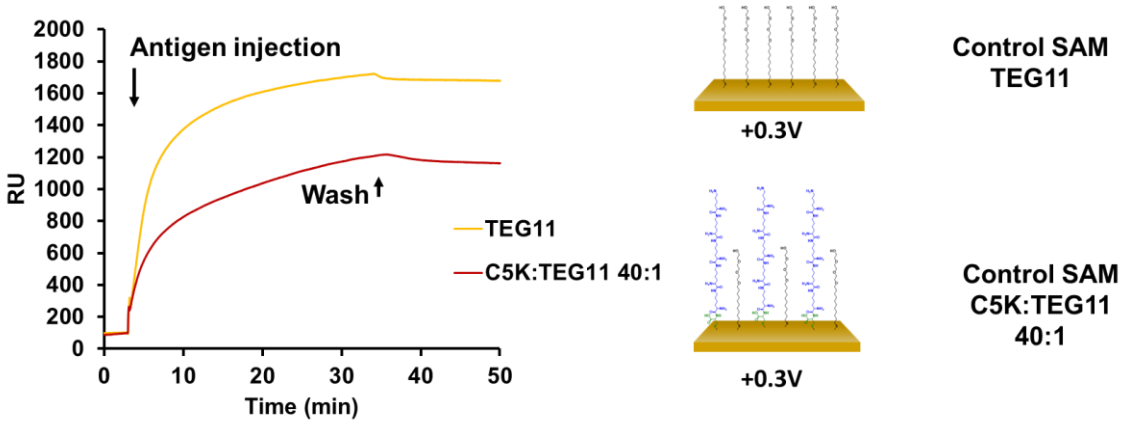

Figure 5.16 – SPR sensorgram for antigen hVCAM1 injection on the control SAMs upon positive potential (+0.3V).

Overall, different SAM surfaces functionalised with positively charged oligopeptides (C5K, C8K, C3βD and C3εK) have been formed and characterised according to their contact angle (advancing and receding), thickness and surface composition (summarised in Table 5.14). All the suggested oligopeptides, in terms of thickness achieved, are potential switchable moeities to be used with nanobody-like structures, potentially being able to provide binding site coverage and consequently nanobody-antigen binding control. However, for non-specific interactions with both nanobody and antigen, the right controls need to be put in place at all the potentials applied.

5.2.2. **Switching moieties: charged oligopeptides compatible with EDC/NHS**

In Chapter 4, it was revealed that the nanobody NbGFP immobilised through EDC/NHS did not change conformation under applied potential (Section 4.2.3), making this nanobody a good candidate to include in an electro-switchable surface. To create an electro-switchable surface with the NbGFP, ideally the switching units would immobilize simultaneously to the nanobody, under the same EDC/NHS conditions. This means that positively charged oligopeptides are not suitable, as their amines could react with the surface. Consequently, the oligopeptides would lose their required elongation and thus ability to protect the nanobodies binding site.

In the previous section, results have shown that C5K thickness, theoretically of 4.3 nm, could potentially be just enough to cover nanobodies binding sites. For this section goal, and following that preliminary evidence, negatively charged oligopeptides, composed by seven glutamic acids and one N-terminal beta alanine, with a theoretical thickness of 4.4 nm were designed (and named 7EA).

As a starting point, 7EA oligopeptides were investigated to bind to the surface through EDC/NHS coupling. Based on the results discussed in Chapter 4, the optimal NbGFP immobilisation though EDC/NHS on mercaptoundecanoic acid terminated surfaces (MUA) was at pH 5.4. Herein, the same conditions were used to immobilize 7EA. To understand how 7EA immobilised at pH 5.4, MUA SAMs and MUA-7EA surfaces were formed and characterised by contact angle and ellipsometry (Figure 5.17).

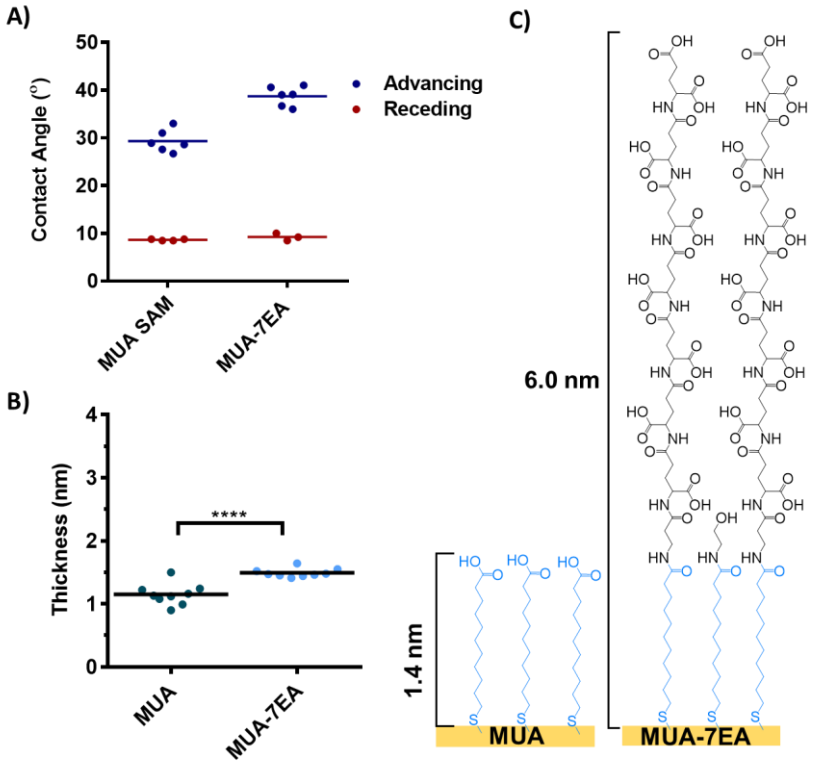

*Figure 5.17 - Ellipsometry and contact angle results for MUA SAM and MUA-7EA after EDC/NHS chemistry. (A) Advancing (blue) and receding (red) contact angle results; (B) ellipsometric thickness results. Significant differences noted as **** (t-test, $p < 0.0001$); (C) schematics and theoretical thickness (ChemDraw) for MUA and MUA-7EA functionalised surfaces.*

Figure 5.17(A) showed an increase in advancing contact angle from the MUA SAM (29.3 ± 2.3°) compared to the MUA-7EA (38.8 ± 2.0°) functionalised surface, indicating that both surfaces kept heir hydrophilic behaviour. Figure 5.17(B) shows that both surface thicknesses as measured by ellipsometry were significantly different (t test, $p < 0.0001$). MUA resulted in thickness of 1.2 ± 0.2 nm and MUA-7EA in 1.9 ± 0.1 nm (which means that 7EA contributed with ~0.7 nm). Although the significant increase in thickness, MUA-7EA only increased by 0.3 fold, whereas a 4.3 fold increase was expected. Such discrepancy between theoretical and actual thickness has been observed along this thesis to some extent (previously in Section 5.2.1, C5K was 1.9 ± 0.2 nm while theoretically 4.3 nm), especially if no support molecule was included

(such as TEG11). However, these results could potentially indicate that MUA-7EA was not successfully formed.

Facing the hypothesis that pH 5.4 is non-optimal for the amino coupling of 7EA oligopeptides, the following study focused on understanding the EDC/NHS amino coupling of small structures (<1 kDa) under these conditions. To do so, dodecylamine (DA) was used instead of the oligopeptides, as a cheaper alternative with one primary amine (Figure 5.18) and the convenient hydrophobic alkyl chain allowing a better demonstration of the reaction success through contact angle.

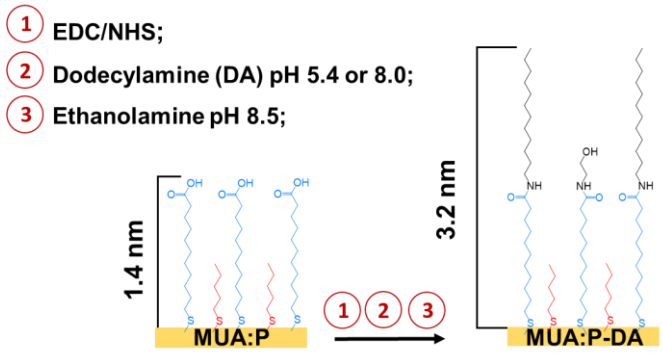

Figure 5.18 – Representative schematics for the EDC/NHS amino coupling between dodecylamine (DA) and mercaptoundecanoic acid (MUA) terminated surfaces. The MUA surfaces were also spaced with pentanethiol (P) at solution ratios MUA:P 1:1 and 1:3. While the surface before EDC/NHS should be hydrophilic, the final surface should be hydrophobic. The theoretical highest thicknesses (ChemDraw) for the MUA SAMs (MUA:P) and after EDC/NHS (MUA:P-DA) are represented.

The success of amino coupling of DA should be easily detected through contact angle, as the hydrophilic initial carboxylic-terminated SAM should change to a hydrophobic alkyl-terminated monolayer. Ellipsometry should also confirm these results with an increase in thickness. First, MUA densities at the surface were investigated to determine if they could

impact the effectiveness of the EDC/NHS reaction. To do so, the initial MUA SAM was mixed with pentanethiol (Figure 5.18)), at solution ratios of MUA:pentanethiol 1:3 and 1:1. Initial contact angle and ellipsometry (Figure 5.19 (B and C)).

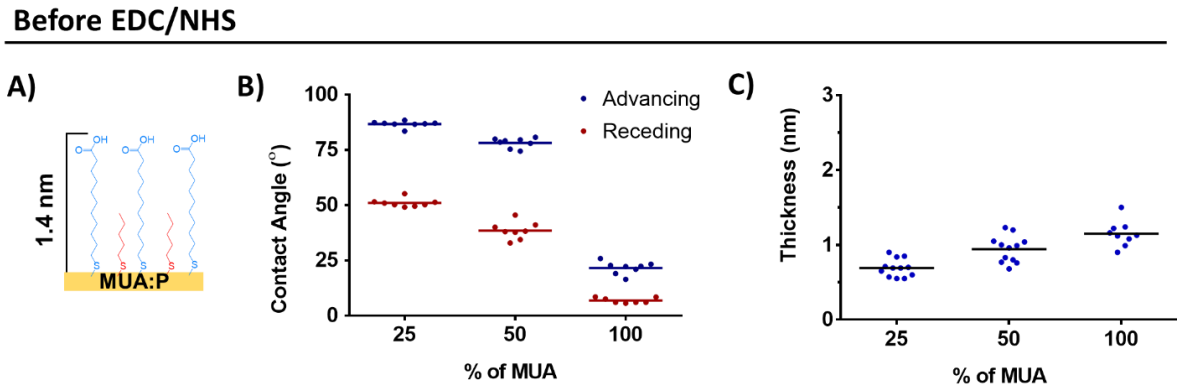

Figure 5.19 – Before EDC/NHS amino coupling, the initial mercaptoundecanoic acid (MUA) mixed with pentanethiol SAM characterisation. (A) Representative schematics with the theoretical highest thicknesses (ChemDraw) for the MUA SAMs (MUA:P). Surface results of the initial MUA:pentanethiol SAMs incubated at the solution ratios of 3:1, 1:1 and 1:0 for (B) advancing (blue dots) and receding (red dots) contact angle, and (C) ellipsometric thickness.

MUA surfaces were analysed before the EDC/NHS reaction. Figure 5.19(B) showed a decrease in the advancing (blue) and receding (red) contact angle as the percentage of MUA in the incubation solution increased. Figure 5.19(C) showed an increase in the thickness average. All the mixed surfaces had a lower advancing angle and higher thickness than the experimental values for a pure pentanethiol SAM (advancing angle of 96° and thickness of 0.5 nm)[213]. These results indicate the presence of MUA in the mixed surfaces, with increased density resulted in in thicker and more hydrophilic surfaces.

In Chapter 4, it was demonstrated the NHS/EDC amino coupling of the NbGFP nanobody at pH 5.4, 7.0 and 8.0. The results obtained at pH 5.4 resulted in the highest nanobody-antigen interaction, making this pH optimal. However, the neutral and basic pH conditions resulted in higher NbGFP immobilisation, which could have impacted the antigen interaction due to steric hindrance at the surface. With interest in the immobilisation of the switching moeities simultaneously to the NbGFP, pH 5.4 was chosen for preliminary studies of the EDC/NHS efficiency between MUA and dodecylamine (DA). Additionally, if the hypothesis that at pH 8.0 the nanobody-antigen interaction did not succeed due to steric hindrance, and considering that the switching moieties could also provide spacing between nanobodies, the pH 8.0 as a basic condition was also studied for comparison (Figure 5.20).

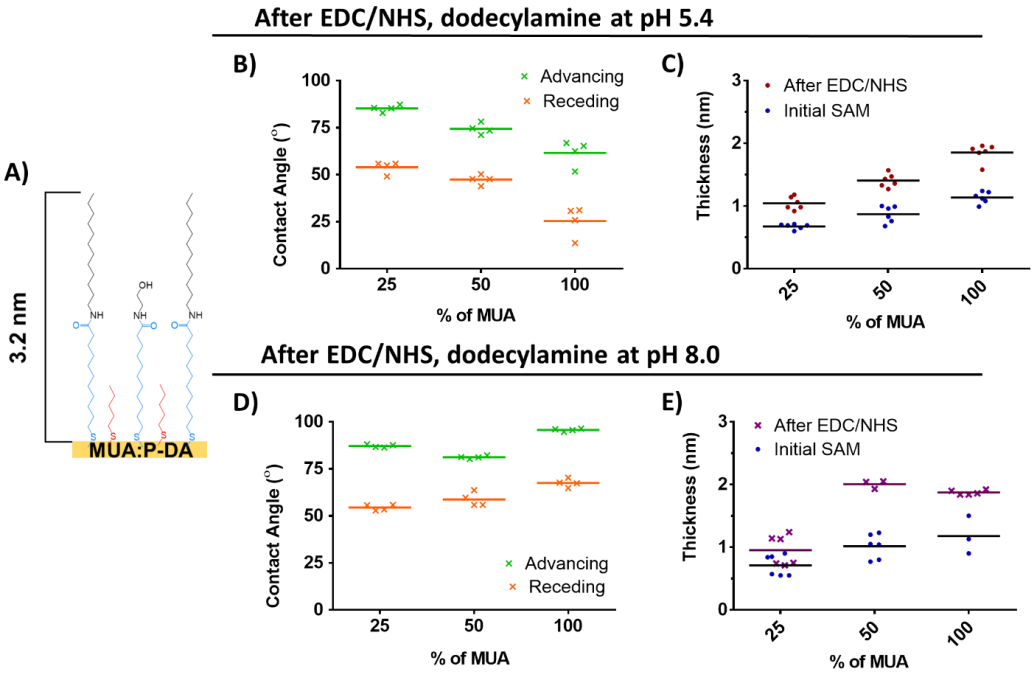

Figure 5.20 – Characterisation of dodecylamine-terminated (-DA) surfaces after EDC/NHS amino coupling on MUA-terminated SAMs: studies at pH 5.4 or 8.0, with different initial MUA SAM densities. (A) Representative schematics with the theoretical highest thickness (ChemDraw) after EDC/NHS, for dodecylamine terminated monolayers, on mixed mercaptoundecanoic acid and penthanethiol SAMs (MUA:P-DA). Results after EDC/NHS of (B) advancing (green crosses) and receding (orange crosses) contact angles at pH 5.4 or pH 8.0 (D); and (C) ellipsometric thickness before (blue dots) and after (red dots) the coupling reaction at pH 5.4 or pH 8.0 (E). Data points are represented with averages.

Comparing the contact angle results from before (Figure 5.19(D)) and after performing EDC/NHS on the MUA-terminated SAMs at pH 5.4 or pH 8.0 (Figure 5.20 (B and D)), different increase rates in contact angle are observed. At pH 5.4 there only appears to be an increase in both receding and advancing angles at surfaces incubated with 100% MUA (Figure 5.20(B)). At pH 8.0 the increase in receding angle is evident from SAMs incubated with 50% MUA (with 61% increase). The ellipsometry results, at pH 5.4, show that the different initial MUA densities contribute to similar thicknesses increase (from 55% to 63% increase), while at pH 8.0, the 50% MUA contributed with the highest increase in thickness (with 98% increase). Comparing the above conditions, the results suggest that EDC/NHS for small structures composed by one primary amine is potentially more efficient if performed at basic pH, which could benefit from spacing out the initial MUA SAM (as when incubated with 50% MUA). However, the same benefit was not seen at the acidic pH, and due to the primary aim being to understand the coupling at acidic pH, the following studies will use 100% MUA surfaces.

The next step was to visualise through the SPR the EDC/NHS amino coupling on MUA surfaces. The following studies used different concentrations of the molecule to couple to understand the impact of higher concentrations on the coupling yield. This time the AminePEG_7Boc (MW=469 g/mol, Figure 5.21(A)) was chosen over the dodecylamine (MW=185 g/mol) due the higher molecular weight, which should be beneficial to increase the signal on the SPR. Results are shown in Figure 5.21(B).

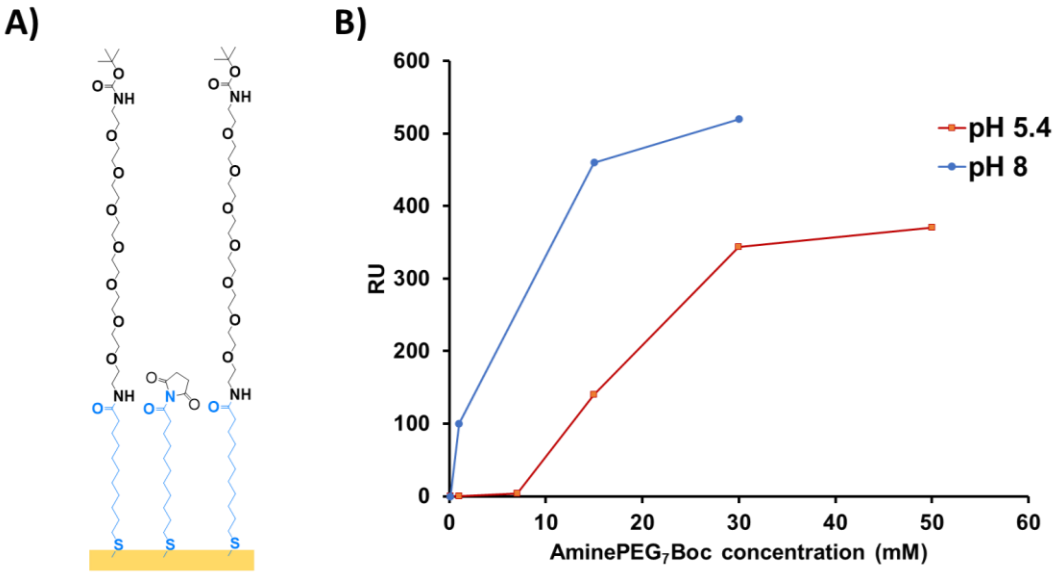

Figure 5.21 – SPR responses obtained with different concentrations of amine-PEG$_7$-Boc, at pH 5.4 or 8.0, on MUA surfaces through EDC/NHS. (A) representative schematics after the amino coupling reaction between the MUA molecules (blue) and the amine-PEG$_7$-Boc, before deactivation of remaining active esters with ethanolamine. (B) SPR responses after amine-PEG$_7$-Boc injection and washing step, representing the increase from the amino coupling between MUA and amine-PEG$_7$-Boc molecules.

The SPR results shown in Figure 5.21(B) showed a clear higher performance from the EDC/NHS when the amine-PEG$_7$-Boc was injected at pH 8.0. At basic pH the results showed an evident increase in signal from lower concentrations, also reaching higher responses at the same concentrations used with pH 5.4. At acidic pH the saturation was reached at lower responses, when compared with the basic pH. These results show that on the same surface more molecules couple when the amino reaction happened under basic conditions. Figure 5.21(B) confirms that higher concentrations of the amine-PEG$_7$-Boc injected will lead to more molecules at the surface, however, such range of molarity is unsuitable to use with oligopeptides, due to cost. To test a lower range of concentrations (≤1 mM), and considering the earlier results with contact angle and ellipsometry obtained with 0.1 mM of dodecylamine (Figure 5.20), it was hypothesized that the lower concentrations of injected amine-PEG$_7$-Boc

instead of not being coupled, were not being detected by SPR. To confirm this, EDC/NHS coupling with lower concentrations was tested and quantified using amine-PEG$_7$-biotin on the SPR, with posterior neutravidin injection (Figure 5.22). The injection of neutravidin allowed the amplification of signal for the concentrations that were undetectable with amine-PEG$_7$-Boc (Figure 5.22(B and C) due to its higher molecular weight.

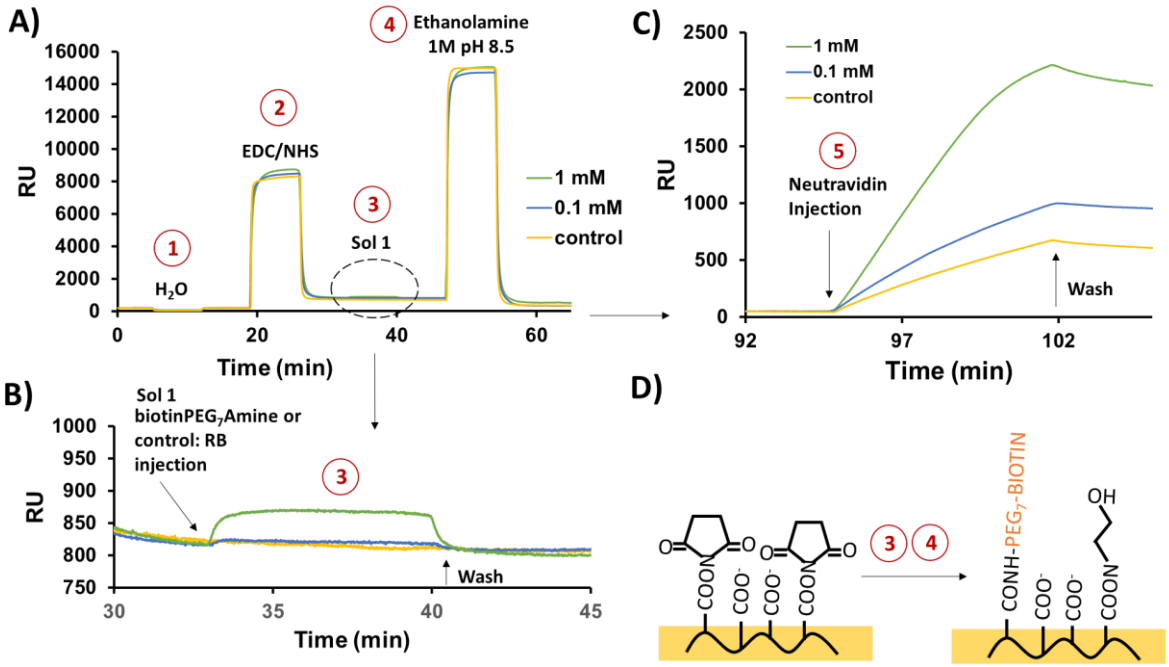

Figure 5.22 – SPR real time visualisation of EDC/NHS coupling of low concentrations of amine-PEG$_7$-biotin on MUA-terminated SAMs and posterior neutravidin injection. (A) SPR sensorgram of initial control water injection followed by EDC/NHS, solution 1 (sol1) amine-PEG$_7$-biotin at concentrations 0.1 (blue line) and 1 mM (green line) or just running buffer (RB pH 5.4, yellow line) for the control, and finally injection of ethanolamine to deactivate potential unreacted esters. (B) Rescaling of previous sensorgram, for better visualisation of solution 1 injection. At this point, the amino coupling is undetectable, being indistinguishable from the control (C) neutravidin injections (20 μg/mL) on the previously functionalised surfaces. (D) Representative schematics from the EDC/NHS activation to the amine-PEG$_7$-biotin coupling and remaining esters deactivation with ethanolamine.

The results from Figure 5.22(A) shown the whole experiment, from the EDC/NHS injection (2), to the injection of either amine-PEG_7-biotin at concentrations 0.1 (blue line) and 1 mM (green line) or just running buffer (RB pH 5.4, yellow) as a control. After this injection, the potential remaining unreacted esters were deactivated with the injection of ethanolamine, in order to avoid the amino-coupling of neutravidin afterwards. Figure 5.22(B) shows in detail the injections of amine-PEG_7-biotin or the control, where it is clear the response of the bulk solution in the case of 1 mM of amine-PEG_7-biotin. However, after the injection finished and the washing with the RB started, both concentrations are undistinguishable from the control as they return to the baseline. Thus the amino coupling was undetectable at this point. Then, Figure 5.22(C) shows the neutravidin injection on the previously functionalised biotin terminated surfaces. Regardless of the considerable non-specific interaction from the neutravidin on the OH-terminated control surface, it was possible to distinguish the surfaces that had been through EDC/NHS coupling with amine-PEG_7-biotin.

As seen previously in Chapter 4 (Section 4.4.1), performing click chemistry on a moving plate was more efficient than using SPR. To investigate if the same conclusion would apply with EDC/NHS coupling, the reaction was performed on a moving plate for 2 h (Figure 5.23) to improve the signal further.

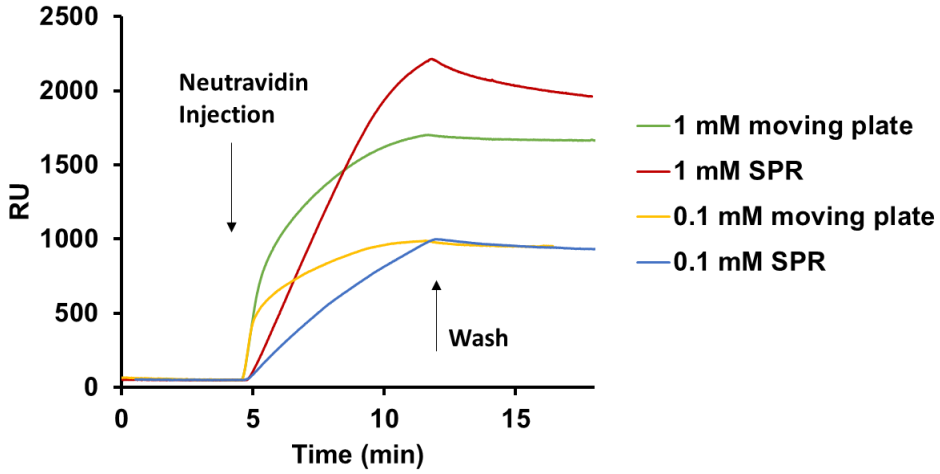

Figure 5.23- Neutravidin injections on biotin-terminated surfaces after EDC/NHS amino coupling on MUA SAMs. The EDC/NHS was performed either on the SPR (red and green colors, for 1 and 0.1 mM respectively) or on the moving plate for 2 h (yellow and blue colors for 1 and 0.1 mM respectively).

The results show that performing the amino coupling in the moving plate did not have an impact on the final response, but there was an effect on the kinetics between biotin-neutravidin interaction as per the response curve shape. Figure 5.23 shows that the EDC/NHS of amine-PEG_7-biotin performed on the moving plate will result in faster kinetics between neutravidin and the biotin, when neutravidin is injected with the SPR. Even though to a different extent, these results agree with the observed previously for the immobilisation of biotin-PEG4-alkyne via click chemistry (Chapter 4, Section 4.4.1). Performing click chemistry or amino coupling under the SPR does not seem to bring much benefit over the incubation on the moving plate.

Considering the final responses from neutravidin (after control subtraction, ~ 1420 RU), the quantity of amine-PEG_7-biotin that coupled at the surface compared to the NbGFP that couple under the same conditions (~ 2200 RU, Chapter 4, section 4.2.2.2) was lower for the biotin moiety (considering one to one binding between biotin and neutravidin). The final densities are 1 NbGFP per 10 nm^2 and 1 biotin-PEG7-biotin per 70 nm^2 . Assuming that the 7EA would

couple similarly as the amine-PEG_7-biotin, then this number would be insufficient to allow the coverage of all nanobodies binding site. Therefore, the tested conditions under acidic pH remain needing further optimisation.

Overall, negatively charged oligopeptides, such as 7EA, were indicated to use with the EDC/NHS immobilisation method due to the presence of only one amine at their extremity. From this point, meeting the same optimal EDC/NHS immobilisation conditions as the nanobody showed to be a challenge throughout this sub chapter, with insufficiently immobilised small uncharged structures (< 1 kDa).

Future studies could include the use of EDC/NHS diluted in buffer instead of water, as a way to understand if that could improve the NHS ester formation at the early stages. Additionally, alternative coupling agents could be studied. Overall, this sub chapter introduced initial insight to the optimisation required on the immobilisation of small structures (1 < kDa). From here, two distinct paths could be followed: either 1) further optimisation with other EDC/NHS variables, in order to find new ways of overcoming the insufficient amino coupling with the investigated conditions, or 2) follow a biorthogonal approach, whereas the oligopeptides will not need to meet the optimal nanobody immobilisation conditions.

5.3 Conclusions and Future Work

The discoveries of this research through ellipsometry allowed to conclude that the studied flexible oligopeptides (C5K and C8K) and rigid oligopeptides (C3εK and C3βD) require the support of an extra molecule (like TEG11) to achieve the required thickness equivalent to, or higher than, the experimental nanobody thickness reference (2.0 ± 0.1 nm). The ellipsometry and contact angle studies on the different mixed SAMs, formed with different incubation ratios of oligopeptide to TEG11, found that TEG11 is a dominant molecule, competing for the surface even when in lower ratio in the incubation solution. Thus, ratios that favoured TEG11 resulted in surfaces lacking the oligopeptides. Only the ratio 40 oligopeptides to 1 TEG11 allowed to observe the increase in thickness and surface ratio obtained initially through the Cassie's equation. Additional XPS studies were performed to further confirm the surface composition of the SAMs formed at the incubation ratio of oligopeptide:TEG11 40:1. The C5K:TEG11 and C8K:TEG11 mixed SAMs resulted in 1: (3 ± 0.2) and 1: (6 ± 0.6) respectively. Regarding the C3εK:TEG11 and C3βD:TEG11 SAMs, the XPS data revealed that these samples could have undergone either 1) sulphur contamination or 2) degradation under dried state (longer than 24 h until XPS analysis). Aside from these hypotheses, the experimental ratios for C3εK:TEG11 and C3βD:TEG11 SAMs indicated ratios of oligopeptide:TEG11 of 1: (17 ± 5.4) and 1: (13 ± 2.5) respectively. Further investigation on potential degradation could be performed by mass spectrometry of the oligopeptide solutions and earlier analysis and temporal monitoring the elemental compositions by XPS. Nonetheless, the thickness and Cassie's results obtained from fresh samples of C3εK:TEG11 40:1 and C3βD:TEG11 40:1 SAMs suggested monolayers with surface ratios of 1:2 and 1:3 formed respectively.

Regarding the aims of this thesis, all the studied oligopeptides could potentially be used with TEG11 to control nanobody antigen binding. Future work should include switching studies with the binding system (nanobody-antigen) which would be novel in the biosensor field. Concerning the literature on similar oligopeptides and switchable systems[7, 96, 214], the findings of this chapter can aid the development of controllable and tailor-made surface materials, particularly for larger structures such as nanobodies which previously have not been addressed. For the first time, this chapter has demonstrated the optimal ratio of longer electrically charged oligopeptides mixed with longer spacer molecules; a step forward on switchable surfaces for nanobodies.

The C5K oligopeptide was chosen to further testing, following the hypothesis that a thickness just above the experimental nanobody thickness reference would be efficient at the antigen binding control. For these studies, C5K:TEG11 was mixed with the nanobody NbVCAM1 studied in Chapter 3, at the ratio of NbVCAM1:C5K:TEG11 of 500:40:1. The SPR studies under open circuit showed promising results, with reduced but selective response after antigen injection. However, when applying positive potential, the control C5K:TEG11 SAMs showed high non-specific interactions with the antigen (which has a highly negative network charge at neutral pH) – making the system C5K:TEG11 unsuitable to use with the nanobody NbVCAM1. The same control used with another antigen (EGFP, studied in Chapter 4, with considerable lower negative network charge at neutral pH) showed no interactions. These findings highlight the importance of the appropriate controls between the switching system (oligopeptides-support molecule) and the binding system (nanobody-antigen). Moreover, it provides valuable insights towards the design of a switching system aiming to be compatible with a large range of nanobody-antigen pairs. Future work on the design of new oligopeptide-based switching moeities could include a non-charged termination (like OH- or alkyl-terminated) that minimises

the likelihood of the non-specific interactions with a large range of antigens. Additionally, for highly charged antigens an efficient antifouling effect is required to overcome the surface attraction when the opposite charge is applied.

Overall, all the studied oligopeptides mixed with TEG11 at the ratios of oligopeptide to TEG11 of 40:1 are potential candidates to control nanobody-like structure binding. Switching studies are the next step, with a compatible nanobody-antigen pair.

Finally, this work also investigated the use of negatively charged oligopeptides (7EA) compatible with amino-coupling immobilisation at carboxylic-terminated SAMs surface, more specifically under acidic pH. Preliminary studies indicated that a switching system that immobilises at the same optimal conditions as a selected nanobody would be convenient but might be challenging if acidic pH is required (like with NbGFP, from Chapter 4, Section 4.2.2.2). Contact angle and ellipsometry studies on 7EA immobilised after EDC/NHS under pH 5.4 required further investigation to confirm that the 7EA successfully reacted at the surface. In order to investigate further, the molecules dodecylamine, aminePEG_7Boc and amine-PEG_7-biotin were selected as cheaper options to preliminary use instead of 7EA oligopeptides. The following ellipsometry and contact angle studies with dodecylamine showed how different carboxylic-acid densities and pH impacts the EDC/NHS reaction. While different densities showed no improvement for the amino-coupling at acidic pH, at basic pH it seemed that spacing out the carboxylic-acid could be beneficial. Overall, EDC/NHS at basic conditions were more efficient. This was further confirmed with SPR studies with aminePEG_7Boc, which also demonstrated increased reaction yields with higher analyte concentrations. Attempting to demonstrate that lower concentrations of coupled analyte were undetectable by SPR, studies with amine-PEG_7-biotin and neutravidin injection amplified the signal of the amino coupling at 0.1 and 1 mM. At the acidic studied conditions, the estimated number of one oligopeptide

for each fourteen nanobodies highlights the need to further optimise the amino-coupling. Future work into the improvement of 7EA amino-coupling at the surface could use different coupling agents, alternative initial carboxylic-acid terminated SAMs. On the other hand, biorthogonal chemistry could also be considered, which would require the design of alternative oligopeptides.

This final section of Chapter 5 attempted the amino coupling of negatively charged oligopeptides under acidic conditions on a surface, an achievement that has not been reported to date. There was an additional challenge of simultaneously coupling oligopeptides and nanobodies, which constrained the conditions. While this was not fully achieved, the benefit of simultaneous coupling nanobodies and oligopeptides would be of great impact not only the in the biosensor field, but also in the fields of surfaces, materials and chemistry.

Custom made switchable surfaces compatible with different nanobodies is a necessity, especially considering the variety of nanobodies and nanobody-like structures (i.e. network charge and localised charge at the biding site, structure and sequence including location of amines, etc.). This Chapter brought together multiple options of electrically charged oligopeptides which represent the beginning of a broad selection of switchable surfaces ready to be used with varied nanobodies as they became available. The potential applications of such surfaces is endless depending only on the nanobody and its specific biological target.

Chapter 6 Experimental Procedures

This section describes in detail the chemicals, biological compounds, materials and procedures adapted and created for the experimental work carried out for this thesis.

6.1 Chemicals and biological compounds

6.1.1. Purchased and used as received

The following chemicals were purchased from Sigma Aldrich and used as received: Sulphuric acid 95-98%, hydrogen peroxide solution 30 wt. % in water, immersion oil ref. 56822 with refractive index 1.515 (used for SPR), S-4(azidobutyl)thioacetate 97%, $CuSO_4$ (copper sulfate), THPTA (tris(3-hydroxypropyltriazolylmethyl)amine) 95%, Sodium L-ascorbate, dihydrogen sodium phosphate dihydrate, EDTA (ethylenediaminetetraacetic acid), SDS (sodium dodecyl sulfate), EDC (1-ethyl-3-(3-dimethylaminopropyl)carbodiimide hydro chloride) and NHS (N-hydroxysuccinimide), sodium acetate phosphate, ethanolamine, HEPES (N-(2-Hydroxyethyl)piperazine-N′-(2-ethanesulfonic acid)), Tween20, TFA (trifluoreacetic acid), TEG11 (triethylene glycol mono-11-mercaptoundecyl ether) 95%, 1,4-benzenedimethanethiol (BDMT), 2-mercaptoethanol (2ME), HCl (hydrochloric acid), NaCl (sodium chloride), mercaptoundecanoic acid, triethylamine, biotin-PEG4-alkyne, dodecylamine, pentanethiol. Amine-PEG7-Boc, biotin-PEG7-amine (*O*-(2-Aminoethyl)-*O′*-[2-(Boc-amino)ethyl]hexa ethylene glycol).

Neutravidin was purchased from Thermo Fischer Scientific Ltd and lysozyme from chicken egg white from Sigma Aldrich.

Green-fluorescent-protein nanobodies (NbGFP) and enhanced-green-fluorescent protein (EGFP) was purchased from ChromoteK. Human vascular cell adhesion molecule-1 (hVCAM1) antigen was purchased from Prepotech.

Oligopeptides C5K (cys-lys(ε-lys)$_4$), C8K (cys-lys(ε-lys)$_7$), C3εK (cys-pro-pro-ε-lys-pro-pro-ε-lys-pro-pro-ε-lys-pro-pro), C3βD (cys-pro-pro-βDap-pro-pro-βDap- pro-pro-βDap-pro-pro) and 7EA ((glu)$_7$-β-ala (all with purities > 90%) was purchased from Peptide Protein Research Ltd (UK).

Phosphate Buffered Saline (PBS) 10x pH 7.4 (KH_2PO_4 1.06 mM, NaCl 155.2 mM, $Na_2HPO_4 \cdot 7H_2O$ 3.0 mM) was purchased from Thermo Fischer Scientific Ltd and freshly diluted 10x with Ultra High Pure (UHP) water (from MilliQ).

HPLC grade solvents (ethanol and acetone) were purchased from the local solvents store.

At all the times, if water is mentioned in the protocols, this refers to Ultra High Pure (UHP) water (from MilliQ).

6.1.2. **Preparation of NbVCAM1 nanobodies**

The engineered nanobody cAbVCAM1-5, in this thesis denoted as NbVCAM1, was provided by the Guedens Group, Hasselt University, Belgium. The NbVCAM1 previously isolated from an immune dromedary library as a lead compound for nuclear imaging of VCAM1-expressing atherosclerotic plaques in mice and in patients.[215] The NbVCAM1 nanobody was extended with amino acids LEY at the C-terminus, expressed as a chimeric protein (fusion with an intein

and a chitin binding domain) in the *E. coli* SHuffle® T7 strain and was subjected to EPL-mediated cleavage with the cysteine-alkyne linker to produce the C-terminally alkynated NbVCAM1-LEY, i.e., NbVCAM1-LEYC-alkyne, as previously described[40] and referred in this thesis as simply NbVCAM1.

6.1.3. **Synthesis of 4-azidobutane-1-thiol (ABT)**

S-(4-azidobutyl)thioacetate was dissolved in an ethanolic solution of KOH (100 mM) to a final concentration of 2.5 mM. Resulting mixture was sonicated 5 min, then magnetically stirred 2h to obtain 4-azidobutane-1-thiol (ABT). Cleavage of the acetate group was confirmed by the disappearance of acetate signal at 2.3 ppm in ^{1}H NMR spectra (Figure 6.1).

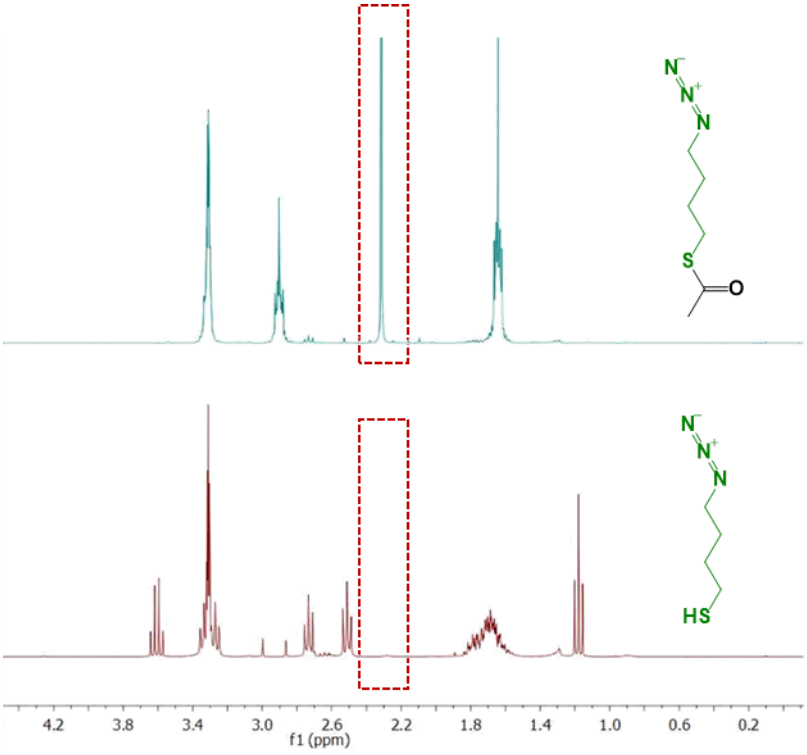

Figure 6.1 – NMR results for ABT synthesis. ^{1}H NMR spectra of S-(4-azidobutyl)thioacetate in methanol-d_4 (top) and ethanolic solution of 4-azidobutane-1-thiol in methanol-d_4 (bottom). Acetate peak position is indicated by dash line frames.

6.2 Materials

6.2.1. Gold substrates

Gold sensor chips used in the SPR experiments were acquired from Reichert Technologies - Ametek Inc (USA) and consisted of polycrystalline gold surfaces (50 nm) on glass substrates sized 1 cm x 1 cm. For ellipsometry, contact angle and XPS studies, gold (100 nm thickness and rms roughness < 2,5 nm) on silicon <100> wafers precoated with titanium were acquired from George Albert PVD (Germany) and cut into 1 cm x 1cm pieces using a diamond scriber.

6.3 Surface functionalisation protocols

6.3.1. Substrate treatment

Before functionalisation, the gold substrates were submerged for 10 min in a strong oxidizing piranha solution (70% H_2SO_4, 30% H_2O_2) to remove organic residues. Subsequently, the gold substrates were rinsed with copious amount of Ultra High Pure (UHP) water and HPLC ethanol and lastly dried under argon.

6.3.2. Self-assembly monolayers (SAMs)

6.3.2.1. NbVCAM1 SAMs

The lyophilized NbVCAM1 was kept at -20°C until further use. Freshly piranha cleaned gold chips were incubated with a solution of 1 µM NbVCAM1 diluted in 1x PBS (1.5 mL/chip) for 24h at room temperature (RT) on a moving plate. As controls, gold chips were immersed in either 1x PBS or HPLC ethanol solutions under the same conditions.

6.3.2.2. NbVCAM1:3-Chloro-1-propanethiol SAMs

Freshly piranha cleaned gold chips were incubated with solutions of 1 µM NbVCAM1 and 3-Cl-1-propanethiol diluted in 1x PBS at molar ratios of Nb:3-Cl-1-propanethiol 500:1, 100:1 and 1:10, (1.5 mL/chip) for 24h at room temperature (RT) on a moving plate. As controls, gold chips were incubated with only NbVCAM1 and only 3Cl-1-propanethiol.

6.3.2.3. Azide-, thiol- and hydroxyl-terminated SAMs

Freshly synthetized 4-azidobutane-1-thiol (ABT) solution was used to incubate freshly cleaned chips for 24h on the shaking plate at RT, allowing to form an azide-terminated SAM. Mixed SAMs of ABT and 1,4-benzenedimethanethiol (BDMT) were formed with chips incubated with ABT and ethanoic solution of BDMT at 1:1 ratio (0.1 mM, 1 mL/chip). Mixed SAMs of ABT and 2-mercaptoethanol (2ME) were formed with chips incubated with ABT and ethanoic solution of 2ME at 1:1 ratio (0.1 mM, 1 mL/chip). The resulting SAMs were characterised by ellipsometry, contact angle, XPS and TOF-SIMS/3D OrbiSIMS.

6.3.2.4. Mercaptoundecanoic acid (MUA) terminated SAMs

Briefly, two different methods were compared: freshly cleaned gold chips were immersed in mercaptoundecanoic acid (MUA) in only ethanol (1) or in ethanol/trifluoroacetic acid (TFA) 3% (v/v) as an improved method (2). Chips were incubated with 0.1 mM of MUA, 1 mL/chip for 24 h on the shaking plate. Differently to method (1), the method (2) aims for the disruption of the formation of interplane hydrogen bonds between the free thiols from the bulk solution and the terminal COOH groups of the bound thiolate at the surface that would lead to double layers, as demonstrated in previous studies[195]. After rinsing with either only ethanol (1) or ethanoic solution 10% (v/v) triethylamine (2) and copious amounts of ethanol HPLC grade, the

chips were dried with argon and measured for their thickness and contact angle. Unless stated, along this thesis formed MUA-terminated chips always refer to the improved method (2).

6.3.2.5. MUA:pentanethiol terminated SAMs

Freshly cleaned gold chips were immersed in MUA 0.1 mM and pentanethiol 0.1 mM at volume ratios 3:1 and 1:1 in ethanol/trifluoroacetic acid (TFA) 3% (v/v) (1 mL/chip). After rinsing with ethanoic solution 10% (v/v) triethylamine and copious amounts of ethanol HPLC grade, the chips were dried with argon and measured for their thickness and contact angle.

6.3.2.6. Oligopeptide, TEG11 and oligopeptide:TEG11 mixed SAMs

Freshly clean gold chips were incubated with TEG11 0.1 mM in solutions of water, ethanol or 1x PBS. To create the oligopeptide SAMs, the chips were emerged with 1x PBS solutions of C5K, C8K, C3εK or C3βD 0.1 mM in 1x PBS. To perform the oligopeptide:TEG11 SAMs, the chips were emerged with 1x PBS solutions of C5K:TEG11 or C8K:TEG11 at the molar ratios of 1:100, 1:40, 1:10, 10:1 and 40:1, and C3εK:TEG11 or C3βD:TEG11 at the molar ratios of 40:1. All the SAMs were formed during 24 h on the shaking plate at RT. Washing steps included rinses with the incubation buffer used, and EtOH. Chips were dried with argon and characterised with ellipsometry, contact angle and XPS.

Chips that were characterised by XPS were individually wrapped in aluminium foil, and shipped to the XPS facilities. Time between SAM formation and analysis were > 24h.

6.3.2.7. Nanobody NbVCAM1:C5K:TEG11 mixed SAMs

Freshly clean gold chips were incubated with 1x PBS solutions of NbVCAM1:C5K:TEG11 at the solution molar ratio of 500:40:1 (with NbVCAM1 1 μM, 1.5 mL/chip), for 24 h on the shaking plate at RT. The surfaces were characterised for the biological activity with SPR.

6.3.3. **Immobilisation *via* copper catalised alkyne cycloaddition (Click Chemistry)**

6.3.3.1. Biotin-PEG4-alkyne immobilisation

Copper-catalysed azide-alkyne cycloaddition (CuAAC) mediated click chemistry was performed on the azide-terminated monolayers with biotin-PEG4-alkyne. The click reaction was prepared with different incubation times (45 min, 1 h, 4 h, 8 h, 14 h and 24 h) using the coupling solution[149]: 1 µM alkyne-terminated biotin; 2.5 mM Sodium L-ascorbate; 1 mM THPTA; 0.5 mM CuSO4 prepared in sodium acetate buffer (10 mM, pH 4). The Cu(II) was reduced to Cu(I) catalyst by sodium ascorbate (reducing agent). Cu(I) was stabilised by THPTA. After Incubation, the chips were washed with washing buffer (200 mM dihydrogen sodium phosphate; 200 mM sodium chloride; 150 mM ethylenediaminetetraacetic acid; 50 mM ethanolamine), 0.5 % (w/v) SDS, 1x PBS and finally with ultra high pure (UHP) water. The incubation was performed either on a shaker plater (2 mL/ chip) or under dynamic flow using the SPR at a flow of 8 µL/min for 45 min, 8 h and 14 h min. Chips were characterised with ellipsometry, contact angle and SPR.

6.3.3.2. NbVCAM1 immobilisation

Copper-catalysed azide-alkyne cycloaddition (CuAAC) mediated click chemistry was executed on the azide-terminated monolayers with NbVCAM1. The click reaction was prepared with different incubation times (45 min, 1 h, 4 h, and 24 h) using the coupling solution[149]: 1 µM nanobody NbVCAM1; 2.5 mM Sodium L-ascorbate; 1 mM THPTA; 0.5 mM $CuSO_4$ prepared in sodium acetate buffer (10 mM, pH 4). The Cu(II) was reduced to Cu(I) catalyst by sodium ascorbate (reducing agent). Cu(I) was stabilised by THPTA. After Incubation, the chips were

washed with washing buffer (200 mM dihydrogen sodium phosphate; 200 mM sodium chloride; 150 mM ethylenediaminetetraacetic acid; 50 mM ethanolamine), 0.5 % (w/v) SDS, 1x PBS and finally with ultra high pure (UHP) water. Chips that were characterised with ellipsometry, contact angle and XPS were incubated for 45 min, while with SPR the additional reaction times were characterised.

6.3.4. Immobilisation via electrostatic interactions

6.3.4.1. Lysozyme interactions

On the automatic Reichert 2-channel SPR, a baseline was obtained with 1x PBS running buffer (RB), following the blank buffers injections, which after recovering to the baseline followed the respective lysozyme (50 μg/mL) diluted in each buffer injections (all with $[Na^+]$= 10 mM: sodium acetate, pH 5.4; sodium phosphate, pH 6, 7.4 and 8) on the MUA surface. As the main interactions that retain the lysozyme at the surface are electrostatic, when switching back to the RB, the response lowers as the lysozyme is washed off the surface. The total response representative of the electrostatic interaction is result from the subtraction of the blanks response to the sample injection response. The injections were performed for 7 min at 30 μL/min.

6.3.5. **Immobilisation *via* amino-coupling**

6.3.5.1. Lysozyme immobilisation

Freshly formed MUA-terminated chips were activated with a water mixture 1:1 of 0.4 M EDC/0.1 M NHS (7 min) followed by incubation with lysozyme 50 μg/mL (7 min) which was dissolved in a sodium phosphate pH 8 buffer with $[Na^+]$= 10 mM: After the lysozyme incubation, the chips were injected with in 1 M ethanolamine, adjusted with HCl to a pH 8.5 (7 min), to deactivate any remaining NHS-ester active groups that did not react. The injections were performed at 30 μL/min, with chips characterised with SPR using an electrochemical cell

6.3.5.2. NbGFP immobilisation

Freshly formed MUA-terminated chips were activated with a water mixture 1:1 of 0.4 M EDC/0.1 M NHS (7 min) followed by incubation with NbGFP 50 μg/mL (7 min) which was dissolved in different buffers, all with $[Na^+]$= 10 mM: sodium acetate, pH 5.4; sodium phosphate, pH 7.4 and 8. After the nanobody incubation, the chips were emersed in 1M ethanolamine, adjusted with HCl to a pH 8.5 (7 min), to deactivate any remaining NHS-ester active groups that did not react. The injections were performed at 30 μL/min, with chips characterised with SPR.

6.3.5.3. 7EA immobilisation

Freshly formed MUA-terminated chips were activated with a water mixture 1:1 of 0.4 M EDC/0.1 M NHS (7 min) followed by incubation with 7EA 0.1 mM (7min) which was dissolved in a sodium acetate buffer, pH 5.4. After incubation at on shaking plate, the chips were emersed in 1 M ethanolamine, adjusted with HCl to a pH 8.5 (7 min), to deactivate any remaining NHS-

ester active groups that did not react. Chips were characterised with ellipsometry and contact angle.

6.3.5.4. Dodecylamine (DA) immobilisation

Freshly formed MUA-terminated chips or mixed MUA:pentanethiol 3:1 and 1:1 chips were activated with a water mixture 1:1 of 0.4 M EDC/0.1 M NHS (7 min) followed by incubation with dodecylamine (DA) 0.1 mM (7 min) which was dissolved in different buffers, all with $[Na^+]$= 10 mM: sodium acetate, pH 5.4; sodium phosphate, pH 8. After incubation on the shaking plate, the chips were emersed in 1 M ethanolamine, adjusted with HCl to a pH 8.5 (7 min), to deactivate any remaining NHS-ester active groups that did not react. Chips were characterised with ellipsometry and contact angle.

6.3.5.5. Amine-PEG7-Boc immobilisation

Freshly formed MUA-terminated chips chips were activated with a water mixture 1:1 of 0.4 M EDC/0.1 M NHS (7 min) followed by incubation with amine-PEG7-Boc 0.1 mM (7min) which was dissolved in different buffers, all with $[Na^+]$= 10 mM: sodium acetate, pH 5.4; sodium phosphate, pH 8. After incubation, the chips were emersed in 1 M ethanolamine, adjusted with HCl to a pH 8.5 (7 min), to deactivate any remaining NHS-ester active groups that did not react. Chips were characterised with ellipsometry and contact angle.

6.3.5.6. Amine-PEG7-biotin immobilisation

Freshly formed MUA-terminated chips were activated with a water mixture 1:1 of 0.4 M EDC/0.1 M NHS (7 min) followed by incubation with amine-PEG7-Biotin (at multiple molarities 0.1, 1, 7, 15, 30, 50 mM) (7 min) which was dissolved in different buffers, all with $[Na^+]$= 10 mM: sodium acetate, pH 5.4; sodium phosphate, pH 8. After incubation, the chips

were emersed in 1 M ethanolamine, adjusted with HCl to a pH 8.5 (7 min), to deactivate any remaining NHS-ester active groups that did not react. The injections were performed at 30 μL/min. Chips were characterised with ellipsometry and contact angle.

6.3.6. Immobilisation of target macromolecules

6.3.6.1. Neutravidin immobilisation

Injections of neutravidin (20 μg/mL) in 1x PBS were performed on biotin-terminated surfaces and respective controls at a flow rate of 8 μL/min during 30 min.

6.3.6.2. hVCAM1 immobilisation

Injections of hVCAM1 (20 μg/mL) in 1x PBS were performed on NbVCAM1-terminated surfaces and respective controls at a flow rate of 8 μL/min during 30 min.

6.3.6.3. EGFP immobilisation

Injections of EGFP (100 nM) in HEPES 10 mM, NaCL 0.15 M, 0.05% Tween, pH 7.4 were performed on NbGFP-terminated surfaces and respective controls at a flow rate of 30 μL/min during 7 min.

6.4 Characterisation techniques

6.4.1. Contact angle

The advancing and receding contact angles were obtained with the instrument OneAttension from Biolin Scientific using the sessile drop analysis mode. Before measurements the

instrument was calibrated for the chosen camera zoom and the syringe filled with fresh water. The drop volume reached 4-10 µL at a rate of 0.5 µL/sec. Two to three measurements per chip (duplicates) were performed in different chip locations.

6.4.2. **Ellipsometry**

Ellipsometry measurements were obtained with a J.A. Woollam alpha-SE instrument using gold on silicon wafers. Data analysis used the Cauchy model that considers three layers: Ambient/Monolayer/Air. The refractive index was fixed at 1.5. Each chip was measured before and after functionalisation. Data was fitted with the software CompleteEASE, with a defined resolution of 0.1 eV. Four measurements per chip (duplicates) were performed in different chip locations.

6.4.3. **X-ray photoelectron spectrometry (XPS)**

XPS measurements were acquired using the Thermo Scientific K-Alpha system with a monochromatic Al kα (photon energy of 1486.68 eV) source. The analysis chamber was under a pressure of ~7.5 x 10^{-9} Torr and data was collected from large areas (400 µm x 400 µm) of the samples surface, the take-off angle being 0 ^{o} (incident angle of 90^{o} to the surface plane). Survey scans were run with an analyser pass energy of 150 eV, 1 eV energy step and 10 ms dwell time. High resolution scans were acquired using a lower analyser pass energy of 40 eV, 0.1 eV energy step and 50 ms dwell time. Survey and high resolution spectrums were results of 10 and 20 scans respectively, except for gold high resolution spectrum that use 4 scans. The charge neutraliser system was used at all the times. The samples and clean gold as control were

analysed at least 48h after being prepared (delivery time to Cardiff facility). Nitrogen spectra was requested to be prioritized, in order to avoid loss of signal[136]. Fitting of XPS peaks was performed using CasaXPS (2.3.22PR1.0) processing software. The binding energy scale calibration was based on the position of the Au $4f_{7/2}$ peak at 84 eV. Shirley background was selected in the case of gold while linear background was selected for the other spectra, and a Gaussian/Lorentzian GL(30) lineshape was applied. Relative sensitivity factors used for quantification were selected as in CasaXPS library (see Table 6.). The C 1s spectra were fitted by setting all the peaks to an equal full width at half maximum (FWHM) and each S doublet was constrained to have a peak separation of 1.16 eV, a 2:1 area ratio ($2p_{3/2}$: $2p_{1/2}$) and identical FWHM. At least 2 measurements per chip (duplicates) were performed in different chips locations.

Table 6.1 – Relative sensitivity factors for CasaXPS.

Element	RSF
Au 4f	6.250
C 1s	1
O 1s	2.93
S $2p_{1/2}$	0.567
S $2p_{3/2}$	1.11
N 1s	1.8

6.4.3.1. Nanobodies to ABT ratio calculation

A deeper analysis could use the molecular formulas for ABT ($C_4H_9N_3S$) and for the NbVCAM1 ($C_{632}H_{941}N_{175}O_{198}S_7$) which allow to write the Equation 6.1 and Equation 6.2, whereas N_{Nb}, N_{ABT} represent the peak area of nitrogen while S_{Nb} and S_{ABT} represent the area of sulphur, for the NbVCAM1 and ABT respectively. The XPS output regarding the total areas for the

elements nitrogen and sulphur, are the sum of the areas of the respective elements from the NbVCAM1 and the ABT moiety (Equation 6.3 and Equation 6.4).

$$N_{Nb} = \frac{175}{7} S_{Nb} \qquad \textit{Equation 6.1}$$

$$N_{ABT} = 3S_{ABT} \qquad \textit{Equation 6.2}$$

$$N_{total} = N_{Nb} + N_{ABT} \qquad \textit{Equation 6.3}$$

$$S_{total} = S_{Nb} + S_{ABT} \qquad \textit{Equation 6.4}$$

The resultant Equation 6.5 solves for the sulphur area for NbVCAM1. Additionally, knowing that the NbVCAM1 has 7 sulphurs, while ABT has 1, it is possible to write Equation 6.6, which gives the experimental ratio between the compounds of the SAM at the surface.

$$N_{total} = \frac{175}{7} S_{Nb} + 3S_{ABT} \iff N_{total} = 25S_{Nb} + 3(S_{total} - S_{Nb}) \iff S_{Nb} = \frac{N_{total} - 3S_{total}}{22} \qquad \text{Equation 6.5}$$

$$Ratio\ between\ Nanobody\ and\ ABT = \frac{S_{Nb}}{7\ S_{ABT}} \qquad \text{Equation 6.6}$$

6.4.4. **Time-of-flight-secondary ion mass spectroscopy (ToF-SIMS) and three dimensional Orbitrap secondary ion mass spectroscopy (3D OrbiSIMS)**

ToF-SIMS spectra were acquired using a TOF IV (IONTOF GmbH) instrument with 25 keV Bi_3^+ primary ion beam raster over 500 × 500 µm area. Additional high lateral resolution ToF-SIMS imaging was acquired using 3D OrbiSIMS instrument with 25 keV Bi_3^+ primary ion beam and delayed extraction. Two 256 × 256 pixel images over area of 100 × 100 µm were acquired on two replicates of each sample type. Measurements were performed in both positive and negative mode. Positive mode spectra were calibrated to: CH_3^+, $C_7H_7^+$, Au_3^+. Negative mode spectra were calibrated to: CH^-, CN^-, CNO^-, Au_3^-. Two measurements were taken for each sample and each polarity.

3D OrbiSIMS measurements were acquired using 20 keV Ar_{3000}^+ as primary ion beam. The current of the primary beam was 220 pA. Each spectrum was acquired from an area of 300 × 300 µm using random raster mode and the crater size was 381.9 × 381.9 µm. The spectra were collected in positive and negative mode, in mass ranges 50-750 *m/z* and 150-2250 *m/z*. Target potential was set to +57.5 V for positive mode and -57.5 V in negative mode. Two separate areas were analysed on each sample and two replicates of each sample type were analysed. Each measurement lasted 30 scans, the total ion dose per measurement was 1.6×10^{10}. Mass resolving power was set to 240,000 at 200 *m/z*.

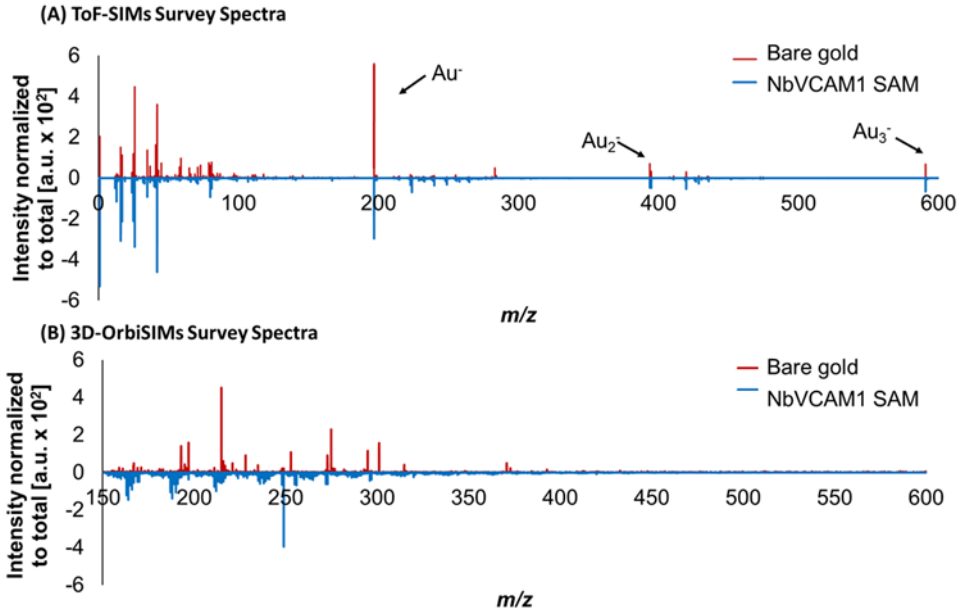

Figure 6.2 - (A) ToF-SIMs and (B) 3D OrbiSIMs survey spectra for the NbVCAM1 SAM (blue) and gold reference (red).

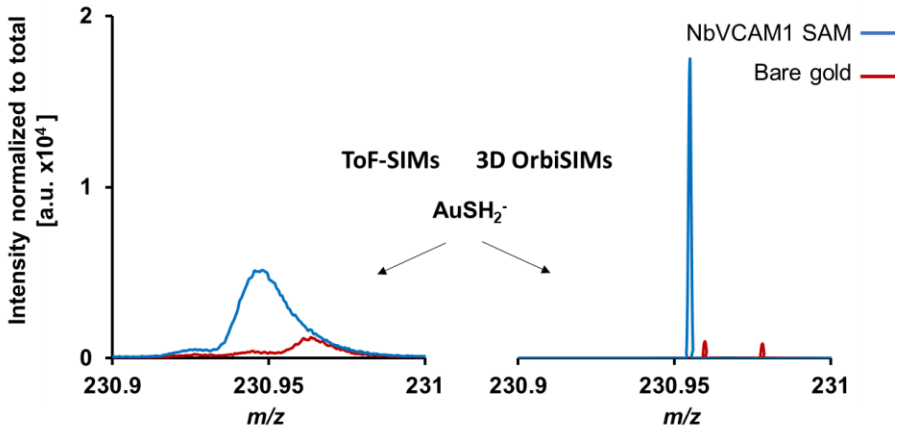

Figure 6.3 - Representative spectra for methods comparison between ToF-SIMs and 3D OrbiSIMs. The mass resolving power of the 3D OrbiSIMS allows to assign peaks representing the AuS^- bond with higher confidence than in the ToF-SIMS spectra.

6.4.5. **Circular dichroism (CD)**

The circular dichroism was performed on a NbVCAM1 SAM surface and with NbVCAM1 in solution, allowing confirmation of its conformation. Studies of the NbVCAM1 in 1xPBS were performed in a Jasco J-1500, using a nanobody concentration of 1 mg/ml, at room temperature. CD analysis of the NbVCAM1 SAM surface were performed using a Chirascan plus. Piranha cleaned quartz slides were incubated overnight with a 4% solution of mercapto-trimethoxysilane (MPTES) in IPA, allowing thiol functionalisation. Following rinsing with IPA to remove the excess of MPTES, the slides were immersed in 15 mM copper perchlorate solution in H_2O for 15 minutes to provide a Cu^{1+} ion surface. Finally, the slides were incubated with NbVCAM1 0.1 mg/ml in 10 mM Phosphate buffer, pH 7.9 for 1h, and rinsed with the same buffer. Three slides were loaded into a quartz cuvette. All measurements were performed with a 10 mM phosphate buffer pH 7.9. These measurements were performed at the University of York, by Dr. Steven Johnson.

6.4.6. **Surface plasmon resonance (SPR)**

Before use, the SPR semi-automatic Reichert Technologies SPR instrument was cleaned with 0.5% sodium dodecyl sulfate (SDS), 50 mM glycine pH 9.5 and water. Running buffers were prepared daily, being filtered (0.2 μm filter), and degassed for 30 min. The fluidic system was flushed with buffer before the experiments. The flow cell was cleaned by sonication in detergent solution and rinsed with water. The injection solutions were also freshly prepared. A drop of matching refractive index oil was placed on the prism surface every time a new sensor slide was loaded, so that the sensor slide is optically coupled to the prism surface. SPR experiments allowed monitoring in real-time the immobilisation of nanobodies onto the surface, followed by antigen binding. Typically, experiments were performed at the set temperature of 25 ºC.

Initial traces were stabilised before each experiment at a flow rate of 100 µl/min with the respective running buffer (usually the same to which the nanobody or the antigen is diluted in). Blank injections (with RB) were 10 to 15 min long and were performed before each experiment to remove any potential loop impurities before and after each experiment to stabilise the final response.

6.4.6.1. Biotin-neutravidin SPR programmes

The immobilisation of biotin-PEG4-alkyne moeities on chips of azide-terminated SAMs was followed by SPR. Chips of freshly formed ABT SAMs were loaded on the instrument. After a stable baseline, each injection of 1 µM biotin-PEG4-alkyne in a solution of 2.5 mM Sodium L-ascorbate; 1 mM THPTA; 0.5 mM CuSO4 prepared in sodium acetate buffer (10 mM, pH 4). The click chemistry solution started after a burst flow of 1500 µl/min for 10 sec and carried on for 45 min, 1, 4, 8, 14 or 24 h at 8 µl/min. After the click chemistry a new baseline was allowed to stabilise. Thereafter an injection of neutravidin 20 µg/ml in 1x PBS took place for 30 min at 8 µl/min.

The amino coupling of biotin-PEG7-amine moeities on MUA-terminated chips was also followed by SPR. Chips of freshly formed MUA SAMs were loaded on the instrument. After a stable baseline, the chips were activated with a water mixture 1:1 of 0.4 M EDC/0.1 M NHS (7 min) followed by incubation biotin-PEG7-amine at 0.1 mM or 1 mM in a buffer of pH 5.4. After incubation, the a solution of 1 M ethanolamine, adjusted with HCl to a pH 8.5 was injected (7 min), to deactivate any remaining NHS-ester active groups that did not react. Finally, the traces were allowed to stabilise before changing the second running buffer (RB2, HEPES 10 mM, NaCl 0.15 M, 0.05% Tween 20, pH 7.4). After changing to RB2, the new baseline was

stablished and the injection of neutravidin (20 µg/mL) had a duration of 7 min. The flow rate for the experiments was 30 µl/min.

6.4.6.2. Boc-PEG7-amine immobilisation programme

The immobilisation of Boc-PEG7-amin on MUA was also followed by SPR. Freshly formed MUA-terminated chips were loaded on the instrument. Chips of freshly formed MUA SAMs were loaded on the instrument. After a stable baseline, the chips were activated with a water mixture 1:1 of 0.4 M EDC/0.1 M NHS (7 min) followed by incubation with amine-PEG7-Boc at different molarities (0.1, 1, 7, 15, 30, 50 mM, for 7min) which was dissolved in different buffers, all with $[Na^+]$= 10 mM: sodium acetate, pH 5.4; sodium phosphate, pH 8. After incubation, the a solution of 1 M ethanolamine, adjusted with HCl to a pH 8.5 was injected (7 min), to deactivate any remaining NHS-ester active groups that did not react.

6.4.6.3. NbVCAM1-hVCAM1 SPR programme

The NbVCAM1 immobilisation and respective antigen hVCAM1 injection was followed by SPR. Freshly clean gold chips were loaded on the instrument. After baseline stabilisation, each injection started with a burst flow of 1500 µl/min for 10 sec (due to electrochemical cell being use, see Section 6.4.6.6). NbVCAM1 1 µM was injected at a flow rate of 8 µl/min for 30 min. After this, the baseline was allowed to stabilise again at 100 µl/min. Then, the injection of hVCAM1 (0.27 µM) started at a flow rate of 8 µl/min for 30 min. The rising step started by injecting the RB at a flow rate of 8 µl/min for 20 min and then changing back to 100 µl/min. The same hVCAM1 antigen programme was applied to loaded chips pre functionalised with NbVCAM1:3Cl-1-propanethiol SAMs and NbVCAM1-terminated monolayers after click chemistry.

6.4.6.4. Lysozyme on MUA SPR programme

The lysozyme electrostatic interactions on MUA were monitored in real-time by SPR, in an automatic Reichert Technologies. Chips functionalised with MUA-terminated SAMs were loaded in the SPR instrument and initial traces were stabilised with water. After stabilisation, blank injections of various buffers were allowed for 7 min. After the baseline recovered with water, an injection of lysozyme diluted in the respective buffers was initiated for 7 min (buffer depending on the pH, all with $[Na^+]$ = 10 mM: sodium acetate, pH 5.4; sodium phosphate, pH 7.4 and 8). The flow rate for the experiments was 30 µl/min.

Besides the electrostatic interactions, also the amino-coupling immobilisation of lysozyme on MUA was followed by SPR. Chips functionalised with MUA-terminated SAMs were loaded in the SPR instrument and initial traces were stabilised with the running buffer (RB1, with $[Na^+]$ = 10 mM: sodium phosphate 8). After baseline stabilisation, each injection started with a burst flow of 1500 µl/min for 10 sec (due to electrochemical cell being use, see Section 6.4.6.6). An injection of 0.4M EDC/ 0.1M NHS (1:1) for 7 min activated the MUA-terminated surface, followed by the lysozyme (50 µg/mL) for 7 min and thereafter an injection of 1 M ethanolamine-HCl at pH 8.5, to deactivate any remaining NHS-ester active groups that did not react. The flow rate for the experiments was 30 µl/min.

6.4.6.5. NbGFP-EGFP SPR programme

The NbGFP immobilisation and respective antigen EGFP was monitored in real-time by SPR. Chips functionalised with MUA-terminated SAMs were loaded in the SPR instrument and initial traces were stabilised with the running buffer (RB1, depending on the pH, all with $[Na^+]$ = 10 mM: sodium acetate, pH 5.4; sodium phosphate, pH 7.4 and 8). After stabilisation, an injection of 0.4M EDC/ 0.1M NHS (1:1) for 7 min activated the MUA-terminated surface,

followed by the NbGFP (50 µg/mL) for 7 min and thereafter an injection of 1 M ethanolamine-HCl at pH 8.5, to deactivate any remaining NHS-ester active groups that did not react. The traces were allowed to stabilise before changing the second running buffer (RB2, HEPES 10 mM, NaCl 0.15 M, 0.05% Tween 20, pH 7.4). After changing to RB2, the new baseline was stablished and the injection of antigen EGFP (100 nM) had a duration of 7 min. The flow rate for the experiments was 30 µl/min.

6.4.6.6. E- SPR programme

The SPR was also used to monitor the biological activity of the immobilised nanobodies under applied potential, by following the respective antigen injection under + 0.3 V and – 0.4 V. To do so, an electrochemical cell was used with a Gamry G300 potentiostat, an Ag/AgCl reference electrode and a platinum counter electrode. The area of the fluidic channel, which corresponds to the surface area of the working electrode (gold), was 8 mm^2. The counter electrode had a surface area of 22.8 mm^2 and the reference electrode had a surface area of 32.2 mm^2. The potentiostat was warmed up for 30 min before use. Nanobody-terminated chips and respective controls were loaded to the instrument, and allowed to stabilise a baseline under open circuit (OC) conditions initially. Thereafter, the respective applied potential was applied and a new baseline was stablished before the respective antigen programmes ran.

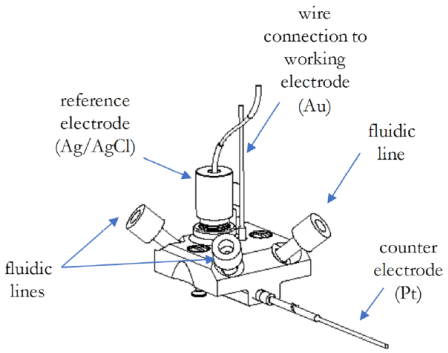

Figure 6.4 - Electrochemical flow cell. Adapted from Reichert electrochemical flow cell user guide v3.

6.4.7. **Molecular dynamic (MD) simulations**

6.4.7.1. Simulation model for nanobody adsorption

In order to study and analyze the adsorption of NbVCAM1 on a model gold surface, the NAMD2.12 [216] software was used with periodic boundary conditions, the TIP3P water model, the CHARMM27 force-field with a 12 Å cut-off for short-range potentials, and smooth particle mesh Ewald summation for the electrostatics. Visual molecular dynamics (VMD) software version 1.9.1 was employed to analyze the results.[217] The NbVCAM1 structure was obtained from Phyre[2] (protein homology/analogy recognition engine) software, [218] that predicted the structure according to the amino-acid sequence.

The predicted structure considered 126 residues (amino-acids), not including the C-terminal termination –LEY linker and cysteine-alkyne linker, which were both added with NAMD2.12 software. This is due to the linker -LEY being an addition to the natural sequence, added artificially, as well as the cysteine-alkyne- linker (EPL).[40] The predicted structure has a total net charge of +1e and a disulfide bridge which was kept throughout the simulations. The

residues belonging to the binding site were identified at the N-terminal by the open source platform for ligand detection *Fpocket* [219].

The simulations were performed in a NaCl solution and with a slab of the gold (81 Å x 86 Å x 14 Å) that consisted of Au atoms. The close packed gold surface of Au,[164] as already reported elsewhere,[174] has been created as a face-centered cubic crystal (fcc) with lattice parameter 4.078 Å. CHARM-METAL[220, 221] has been used for gold force-field parameters. The gold atoms were kept immobile during the simulation.

The simulations start with the protein above the solid surface, with a minimum protein-gold separation of 20 Å, so that the protein is free to diffuse before it contacts the neutral gold surface. In order to not bias the adsorption process, the protein starts in different orientations in different trajectories, as illustrated in Figure 6.5.

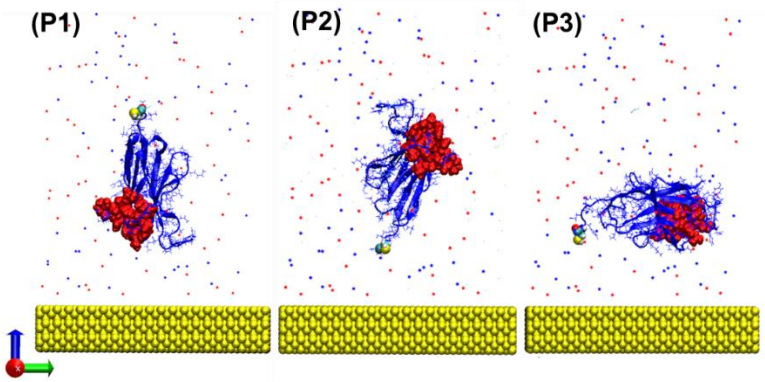

Figure 6.5 - Starting positions for MD simulations of NbVCAM1 adsorption at the surface. The gold atoms (yellow), the binding site (red) and the modified cysteine at the C-terminus (oxygen – red; carbon – cyan; nitrogen – blue; hydrogen – white and sulphur - yellow) are represented as van der Walls (VDW) spheres, while the other elements of the protein are represented by lines and new cartoon superposed. The NaCl ions in solution are also shown, but the water is not for clarity.

In P1, the N-C axis is normal to the surface with the C-terminal facing away from the surface, and in P2 it faces towards the surface. In P3, the N-C axis lies parallel to the surface. In all these starting configurations, the simulation box is then solvated with the TIP3P waters, neutralized by addition of one Cl^- ion, and then brought to 150 mM NaCl concentration.

The C-terminal modified cysteine is important due to the possibility for a thiolate bond forming with the surface, anchoring the nanobody in a favorable orientation for antigen binding. While these classical MD simulations do not attempt to create the thiolate bond during the simulation, it is still important to understand whether its formation is favourable due to the initial physical adsorption of the nanobody to the surface. At least three trajectories from each initial position (P1, P2, P3) were performed. The system minimisation was performed sequentially in two steps, first allowing water and ion movements, and then freeing the protein. The system is then heated to 310 K temperature over 30 ps, followed by 270 ps equilibration at constant temperature. Finally, the production simulations were performed for 100 ns with a time-step of 2 fs. Periodic Boundary conditions and NVT ensemble were applied in the simulations together with the smooth Particle Mesh Ewald (SPME)[222] for the Coulomb interactions. For ionizable residues the most probable charge states at pH 7 were chosen and no additional restrictions on momentum were applied.

6.4.7.2. Simulation model for nanobody anchored by a thiolate bond to gold

So far it is not possible to simulate a bond formation event such as the thiolate bond between the nanobody and gold surface, hence this bond had to be created with the force field parameters described below (Table 6.2), which were added to the parameters and topology files.

Table 6.2 - Force field parameters

Bond stretching				REF
Bond	b_0(Å)	$K_b(kcal/(mol/Å^2))$		
S-Au	2.4	1000		[223]
Angle bending				
Angle	$\theta_0(°)$	$k_\theta(kcal/(mol/rad^2))$		
Au-S-C	120.0	124.28		ChemBio 3D; [223]
Torsion				
Dihedrals	K_ϕ $(kcal/mol)$	n	δ (°)	
Au-S-C-C	0.310	3	0.00	Like S-S-C-C
Au-S-C-C	0.310	3	0.00	Like S-S-C-C
Au-S-C-H	0.158	3	0.00	Like S-S-C-H

6.4.7.3. Analysis: RMSD, RMSF

Both root-mean-square distance (RMSD) and fluctuations (RMSF) are tools of analysis to quantify the variability on conformation within a protein.[74] RMSD measures the degree of similarity between two protein three-dimensional (3D) structures with the same number of atoms. It is defined as

$$RMSD = \sqrt{\frac{\sum_{i=1}^{Natoms} |\vec{r}_i(t_1) - \vec{r}_i(t_2)|^2}{Natoms}}$$

Where the parameter $Natoms$ is the number of atoms in the protein structure and $\vec{r}_i(t_1)$ is the position of the i^{th} atom at a given time t. The RMSD calculation treats two protein structures to be compared as two rigid bodies (no internal flexibility allowed), then overlaps (aligns) using translations and rotations. In this case, the nanobody NbVCAM1 is compared with itself, between the final and initial defined structures. Herein, the RMSD results were applied to the alpha carbons that composed every residue of the nanobody or oligopeptide.

For RMSF, the RMSD is calculated for each nanobody's residue. It reflects each residue's mobility during the MD trajectory, by reporting an amplitude of residue movement (fluctuation) from the average position (in the aligned structures) over the total length of the MD trajectory. The time average for the atoms belonging to the same residue were calculated from the formula

$$RMSF_k = \sqrt{\langle \frac{\sum_{i=1}^{N_k} |\vec{r}_i(t) - \langle \vec{r}_i \rangle_T|^2}{N_k} \rangle_T}$$

Where $\vec{r}_i(t)$ is the position of the atom i in residue k at the time t, N_k is the number of atoms in the residue, and $\langle \vec{r}_i \rangle_T$ is the time average over the trajectory.

Chapter 7 Conclusions and future work

This thesis involved a range of studies which together guide the development of on demand biosensing platforms based on electrically switchable surfaces. Specifically, this research is fundamental to future investigations involving nanobodies and electrical switching units on surfaces which can provide a novel platform for controlled biosensing. Advanced analysis techniques such as XPS, SPR and TOF/3D OrbiSIMS, added valuable surface characterisation which with computational studies, compiled the conclusions from this thesis. The described strategies can be applied to the development of a variety of systems incorporating other macromolecules of interest for a wide range of biomedical and biotechnological applications. Nanobodies and charged oligopeptides as electro-switching units are promising building blocks for future electrical switchable surfaces for on demand biosensing.

A summary of the findings and conclusions outlined from the research described in chapters 3, 4 and 5 is herein presented, together with suggestions for further investigations and the author's perspectives.

Concerning the immobilisation of nanobodies on surfaces, limited approaches have been previously reported[88, 149, 150]. One approach included gold nanoparticles that had nanobodies immobilised through physical adsorption[150], while another approach had an engineered nanobody clicked to the sensor surface through alkyne-azide click chemistry[149]. An approach that has not been tried before included the immobilisation of nanobodies on gold through a cysteine, a method that could be oriented as click chemistry and easily achieved similar to physical adsorption without the need of extra monolayers. Hence, this new approach offers advantages compared to previously reported approaches. To attempt this, **Chapter 3**

investigated the direct immobilisation of engineered nanobodies (NbVCAM1) with a strategically C-terminal cysteine to bind to gold via the thiol moiety and provided the evidence of the biologically active, well-pack nanobody SAM formation. Firstly, the NbVCAM1 SAM formation was confirmed through surface characterisation via contact angle and ellipsometry which showed an increase in thickness. Thereafter, the hypothesis of a thiolate bond formation between the SAM engineered nanobodies and the gold surface was confirmed with OrbiSIMs and ToF-SIMS, revealing clear peaks for the S-Au bond, otherwise absent in the control bare gold samples. This confirmation allowed to postulate that the SAM nanobodies were well-oriented at the surface and could potentially be able to bind to their antigen (hVCAM1), being biologically active. The structural conformation of the NbVCAM1 on the surface was investigated by circular dichroism, which indicated the typical nanobody large composition of secondary β-sheet structures. Further molecular dynamic simulations predicted the direct immobilisation of NbVCAM1, where the final orientations could result in 1) well-oriented NbVCAM1 with the C-terminal cysteine close to the surface and the binding site facing the bulky solution, and in 2) randomly oriented NbVCAM1 with the binding site facing the surface. The appropriate orientation and biological activity of NbVCAM1 SAM was confirmed through SPR, with a higher antigen response relatively to the non-engineered randomly oriented NbVCAM1 monolayer.

This investigation contributed with a novel, efficient and stable approach to immobilise nanobodies on the surface. This novel immobilisation strategy has proven to be simple as physical adsorption and directional as consequence of the thiolate formation between the surface and the nanobodies. This Chapter has achieved a robust nanobody-based surface that can be widely extended as a biosensor platform with impact in biotechnological, biomedical and food applications. The direct immobilisation strategy can be transferred to numerous

nanobody-antigen systems, providing new options for the design of robust biosensing platforms. Additionally, due to the nanobody-antigen proximity to the surface the detection methods can include, besides optical techniques such as SPR that was used in Chapter 3, electrochemical measurements such as impedance.

Future studies could include the investigation of NbVCAM1 robustness under applied potential and investigate the stability of immobilised nanobodies for longer periods of time, increasing the potential of these nanobodies as tools for on demand biosensing.

On-demand sensing of hVCAM1 could allow the monitoring of inflammation and progress of atherosclerosis. To achieve on-demand biosensing, the and the possibility of having randomly oriented nanobodies on the NbVCAM1 SAM upon direct immobilisation needed to be addressed. In order to exclusively allow appropriate orientation, **Chapter 4** studied NbVCAM1 clicked to the surface *via* copper Cu(I) catalysed azide-alkyne cycloaddition applied to an initial azide-terminated SAM as inspired by Adriaensens and co-workers[149]. The NbVCAM1 antigen (hVCAM1) is a relatively large structure, thus, in addition to assuring that only well oriented nanobodies would be at the surface, another nanobody (NbGFP) was investigated due to the smaller antigen size (EGFP). NbGFP-EGFP was studied by Della Pia and co-workers[39] demonstrating nanobodies as powerful SPR tools. This Chapter accomplished appropriate orientation by immobilising NbGFP through EDC/NHS on a carboxylic acid terminated SAM, instead of on a dextran based matrix as previously published[39]. This is further demonstration that nanobodies can strongly perform on various functionalised surfaces.

The comparison between performances of the NbVCAM1 immobilisation strategies showed that both, direct and click chemistry immobilisation had similar antigenic SPR response. The next comparison between the well oriented clicked NbVCAM1 and amino coupled NbGFP

showed that NbGFP captured approximately 7 fold more antigens than NbVCAM1, a difference that is likely explained with surface constraints that the antigen encounters (such as steric hindrance). Such results demonstrated that the nanobodies orientation at the surface play an important role for the sensitivity along side with other factors, such as antigen size. After successful SPR response obtained with the NbGFP-EGFP pair, the NbGFP biological activity under applied electrical potential was verified alongside the absence of non-specific interactions between the antigen and C5K switching units. These results indicated the NbGFP-EGFP pair as a promising choice for integration on an electrical switchable biosensor. Future steps that include NbVCAM1 either in the format of SAM or clicked at the surface, could investigate alternative strategies to improve further the yield of captured antigens. For example, inspired by previous literature[67], an approach could include additional spacing between the nanobodies and the surface, perhaps allowing a more flexible monolayer that could adjust upon antigen approximation. Future steps regarding the NbGFP-EGFP pair should include switching studies that involve the optimisation of the ratio between NbGFP-EGFP and appropriate switching units towards high switching efficiency.

Combined, Chapter 3 and 4 through diverse immobilisation methods and nanobodies, built strong evidence on the potential of using nanobodies as capture entities for on demand biosensing. The most significant findings of these two chapters for the biosensing field included the ability to directly immobilise gold surfaces with nanobodies and evidence of these systems' stability upon applied charge, answering fundamental questions concerning robustness that were previously unanswered. The nanobodies capability to keep their biological activity when directly on gold and under applied electrical potential are characteristics likely common to other nanobodies due to their similar structural robustness[4]. The extension of these findings to other nanobody like structures has the potential to start novel scientific and bioengineering directions,

including for instance new formats for biosensing and implantable devices, where the applications are countless and only dependent on the nanobody specific targets. Therefore, these findings are a step forward for the design and fabrication of the next generation of nanobody-based surfaces.

Overall, upcoming steps should include the integration of binding and switching systems (nanobodies and switching units, respectively). To date, proof of concept for on demand biosensing was demonstrated through aptamers and low molecular weight entities for equally small biomarkers[1, 7, 119, 120]. If a nanobody-based switchable surface can successfully demonstrate switching efficiency and control over bio detection, such novel integrated system becomes an excellent proof of concept for platforms that could provide on demand biosensing of biomarkers with higher molecular weight.

Ultimately, the design of nanobody-based electrically switchable surfaces requires suitable switching units for the control over detection. Electrically switchable surfaces have been developed with oligopeptides up to 4 potentially charged peptides for different applications including cell release and attachment[112], and the control over binding of small antigen-antibody moeities[7]. However, to date there are no studies performed on longer charged oligopeptides that would aim to control larger nanobody-like structures. To address this need, **Chapter 5** focused on the design and development of surfaces containing charged oligopeptides, known to be successful switching units[7, 20, 118]. Charged oligopeptides that would be compatible with the immobilisation methods studied in Chapter 3 and 4 were explored. The initial investigation used thiol-terminated positively charged oligopeptides of different lengths and rigid or flexible backbones. It consisted in finding the right balance between oligopeptide and support molecule (oligopeptide:TEG11).

The requirement for any switching units to use with nanobodies includes 1) sufficient elongation to cover the binding site of nanobodies and 2) capacity to retract towards the surface allowing biodetection when triggered. Initial surface characterisation of thiol-terminated oligopeptide SAMs with ellipsometry and contact angle permitted to identify the optimal solution ratio for oligopeptide:TEG11 as 40:1, which resulted in potential thicknesses for all the tested oligopeptides to cover a standard nanobody. XPS studies provided the surface composition after the incubation with the oligopeptide:TEG11 at 40:1 solution ratio. All the thiol-terminated oligopeptides were considered potential candidates as switching units to use with nanobodies. Whilst previously studies have found the optimal ratio between C4K and a smaller spacer[214], this chapter has contributed with the optimal solution ratio between longer charged oligopeptides mixed with longer support molecules, a combination that has not been studied before. Such findings aid to a broader range of electrically charged oligopeptides available for custom made switchable surfaces that could be compatible with binding systems of low to higher molecular weights, including nanobodies like structures.

Preliminary studies involving nanobodies and switching units showed promising results under open circuit conditions, with partial coverage of the nanobodies binding sites. Non-specific interactions between the switching system and the binding system upon applied potential emerged as a drawback, potentially due to the high net charge of the antigen. These studies highlight that special attention must be given to the charge of the antigens of interest. Future studies could redesign the tail group of the switching units that can account for the charged target proteins. For example, one could consider to use the switching unit with identical charge to the antigen as means to repeal the antigen under OFF conditions. Potentially this would allow that once the oppositive potential is applied at the surface (ON conditions), the switching units would retract and antigens would simultaneously be attracted to surface to approach and bind.

In conclusion, any of the studied oligopeptides are potential switching units and must be assessed with the appropriate nanobody-antigen pair. Future work should combine the studied oligopeptides with appropriate nanobodies, as the combination of the binding and switching systems will allow the verification for best switching performance between rigid and flexible oligopeptides.

Chapter 5 provided potential choices of rigid and flexible charged oligopeptides to use with thiol-terminated nanobodies. However, the same switching studies would not be suitable to use in a system that relies on amino-coupling. Envisioning the convenient approach of simultaneous amino-coupling nanobodies and switching units, meant that the charged oligopeptides could not be based on amines from lysines, but instead on carboxyl groups from glutamic acids. A few challenges were found with this strategy and further investigations, such as using different pHs for EDC/NHS, will be required before proceeding with such system. From following the conditions used by the nanobody in Chapter 4 (NbGFP) to immobilise amino-terminated charged oligopeptides, the ellipsometry and contact angle measurements were not conclusive of the coupling success. Additional studies highlighted the non triviality of successfully achieving amino-coupling of negatively charged oligopeptides without falling into considerably high quantities (higher than the millimolar range), which would consequently increase associated costs. Whilst such a strategy would simplify the immobilisation workflow, the underlying requisite consists in finding the conditions that agree for both nanobody and switching units best density at the surface. In this case, not only the solution ratios will play a role, but also the selection of appropriate pH and initial SAMs. Following this direction, future work could attempt to improve the amino coupling of model oligopeptides, through the use of different coupling agents. Alternatively, biorthogonal chemistry could be considered along with a different design of charged oligopeptides.

In conclusion, Chapter 5 revealed the experimental conditions for the theoretical thickness to cover the binding site of a nanobody. These showed to be compatible with the four different switching units, demonstrating that the strategy can be applied with other switching units of similar lengths. Additionally, a few limitations were also revealed, which need careful consideration when developing similar switching systems. Systems that are based on amino-coupling will require additional optimisation in order to find the adequate conditions and avoid complex multi-step processes. Furthermore, interactions between the binding and the switching system must be investigated in order to avoid non-specific interactions.

Altogether, this thesis has contributed with insight on switchable surfaces including the possibility for combining nanobodies and creation of novel biodetection platforms. This thesis has hypothesized and proved that it is possible to potentially obtain a robust biosensor by directly immobilising nanobodies on gold surfaces. These findings have contributed to the field of biosensors by addressing the gap of using nanobodies directly on the surface and proving their biological activity and biodetection performance.

Additionally, this thesis has highlighted crucial factors for optimisation of nanobody-based switchable platforms and found that nanobodies are capable of remaining biologically active upon applied potentials. Although not published, this discovery addresses a fundamental requirement for any prospective biological structure to be used on electrically switchable surfaces. In addition, the confirmation of nanobodies' robustness upon applied potential strengthens the benefits of choosing electrical stimulus for switchable surfaces.

Finally, the findings of this thesis related to the switching systems addressed carefully designed oligopeptides with new lengths and different composition. The research of switchable systems on its own can contribute to diverse biomedical applications beyond the biosensing field,

including *in vitro* cell studies, drug delivery and *in vivo* implantable devices. In particular to the biosensing field, this thesis lays the groundwork for understanding electrically charged oligopeptides for the purpose of manipulating the biomolecular binding of nanobodies at the surface. Thus, this work builds the foundation of future switchable surfaces composed by nanobodies and charged oligopeptides with capability to create endless robust biosensors, only depending on the biomarkers required to target.

The biosensing field has been growing over the years with the advance of nanotechnology that allows smaller and precise devices, with the discoveries of new medically relevant biomarkers and with the need to monitor health and diagnose diseases. Alongside with progress, new challenges arise and the biosensing field is facing newer and higher demands. Such challenges include sensitivity, stability over long periods of time, reusability and on demand sensing. All of these challenges could be addressed by biological switchable surfaces for on demand biosensing, and this thesis has contributed to the foundation of that achievement.

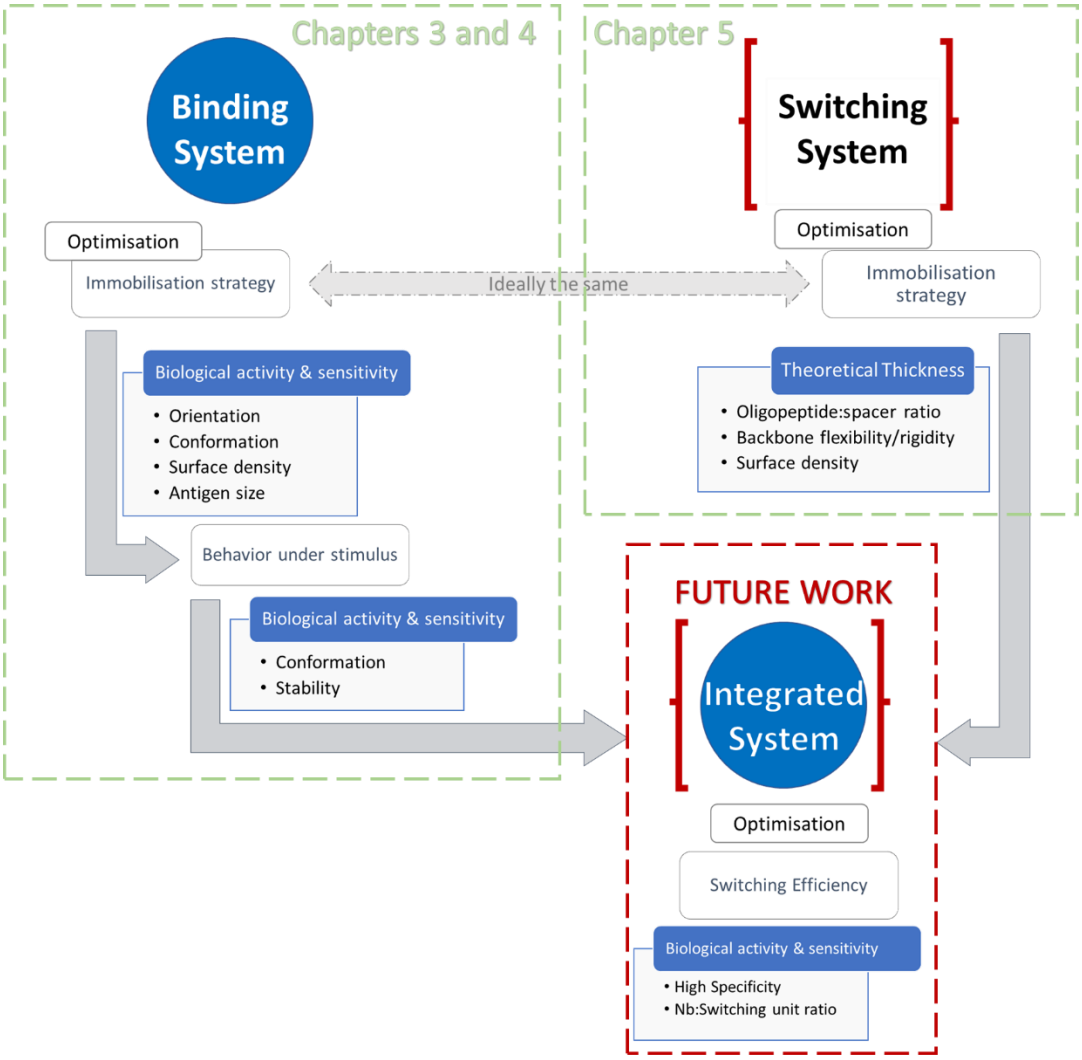

Figure 7.1 -Schematic overview of this thesis achievements and future work.

Chapter 8 References

1. Gomes, B. S.; Simões, B.; Mendes, P. M., The increasing dynamic, functional complexity of bio-interface materials. *Nature Reviews Chemistry* **2018,** *2* (3), 0120.
2. Simões, B.; Guedens, W. J.; Keene, C.; Kubiak-Ossowska, K.; Mulheran, P.; Kotowska, A. M.; Scurr, D. J.; Alexander, M. R.; Broisat, A.; Johnson, S.; Muyldermans, S.; Devoogdt, N.; Adriaensens, P.; Mendes, P. M., Direct Immobilization of Engineered Nanobodies on Gold Sensors. *ACS Applied Materials & Interfaces* **2021,** *13* (15), 17353-17360.
3. Wen, W.; Yan, X.; Zhu, C.; Du, D.; Lin, Y., Recent Advances in Electrochemical Immunosensors. *Analytical Chemistry* **2017,** *89* (1), 138-156.
4. Muyldermans, S., Applications of Nanobodies. *Annual Review of Animal Biosciences* **2021,** *9* (1), 401-421.
5. Kijanka, M.; Dorresteijn, B.; Oliveira, S.; van Bergen en Henegouwen, P. M. P., Nanobody-based cancer therapy of solid tumors. *Nanomedicine* **2015,** *10* (1), 161-174.
6. De Moraes, A. C.; Kubota, L. T., Recent Trends in Field-Effect Transistors-Based Immunosensors. *Chemosensors* **2016,** *4* (4).
7. Santos Gomes, B.; Cantini, E.; Tommasone, S.; Gibson, J. S.; Wang, X.; Zhu, Q.; Ma, J.; McGettrick, J. D.; Watson, T. M.; Preece, J. A.; Kirkman-Brown, J. C.; Publicover, S. J.; Mendes, P. M., On-Demand Electrical Switching of Antibody–Antigen Binding on Surfaces. *ACS Applied Bio Materials* **2018,** *1* (3), 738-747.
8. Elnathan, R.; Kwiat M Fau - Pevzner, A.; Pevzner A Fau - Engel, Y.; Engel Y Fau - Burstein, L.; Burstein L Fau - Khatchtourints, A.; Khatchtourints A Fau - Lichtenstein, A.; Lichtenstein A Fau - Kantaev, R.; Kantaev R Fau - Patolsky, F.; Patolsky, F., Biorecognition layer engineering: overcoming screening limitations of nanowire-based FET devices. (1530-6992 (Electronic)).
9. Zucolotto, V., Specialty Grand Challenges in Biosensors. *Frontiers in Sensors* **2020,** *1* (3).
10. Mendes, P. M., Stimuli-responsive surfaces for bio-applications. *Chemical Society Reviews* **2008,** *37* (11), 2512-2529.
11. Bowden, N.; Terfort A Fau - Carbeck, J.; Carbeck J Fau - Whitesides, G. M.; Whitesides, G. M., Self-Assembly of Mesoscale Objects into Ordered Two-Dimensional Arrays. (1095-9203 (Electronic)).
12. Casalini, S.; Bortolotti, C. A.; Leonardi, F.; Biscarini, F., Self-assembled monolayers in organic electronics. *Chemical Society Reviews* **2017,** *46* (1), 40-71.
13. Love, J. C.; Estroff, L. A.; Kriebel, J. K.; Nuzzo, R. G.; Whitesides, G. M., Self-Assembled Monolayers of Thiolates on Metals as a Form of Nanotechnology. *Chemical Reviews* **2005,** *105* (4), 1103-1170.
14. Xue, Y.; Li, X.; Li, H.; Zhang, W., Quantifying thiol–gold interactions towards the efficient strength control. *Nature Communications* **2014,** *5* (1), 4348.
15. Vericat, C.; Vela, M. E.; Benitez, G.; Carro, P.; Salvarezza, R. C., Self-assembled monolayers of thiols and dithiols on gold: new challenges for a well-known system. *Chemical Society Reviews* **2010,** *39* (5), 1805-1834.
16. Ulman, A., Formation and Structure of Self-Assembled Monolayers. *Chem Rev* **1996,** *96* (4), 1533-1554.
17. Bain, C. D.; Troughton, E. B.; Tao, Y. T.; Evall, J.; Whitesides, G. M.; Nuzzo, R. G., Formation of monolayer films by the spontaneous assembly of organic thiols from solution onto gold. *Journal of the American Chemical Society* **1989,** *111* (1), 321-335.
18. Vericat, C.; Vela, M. E.; Salvarezza, R. C., Self-assembled monolayers of alkanethiols on Au(111): surface structures, defects and dynamics. *Physical Chemistry Chemical Physics* **2005,** *7* (18), 3258-3268.
19. Schwartz, D. K., MECHANISMS AND KINETICS OF SELF-ASSEMBLED MONOLAYER FORMATION. *Annual Review of Physical Chemistry* **2001,** *52* (1), 107-137.

20. Yeung, C. L.; Iqbal, P.; Allan, M.; Lashkor, M.; Preece, J. A.; Mendes, P. M., Tuning Specific Biomolecular Interactions Using Electro-Switchable Oligopeptide Surfaces. *Advanced Functional Materials* **2010,** *20* (16), 2657-2663.
21. Zhong, C.-J.; Zak, J.; Porter, M. D., Voltammetric reductive desorption characteristics of alkanethiolate monolayers at single crystal Au(111) and (110) electrode surfaces. *Journal of Electroanalytical Chemistry* **1997,** *421* (1), 9-13.
22. Widrig, C. A.; Chung, C.; Porter, M. D., The electrochemical desorption of n-alkanethiol monolayers from polycrystalline Au and Ag electrodes. *Journal of Electroanalytical Chemistry and Interfacial Electrochemistry* **1991,** *310* (1), 335-359.
23. Khan, M. Z. H., Effect of ITO surface properties on SAM modification: A review toward biosensor application. *Cogent Engineering* **2016,** *3* (1), 1170097.
24. Lee, J. M.; Park, H. K.; Jung, Y.; Kim, J. K.; Jung, S. O.; Chung, B. H., Direct Immobilization of Protein G Variants with Various Numbers of Cysteine Residues on a Gold Surface. *Analytical Chemistry* **2007,** *79* (7), 2680-2687.
25. Magis, G. J.; Olsen, J. D.; Reynolds, N. P.; Leggett, G. J.; Hunter, C. N.; Aartsma, T. J.; Frese, R. N., Use of Engineered Unique Cysteine Residues to Facilitate Oriented Coupling of Proteins Directly to a Gold Substrate. *Photochemistry and Photobiology* **2011,** *87* (5), 1050-1057.
26. Park, K.; Lee, J. M.; Jung, Y.; Habtemariam, T.; Salah, A. W.; Fermin, C. D.; Kim, M., Combination of cysteine- and oligomerization domain-mediated protein immobilization on a surface plasmon resonance (SPR) gold chip surface. *Analyst* **2011,** *136* (12), 2506-2511.
27. Gobi, K. V.; Matsumoto, K.; Toko, K.; Ikezaki, H.; Miura, N., Enhanced sensitivity of self-assembled-monolayer-based SPR immunosensor for detection of benzaldehyde using a single-step multi-sandwich immunoassay. *Analytical and Bioanalytical Chemistry* **2007,** *387* (8), 2727-2735.
28. Chen, S.; Li, L.; Zhao, C.; Zheng, J., Surface hydration: Principles and applications toward low-fouling/nonfouling biomaterials. *Polymer* **2010,** *51* (23), 5283-5293.
29. Liu, B.; Liu, X.; Shi, S.; Huang, R.; Su, R.; Qi, W.; He, Z., Design and mechanisms of antifouling materials for surface plasmon resonance sensors. *Acta Biomaterialia* **2016,** *40*, 100-118.
30. Prime, K. L.; Whitesides, G. M., Adsorption of proteins onto surfaces containing end-attached oligo(ethylene oxide): a model system using self-assembled monolayers. *Journal of the American Chemical Society* **1993,** *115* (23), 10714-10721.
31. Kanari, Y.; Shoji, Y.; Ode, H.; Miyake, T.; Tanii, T.; Hoshino, T.; Ohdomari, I., Protein Adsorption on Self-Assembled Monolayers Induced by Surface Water Molecule. *Japanese Journal of Applied Physics* **2007,** *46* (9B), 6303-6308.
32. Li, L.; Chen, S.; Zheng, J.; Ratner, B. D.; Jiang, S., Protein Adsorption on Oligo(ethylene glycol)-Terminated Alkanethiolate Self-Assembled Monolayers: The Molecular Basis for Nonfouling Behavior. *The Journal of Physical Chemistry B* **2005,** *109* (7), 2934-2941.
33. Lashkor, M.; Rawson, F. J.; Preece, J. A.; Mendes, P. M., Switching specific biomolecular interactions on surfaces under complex biological conditions. *Analyst* **2014,** *139* (21), 5400-5408.
34. Ravi Shankaran, D.; Miura, N., Trends in interfacial design for surface plasmon resonance based immunoassays. *Journal of Physics D: Applied Physics* **2007,** *40* (23), 7187-7200.
35. Ferretti, S.; Paynter, S.; Russell, D. A.; Sapsford, K. E.; Richardson, D. J., Self-assembled monolayers: a versatile tool for the formulation of bio-surfaces. *TrAC Trends in Analytical Chemistry* **2000,** *19* (9), 530-540.
36. Li, L.; Chen, S.; Jiang, S., Protein Adsorption on Alkanethiolate Self-Assembled Monolayers: Nanoscale Surface Structural and Chemical Effects. *Langmuir* **2003,** *19* (7), 2974-2982.
37. Hyun, J.; Ahn, S. J.; Lee, W. K.; Chilkoti, A.; Zauscher, S., Molecular Recognition-Mediated Fabrication of Protein Nanostructures by Dip-Pen Lithography. *Nano Letters* **2002,** *2* (11), 1203-1207.
38. Ta, D. T.; Guedens, W.; Vranken, T.; Vanschoenbeek, K.; Steen Redeker, E.; Michiels, L.; Adriaensens, P., Enhanced Biosensor Platforms for Detecting the Atherosclerotic Biomarker VCAM1

Based on Bioconjugation with Uniformly Oriented VCAM1-Targeting Nanobodies. LID - 10.3390/bios6030034 [doi] LID - 34. (2079-6374 (Electronic)).
39. Della Pia, E. A.; Martinez, K. L., Single Domain Antibodies as a Powerful Tool for High Quality Surface Plasmon Resonance Studies. *PLOS ONE* **2015,** *10* (3), e0124303.
40. Ta, D. T.; Redeker, E. S.; Billen, B.; Reekmans, G.; Sikulu, J.; Noben, J. P.; Guedens, W.; Adriaensens, P., An efficient protocol towards site-specifically clickable nanobodies in high yield: cytoplasmic expression in Escherichia coli combined with intein-mediated protein ligation. (1741-0134 (Electronic)).
41. Rao, S. V.; Anderson, K. W.; Bachas, L. G., Oriented immobilization of proteins. *Microchimica Acta* **1998,** *128* (3), 127-143.
42. Lee, W.; Oh, B.-K.; Lee, W. H.; Choi, J.-W., Immobilization of antibody fragment for immunosensor application based on surface plasmon resonance. *Colloids and Surfaces B: Biointerfaces* **2005,** *40* (3), 143-148.
43. Kausaite-Minkstimiene, A.; Ramanaviciene, A.; Kirlyte, J.; Ramanavicius, A., Comparative Study of Random and Oriented Antibody Immobilization Techniques on the Binding Capacity of Immunosensor. *Analytical Chemistry* **2010,** *82* (15), 6401-6408.
44. Vikholm-Lundin, I.; Albers, W. M., Site-directed immobilisation of antibody fragments for detection of C-reactive protein. *Biosensors and Bioelectronics* **2006,** *21* (7), 1141-1148.
45. Karyakin, A. A.; Presnova, G. V.; Rubtsova, M. Y.; Egorov, A. M., Oriented Immobilization of Antibodies onto the Gold Surfaces via Their Native Thiol Groups. *Analytical Chemistry* **2000,** *72* (16), 3805-3811.
46. Fischer, M. J. E., Amine Coupling Through EDC/NHS: A Practical Approach. In *Surface Plasmon Resonance: Methods and Protocols*, Mol, N. J.; Fischer, M. J. E., Eds. Humana Press: Totowa, NJ, 2010; pp 55-73.
47. Johnsson, B.; Löfås, S.; Lindquist, G., Immobilization of proteins to a carboxymethyldextran-modified gold surface for biospecific interaction analysis in surface plasmon resonance sensors. *Analytical Biochemistry* **1991,** *198* (2), 268-277.
48. Risse, F.; Gedig, E. T.; Gutmann, J. S., Carbodiimide-mediated immobilization of acidic biomolecules on reversed-charge zwitterionic sensor chip surfaces. *Analytical and Bioanalytical Chemistry* **2018,** *410* (17), 4109-4122.
49. Reynolds, N. P.; Janusz, S.; Escalante-Marun, M.; Timney, J.; Ducker, R. E.; Olsen, J. D.; Otto, C.; Subramaniam, V.; Leggett, G. J.; Hunter, C. N., Directed Formation of Micro- and Nanoscale Patterns of Functional Light-Harvesting LH2 Complexes. *Journal of the American Chemical Society* **2007,** *129* (47), 14625-14631.
50. Kolb, H. C.; Finn, M. G.; Sharpless, K. B., Click Chemistry: Diverse Chemical Function from a Few Good Reactions. *Angewandte Chemie International Edition* **2001,** *40* (11), 2004-2021.
51. Yáñez-Sedeño, P.; González-Cortés, A.; Campuzano, S.; Pingarrón, J. M., Copper(I)-Catalyzed Click Chemistry as a Tool for the Functionalization of Nanomaterials and the Preparation of Electrochemical (Bio)Sensors. *Sensors* **2019,** *19* (10), 2379.
52. Hudalla, G. A.; Murphy, W. L., Using "Click" Chemistry to Prepare SAM Substrates to Study Stem Cell Adhesion. *Langmuir* **2009,** *25* (10), 5737-5746.
53. Nie, J.; Li, J.-P.; Deng, H.; Pan, H.-C., Progress on Click Chemistry and Its Application in Chemical Sensors. *Chinese Journal of Analytical Chemistry* **2015,** *43* (4), 609-617.
54. Trilling, A. K.; Hesselink, T.; Houwelingen, A. v.; Cordewener, J. H. G.; Jongsma, M. A.; Schoffelen, S.; Hest, J. C. M. v.; Zuilhof, H.; Beekwilder, J., Orientation of llama antibodies strongly increases sensitivity of biosensors. *Biosensors and Bioelectronics* **2014,** *60*, 130-136.
55. Chelmowski, R.; Käfer, D.; Köster, S. D.; Klasen, T.; Winkler, T.; Terfort, A.; Metzler-Nolte, N.; Wöll, C., Postformation Modification of SAMs: Using Click Chemistry to Functionalize Organic Surfaces. *Langmuir* **2009,** *25* (19), 11480-11485.

56. Tolstyka, Z. P.; Richardson, W.; Bat, E.; Stevens, C. J.; Parra, D. P.; Dozier, J. K.; Distefano, M. D.; Dunn, B.; Maynard, H. D., Chemoselective Immobilization of Proteins by Microcontact Printing and Bio-orthogonal Click Reactions. *ChemBioChem* **2013,** *14* (18), 2464-2471.
57. Chen, Y.; Xianyu, Y.; Wu, J.; Yin, B.; Jiang, X., Click Chemistry-Mediated Nanosensors for Biochemical Assays. (1838-7640 (Electronic)).
58. Presolski, S. I.; Hong Vp Fau - Finn, M. G.; Finn, M. G., Copper-Catalyzed Azide-Alkyne Click Chemistry for Bioconjugation. (2160-4762 (Electronic)).
59. Li, L.; Zhang, Z., Development and Applications of the Copper-Catalyzed Azide-Alkyne Cycloaddition (CuAAC) as a Bioorthogonal Reaction. *Molecules* **2016,** *21* (10), 1393.
60. Yu, X. Y.; Xu, Q. L.; Wu, Y.; Jiang, H. J.; Wei, W.; Zulipikaer, A.; Guo, Y.; Jirimutu; Chen, J., Nanobodies derived from Camelids represent versatile biomolecules for biomedical applications. *Biomater. Sci.* **2020,** *8* (13), 3559-3573.
61. Tillib, S. V., Prospective Applications of Single-Domain Antibodies in Biomedicine. *Mol. Biol.* **2020,** *54* (3), 317-326.
62. Gonzalez-Sapienza, G.; Sofia, M. A. R.; Tabares-da, R., Single-Domain Antibodies As versatile Affinity Reagents for Analytical and Diagnostic Applications. *Front. Immunol.* **2017,** *8*, 12.
63. Muyldermans, S., Nanobodies: Natural Single-Domain Antibodies. In *Annual Review of Biochemistry, Vol 82*, Kornberg, R. D., Ed. 2013; Vol. 82, pp 775-797.
64. Dumoulin M; Conrath K; Van Meirhaeghe A; Meersman F, H. K.; Frenken LG; Muyldermans S, W. L.; A, M., Single-domain antibody fragments with high conformational stability. *Protein Sci* **2002,** (0961-8368 (Print)).
65. Saerens, D.; Frederix, F.; Reekmans, G.; Conrath, K.; Jans, K.; Brys, L.; Huang, L.; Bosmans, E.; Maes, G.; Borghs, G.; Muyldermans, S., Engineering Camel Single-Domain Antibodies and Immobilization Chemistry for Human Prostate-Specific Antigen Sensing. *Analytical Chemistry* **2005,** *77* (23), 7547-7555.
66. Hu, Y.; Liu, C.; Muyldermans, S., Nanobody-Based Delivery Systems for Diagnosis and Targeted Tumor Therapy. *Front. Immunol.* **2017,** *8*, 1442-1442.
67. Goode, J.; Dillon, G.; Millner, P. A., The development and optimisation of nanobody based electrochemical immunosensors for IgG. *Sensors and Actuators B: Chemical* **2016,** *234*, 478-484.
68. Filipiak, M. S.; Rother, M.; Andoy, N. M.; Knudsen, A. C.; Grimm, S.; Bachran, C.; Swee, L. K.; Zaumseil, J.; Tarasov, A., Highly sensitive, selective and label-free protein detection in physiological solutions using carbon nanotube transistors with nanobody receptors. *Sensors and Actuators B: Chemical* **2018,** *255*, 1507-1516.
69. Fischer, D.; Curioni, A.; Andreoni, W., Decanethiols on Gold: The Structure of Self-Assembled Monolayers Unraveled with Computer Simulations. *Langmuir* **2003,** *19* (9), 3567-3571.
70. Penna, M. J.; Mijajlovic, M.; Biggs, M. J., Molecular-Level Understanding of Protein Adsorption at the Interface between Water and a Strongly Interacting Uncharged Solid Surface. *Journal of the American Chemical Society* **2014,** *136* (14), 5323-5331.
71. Quan, X.; Liu, J.; Zhou, J., Multiscale modeling and simulations of protein adsorption: progresses and perspectives. *Current Opinion in Colloid & Interface Science* **2019,** *41*, 74-85.
72. Marquetti, I.; Desai, S., Molecular modeling the adsorption behavior of bone morphogenetic protein-2 on hydrophobic and hydrophilic substrates. *Chemical Physics Letters* **2018,** *706*, 285-294.
73. Malaspina, D. C.; Pérez-Fuentes, L.; Drummond, C.; Bastos-González, D.; Faraudo, J., Protein-surface interactions at the nanoscale: Atomistic simulations with implicit solvent models. *Current Opinion in Colloid & Interface Science* **2019,** *41*, 40-49.
74. Al Qaraghuli, M. M.; Kubiak-Ossowska, K.; Mulheran, P. A., Thinking outside the Laboratory: Analyses of Antibody Structure and Dynamics within Different Solvent Environments in Molecular Dynamics (MD) Simulations. *Antibodies* **2018,** *7* (3), 21.

75. Kubiak-Ossowska, K.; Jachimska, B.; Al Qaraghuli, M.; Mulheran, P. A., Protein interactions with negatively charged inorganic surfaces. *Current Opinion in Colloid & Interface Science* **2019,** *41*, 104-117.
76. Mohseni, A.; Molakarimi, M.; Taghdir, M.; Sajedi, R. H.; Hasannia, S., Exploring single-domain antibody thermostability by molecular dynamics simulation. *Journal of Biomolecular Structure and Dynamics* **2019,** *37* (14), 3686-3696.
77. Gray, E. R.; Brookes, J. C.; Caillat, C.; Turbé, V.; Webb, B. L. J.; Granger, L. A.; Miller, B. S.; McCoy, L. E.; El Khattabi, M.; Verrips, C. T.; Weiss, R. A.; Duffy, D. M.; Weissenhorn, W.; McKendry, R. A., Unravelling the Molecular Basis of High Affinity Nanobodies against HIV p24: In Vitro Functional, Structural, and in Silico Insights. *ACS Infectious Diseases* **2017,** *3* (7), 479-491.
78. Hacisuleyman, A.; Erman, B., ModiBodies: A computational method for modifying nanobodies in nanobody-antigen complexes to improve binding affinity and specificity. *Journal of Biological Physics* **2020,** *46* (2), 189-208.
79. Huang, L.; Reekmans, G.; Saerens, D.; Friedt, J.-M.; Frederix, F.; Francis, L.; Muyldermans, S.; Campitelli, A.; Hoof, C. V., Prostate-specific antigen immunosensing based on mixed self-assembled monolayers, camel antibodies and colloidal gold enhanced sandwich assays. *Biosensors and Bioelectronics* **2005,** *21* (3), 483-490.
80. Patris, S.; De Pauw, P.; Vandeput, M.; Huet, J.; Van Antwerpen, P.; Muyldermans, S.; Kauffmann, J.-M., Nanoimmunoassay onto a screen printed electrode for HER2 breast cancer biomarker determination. *Talanta* **2014,** *130*, 164-170.
81. Mars, A.; Bouhaouala-Zahar, B.; Raouafi, N., Ultrasensitive sensing of Androctonus australis hector scorpion venom toxins in biological fluids using an electrochemical graphene quantum dots/nanobody-based platform. *Talanta* **2018,** *190*, 182-187.
82. Morales-Yanez, F. J.; Sariego, I.; Vincke, C.; Hassanzadeh-Ghassabeh, G.; Polman, K.; Muyldermans, S., An innovative approach in the detection of Toxocara canis excretory/secretory antigens using specific nanobodies. *International Journal for Parasitology* **2019,** *49* (8), 635-645.
83. Guo, K.; Wustoni, S.; Koklu, A.; Díaz-Galicia, E.; Moser, M.; Hama, A.; Alqahtani, A. A.; Ahmad, A. N.; Alhamlan, F. S.; McCulloch, I.; Arold, S. T.; Grünberg, R.; Inal, S., A nanobody-functionalized organic electrochemical transistor for the rapid detection of SARS-CoV-2 and MERS antigens at the physical limit. *medRxiv* **2020**, 2020.11.12.20228874.
84. Doerflinger Sylvie, Y.; Tabatabai, J.; Schnitzler, P.; Farah, C.; Rameil, S.; Sander, P.; Koromyslova, A.; Hansman Grant, S.; Coyne Carolyn, B., Development of a Nanobody-Based Lateral Flow Immunoassay for Detection of Human Norovirus. *mSphere 1* (5), e00219-16.
85. Gelkop, S.; Sobarzo, A.; Brangel, P.; Vincke, C.; Romão, E.; Fedida-Metula, S.; Strom, N.; Ataliba, I.; Mwiine, F. N.; Ochwo, S.; Velazquez-Salinas, L.; McKendry, R. A.; Muyldermans, S.; Lutwama, J. J.; Rieder, E.; Yavelsky, V.; Lobel, L., The Development and Validation of a Novel Nanobody-Based Competitive ELISA for the Detection of Foot and Mouth Disease 3ABC Antibodies in Cattle. *Frontiers in Veterinary Science* **2018,** *5* (250).
86. Pinto Torres, J. E.; Goossens, J.; Ding, J.; Li, Z.; Lu, S.; Vertommen, D.; Naniima, P.; Chen, R.; Muyldermans, S.; Sterckx, Y. G. J.; Magez, S., Development of a Nanobody-based lateral flow assay to detect active Trypanosoma congolense infections. *Scientific Reports* **2018,** *8* (1), 9019.
87. Zhong, W.; Li, G.; Yu, X.; Zhu, M.; Gong, L.; Wan, Y., Sensitive detection of Bacillus thuringiensis Cry1B toxin based on camel single-domain antibodies. *MicrobiologyOpen* **2018,** *7* (4), e00581.
88. Xu, L.; Cao, H. Y.; Huang, C. D.; Jia, L. Y., Oriented Immobilization and Quantitative Analysis Simultaneously Realized in Sandwich Immunoassay via His-Tagged Nanobody. *Molecules* **2019,** *24* (10), 11.
89. Li, H.; Yan, J.; Ou, W.; Liu, H.; Liu, S.; Wan, Y., Construction of a biotinylated cameloid-like antibody for lable-free detection of apolipoprotein B-100. *Biosensors and Bioelectronics* **2015,** *64*, 111-118.

90. Campuzano, S.; Salema, V.; Moreno-Guzmán, M.; Gamella, M.; Yáñez-Sedeño, P.; Fernández, L. A.; Pingarrón, J. M., Disposable amperometric magnetoimmunosensors using nanobodies as biorecognition element. Determination of fibrinogen in plasma. *Biosensors and Bioelectronics* **2014,** *52*, 255-260.
91. Li, D.; Morisseau, C.; McReynolds, C. B.; Duflot, T.; Bellien, J.; Nagra, R. M.; Taha, A. Y.; Hammock, B. D., Development of Improved Double-Nanobody Sandwich ELISAs for Human Soluble Epoxide Hydrolase Detection in Peripheral Blood Mononuclear Cells of Diabetic Patients and the Prefrontal Cortex of Multiple Sclerosis Patients. *Analytical Chemistry* **2020,** *92* (10), 7334-7342.
92. Brilhante-da-Silva, N.; de Oliveira Sousa, R. M.; Arruda, A.; dos Santos, E. L.; Marinho, A. C. M.; Stabeli, R. G.; Fernandes, C. F. C.; Pereira, S. d. S., Camelid Single-Domain Antibodies for the Development of Potent Diagnosis Platforms. *Molecular Diagnosis & Therapy* **2021,** *25* (4), 439-456.
93. Zakeri, B.; Fierer, J. O.; Celik, E.; Chittock, E. C.; Schwarz-Linek, U.; Moy, V. T.; Howarth, M., Peptide tag forming a rapid covalent bond to a protein, through engineering a bacterial adhesin. *Proceedings of the National Academy of Sciences* **2012,** *109* (12), E690.
94. Oloketuyi, S.; Mazzega, E.; Zavašnik, J.; Pungjunun, K.; Kalcher, K.; de Marco, A.; Mehmeti, E., Electrochemical immunosensor functionalized with nanobodies for the detection of the toxic microalgae Alexandrium minutum using glassy carbon electrode modified with gold nanoparticles. *Biosensors and Bioelectronics* **2020,** *154*, 112052.
95. Andersson, K.; Areskoug D Fau - Hardenborg, E.; Hardenborg, E., Exploring buffer space for molecular interactions. (0952-3499 (Print)).
96. Cantini, E.; Wang, X.; Koelsch, P.; Preece, J. A.; Ma, J.; Mendes, P. M., Electrically Responsive Surfaces: Experimental and Theoretical Investigations. *Accounts of Chemical Research* **2016,** *49* (6), 1223-1231.
97. Polte, T. R.; Shen M Fau - Karavitis, J.; Karavitis J Fau - Montoya, M.; Montoya M Fau - Pendse, J.; Pendse J Fau - Xia, S.; Xia S Fau - Mazur, E.; Mazur E Fau - Ingber, D. E.; Ingber, D. E., Nanostructured magnetizable materials that switch cells between life and death. (0142-9612 (Print)).
98. Epstein, A. K.; Hong, D.; Kim, P.; Aizenberg, J., Biofilm attachment reduction on bioinspired, dynamic, micro-wrinkling surfaces. *New Journal of Physics* **2013,** *15* (9), 095018.
99. Wegner, S. V.; Sentürk, O. I.; Spatz, J. P., Photocleavable linker for the patterning of bioactive molecules. *Scientific Reports* **2015,** *5* (1), 18309.
100. Kadem, L. F.; Holz, M.; Suana, K. G.; Li, Q.; Lamprecht, C.; Herges, R.; Selhuber-Unkel, C., Rapid Reversible Photoswitching of Integrin-Mediated Adhesion at the Single-Cell Level. *Advanced Materials* **2016,** *28* (9), 1799-1802.
101. Ashaduzzaman, M.; Anto Antony, A.; Arul Murugan, N.; Deshpande, S. R.; Turner, A. P. F.; Tiwari, A., Studies on an on/off-switchable immunosensor for troponin T. *Biosensors and Bioelectronics* **2015,** *73*, 100-107.
102. Yu, Q.; Shivapooja, P.; Johnson, L. M.; Tizazu, G.; Leggett, G. J.; López, G. P., Nanopatterned polymer brushes as switchable bioactive interfaces. *Nanoscale* **2013,** *5* (9), 3632-3637.
103. Shastri, A.; McGregor, L. M.; Liu, Y.; Harris, V.; Nan, H.; Mujica, M.; Vasquez, Y.; Bhattacharya, A.; Ma, Y.; Aizenberg, M.; Kuksenok, O.; Balazs, A. C.; Aizenberg, J.; He, X., An aptamer-functionalized chemomechanically modulated biomolecule catch-and-release system. (1755-4349 (Electronic)).
104. Zelzer, M.; McNamara, L. E.; Scurr, D. J.; Alexander, M. R.; Dalby, M. J.; Ulijn, R. V., Phosphatase responsive peptide surfaces. *Journal of Materials Chemistry* **2012,** *22* (24), 12229-12237.
105. Jariwala, T.; Ico, G.; Tai, Y.; Park, H.; Myung, N. V.; Nam, J., Mechano-Responsive Piezoelectric Nanofiber as an On-Demand Drug Delivery Vehicle. *ACS Applied Bio Materials* **2021,** *4* (4), 3706-3715.
106. Mertz, D.; Vogt C Fau - Hemmerlé, J.; Hemmerlé J Fau - Mutterer, J.; Mutterer J Fau - Ball, V.; Ball V Fau - Voegel, J.-C.; Voegel Jc Fau - Schaaf, P.; Schaaf P Fau - Lavalle, P.; Lavalle, P., Mechanotransductive surfaces for reversible biocatalysis activation. (1476-1122 (Print)).

107. Parlak, O.; Turner, A. P. F.; Tiwari, A., On/Off-Switchable Zipper-Like Bioelectronics on a Graphene Interface. *Advanced Materials* **2014,** *26* (3), 482-486.
108. Pinyou, P.; Ruff, A.; Pöller, S.; Barwe, S.; Nebel, M.; Alburquerque, N. G.; Wischerhoff, E.; Laschewsky, A.; Schmaderer, S.; Szeponik, J.; Plumeré, N.; Schuhmann, W., Thermoresponsive amperometric glucose biosensor. *Biointerphases* **2015,** *11* (1), 011001.
109. Horsley, J. R.; Yu, J.; Wegener, K. L.; Hoppmann, C.; Rück-Braun, K.; Abell, A. D., Photoswitchable peptide-based 'on-off' biosensor for electrochemical detection and control of protein-protein interactions. *Biosensors and Bioelectronics* **2018,** *118*, 188-194.
110. Pearson, D.; Downard Aj Fau - Muscroft-Taylor, A.; Muscroft-Taylor A Fau - Abell, A. D.; Abell, A. D., Reversible photoregulation of binding of alpha-chymotrypsin to a gold surface. (1520-5126 (Electronic)).
111. Lee, E.-j.; Luo, W.; Chan, E. W. L.; Yousaf, M. N., A Molecular Smart Surface for Spatio-Temporal Studies of Cell Mobility. *PLOS ONE* **2015,** *10* (6), e0118126.
112. Ng, C. C. A.; Magenau, A.; Ngalim, S. H.; Ciampi, S.; Chockalingham, M.; Harper, J. B.; Gaus, K.; Gooding, J. J., Using an Electrical Potential to Reversibly Switch Surfaces between Two States for Dynamically Controlling Cell Adhesion. *Angewandte Chemie International Edition* **2012,** *51* (31), 7706-7710.
113. Wei, Y.; Zeng, Q.; Huang, J.; Hu, Q.; Guo, X.; Wang, L., An electro-responsive imprinted biosensor with switchable affinity toward proteins. *Chemical Communications* **2018,** *54* (66), 9163-9166.
114. Lahann, J.; Mitragotri S Fau - Tran, T.-N.; Tran Tn Fau - Kaido, H.; Kaido H Fau - Sundaram, J.; Sundaram J Fau - Choi, I. S.; Choi Is Fau - Hoffer, S.; Hoffer S Fau - Somorjai, G. A.; Somorjai Ga Fau - Langer, R.; Langer, R., A reversibly switching surface. (1095-9203 (Electronic)).
115. Pranzetti, A.; Mieszkin S Fau - Iqbal, P.; Iqbal P Fau - Rawson, F. J.; Rawson Fj Fau - Callow, M. E.; Callow Me Fau - Callow, J. A.; Callow Ja Fau - Koelsch, P.; Koelsch P Fau - Preece, J. A.; Preece Ja Fau - Mendes, P. M.; Mendes, P. M., An electrically reversible switchable surface to control and study early bacterial adhesion dynamics in real-time. (1521-4095 (Electronic)).
116. Liu, Y.; Mu, L.; Liu, B.; Zhang, S.; Yang, P.; Kong, J., Controlled protein assembly on a switchable surface. *Chemical Communications* **2004,** (10), 1194-1195.
117. Mu, L.; Liu, Y.; Cai, S.; Kong, J., A Smart Surface in a Microfluidic Chip for Controlled Protein Separation. *Chemistry – A European Journal* **2007,** *13* (18), 5113-5120.
118. Lashkor, M.; Rawson, F. J.; Stephenson-Brown, A.; Preece, J. A.; Mendes, P. M., Electrically-driven modulation of surface-grafted RGD peptides for manipulation of cell adhesion. *Chemical Communications* **2014,** *50* (98), 15589-15592.
119. Rant, U.; Arinaga, K.; Scherer, S.; Pringsheim, E.; Fujita, S.; Yokoyama, N.; Tornow, M.; Abstreiter, G., Switchable DNA interfaces for the highly sensitive detection of label-free DNA targets. *Proceedings of the National Academy of Sciences* **2007,** *104* (44), 17364.
120. Ma, X.; Gosai, A.; Balasubramanian, G.; Shrotriya, P., Aptamer based electrostatic-stimuli responsive surfaces for on-demand binding/unbinding of a specific ligand. *Journal of Materials Chemistry B* **2017,** *5* (20), 3675-3685.
121. Parthasarathy, P.; Mendes Pm Fau - Schopf, E.; Schopf E Fau - Preece, J. A.; Preece Ja Fau - Stoddart, F.; Stoddart F Fau - Chen, Y.; Chen, Y., Spatially controlled assembly of nanomaterials at the nanoscale. (1533-4880 (Print)).
122. W, D. J.; Ludmila, B.; Emil, C.; Claudio, D. V.; Lucyna, H.; Abraham, M.; Stefano, S., Contact angles: history of over 200 years of open questions. *Surface Innovations* **2020,** *8* (1-2), 3-27.
123. Law, K. Y., Definitions for Hydrophilicity, Hydrophobicity, and Superhydrophobicity: Getting the Basics Right. (1948-7185 (Electronic)).
124. Wang, J.; Wu, Y.; Cao, Y.; Li, G.; Liao, Y., Influence of surface roughness on contact angle hysteresis and spreading work. *Colloid and Polymer Science* **2020,** *298* (8), 1107-1112.
125. Cassie, A. B. D., Contact angles. *Discussions of the Faraday Society* **1948,** *3* (0), 11-16.

126. Collins, R. W.; Fujiwara, H., *Spectroscopic Ellipsometry for Photovoltaics : Volume 1: Fundamental Principles and Solar Cell Characterization*. 1st ed.; Springer International Publishing : Imprint: Springer,: Cham, 2018.
127. Tompkins, H. G., *A user's guide to ellipsometry*. Academic Press: Boston, 1993; p xv, 260 p.
128. Eichhorn, K.-J.; Hinrichs, K., *Ellipsometry of Functional Organic Surfaces and Films*. 2nd ed.; Springer International Publishing : Imprint: Springer,: Cham, 2018.
129. Mora, M. F.; Wehmeyer, J. L.; Synowicki, R.; Garcia, C. D., Investigating Protein Adsorption via Spectroscopic Ellipsometry. In *Biological Interactions on Materials Surfaces: Understanding and Controlling Protein, Cell, and Tissue Responses*, Puleo, D. A.; Bizios, R., Eds. Springer US: New York, NY, 2009; pp 19-41.
130. Stevie, F. A.; Donley, C. L., Introduction to x-ray photoelectron spectroscopy. *Journal of Vacuum Science & Technology A* **2020,** *38* (6), 063204.
131. Stojilovic, N., Why Can't We See Hydrogen in X-ray Photoelectron Spectroscopy? *Journal of Chemical Education* **2012,** *89* (10), 1331-1332.
132. Cushman, C.; Chatterjee, S.; Major, G.; Smith, N.; Roberts, A.; Linford, M., Trends in Advanced XPS Instrumentation. 1. Overview of the Technique, Automation, High Sensitivity, Imaging, Snapshot Spectroscopy, Gas Cluster Ion Beams, and Multiple Analytical Techniques on the Instrument. *Vacuum Technology & Coating* **2016**.
133. Fairley, N., *CasaXPS manual 2.3.15*. Casa Software Ltd.: [Place of publication not identified], 2009.
134. Briggs, D., Handbook of X-ray Photoelectron Spectroscopy C. D. Wanger, W. M. Riggs, L. E. Davis, J. F. Moulder and G. E.Muilenberg Perkin-Elmer Corp., Physical Electronics Division, Eden Prairie, Minnesota, USA, 1979. 190 pp. $195. *Surface and Interface Analysis* **1981,** *3* (4), v-v.
135. Smith, G., Evaluation of a Simple Correction for the Hydrocarbon Contamination Layer in Quantitative Surface Analysis by XPS. *Journal of Electron Spectroscopy and Related Phenomena* **2005,** *148*, 21–28.
136. Zorn, G.; Liu, L.-H.; Árnadóttir, L.; Wang, H.; Gamble, L. J.; Castner, D. G.; Yan, M., X-ray Photoelectron Spectroscopy Investigation of the Nitrogen Species in Photoactive Perfluorophenylazide-Modified Surfaces. *The Journal of Physical Chemistry C* **2014,** *118* (1), 376-383.
137. Bailey, J.; Havelund, R.; Shard, A. G.; Gilmore, I. S.; Alexander, M. R.; Sharp, J. S.; Scurr, D. J., 3D ToF-SIMS Imaging of Polymer Multilayer Films Using Argon Cluster Sputter Depth Profiling. *ACS Applied Materials & Interfaces* **2015,** *7* (4), 2654-2659.
138. Huang, D.; Hua, X.; Xiu, G. L.; Zheng, Y. J.; Yu, X. Y.; Long, Y. T., Secondary ion mass spectrometry: The application in the analysis of atmospheric particulate matter. (1873-4324 (Electronic)).
139. Broekaert, J. A. C.; Hywel Evans, E., Atomic Spectroscopy. *Handbook of Analytical Techniques* **2001**, 627-726.
140. Kotowska, A. M.; Trindade, G. F.; Mendes, P. M.; Williams, P. M.; Aylott, J. W.; Shard, A. G.; Alexander, M. R.; Scurr, D. J., Protein identification by 3D OrbiSIMS to facilitate in situ imaging and depth profiling. *Nature Communications* **2020,** *11* (1), 5832.
141. Passarelli, M. K.; Pirkl, A.; Moellers, R.; Grinfeld, D.; Kollmer, F.; Havelund, R.; Newman, C. F.; Marshall, P. S.; Arlinghaus, H.; Alexander, M. R.; West, A.; Horning, S.; Niehuis, E.; Makarov, A.; Dollery, C. T.; Gilmore, I. S., The 3D OrbiSIMS—label-free metabolic imaging with subcellular lateral resolution and high mass-resolving power. *Nature Methods* **2017,** *14* (12), 1175-1183.
142. Gill, P.; Ranjbar, B., Circular Dichroism Techniques: Biomolecular and Nanostructural Analyses- A Review. *Chemical biology & drug design. 74* (2), 101-120.
143. Kelly, S. M.; Price, N. C., The use of circular dichroism in the investigation of protein structure and function. (1389-2037 (Print)).
144. Pignataro, M. F.; Herrera, M. G.; Dodero, V. I., Evaluation of Peptide/Protein Self-Assembly and Aggregation by Spectroscopic Methods. *Molecules* **2020,** *25* (20), 4854.

145. Bulheller, B. M.; Rodger, A.; Hirst, J. D., Circular and linear dichroism of proteins. *Physical Chemistry Chemical Physics* **2007,** *9* (17), 2020-2035.
146. Schasfoort, R. B. M., Chapter 2 History and Physics of Surface Plasmon Resonance. In *Handbook of Surface Plasmon Resonance (2)*, The Royal Society of Chemistry: 2017; pp 27-59.
147. de Mol, N. J.; Fischer, M. J. E., Surface Plasmon Resonance: A General Introduction. In *Surface Plasmon Resonance: Methods and Protocols*, Mol, N. J.; Fischer, M. J. E., Eds. Humana Press: Totowa, NJ, 2010; pp 1-14.
148. Juan-Colás, J.; Johnson, S.; Krauss, T. F., Dual-Mode Electro-Optical Techniques for Biosensing Applications: A Review. *Sensors* **2017,** *17* (9).
149. Ta, D. T.; Guedens, W.; Vranken, T.; Vanschoenbeek, K.; Redeker, E. S.; Michiels, L.; Adriaensens, P., Enhanced Biosensor Platforms for Detecting the Atherosclerotic Biomarker VCAM1 Based on Bioconjugation with Uniformly Oriented VCAM1-Targeting Nanobodies. *Biosensors-Basel* **2016,** *6* (3), 34.
150. Goossens, J.; Sein, H.; Lu, S.; Radwanska, M.; Muyldermans, S.; Sterckx, Y. G. J.; Magez, S., Functionalization of gold nanoparticles with nanobodies through physical adsorption. *Analytical Methods* **2017,** *9* (23), 3430-3440.
151. Van de Broek, B.; Devoogdt, N.; D'Hollander, A.; Gijs, H. L.; Jans, K.; Lagae, L.; Muyldermans, S.; Maes, G.; Borghs, G., Specific Cell Targeting with Nanobody Conjugated Branched Gold Nanoparticles for Photothermal Therapy. *ACS Nano* **2011,** *5* (6), 4319-4328.
152. Fu, J.; Li, J.; Wang, W.; Wu, H.; Zhou, P.; Li, Y.; He, Q.; Tu, Z., One-step orientated immobilization of nanobodies and its application for immunoglobulin purification. *Journal of Chromatography A* **2019,** *1603*, 15-22.
153. Steen Redeker, E.; Ta, D. T.; Cortens, D.; Billen, B.; Guedens, W.; Adriaensens, P., Protein Engineering For Directed Immobilization. *Bioconjug. Chem.* **2013,** *24* (11), 1761-1777.
154. Liu, J.; Jalali, M.; Mahshid, S.; Wachsmann-Hogiu, S., Are plasmonic optical biosensors ready for use in point-of-need applications? *Analyst* **2020,** *145* (2), 364-384.
155. Prats-Alfonso, E.; Albericio, F., Functionalization of gold surfaces: recent developments and applications. *J. Mater. Sci.* **2011,** *46* (24), 7643-7648.
156. Ding, S. W.; Mosher, C.; Lee, X. Y.; Das, S. R.; Cargill, A. A.; Tang, X. H.; Chen, B. L.; McLamore, E. S.; Gomes, C.; Hostetter, J. M.; Claussen, J. C., Rapid and Label-Free Detection of Interferon Gamma via an Electrochemical Aptasensor Comprising a Ternary Surface Monolayer on a Gold Interdigitated Electrode Array. *ACS Sens.* **2017,** *2* (2), 210-217.
157. Porada, R.; Jedlinska, K.; Lipinska, J.; Bas, B., Review-Voltammetric Sensors with Laterally Placed Working Electrodes: A Review. *Journal of the Electrochemical Society* **2020,** *167* (3), 037536.
158. Chen, Z.; Zhou, J.; Tang, H.; Liu, Y.; Shen, Y. P.; Yin, X. B.; Zheng, J. P.; Zhang, H. S.; Wu, J. H.; Shi, X. L.; Chen, Y. Q.; Fu, Y. Q.; Duan, H. G., Ultrahigh-Frequency Surface Acoustic Wave Sensors with Giant Mass-Loading Effects on Electrodes. *ACS Sens.* **2020,** *5* (6), 1657-1664.
159. Ripa, R.; Shen, A. Q.; Funari, R., Detecting Escherichia coli Biofilm Development Stages on Gold and Titanium by Quartz Crystal Microbalance. *ACS Omega* **2020,** *5* (5), 2295-2302.
160. Stephenson-Brown, A.; Wang, H. C.; Iqbal, P.; Preece, J. A.; Long, Y. T.; Fossey, J. S.; James, T. D.; Mendes, P. M., Glucose selective Surface Plasmon Resonance-based bis-boronic acid sensor. *Analyst* **2013,** *138* (23), 7140-7145.
161. Hutter, E.; Fendler, J. H., Exploitation of localized surface plasmon resonance. *Advanced Materials* **2004,** *16* (19), 1685-1706.
162. Rickard, J. J. S.; Di-Pietro, V.; Smith, D. J.; Davies, D. J.; Belli, A.; Oppenheimer, P. G., Rapid optofluidic detection of biomarkers for traumatic brain injury via surface-enhanced Raman spectroscopy. *Nature Biomedical Engineering* **2020,** *4* (6), 610-623.
163. Bala, G.; Blykers, A.; Xavier, C.; Descamps, B.; Broisat, A.; Ghezzi, C.; Fagret, D.; Van Camp, G.; Caveliers, V.; Vanhove, C.; Lahoutte, T.; Droogmans, S.; Cosyns, B.; Devoogdt, N.; Hernot, S.,

Targeting of vascular cell adhesion molecule-1 by 18F-labelled nanobodies for PET/CT imaging of inflamed atherosclerotic plaques. (2047-2412 (Electronic)).
164. Cooper, E.; Krebs, F.; Smith, M.; Raval, R., The interaction of amino acids with metals: Methionine on gold. *Journal of Electron Spectroscopy and Related Phenomena* **1993,** *64-65*, 469-475.
165. Naitabdi, A.; Humblot, V., Chiral self-assemblies of amino-acid molecules: D- and L-methionine on Au(111) surface. *Appl. Phys. Lett.* **2010,** *97* (22), 223112.
166. Humblot, V.; Tielens, F.; Luque, N. B.; Hampartsoumian, H.; Méthivier, C.; Pradier, C.-M., Characterization of Two-Dimensional Chiral Self-Assemblies l- and d-Methionine on Au(111). *Langmuir* **2014,** *30* (1), 203-212.
167. Rios, F.; Smirnov, S., Biochemically Responsive Smart Surface. *ACS Applied Materials & Interfaces* **2009,** *1* (4), 768-774.
168. Nikonenko, N. A.; Bushnak, B. A.; Keddie, J. L., Spectroscopic Ellipsometry of Mucin Layers on an Amphiphilic Diblock Copolymer Surface. *Appl. Spectrosc.* **2009,** *63* (8), 889-898.
169. Schnyder, B.; Kötz, R.; Alliata, D.; Facci, P., Comparison of the self-chemisorption of azurin on gold and on functionalized oxide surfaces. *Surface and Interface Analysis* **2002,** *34* (1), 40-44.
170. Lhoest, J. B.; Wagner Ms Fau - Tidwell, C. D.; Tidwell Cd Fau - Castner, D. G.; Castner, D. G., Characterization of adsorbed protein films by time of flight secondary ion mass spectrometry. *J Biomed Mater Res* **2001,** *57* (3), 432-440.
171. White, S. J.; Johnson, S. D.; Sellick, M. A.; Bronowska, A.; Stockley, P. G.; Wälti, C., The Influence of Two-Dimensional Organization on Peptide Conformation. *Angewandte Chemie International Edition* **2015,** *54* (3), 974-978.
172. Dmitriev, O. Y.; Lutsenko, S.; Muyldermans, S., Nanobodies as Probes for Protein Dynamics in Vitro and in Cells. *J. Biol. Chem.* **2016,** *291* (8), 3767-3775.
173. Muyldermans, S., Single domain camel antibodies: current status. *J. Biotechnol.* **2001,** *74* (4), 277-302.
174. Kubiak-Ossowska, K.; Mulheran, P. A.; Nowak, W., Fibronectin module FN(III)9 adsorption at contrasting solid model surfaces studied by atomistic molecular dynamics. *J. Phys. Chem. B* **2014,** *118* (33), 9900-9908.
175. Wang, A.; Vangala, K.; Vo, T.; Zhang, D.; Fitzkee, N. C., A Three-Step Model for Protein–Gold Nanoparticle Adsorption. *The Journal of Physical Chemistry C* **2014,** *118* (15), 8134-8142.
176. Bekker, G.-J.; Ma, B.; Kamiya, N., Thermal stability of single-domain antibodies estimated by molecular dynamics simulations. *Protein Sci.* **2019,** *28* (2), 429-438.
177. Selvakannan, P. R.; Mandal, S.; Phadtare, S.; Pasricha, R.; Sastry, M., Capping of Gold Nanoparticles by the Amino Acid Lysine Renders Them Water-Dispersible. *Langmuir* **2003,** *19* (8), 3545-3549.
178. de la Llave, E.; Clarenc, R.; Schiffrin, D. J.; Williams, F. J., Organization of Alkane Amines on a Gold Surface: Structure, Surface Dipole, and Electron Transfer. *The Journal of Physical Chemistry C* **2014,** *118* (1), 468-475.
179. Liu, Y.; Yu, J., Oriented immobilization of proteins on solid supports for use in biosensors and biochips: a review. *Microchimica Acta* **2016,** *183* (1), 1-19.
180. Yong, K. W.; Yuen, D.; Chen, M. Z.; Porter, C. J. H.; Johnston, A. P. R., Pointing in the Right Direction: Controlling the Orientation of Proteins on Nanoparticles Improves Targeting Efficiency. *Nano Letters* **2019,** *19* (3), 1827-1831.
181. Sun, X.-L.; Stabler, C. L.; Cazalis, C. S.; Chaikof, E. L., Carbohydrate and Protein Immobilization onto Solid Surfaces by Sequential Diels−Alder and Azide−Alkyne Cycloadditions. *Bioconjug. Chem.* **2006,** *17* (1), 52-57.
182. Rothbauer, U.; Zolghadr, K.; Muyldermans, S.; Schepers, A.; Cardoso, M. C.; Leonhardt, H., A Versatile Nanotrap for Biochemical and Functional Studies with Fluorescent Fusion Proteins *. *Molecular & Cellular Proteomics* **2008,** *7* (2), 282-289.

183. Kubala, M. H.; Kovtun, O.; Alexandrov, K.; Collins, B. M., Structural and thermodynamic analysis of the GFP:GFP-nanobody complex. *Protein Sci* **2010,** *19* (12), 2389-401.
184. Fies, W. A.; Dugger, J. W.; Dick, J. E.; Wilder, L. M.; Browning, K. L.; Doucet, M.; Browning, J. F.; Webb, L. J., Direct Measurement of Water Permeation in Submerged Alkyl Thiol Self-Assembled Monolayers on Gold Surfaces Revealed by Neutron Reflectometry. *Langmuir* **2019,** *35* (16), 5647-5662.
185. Shakiba, A.; Jamison, A. C.; Lee, T. R., Poly(l-lysine) Interfaces via Dual Click Reactions on Surface-Bound Custom-Designed Dithiol Adsorbates. *Langmuir* **2015,** *31* (22), 6154-6163.
186. Dodero, G.; Michieli, L. D.; Cavalleri, O.; Rolandi, R.; Oliveri, L.; Daccà, A.; Parodi, R., L-Cysteine chemisorption on gold: an XPS and STM study. *Colloids and Surfaces* **2000,** *175*, 121-128.
187. Arisnabarreta, N.; Ruano, G. D.; Lingenfelder, M.; Patrito, E. M.; Cometto, F. P., Comparative Study of the Adsorption of Thiols and Selenols on Au(111) and Au(100). *Langmuir* **2017,** *33* (48), 13733-13739.
188. Darlatt, E.; Traulsen, C. H. H.; Poppenberg, J.; Richter, S.; Kühn, J.; Schalley, C. A.; Unger, W. E. S., Evidence of click and coordination reactions on a self-assembled monolayer by synchrotron radiation based XPS and NEXAFS. *Journal of Electron Spectroscopy and Related Phenomena* **2012,** *185* (3), 85-89.
189. Sinha, S.; Mukherjee, M., A study of adventitious contamination layers on technically important substrates by photoemission and NEXAFS spectroscopies. *Vacuum* **2018,** *148*, 48-53.
190. Strong, L.; Whitesides, G. M., Structures of self-assembled monolayer films of organosulfur compounds adsorbed on gold single crystals: electron diffraction studies. *Langmuir* **1988,** *4* (3), 546-558.
191. Harder, P.; Grunze, M.; Dahint, R.; Whitesides, G. M.; Laibinis, P. E., Molecular Conformation in Oligo(ethylene glycol)-Terminated Self-Assembled Monolayers on Gold and Silver Surfaces Determines Their Ability To Resist Protein Adsorption. *The Journal of Physical Chemistry B* **1998,** *102* (2), 426-436.
192. Sokalingam, S.; Raghunathan G Fau - Soundrarajan, N.; Soundrarajan N Fau - Lee, S.-G.; Lee, S. G., A study on the effect of surface lysine to arginine mutagenesis on protein stability and structure using green fluorescent protein. (1932-6203 (Electronic)).
193. Wu, M.; Feng, Q.; Sun, X.; Wang, H.; Gielen, G.; Wu, W., Rice (Oryza sativa L) plantation affects the stability of biochar in paddy soil. *Scientific Reports* **2015,** *5* (1), 10001.
194. Nelson, K. E.; Gamble, L.; Jung, L. S.; Boeckl, M. S.; Naeemi, E.; Golledge, S. L.; Sasaki, T.; Castner, D. G.; Campbell, C. T.; Stayton, P. S., Surface Characterization of Mixed Self-Assembled Monolayers Designed for Streptavidin Immobilization. *Langmuir* **2001,** *17* (9), 2807-2816.
195. Wang, H.; Chen, S.; Li, L.; Jiang, S., Improved Method for the Preparation of Carboxylic Acid and Amine Terminated Self-Assembled Monolayers of Alkanethiolates. *Langmuir* **2005,** *21* (7), 2633-2636.
196. Bae, Y.; Oh, B.-K.; Lee, W.; Lee, W.; Choi, J.-W., Study on orientation of immunoglobulin G on protein G layer. *Biosensors and Bioelectronics* **2005,** *21* (1), 103-110.
197. Yeung Chun, L.; Iqbal, P.; Allan, M.; Lashkor, M.; Preece Jon, A.; Mendes Paula, M., Tuning Specific Biomolecular Interactions Using Electro-Switchable Oligopeptide Surfaces. *Advanced Functional Materials* **2010,** *20* (16), 2657-2663.
198. Pranzetti, A.; Davis, M.; Yeung, C. L.; Preece, J. A.; Koelsch, P.; Mendes, P. M., Direct Observation of Reversible Biomolecule Switching Controlled By Electrical Stimulus. *Adv Mater Interfaces* **2014,** *1* (5).
199. Yeung, C. L.; Wang, X. Y.; Lashkor, M.; Cantini, E.; Rawson, F. J.; Iqbal, P.; Preece, J. A.; Ma, J.; Mendes, P. M., Modulation of Biointeractions by Electrically Switchable Oligopeptide Surfaces: Structural Requirements and Mechanism. *Adv Mater Interfaces* **2014,** *1* (2).
200. Safazadeh, L.; Berron, B. J., Photopatterning of Stable, Low-Density, Self-Assembled Mono layers on Gold. *Langmuir* **2015,** *31* (9), 2689-2696.

201. Love, J. C.; Wolfe, D. B.; Haasch, R.; Chabinyc, M. L.; Paul, K. E.; Whitesides, G. M.; Nuzzo, R. G., Formation and Structure of Self-Assembled Monolayers of Alkanethiolates on Palladium. *Journal of the American Chemical Society* **2003,** *125* (9), 2597-2609.
202. Fears, K. P.; Creager, S. E.; Latour, R. A., Determination of the Surface pK of Carboxylic- and Amine-Terminated Alkanethiols Using Surface Plasmon Resonance Spectroscopy. *Langmuir* **2008,** *24* (3), 837-843.
203. Lahiri, J.; Isaacs L Fau - Tien, J.; Tien J Fau - Whitesides, G. M.; Whitesides, G. M., A strategy for the generation of surfaces presenting ligands for studies of binding based on an active ester as a common reactive intermediate: a surface plasmon resonance study. (0003-2700 (Print)).
204. Yeo, W.-S.; Yousaf, M. N.; Mrksich, M., Dynamic Interfaces between Cells and Surfaces: Electroactive Substrates that Sequentially Release and Attach Cells. *Journal of the American Chemical Society* **2003,** *125* (49), 14994-14995.
205. Chen, X.; Zaro, J. L.; Shen, W.-C., Fusion protein linkers: Property, design and functionality. *Advanced Drug Delivery Reviews* **2013,** *65* (10), 1357-1369.
206. Canaria, C. A.; So, J.; Maloney, J. R.; Yu, C. J.; Smith, J. O.; Roukes, M. L.; Fraser, S. E.; Lansford, R., Formation and removal of alkylthiolate self-assembled monolayers on gold in aqueous solutions. *Lab on a Chip* **2006,** *6* (2), 289-295.
207. Kankate, L.; Werner U Fau - Turchanin, A.; Turchanin A Fau - Gölzhäuser, A.; Gölzhäuser A Fau - Grossmann, H.; Grossmann H Fau - Tampé, R.; Tampé, R., Protein resistant oligo(ethylene glycol) terminated self-assembled monolayers of thiols on gold by vapor deposition in vacuum. (1559-4106 (Electronic)).
208. Zhang, J.; Parlak, Z.; Bowers, C. M.; Oas, T.; Zauscher, S., Mapping mechanical properties of organic thin films by force-modulation microscopy in aqueous media. *Beilstein J Nanotechnol* **2012,** *3*, 464-74.
209. Laibinis, P. E.; Fox, M. A.; Folkers, J. P.; Whitesides, G. M., Comparisons of Self-Assembled Monolayers on Silver and Gold: Mixed Monolayers Derived from HS(CH2)21X and HS(CH2)10Y (X, Y = CH3, CH2OH) Have Similar Properties. *Langmuir* **1991,** *7*, 3167-3173.
210. Ishida, T.; Nishida, N.; Tsuneda, S.; Hara, M.; Sasabe, H.; Knoll, W., Alkyl Chain Length Effect on Growth Kinetics of n-Alkanethiol Self-Assembled Monolayers on Gold Studied by X-Ray Photoelectron Spectroscopy. *Japanese Journal of Applied Physics* **1996,** *35* (Part 2, No. 12B), L1710-L1713.
211. Zubavichus, Y.; Fuchs O Fau - Weinhardt, L.; Weinhardt L Fau - Heske, C.; Heske C Fau - Umbach, E.; Umbach E Fau - Denlinger, J. D.; Denlinger Jd Fau - Grunze, M.; Grunze, M., Soft X-ray-induced decomposition of amino acids: an XPS, mass spectrometry, and NEXAFS study. (0033-7587 (Print)).
212. Gao, F.; Wang, Y.; Burkholder, L.; Tysoe, W. T., Chemistry of l-proline on Pd(111): Temperature-programmed desorption and X-ray photoelectron spectroscopic study. *Surface Science* **2007,** *601* (17), 3579-3588.
213. Chang, Y.-W.; Ukiwe, C.; Kwok, D. Y., Chain length effect of alkanethiol self-assembled monolayers on the maximum spreading ratio of impacting water droplets. *Colloids and Surfaces A: Physicochemical and Engineering Aspects* **2005,** *260* (1), 255-263.
214. Yeung, C. L.; Wang, X.; Lashkor, M.; Cantini, E.; Rawson, F. J.; Iqbal, P.; Preece, J. A.; Ma, J.; Mendes, P. M., Modulation of Biointeractions by Electrically Switchable Oligopeptide Surfaces: Structural Requirements and Mechanism. *Advanced Materials Interfaces* **2014,** *1* (2), 1300085.
215. Broisat, A.; Hernot, S.; Toczek, J.; De Vos, J.; Riou, L. M.; Martin, S.; Ahmadi, M.; Thielens, N.; Wernery, U.; Caveliers, V.; Muyldermans, S.; Lahoutte, T.; Fagret, D.; Ghezzi, C.; Devoogdt, N., Nanobodies Targeting Mouse/Human VCAM1 for the Nuclear Imaging of Atherosclerotic Lesions. *Circulation Research* **2012,** *110* (7), 927-937.

216. Phillips, J. C.; Braun, R.; Wang, W.; Gumbart, J.; Tajkhorshid, E.; Villa, E.; Chipot, C.; Skeel, R. D.; Kalé, L.; Schulten, K., Scalable molecular dynamics with NAMD. *Journal of Computational Chemistry* **2005,** *26* (16), 1781-1802.
217. Humphrey, W.; Dalke, A.; Schulten, K., VMD: Visual molecular dynamics. *Journal of Molecular Graphics* **1996,** *14* (1), 33-38.
218. Kelley, L. A.; Mezulis, S.; Yates, C. M.; Wass, M. N.; Sternberg, M. J. E., The Phyre2 web portal for protein modeling, prediction and analysis. *Nature Protocols* **2015,** *10* (6), 845-858.
219. Le Guilloux, V.; Schmidtke, P.; Tuffery, P., Fpocket: An open source platform for ligand pocket detection. *BMC Bioinformatics* **2009,** *10* (1), 168.
220. Heinz, H.; Farmer, B. L.; Pandey, R. B.; Slocik, J. M.; Patnaik, S. S.; Pachter, R.; Naik, R. R., Nature of molecular interactions of peptides with gold, palladium, and Pd-Au bimetal surfaces in aqueous solution. *J Am Chem Soc* **2009,** *131* (28), 9704-14.
221. Feng, J.; Pandey, R. B.; Berry, R. J.; Farmer, B. L.; Naik, R. R.; Heinz, H., Adsorption mechanism of single amino acid and surfactant molecules to Au {111} surfaces in aqueous solution: design rules for metal-binding molecules. *Soft Matter* **2011,** *7* (5), 2113-2120.
222. Kastenholz, M. A.; Hünenberger, P. H., Influence of Artificial Periodicity and Ionic Strength in Molecular Dynamics Simulations of Charged Biomolecules Employing Lattice-Sum Methods. *The Journal of Physical Chemistry B* **2004,** *108* (2), 774-788.
223. Rai, B.; Sathish, P.; Malhotra, C. P.; Pradip; Ayappa, K. G., Molecular Dynamic Simulations of Self-Assembled Alkylthiolate Monolayers on an Au(111) Surface. *Langmuir* **2004,** *20* (8), 3138-3144.